# Thermal transport mechanisms across solid-state phase transformations

---

A Dissertation Presented to the
Faculty of the School of Engineering and Applied Science
University of Virginia

In Partial Fulfillment
of the Requirements for the Degree of
Doctor of Philosophy
Mechanical and Aerospace Engineering

---

Kiumars Aryana
March 2022

# APPROVAL SHEET

The dissertation is submitted in partial fulfillment of the
requirements for the degree of

Doctor of Philosophy in Mechanical and Aerospace Engineering

Kiumars Aryana

This dissertation has been read and approved by the Examining Committee:

Patrick E. Hopkins, Advisor

Keivan Esfarjani, Chair

Nikhil Shukla

Stephen J. McDonnell

Derek A. Stewart

Michael K. Grobis

Accepted for the School of Engineering and Applied Science:

Jennifer L. West, Dean
School of Engineering and Applied Science

March 2022

# Abstract

The primary objective of this dissertation is to provide insight into how thermal transport mechanisms change as a result of solid-state phase transformations. In this respect, depending on the nature of the change in the atomic or electronic structure, various forms of solid-state phase transformations could take place. For instance, phase transformations could occur as a result of structural changes in the material either from amorphous-to-crystalline phases such as chalcogenide-based phase-change materials, or crystalline-to-crystalline phases such as ferroelectric and antiferroelectric materials. Alternatively, the phase transformation could occur as a result of a purely electronic change such as metal-insulator transition or threshold switching. Regardless of the phase transformation mechanism, all of these processes lead to substantial changes in the electrical, optical, and thermal properties of materials.

In this dissertation, I strive to improve our understanding of these reversible phase transformations and the degree to which each mechanism could alter the transport of energy carriers in materials from a nanoscale thermal science perspective. Specifically, using conventional optical pump-probe thermometry techniques, this dissertation aims to interrogate the changes in thermal properties such as thermal conductivity, thermal boundary conductance, specific heat, and sound velocity upon phase transformations. For this purpose, I target four prevalent classes of phase transformation mechanisms: (i) metallic phase transformation, i.e. amorphous-to-crystalline *with* metal-insulator transition, (ii) non-metallic phase transformation, i.e. amorphous-to-crystalline *without* metal-insulator transition, (iii) antiferroelectric-to-ferroelectric, and (iv) antiferroelectric-to-paraelectric. I explore phase transformation across a wide range of materials, from chalcogenide-based phase-change materials such as $Ge_2Sb_2Te_4$ to antiferroelectric perovskites such as $PbZrO_3$. This work not only has far-reaching implications in both foundational physics and engineering but also

due to the ubiquity of phase transformation phenomena in the industry, it has direct applications in the improvement of future nanoscale electronics, photonics, thermoelectrics, and thermal circuits.

# Acknowledgements

The work presented in this dissertation would not have been possible without the continuous support, sacrifice, and encouragement of great people around me who helped shape my character both on a personal and professional level. I feel deeply indebted to my family, advisors, mentors, colleagues, and friends who have stood by my side and supported me throughout my academic journey for the past 12 years.

My primary appreciation is owed to my Ph.D. advisor, Prof. Patrick Hopkins, whose enthusiasm and passion for research has been a constant source of inspiration and scientific curiosity throughout my Ph.D. While I was thinking about transitioning to industry after I completed my master's, talking with Patrick for fifteen minutes over the phone was sufficient to persuade me to change my mind and join his lab. As I look back on my four years as Patrick's student, I consider myself extremely lucky to have had him as an advisor. I was astonished from the beginning at how much Patrick was involved in research, and the extensive guidance and support I received from him has been a major factor in what I have achieved today.

Next, I would like to thank my committee members, Prof. Keivan Esfarjani, Prof. Nikhil Shukla, Dr. Derek Stewart, and Dr. Michael Grobis, for their guidance through my Ph.D. projects and the drafting of this dissertation. Moreover, I would like to particularly thank Prof. Stephen McDonnell for agreeing to step in as a committee member on short notice. My heartfelt thanks to Derek and Mike for allowing me to work closely with them on the development of next-generation phase-change memory devices; their insight and guidance in our biweekly meetings fueled my motivation and added significant value to my studies.

I would also like to extend a huge thanks to all the ExSiTE lab members, past and present. I am extremely grateful to have had the opportunity to join the ExSiTE lab at the time of legendary researchers such as Dr. John Gaskins, Dr. Jeff Braun, Dr. Rouzbeh Rastgar, Dr. John Tomko, Dr. Dave Olson, and Dr. Ethan Scott, from whom I have learned

a great deal and shared wonderful times. Graduate school would not have been the same without my late-night research companions and good friends, Shafkat and Yee Rui who have constantly supported and encouraged me in the past few years. I would like to thank Dr. Eric Hoglund for his unprecedented spectroscopy skills that elevated my research to another level. I wish to thank current ExSiTE lab members, Thomas, Emma, Milena, Will, Rafiqul, Sara, Daniel, Riffe, and Mahboube for cheering me up with interesting conversations during our break times. Also, a huge thanks to my gym buddies, Tomko and Rafiqul, who constantly pushed me and inspired me to a healthier lifestyle.

I wish to acknowledge the contributions and collaboration of multiple researchers and scientists from academia to the industry. I owe a huge debt to our research collaborators at Western Digital, Dr. Joyeeta Nag, Dr. Derek A. Stewart, Dr. Michael K. Grobis, Dr. John C. Read, and Dr. Zhaoqiang Bai, who not only provided the PCM samples and scientific insight about the project but also financially supported my research in the past four years. I would like to thank our collaborators at MIT, Dr. Yifei Zhang, Prof. Carlos Ríos, and Prof. Juejun Hu, as well as our collaborators at UC Berkeley, Dr. Ran Gao, and Prof. Lane W. Martin, for providing us with great samples for characterizing their thermal properties. I would also like to thank our collaborators here at UVA, Prof. Jon F. Ihlefeld and Dr. Takanori Mimura, for their great sample fabrication and characterization. I would like to thank Dr. Catherine A. Dukes for her patience in teaching me how to use the XPS tool and her constant support throughout my measurements.

Last but not least, I am deeply grateful to my loving family, who have devoted a great deal of time and energy to guiding and educating me since the very beginning and never gave up on me. There is no doubt that the guidance and life lessons that I have received from my parents, brothers, sisters, and brother-in-laws have provided me with the foundation for everything I have accomplished in life. There are no words to express the love and respect I hold for each of you, and I pray to God that I have lived up to your expectations. A special thanks goes out to my best friend and brother, Saeed Azami, who has stood by my side through thick and thin and has been a true symbol of friendship for me. I want to thank

my friends, Dr. Nazanin Mirshahi, Mr. Amir Ghiami, and Mr. Arman Motaghi for their support and encouragement. I would like to express my deepest thanks to my extended family in the USA, the Fathizadeh family, who have given me the love and affection of a real family in the years I have been away from home. Finally, I have been exceptionally fortunate to have had the greatest second parents in the world, Homa and Houshang, who have treated me like their own son over the past few years. I am genuinely grateful to you for all you have done for me.

Above all my achievements in the past few years, I have been truly blessed to have found my greatest companion and advocate in life, my loving girlfriend Negin, who has helped me thrive both in my professional and personal life. Going to her on the weekends has been the highlight of my every week since the beginning of my Ph.D. career. As a graduate student, I was at times stressed and difficult to cope with, and I am incredibly grateful for the patience you have shown and all the love and care you have given me throughout these years.

“*I dedicate this dissertation to the memory of my beloved father,* ***Shahreza Aryana****, who has been a source of inspiration and principle throughout my life.*”

# Contents

# List of Figures

# List of Tables

# Chapter 1

# Introduction

## 1.1 Background

In 1959, when computers filled up an entire room and lasers were only a theoretical possibility, Richard Feynman gave an iconic talk at the annual American Physical Society meeting titled “There’s Plenty of Room at the Bottom” in which he shared his vision of the possibility of storing the information of all the books in the world in a single piece of dust, incorporating microchips into the human body for assisting organs, and manipulating particles at the atomic length scale [1, 2]. Although Feynman’s vision at the time was considered bold and more of a humorous speech rather than actual scientific possibilities, today, more than 60 years after his talk, we have developed transistors with only a few atoms channel width that are as small as 2 nm [3], optical tweezers that can move a single atom [4, 5], and microscopes that can produce images of atomic structure with sub-Angstrom spatial resolution [6, 7]. As a result of our improved understanding of quantum mechanics, paralleled with breakthroughs in nanotechnology, we have experienced the booming era of information technology since the beginning of $21^{\text{st}}$ century.

One of the major drivers that pushed nanotechnology forward is the relentless search for superior computing architecture that process, transmit, and store information faster and more efficiently. In these technologies, the primary energy carriers that facilitate the processing and transmission of data are electrons in the electronic circuits and more recently photons in the photonic circuits. The transport of these energy carriers usually is followed by generation of unwanted heat which not only results in overheating the circuits but also leads to higher power consumption. This issue became pronounced during 1990's when rapid advancements in nanofabrication led to compacting more and more devices into a unit of area which imposed aggressive thermal loads on the electronic circuits and resulted in impaired performance and malfunctioning of electrical devices. This major issue raised the demand for a greater understanding of thermal transport in nanoscale and fueled the incentive for managing energy flow in the nanoscale leading to the emergence of a more focused discipline commonly referred to as *nanoscale heat transfer.* This subset of thermal transport is concerned with the behavior of materials at dimensions on the order of carriers' mean free paths, which could be drastically different from their bulk counterparts.

## 1.2 Motivation

Thermal management, or the ability to control and engineer the propagation of heat in materials has a plethora of applications from the nanoscale, such as dissipating excessive heat in electronic devices, to the macroscale, such as temperature stabilization of space voyagers and planetary rovers [8–10]. For instance, in deep-space explorations where electronic devices are prone to damage due to intense radiation or extreme temperatures, thermal memory and logic devices that use heat instead of electricity to perform computation could be an alternative backup plan for electronic devices [11, 12]. In this regard, materials that undergo solid-state phase transformations are appealing for actively controlling the electrical [13], optical [14], and thermal properties [15] of materials due to their fast and reversible phase transformations, relatively simple trigger mechanisms, and the absence of any moving components. Understating the mechanism of energy transport in materials that undergo phase transition is fundamentally important as their thermal properties could alter by up to an order of magnitude between their two solid-state phases [16].

One of the most rapidly growing applications of materials that undergo solid-state phase transformations is associated with the storage and processing of information. The thriving data-centric technologies such as the internet of things, machine learning, and artificial intelligence have created unprecedented global demands for faster processing units and high-volume storage devices [17–20]. One major bottleneck in the development of these technologies is the traditional von Neumann computing architecture which separates the memory from the processing unit [21, 22]. This device architecture requires the data to be constantly shuttled back and forth between the memory and processing units, which inflicts considerable costs in latency and power consumption [23]. This has sparked a worldwide effort to find alternative computational paradigms beyond the existing technologies. A potential route for next-generation memory devices is non-von Neumann neuro-inspired memory that mimics the human brain on the basis of resistive memory by storing and processing the data within the memory cell itself [24–26]. In addition, with recent breakthroughs in integrated photonic circuits, information can now be stored and processed optically within the memory cell which offers great advancements such as higher speed, minimal Joule heating and crosstalk, and larger bandwidth compared to electronic devices [27–29].

Solid-state phase transformation in materials could appear in various forms from a structural phase transformation like amorphous-to-crystalline or a purely electronic phase transition like the metal-insulator transition. Throughout this dissertation, I use the term “phase transition” to describe any solid-state structural or electronic changes in the material property as a result of an external stimulus such as heat or electric field. The phase-change materials (PCMs) that are chosen for this work are amongst those that are widely used in the industry, yet their thermal properties have not been extensively characterized at the nanoscale. In addition to investigating how phase transformation would alter the thermal properties of materials, I will also examine the impact of the neighboring materials on thermal transport and quantify their corresponding interfacial thermal resistances.

During the past decade, with advancements in nanofabrication and improved under-

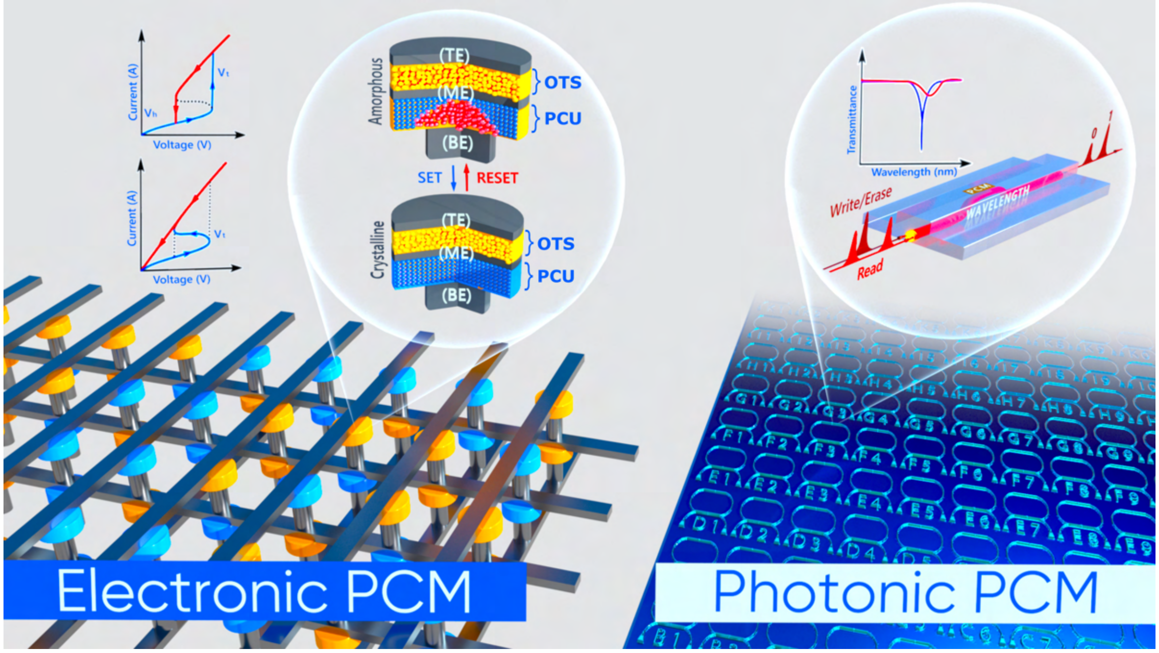

Figure 1.1: Schematic of memory cell architecture used in electronic and photonic phase-change memories. The plots on the right demonstrate the typical I-V trend for OTS and PCM showing volatile and non-volatile behavior in these materials.

standing of nanoscale energy transport mechanisms, phase-change random access memory (PRAM) technology has experienced great breakthroughs in both electronic and photonic integrated circuits [30–34]. Figure 1.1 shows the memory architecture and the mechanism of data storage in both electronic and photonic memory devices. The first electronic PRAM was released to the market through a joint project by Intel and Micron in 2017 under the commercial name of *Optane Memory*. In this technology, owing to the development of two-terminal selectors that works on the basis of threshold switching, the memory cells in PRAMs can be stacked on top of each other and create a 3D cross-bar architecture of memory cells that allows significantly higher ($\times 10$) storage capacity compared to DRAMs while providing a significantly faster processing time compared to NAND Flash memories. As a result, PRAM is expected to bridge the gap in speed and storage capacity between NAND Flash memory and DRAM.

More recently, integrated nanophotonic memory devices have emerged that make use of the different absorption coefficients between the amorphous and crystalline phases of

PCM to store information. In these photonic memory devices, the entire operation from write, erase, and read is performed with optical measurements, which is generally referred to as all-optic memory devices. The memory cell architecture in these devices consists of a microring resonator that is coupled with a nanophotonic waveguide as depicted in Fig. 1.1. The microring resonator is coated with a thin layer of PCM where its structural phase transition would change the degree of optical loss in the resonator. The PCM in the amorphous phase has a low absorption coefficient and therefore does not couple with electromagnetic waves, while its crystalline phase strongly couples with the waves and thus increases the optical loss. The waveguide is designed to operate at a wavelength where the PCM has the greatest change in the absorption between the two phases which is in the near-infrared spectrum. In this architecture, by measuring how much of the light is transmitted through the waveguide, one can optically store binary digits.

In phase-change memory devices, each memory cell must withstand millions of thermal cycles with unprecedented temperature fluctuations on the order of $\Delta T = 600°C$ where temporal and spatial temperature changes are $\sim 10^{10}$ K/s and $\sim 10^{3}$ K/nm, respectively [35]. As depicted in Fig. 1.2, in order to switch between amorphous and crystalline phases, thermal excitation in the form of electrical pulses is applied to an electrode that is in close contact with the PCM, commonly referred to as *bottom electrode* (BE). For crystallization of the PCM, a long medium-amplitude pulse on the order of hundreds of seconds is applied to the electrode, which heats up as a result of resistive heating and raises the temperature of PCM above its crystallization point ($\sim$ 150 °C). In order to switch the PCM back to amorphous, a high-amplitude but short pulse on the order of tens of seconds is applied to the electrode that raises the temperature of PCM above its melting point ($\sim$ 600 °C) and upon rapid cooling, freezes the atoms in their amorphous phase. Due to the aforementioned extreme thermal conditions, managing heat in these devices is of critical importance. For an efficient thermal management in these devices, a thorough understanding of the thermal transport in each component as well as between different components at their interfaces is essential.

The purpose of this dissertation is to shed light on the mechanism of energy transport in these memory devices from a thermal science perspective. In particular, I will examine the changes in the thermal conductivity of phase-change materials and the energy transport with their neighboring materials, such as electrodes and insulators, that are commonly used in electronic and photonic memory devices. Through detailed measurements, characterizations, and analyses, the parameters that are critical in thermal transport at length scales on the order of a few tens of nanometers are identified. As I will show in Chapter 4, the experimental measurements would not only provide a better understanding of thermal transport in the memory cell but also would provide a benchmark for modeling and designing higher efficiency memory devices with lower power consumption.

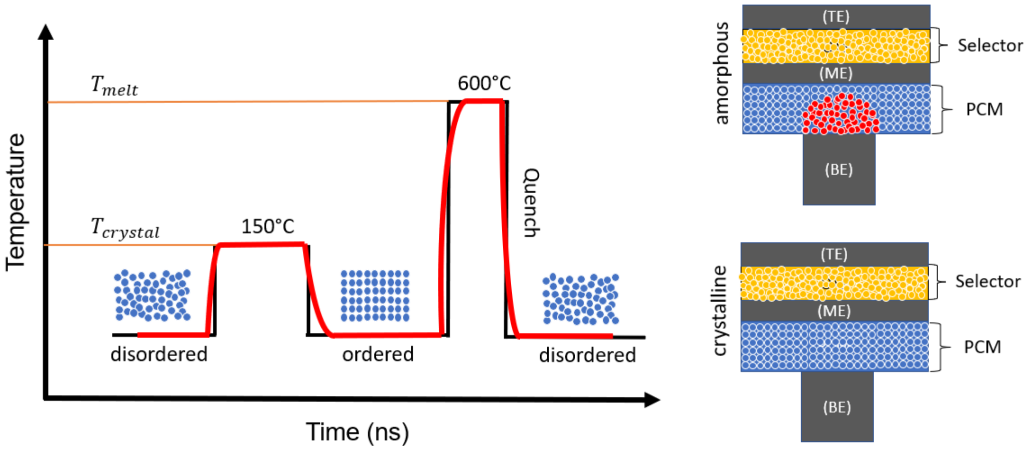

Figure 1.2: Switching mechanism between different phases in chalcogenide-based phase-change materials showing a medium-amplitude long pulse for crystallization and a high-amplitude short pulse for amorphization of phase-change material. The schematics show electronic memory cell architecture in amorphous and crystalline states.

## 1.3 Statement of Objectives and Scope

The overarching objective of this dissertation is to provide insight into the mechanisms and the extent of which thermal transport is affected by solid-state phase transformations as the length scale of materials shrinks to that of the carriers' mean free paths and wavelengths.

Through experimental measurements and theoretical analyses, I attempt to determine the limits where thermal transport transitions from a diffusive to a ballistic regime and ways one can mitigate the effect of ballistic heat transport. In addition, this work examines the ways in which the thermal conductivity can be suppressed either by manipulating extrinsic phenomena such as boundary scattering of the heat carriers or by manipulation of intrinsic properties such as alloying. For this, I investigate various solid-state materials with different degrees of structural disorder, ranging from amorphous to polycrystalline at various thicknesses. I use experiments supported by numerical analysis and mathematical models to provide physical insight into the thermal transport properties across phase transitions.

- **Chapter 2: Theory of thermal conductivity** - In this chapter, I will discuss theoretical models that have been developed thus far to explain *conduction* thermal transport in solid-state media with different microstructure. I introduce the primary heat carriers in different materials, from non-metallic to metallic, crystals to amorphous, and provide qualitative and quantitative approaches to distinguish the contribution of each heat carrier to the thermal transport. I will evaluate the applicability of Fourier's law as the characteristic length of materials shrinks to the length scale on the order of energy carrier wavelengths and demonstrate that thermal transport at the nanoscale is affected by parameters that are not effective in bulk materials, such as boundary scattering and ballistic thermal transport.

- **Chapter 3: Experimental measurements and analysis** - This chapter provides necessary background and details regarding the primary measurement technique, time-domain thermoreflectance, that has been employed throughout this dissertation to measure thermophysical properties such as thermal conductivity, heat capacity, and sound velocity. Necessary fundamental concepts that are integral in these measurements such as thermoreflectivity and lock-in amplification are reviewed and the models that relate experimental data to the thermal properties are presented. In addition, a detailed demonstration of interpreting the experimental data to obtain thermal properties and the uncertainty associated with the measurements is provided.

- **Chapter 4: Heat confinement through interfacial engineering** - In this chapter, I attempt to tackle high power consumption in electronic PRAM by identifying the effective parameters and engineering them. In particular, I will examine the degree to which interfacial thermal resistance can impact thermal transport in phase-change memory architectures. Through experiments and simulations, I demonstrate that the interfacial thermal resistance between a well-known PCM, $Ge_2Sb_2Te_4$, and its adjacent layers could suppress the thermal transport in memory cells without incorporating additional insulating layers at their interfaces. The mechanisms of phase transformations and their impacts on thermal properties are discussed.

- **Chapter 5: Heat confinement through suppressing electrons** - This chapter focuses on investigating the thermal properties of a novel class of phase-change materials that have been particularly developed for optical devices and photonic applications. The chapter discusses how thermal transport is affected by the partial substitution of tellurium with selenium in Ge-Sb-Te. In addition, by implementing an ultrafast mid-infrared pump-probe spectroscopy technique that allows for direct monitoring of electronic and vibrational energy carrier lifetimes in these materials, I experimentally demonstrate a substantial change in the electron contribution to the thermal transport mechanism upon selenium substitution. I provide additional evidence for this hypothesis by comparing the thermal conductivity trend as a function of temperature in Ge-Sb-Te and Ge-Sb-Se-Te.

- **Chapter 6: Towards lower thermal conductivity** - This chapter discusses the mechanism of thermal transport in amorphous solids and provides new insights on how to reach ultralow thermal conductivities. The material that is investigated in this chapter is a common material for two-terminal selector devices in phase-change memories that acts as a electrical gate and enables selective access to a particular memory cell. Through experimental measurements supported by *ab-initio* molecular dynamics simulations, I demonstrate that by breaking the connectivity network in the atomic structure of silicon telluride (SiTe), vibrational modes can become strongly localized, leading to a large suppression of heat carriers and ultralow thermal conductivities.

- **Chapter 7: Thermal conductivity manipulation through phonon engineering**: This chapter focuses on the development of a bidirectional thermal conductivity switch by taking advantage of two separate phase transformations in antiferroelectric lead zirconate ($PbZrO_3$) as a result of electrical or thermal excitation. In this material, each phase transition alters the phonon scattering rate in a different manner, which enables on-demand control of thermal conductivity to higher or lower values. In this chapter, through thermal conductivity measurements supported by detailed characterization, I demonstrate that the thermal conductivity of $PbZrO_3$ can be bidirectionally switched by -10% and +25% upon application of an electric field or thermal excitation, respectively.

- **Chapter 8: Summary and future projects** - In this chapter, the major findings of this dissertation are summarized, and a conclusion regarding the overarching purpose of this dissertation is presented. Further, a discussion regarding some of the opportunities and follow-up studies that would answer some of the questions that were not addressed in this dissertation and would provide a more complete understanding of thermal transport processes across solid-state phase transformation is presented.

# Chapter 2

# Theory of Heat Conduction

Thermal transport is categorized into three basic forms of energy transfer; *conduction*, *convection*, and *radiation*. Conduction is the flow of energy as a result of the random motion of heat carriers, directly transmitting the heat through a medium or multiple media without spatial movement of matter. Convection, on the other hand, occurs when the atoms move in the form of fluids from a hotter to a colder region. Radiation is the energy emitted from hotter bodies via electromagnetic waves, which does not require a medium for transmitting the energy. The primary focus of this dissertation is concerned with heat transfer via conduction mechanisms for fully dense solids and the interfaces between them. In the classical limit, heat conduction is governed by Fourier's law, which states that the rate at which heat is conducted through a material per unit area is proportional to the temperature difference across the material:

$$\mathbf{q} = -\kappa \nabla T, \tag{2.1}$$

where $\mathbf{q}$ is the heat flux (W m$^{-2}$), $\kappa$ is the thermal conductivity (W m$^{-1}$ K$^{-1}$), and $\nabla T$ is the temperature gradient (K m$^{-1}$). Thermal conductivity is a constant material-dependent property at a fixed temperature that determines the ability of a medium to conduct heat. Generally, Fourier's law is valid as long as the system is in a steady state and the mean free paths of fundamental energy carriers, defined as the average distance between two successive collisions, is sufficiently smaller than the system size. In the case of time-dependent heat transfer processes, or the *transient* regime, the thermal transport is governed by the heat diffusion equation that accounts for time-dependent changes in the energy density of the material:

$$C\frac{\partial T}{\partial t} = \nabla \cdot (\kappa \nabla T) + Q_{gen}, \tag{2.2}$$

where $t$ is time and $Q_{gen}$ is the amount of generated heat from a heat source. Note, in a steady-state regime, the above equation simplifies to Fourier's law, where the effect of the heat capacity on the thermal transport goes to zero. At the high temperature limit, the variation of heat capacity across different materials for fully dense solids is small and usually falls in the range of 1 to 4 MJ $\mathrm{m^{-3}\ K^{-1}}$. In contrast, the thermal conductivity is largely dictated by the material's atomic and electronic structure and could change by up to six orders of magnitude. For instance, carbon in its crystalline state has almost $>$1000 times higher thermal conductivity than its amorphous state [36–40]. Similarly, in chalcogenide-based phase change materials, as a result of a purely electronic structure change, metal-insulator transition, the thermal conductivity can change by more than a factor of two, with a relatively negligible change in heat capacity [41].

Thermal conductivity largely depends on the phase and structure of the materials. Typically, the thermal conductivities of gases are significantly lower than those of liquids and solids, which is the reason why birds fluff out their feathers in winter to form air pockets to protect them from cold temperatures. A similar concept has been used to create super-insulating materials to save energy in buildings or protect equipment from extreme conditions by harnessing the unparalleled insulative properties of aerogels that are highly porous. To-date, the lowest thermal conductivity measured is recorded for aerogels ($>$99% porous) in *vacuum* with an ultra-low thermal conductivity of 0.0024 W $\mathrm{m^{-1}\ K^{-1}}$ and the highest measured thermal conductivity is diamond with a record high thermal conductivity exceeding $\sim$2000 W $\mathrm{m^{-1}\ K^{-1}}$ at room temperature [38–40, 42–44]. Although higher thermal conductivity than diamond has been reported for graphene [45–47] and carbon nanotubes (CNT) [48, 49], their large anisotropy in thermal conductivity and poor mechanical properties lead to major limitations for integration into device architecture [50–52]. Figure 2.1 depicts the thermal conductivity spectrum for several notable materials.

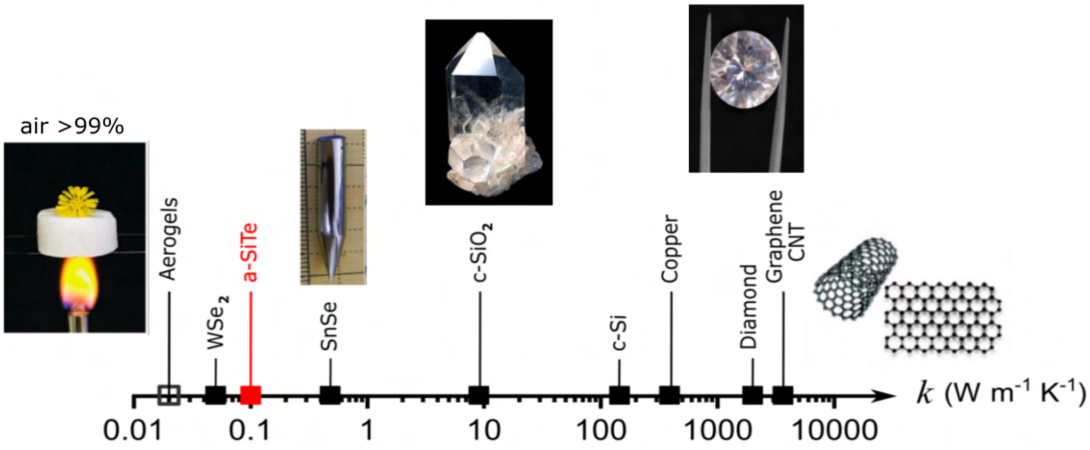

Figure 2.1: Thermal conductivity for several notable materials that are widely used in the industry from ultra-insulative to ultra-conductive.

From nanoscale perspective, in solid media the heat is primarily transferred via *electrons* and *phonons* (atomic vibrations). In this limit, the classical Fourier's law still holds true as long as the average of these microscopic vibrations is taken into account for a sufficiently large domain size and over sufficiently long periods of time ($>$ nanoseconds). For thin films at submicron length scales, this criterion is rarely met as various scattering events such as boundary or impurity scattering could play a significant role in the rate of their energy transfer. As a result, in order to study thermal transport at nanoscale a thorough understanding of fundamental energy carriers and the effective parameters in their transport is critical. In this regard, since the dominant heat carriers in non-metallic versus metallic solids are fundamentally different, it is important to separate them into two subcategories and discuss each phenomenon individually. For instance, in non-metallic systems such as dielectrics (silica) and semiconductors (silicon), the thermal conductivity is primarily dictated by atomic or lattice vibrations, while in metallic systems (copper), the primary heat carriers are electrons. The *total* thermal conductivity of a material is the summation of contributions from lattice vibrations, $\kappa_{\text{lattice}}$, and electronic vibrations, $\kappa_{\text{electron}}$:

$$\kappa_{\text{tot}} = \kappa_{\text{electron}} + \kappa_{\text{lattice}}. \tag{2.3}$$

Although differentiating the contributions of electrons from those of phonons to the thermal conductivity of materials is not trivial, there are theoretical models that provide a reasonable approximation for each. In the following, I will discuss important concepts related to nanoscale thermal transport in various solids, from non-metallic to metallic, and provide theoretical models for explaining their transport properties at the nanoscale. First, thermal transport in non-metallic crystalline solids in which phonons are the dominant heat carriers will be discussed, and a mathematical equation will be presented to estimate the lattice thermal conductivity. Then, I outline the transport processes in disordered and amorphous solids and discuss the accuracy of existing models to explain thermal transport in disordered solids. Finally, I briefly review the transport processes in metallic solids and present the Wiedmann-Franz law, which is an empirical equation for estimating the electronic contribution to the thermal conductivity of metallic solids.

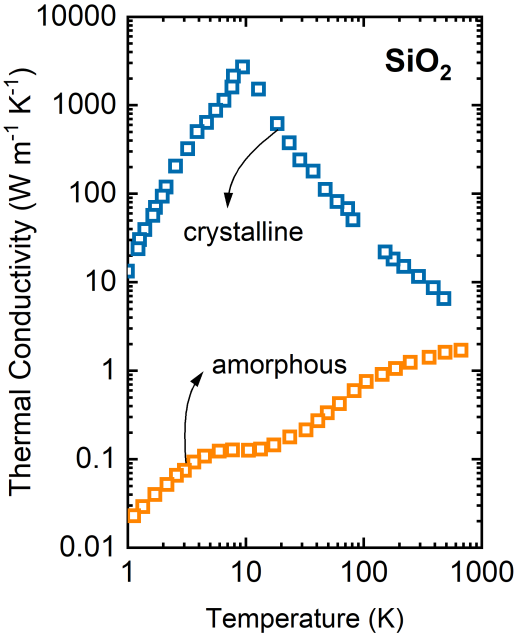

Figure 2.2: Thermal conductivity of amorphous $SiO_2$ (silica) and crystalline $SiO_2$ ($\alpha$-quartz) as a function of temperature reprinted from ref [53].

## 2.1 Thermal Transport in Non-metallic Crystalline Solids

The thermal conductivity of solids is largely dependent upon their atomic structure. A simple example of the difference between the thermal conductivity of amorphous and crystalline phase is their trend as a function of temperature. The thermal conductivity trend for amorphous and crystalline $SiO_2$ as a representative system is presented in Fig. 2.2. As can be seen, the thermal conductivity of crystalline $SiO_2$ increases rapidly with temperature and after reaching a maximum, as a result of the dominance of anharmonicity and Umklapp scattering decreases again at higher temperatures. On the other hand, the thermal conductivity of amorphous $SiO_2$, increases with temperature and flattens out after the Debye temperature. This behavior is commonly observed among crystalline and amorphous solids.

Typically, higher order and symmetry in the atomic structure of a given solid lead to higher thermal conductivities. Crystals are defined as materials in which atoms, molecules, ions, etc. are arranged in an ordered periodic pattern which extends throughout the entire structure. In these systems, the crystal structures are identified by their smallest repeating pattern, the unit cell, that extends in all three directions within the crystal. The constituent elements of a crystal are uniformly held together by interatomic forces such as covalent, metallic, or ionic bonds. In non-metallic crystals, the heat is primarily transported by the collective motion of atoms, commonly referred to as *phonons*. Phonons are quasiparticles that their energy state is best described by their wave-like behavior and their propagation through materials is best described by considering their particle-like behavior. In the following, I will describe the analytical details related to thermal conductivity modeling and how these models can provide a better understanding of nanoscale thermal transport.

One of the early approaches to estimate the rate of heat conduction in solids is derived from classical kinetic theory, which treats energy carriers as the equivalent to the interactions in gas particles. Figure 2.3 shows a random distribution of particles within a medium that is exposed to a temperature gradient. Considering an imaginary plane ($x_0$) perpendic-

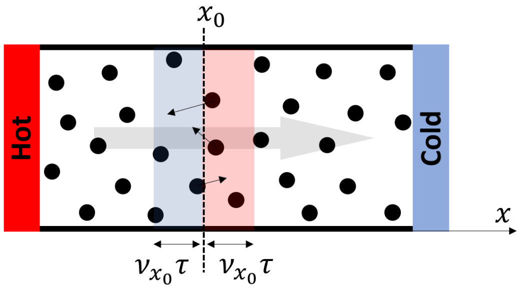

Figure 2.3: Microscopic heat conduction through a gas showing thermal transport from hot to cold region.

ular to the heat flow direction, the total heat flux across this plane is the sum of particles that jump across the plane in positive and negative directions. In this scenario, $v_x$ is the velocity of the particle and $\tau$ is the average time between two consecutive collisions (relaxation time). Hence, the distance traveled by each particle across the $x_0$ plane before they scatter with another particle is $v_x\tau$. The net heat flux can be estimated by the total amount of energy crossing the imaginary plane:

$$q_{x_0} = q_{+x_0} - q_{-x_0} = \frac{1}{2}(nEv_x)\bigg|_{x_0+v_x\tau} - \frac{1}{2}(nEv_x)\bigg|_{x_0-v_x\tau}, \tag{2.4}$$

where, $n$ is the number of particles or energy carriers per unit volume and $E$ is the amount of energy they carry, where internal energy of the system can be obtained from $U = nE$. The 1/2 prefactor indicates that only half of the particles move in the positive direction and the other half move in the negative direction, which is valid at the limit of a large number of particles (i.e., $10^{23}$). Assuming an isotropic material where $v_x$ is independent of $x$, $v_x^2 = v^2/3$, and using Taylor expansion, the above equation can be rewritten as follows:

$$q_{x_0} = v_x\tau\frac{d(nEv_x)}{dx} = -\frac{v_x^2\tau}{3}\frac{dU}{dx}\frac{dT}{dx}. \tag{2.5}$$

Considering that $C = \frac{dU}{dx}$, and the fact that $q_{x_0} = -\kappa dT/dx$, we can write the above equation:

$$q_{x_0} = -(Cv^2\tau/3)dT/dx = -\kappa dT/dx. \tag{2.6}$$

Using this fairly crude model from kinetic theory, we can obtain a surprisingly reasonable approximation for the thermal conductivity:

$$\kappa = \frac{1}{3}Cv^2\tau = \frac{1}{3}Cvl, \tag{2.7}$$

where $C$ is the carrier's specific heat, $\tau$ is relaxation time, and $l$ is their mean free paths. Several key takeaways can be interpreted from this expression. According to this, we can identify three major parameters that affect the thermal conductivity; heat capacity, carrier velocity, and average relaxation time, or average mean free paths of energy carriers, in this case phonons, before they scatter. As mentioned earlier, the thermal conductivity of fully dense solids can span by orders of magnitudes (0.05-2000 W $m^{-1}$ $K^{-1}$) while the specific heat of materials at high temperatures is relatively the same, which is $3k_B$ per atom in the classical limit. In a similar way, as will be discussed in the subsequent sections, to a first approximation, the carriers' velocity can be considered as the sound velocity in materials, which varies in the range of 1,000-10,000 m $s^{-1}$ for fully dense solids. This implies that heat capacity and sound velocity alone cannot explain such a large distribution in the thermal conductivity of materials. On the other hand, the phonon relaxation time could vary by more than three orders of magnitudes, which highlights the importance of relaxation time on the thermal transport properties. In the following, I provide a more in-depth analysis of thermal conductivity by considering phonons as quasiparticles.

### 2.1.1 Phonon Dispersion

In order to provide a model for estimating the thermal conductivity, it is essential to have a deep understanding of the allowable energy levels within the crystal. In this regard, dispersion relation, which connects the angular frequency of phonons to their wavevector, can be used to determine the phonon energy states and momentum. From a classical approach, we can derive the dispersion relation and describe the energy states of a crystal and how they propagate in a material based on the crystal properties such as atomic mass, crystal structure, and bonding strength. This section provides an analytical approach to obtain the dispersion relation for a simple model by relating the frequency of vibrational modes to their wavevector.

For a crystal in equilibrium, the atoms are positioned perfectly at their lattice sites, which could only take place at absolute zero. As the temperature increases, the atoms start to oscillate around their equilibrium position and interact with their neighboring lattice sites. This atomic motion can only occur at specific modes of vibration based on the atomic mass, crystal structure, and bonding strength, which can be described by dispersion relation. In order to show this and derive the dispersion relation for a representative system, we consider a very simplistic spring-mass model that has proven to render a reasonable approximation of the energy state in a crystal. For this, we assume an infinite 1-D chain of atoms with similar masses, $m$, that are connected together by springs with a spring constant, $K$, at equilibrium distance of $a$ as depicted in Fig. 2.4(a). Considering each atom is only interacting with its nearest neighbors, i.e., left and right, the forces acting on each atom are governed by Newton's second law of motion:

$$m\frac{d^2u_n}{dt^2} = K(u_{n+1} - u_n) + K(u_n - u_{n-1}). \tag{2.8}$$

After solving the above equation, a simple relation is obtained for the dispersion of phonons, which is commonly referred to as *harmonic approximation*:

$$\omega(k) = \sqrt{\frac{4K}{m}} sin\left(\frac{ka}{2}\right), \tag{2.9}$$

where $k = 2\pi/\lambda$ is wavevector and $a$ is the periodicity of atoms. The obtained dispersion relation yields important information about phonon properties in the spring-mass system. First, the frequency relation with the displacement of atoms is a periodic function which means the solution for $k$ or $k + 2\pi/a$ are physically identical. This allows limiting the solution within the first Brillouin zone $[-\frac{\pi}{a} \leq k \leq \frac{\pi}{a}]$ which is shown in Fig. 2.4(b). Another important piece of information that can be obtained from the dispersion relation is the velocity of propagation of wave packets, also known as group velocity:

$$v_g(k) = \frac{\partial \omega}{\partial k}. \tag{2.10}$$

Now, let's take a closer look into the two limiting scenarios where $k \to 0$ and $k \to \pi/a$. In the case of $k \to 0$, which means the wavelength of oscillation is significantly larger than the atomic spacing, $\lambda >> a$, we can expand the Sine function in equation 2.9 and obtain:

$$\omega(k) = \left( a\sqrt{\frac{K}{m}} \right) k, \tag{2.11}$$

where the expression in the parenthesis is a proportionality constant relating the frequency of vibrations to the wavevector which is the sound velocity of a purely one dimensional system. Thus, at these long wavelengths, phonons propagate at a constant speed, which is the speed of sound $v_s$ in the materials. Fundamentally, the fact that the energy of a crystal must remain constant when all the atoms are displaced by a similar amount requires the existence of a solution where the frequency of the mode vanishes when the wavevector vanishes. As a result, such a mode will always appear in the solution regardless of how many more complicated interactions (adding the effects of second nearest neighbor) or higher dimensions are incorporated into the initial assumptions. Since the dispersion of these modes is closer to the Brillouin zone center and is linearly proportional to $k$, a characteristic for sound waves, they are commonly referred to as *acoustic modes*. These acoustic modes are coherent motion of atoms where all the atoms move in-phase with their neighboring atoms as $k \to 0$ as depicted in Fig. 2.4(c). This was realized by Debye when he observed that low-energy vibrations of a crystal were not vibrations of a single atom, but collective motions of atoms similar to sound waves. Using this, he provided a crude yet fair approximation for dispersion relation known as Debye model which assumes the frequency is linearly proportional to the wavevector and the constant of proportionality is the speed of

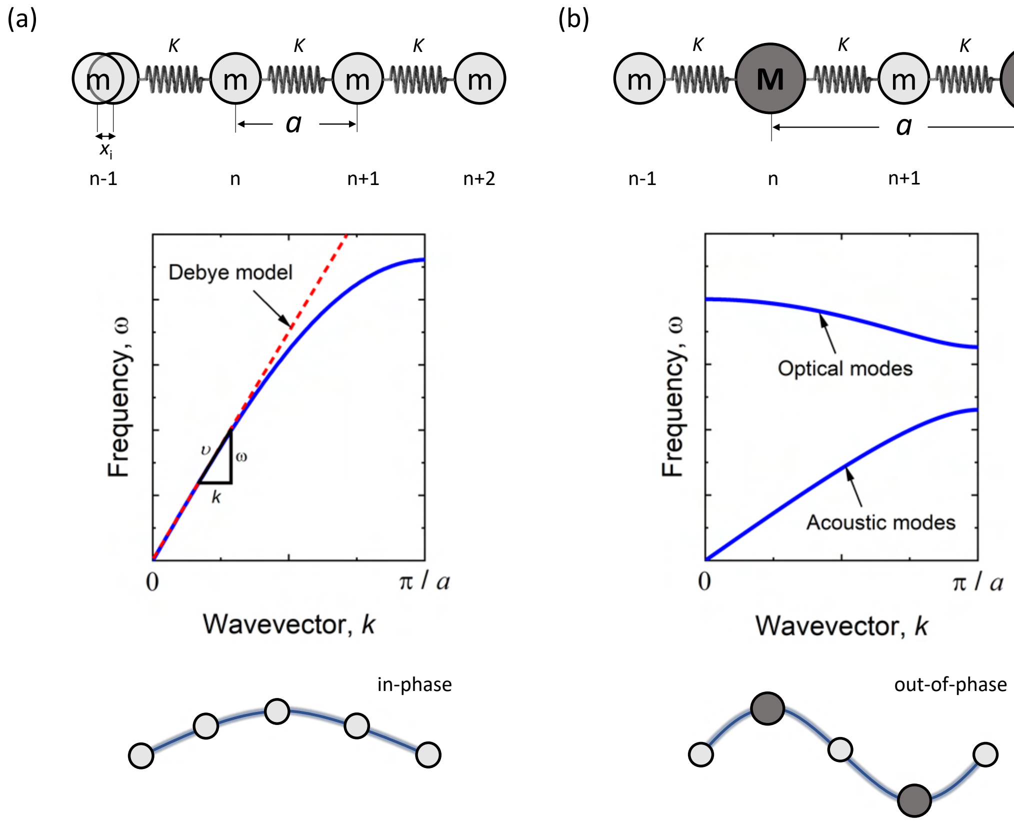

Figure 2.4: (a) Schematic of spring-mass model and real dispersion versus Debye approximation for a 1-D atomic chain with similar atomic masses $m = m_0$. (b) Schematic of spring-mass model and and real dispersion for a 1-D diatomic chain with different atomic masses $M = 2m = 2m_0$.

sound $\omega(k) = v_s k$ as depicted in Fig. 2.4(a). In addition, since this model is presented for only one-dimensional chains of atoms, the modes are bounded to one polarization (longitudinal), which is the reason why there is only one acoustic branch present in the dispersion relation. In the case of three-dimensional systems, the atoms can oscillate perpendicular to the propagation of waves and give rise to two additional transverse branches.

In the second scenario, where $k \rightarrow \pi/a$, or the wavelengths of modes are comparable to the interparticle spacing, such a linear relationship between frequency and wavevector breaks down. At the zone boundary, $(k = \pi/a)$, the dispersion relation begins to flatten out $\frac{\partial \omega}{\partial k} = 0$, which is required by the symmetry. This occurs because the dispersion relation is a periodic function which extends to the next Brillouin zone and any sharp curvature or kink is forbidden.

Next, we consider a linear chain of atoms with two different atomic species, i.e., a two-atom basis unit cell, where the mass of atom $a$ is twice the atom $b$ $M = 2m$ (see Fig. 2.4(d)). Similar to the previous section, after solving the equations of motion, we obtain the following relation for the phonon dispersion:

$$\omega(k) = K\left(\frac{1}{m}+\frac{1}{M}\right) \pm K\left[\left(\frac{1}{m}+\frac{1}{M}\right)^2 - \frac{4}{mM}\sin^2\left(\frac{ka}{2}\right)\right]^{1/2}. \tag{2.12}$$

According to the solution for the two-atom basis system, there are two phonon branches in the dispersion as presented in Fig. 2.4(f). As apparent, similar to the monotonic case, there is an *acoustic branch* that goes to zeros when $k \to 0$. The second branch, however, exhibits a weaker dispersion over the Brillouin zone and maintains its high-frequency modes as the wavevector goes to zero. These modes are out-of-phase vibrations of atoms that arise as a result of two adjacent atoms oscillating against each other, as depicted in Fig. 2.4(e).

### 2.1.2 Phonon Density of States

From the one-dimensional atomic chain model, we observed that each wavevector $k$ corresponds to a specific frequency. Now, taking the periodicity of the system into account, there are two degenerate frequency states within each Brillouin zone for the positive and negative wavevectors. Upon incorporating additional dimensions and atomic species into the system, more and more degenerate states arise in the system at a given wavevector. Phonon density of states is a mathematical representation that provides useful information about available energy states that phonons can occupy at a given frequency. In this respect, the phonon density of states is described as the number of vibrational energy states per unit volume per frequency. For an isotropic 3-D crystal using simplistic Debye approximation $\omega = vk$, the density of states $D_j(\omega)$ is described by:

$$D(\omega) = \sum_{j=1}^{n} \frac{\omega^2}{2\pi^2 v_j^3(\omega)}, \tag{2.13}$$

where the summation is over different phonon polarizations. The maximum frequency in Debye approximation is $\omega_{\max,j} = 2\pi v_j/a$. In order to demonstrate the accuracy of the Debye model with respect to a real density of states, we calculate $D_j(\omega)$ for solid argon, which has a face-centered cubic lattice. Assuming a longitudinal sound speed of $v_L = 1500$ m s$^{-1}$ and a doubly degenerate transverse sound speed of $v_L = 1150$ m s$^{-1}$ we calculate the phonon density of states in solid argon as depicted in Fig. 2.5.

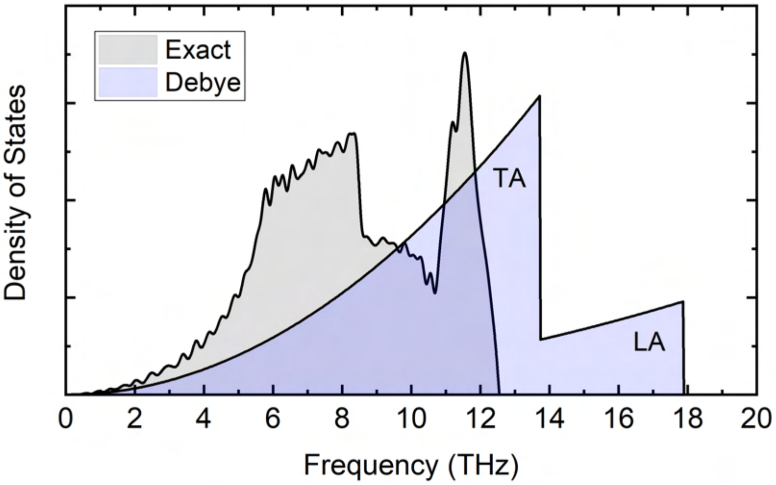

Figure 2.5: Exact and theoretical phonon density of states for solid Argon based on Debye approximation with varying longitudinal and transverse sound velocities.

### 2.1.3 Phonon Heat Capacity

Heat capacity is a material property that relates the absorbed energy to the corresponding temperature rise. From thermodynamics, we recall that at constant volume, the volumetric heat capacity $C_V$ [J m$^{-3}$ K$^{-1}$] is defined as the gradient of change in the average internal energy (U) with respect to temperature:

$$C_V = \left(\frac{\partial U}{\partial T}\right)_V . \tag{2.14}$$

In the previous section, we demonstrated a mathematical model that describes the allowable energy states of vibrational modes. Simply by adding the contribution from each vibrational mode, we can determine the total internal energy of the system. As discussed earlier, the density of states $D_j(\omega)$ determines the *available* energy states that a vibrational mode can occupy. Now, in order to identify the *occupied* states, we turn to statistical mechanics and use the Bose-Einstein distribution to find their equilibrium occupation function:

$$f(\omega,T) = \frac{1}{\exp\left[\frac{\hbar\omega}{k_B T}\right]-1}, \tag{2.15}$$

where $\hbar$ is the reduced Planck's constant, $k_B$ is Boltzmann's constant, and $T$ is the absolute temperature. Now, with the knowledge of the energy states that phonons have occupied, the total internal energy of the system can be obtained from:

$$U = \sum_j \int_0^{\omega_{\max,j}} \hbar\omega f(\omega,T) D_j(\omega) d\omega. \tag{2.16}$$

By taking the derivative of the internal energy with temperature, the heat capacity can be calculated from:

$$C_V = \sum_j \frac{\hbar^2}{2\pi^2 k_B T^2 v_j^3} \int_0^{\omega_{\max,j}} \frac{\omega^4 \exp\left[\frac{\hbar\omega}{k_B T}\right]}{\left(\exp\left[\frac{\hbar\omega}{k_B T}\right]-1\right)^2} d\omega. \tag{2.17}$$

With a simple change of variables, $x = \hbar\omega/k_B T$ we can obtain the following equation for the heat capacity:

$$C_V = \sum_j k_B \left(\frac{T}{\theta}\right)^3 \int_0^{\left(\frac{\theta}{T}\right)_j} \frac{x^4 e^x}{(e^x-1)^2} dx, \tag{2.18}$$

where $\theta$ is the debye temperature.

### 2.1.4 Phonon Thermal Conductivity

Once the energy states of the system (DOS), their distribution ($\frac{\partial f}{\partial T}$), and their propagation velocity ($v_g$) is determined, the thermal conductivity can be calculated by the following equation:

$$\kappa = \frac{1}{3}\sum_j \int_0^{\omega_{\max,j}} \hbar\omega D_j(\omega)\frac{\partial f(\omega,T)}{\partial T} v_j^2(\omega)\tau_j(\omega)d\omega. \tag{2.19}$$

The relaxation time in materials depends on the properties such as temperature, thickness, atomic crystal structure, and bonding and is calculated by considering all the scattering processes via Matthiessen's rule:

$$\tau_j^{-1} = \sum_i \tau_{i,j}, \tag{2.20}$$

where the summation is over different scattering processes that could take place in a crystal. As mentioned earlier, the scattering of phonons in crystals plays such a prominent role in energy transport processes that these processes could suppress their thermal conductivity by orders of magnitudes. As a result, the key to accurately estimating the thermal conductivity is to have a proper understanding of all the possible scattering mechanisms. In general, phonon scattering processes are classified into two major categories: intrinsic scattering and extrinsic scattering. Intrinsic phonon scattering is the reason why the thermal conductivity of perfectly pure crystals is not infinite. These intrinsic scattering events are the result of anharmonicity in the lattice, with three-phonon processes being the most prominent scattering process at non-cryogenic temperatures. Recently, through calculations[54, 55] and experimental measurements [56, 57], it has been demonstrated that the effect of four-phonon and higher-order scattering could be significant for many materials at medium or high temperatures. Regardless of the order of scattering, in these phonon-phonon scattering processes, if the energy and crystal momentum of the phonons are conserved, they are referred to as normal (N) processes, whereas if energy is conserved but not crystal momentum, they are referred to as Umklapp processes. The intrinsic scattering in materials can be estimated by:

$$\tau_{\text{int}}^{-1} = B\omega^2 T e^{-C/T},$$

where B and C are fitting constants. Extrinsic scattering processes could occur as a result of any inhomogeneity, mismatch, or disruption of symmetry in the crystal structure. By nature, any given material has some degree of defects, such as isotopes, impurities, and vacancies, or inhomogeneity embedded in their crystal structure, such as grain boundaries. Defect scattering is an elastic process that primarily occurs due to atomic mass mismatches and local bonding changes [58]. The equation that describes this scattering takes the form of Rayleigh scattering, $A\omega^4$. Boundary scattering becomes dominant in systems where the mean free paths of the phonons are larger than the characteristic length (d) of the system, such as the thickness of the film or grain size in polycrystalline solids and is estimated by $v/d$. Using Matthiessen's rule, the extrinsic scattering process can be calculated:

$$\tau_{\text{ext}}^{-1} = A\omega^4 + v/d.$$

## 2.2 Thermal Transport in Non-metallic Amorphous Solids

Unlike crystals, the atomic arrangement of amorphous solids lacks any periodicity or long-range order. As a result, the concept of a phonon that was built upon the symmetry and periodicity of a defined unit cell collapses. This imposes great challenges for modeling thermal conductivity as the use of periodic boundary conditions would no longer be applicable unless the selected unit cell is sufficiently large (super cell) to avoid the formation of artificial periodicity in the system, which is computationally burdensome. In order to model thermal transport in amorphous solids, alternative simplified approaches have been proposed, such as phonon-mediated minimum limit and diffuson-mediated minimum limit, each of which has shown great agreement with experimental measurements for their respective systems. In the following, I will discuss the theoretical background that leads to the emergence of these models and their accuracy for different amorphous solids.

### 2.2.1 Propagons, Diffusons, and Locons

Since the concept of a phonon is no longer applicable in amorphous solids, harmonic modes of vibration are categorized into two separate groups: extended vibrations and localized vibrations. Extended modes of vibration, or extendons (E) are the primary heat carriers in amorphous solids, whereas localized modes, or locons (L) are high frequency vibrations that do not transport energy and do not directly contribute to the thermal conductivity. Typically, vibrational modes can be identified based on their frequencies. The frequency onset that separates extendons from locons is called the mobility edge, which typically for three-dimensional systems is very narrow and has a sharp transition [59]. Extendons, which are the heat carrying modes, can be classified into two separate types of vibrations: propagating non-localized modes or propagons (P) and non-propagating non-localized modes or diffusons (D). Propagons are low-frequency vibrations that typically travel as wave-packets at the speed of sound and a wavevector can be assigned to them. Propagons in amorphous media are the counterparts of phonons in crystals with a mean free path longer than a few interatomic spacings [60]. Diffusons are medium-range frequency modes that scatter within a few interatomic spacing and a wavevector cannot be assigned to their propagation. In the frequency domain, the limit where the modes transition from propagon to diffuson is referred to as the Ioffe-Regel limit, which is broader and not as definitive and sharp as the mobility edge. Figure 2.6(a) shows the vibrational density of states for amorphous silicon with the corresponding frequency range for different vibrational modes and their cutoff limits.

The extent to which each specific mode of vibration, namely propagons, diffusons, and locons, could contribute to the thermal conductivity depends on the atomic structure, such as the atomic mass mismatch or network connectivity between the constituent elements. Usually, diffusons are the dominant modes of vibration in amorphous solids, while the effects of propagons and locons are negligible. In certain cases, the pronounced contribution

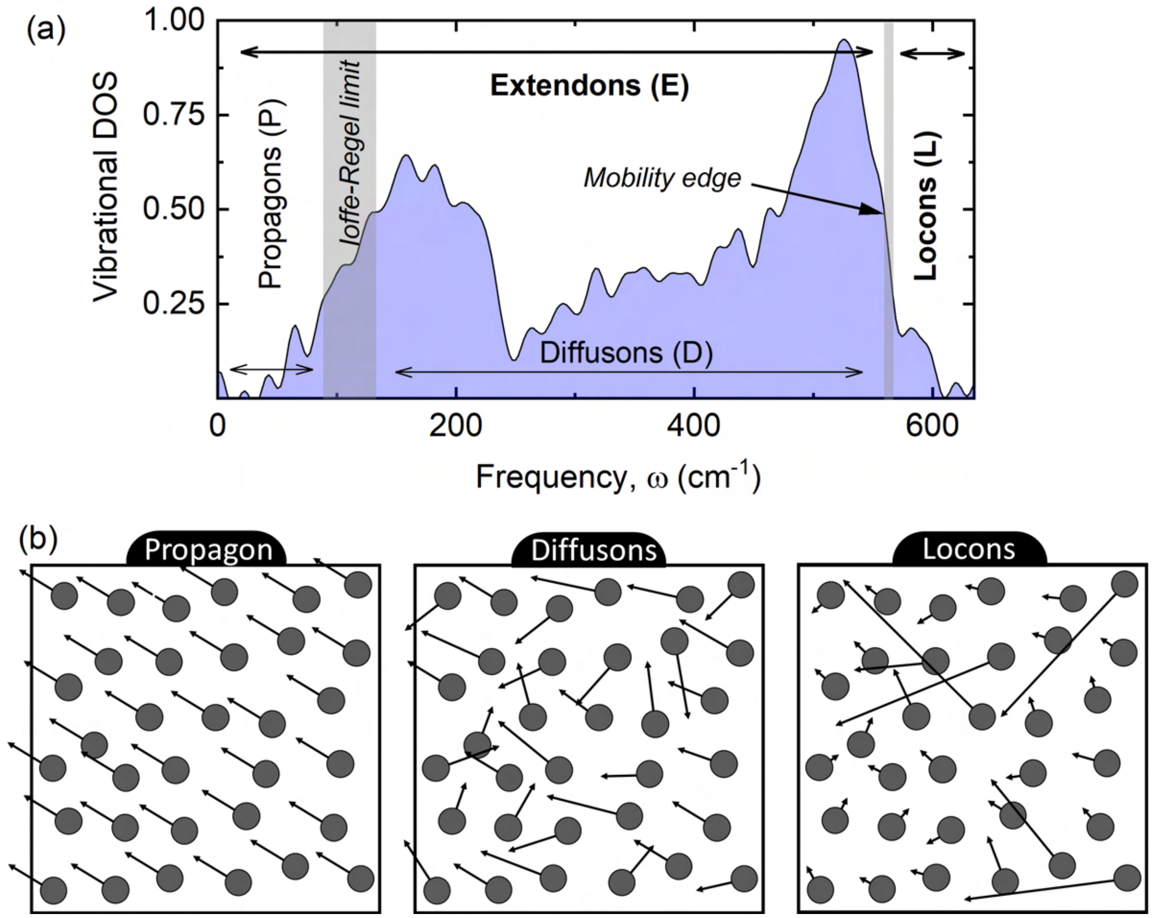

Figure 2.6: (a) Density of states for amorphous silicon showing the frequency range for propagons, diffusons, and locons. (b) Schematic of different vibrational modes in amorphous media and their corresponding eigenvectors.

of propagons or locons can lead to higher or lower thermal conductivities, respectively. For instance, it has been shown that in pure amorphous silicon, more than 40% of modes are propagons [61], which leads to almost a factor of two higher thermal conductivity. On the other hand, if silicon is alloyed with high tellurium content, not only is the effect of propagons eliminated but also, more than 40% of modes become localized leading to ultralow thermal conductivities [62]. In solids where propagons play a significant role, thermal conductivity is best described by a model derived from kinetic theory, while, in material compositions where diffusons are the dominant carriers, the thermal transport is best described by diffuson-mediated thermal transport. For systems where a large portion of vibrational modes are localized, diffuson mediated-model is still capable of providing an estimation for thermal conductivity with reasonable accuracy. In this case, the prefactor, *P*, which is the *probability* of successful energy transfer accounts for the degree of localized mode in the system. For amorphous solids where the locons are not dominant, *P* is assumed to be 1. However, for materials where the localized modes are dominant, $P<1$, must be modified. In the following, I will outline the details of these two models.

### 2.2.2 Phonon-mediated Minimum Limit

The heat transport mechanisms in highly disordered crystals and generally low thermal conductivity materials are often described using formalisms originally put forth by Einstein, and later refined by others [63–66], which account for some degree of localization of the vibrational modes or strong suppression of vibrational scattering length scales. These concepts, which partially form the basis of analytical minimum thermal conductivity models, are able to successfully predict the thermal conductivity of a wide range of amorphous solids. According to Cahill and Pohl [67], a lower limit to the thermal conductivity of materials is obtained by assuming the phonon mean free paths cannot be longer than half of their period of oscillation $l < \lambda/2$, where $l$ is phonon mean free path and $\lambda$ is their wavelengths. Using this minimum limit model, which is derived from the kinetic theory of gases, the thermal conductivity of disordered solids can be estimated by:

$$\kappa_{\text{min},\mathbf{P}} = \left(\frac{\pi}{6}\right)^{1/3} k_B n^{2/3} \sum_i v_i \left(\frac{T}{\Theta_i}\right)^2 \int_0^{\Theta_i/T} \frac{x^3 e^x}{(e^x-1)^2}, \tag{2.21}$$

where k$_B$ is the Boltzmann constant, $n$ is the number density, $\Theta_i$ is the Debye temperature of the material, $v_i$ is the sound velocity, and the summation is over different phonon polarization modes. In the high-temperature limit, the above equation can be simplified to:

$$\kappa_{\text{min},\mathbf{P}} = 1.21 k_B n^{2/3} v_g, \tag{2.22}$$

where $v_g$ is the average sound velocity in the material. The average sound velocity can be written in terms of the longitudinal ($v_L$) and transverse ($v_T$) sound velocities as:

$$v_g = \left(\frac{1}{3}\left[\frac{2}{v_T^2} + \frac{1}{v_L^2}\right]\right)^{-1/2}. \tag{2.23}$$

### 2.2.3 Diffuson-mediated Minimum Limit

Although the phonon-mediated minimum limit to thermal conductivity described above has served as a successful approach to predict the thermal conductivity of a variety of disordered crystals and amorphous materials, several recent works have experimentally measured values well below this limit [15, 62, 68–70]. This has motivated others to model the thermal conductivity in amorphous solids as a form of energy hopping between localized vibrational eigenstates. According to Allen and Feldman (AF) [71], a large portion of the heat in disordered solids is transferred by quantized vibrations that are neither localized nor propagating. These delocalized non-propagating vibrational modes, *diffusons*, carry heat by diffusion with a wavelength on the order of the inter-atomic spacing. Based on the AF formalism, Agne et al. [65] suggested a modified minimum limit model for heat transport in disordered solids that relies on the concept of diffusons rather than propagating modes. They argued that in a disordered solid, the lower bound to thermal conductivity occurs when the thermal transport is entirely driven by diffusons. This approach, albeit with the heat transfer carrier length scale being fundamentally different from those modeled in Eq. 2.22, leads to a similar functional form for the thermal conductivity of disordered materials:

$$\kappa_{\min,\mathbf{D}} \approx 0.76 P k_B n^{2/3} v_g. \tag{2.24}$$

According to this diffuson-mediated minimum model, in one period of oscillation, each vibrating carrier will make two attempts to transfer energy, where $P$ is the probability of a successful energy transfer. In the high-temperature limit and maximum diffusivity where $P = 1$, the calculated thermal conductivity is $\sim$37% lower than the phonon minimum limit model. As I will show in Chapter 6, for materials with a coordination number close to or below 2.4 where a large portion of the modes are localized, the assumption of maximum diffusivity no longer holds true. In this case, using a model proposed by Xi et al. [72] that relates the average coordination number to the thermal conductivity, the probability of successful energy transfer can be estimated.

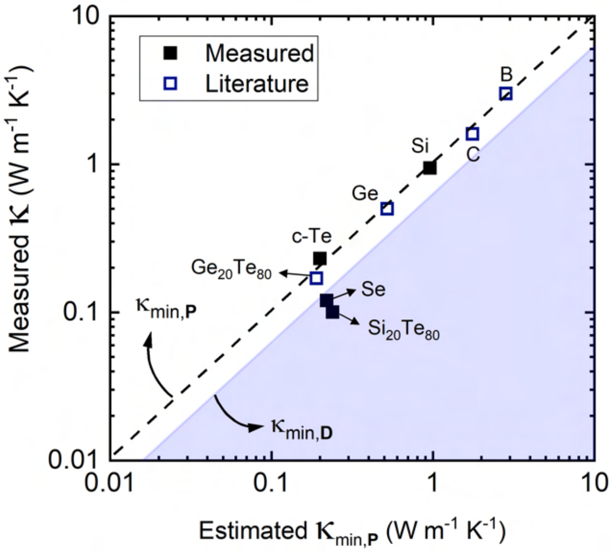

Figure 2.7: Measured thermal conductivity as a function of estimated thermal conductivity for amorphous single element and binary alloys with respect to the phonon-mediated minimum limit.

In order to compare the calculated thermal conductivity from the minimum limit models with experimental measurements, their values are plotted in Fig. 2.7. For this comparison, single-element amorphous solids and binary amorphous alloys are selected to limit the number of effective parameters in thermal transport to atomic mass and network. At first glance, it would appear that phonon-mediated minimum limit model provides a more accurate estimation of the thermal conductivity of amorphous solids and highly disordered crystals. However, this is true for highly coordinated materials with a substantial contribution from the propagons to the thermal transport, such as silicon. In amorphous solids, as soon as the contribution from propagons is suppressed and diffusons become the primary energy carriers, the diffuson-mediated minimum limit model provides a better estimation for the thermal conductivity. Furthermore, for low coordinated amorphous solids such as amorphous selenium or amorphous $Si_{20}Te_{80}$, the measured thermal conductivity is lower than that of the diffuson-mediated minimum limit model. In this case, a modified probability of successful energy transfer $P < 1$ must be used to account for the emergence of localized vibrational modes, which will be discussed in greater detail in Chapter 6.

## 2.3 Thermal Conductivity of Metals

The thermal transport in metals is primarily driven by electrons. In principle, while atomic vibrations are always a contributor to heat transport, the degree to which electrons can contribute to the thermal conductivity depends on their electrical conductivity. The electrical conductivity of materials can vary by more than 32 orders of magnitudes, from highly conductive metals such as silver and copper with electrical conductivity higher than $>5\times10^{7}$ S m$^{-1}$ to insulators such as teflon with an electrical conductivity less than $<10^{-25}$ S m$^{-1}$. The electrical conductivity of materials can be related to their thermal conductivity through an empirical equation introduced in mid 19th century, widely known as Wiedemann–Franz law [73]:

$$\kappa_{\text{electron}} = L_0 \sigma T, \tag{2.25}$$

where $\sigma$ is the electrical resistivity, $T$ is the absolute temperature, and $L_0$ is a constant commonly referred as to Lorenz number and is given by:

$$L_0 = \left(\frac{k_B}{e}\right)^2 \frac{\pi^2}{3} = 2.44 \times 10^{-8} \ \mathrm{W\,\Omega\,K^{-2}}, \tag{2.26}$$

where $k_B$ is Boltzmann constant and $e$ is electronic charge. Experiments have demonstrated that although $L_0$ can be roughly considered as a constant, it is not the same for all materials [74–76]. Kittel [77] has shown that the Lorenz number changes from $2.23 \times 10^{-8}$ W Ω K$^{-2}$ at 0°C for copper to $3.2 \times 10^{-8}$ W Ω K$^{-2}$ for tungsten at 100°C. In another work, Thesberg et al. [78] showed that in semiconductors the Lorenz number can vary in the range of 1.49-2.45 $\times$ $10^{-8}$ W $\Omega$ $K^{-2}$ for nondegenerate to degenerate semiconductors.

Apart from the small deviations in the Lorenz number across different materials, the Wiedemann–Franz law has been shown to break down in certain materials where Lorenz number must be an order of magnitude smaller than $L_0$ to match the experimental results. While the Wiedemann–Franz relation has been a powerful tool for estimating thermal conductivity in material systems where electrons are the dominant heat carriers, such as metals, it has been demonstrated that the relation fails in materials where charge and heat diffuse independently, such as strongly correlated electrons in vanadium dioxide ($VO_2$) [79]. According to this expression, and assuming that any contribution less than $<0.01$ W $m^{-1}$ $K^{-1}$ to the thermal conductivity as negligible, we can estimate that any material with electrical conductivity less than $<1.4\times10^3$ S $m^{-1}$ would not have a negligible electronic contribution to the thermal conductivity.

## 2.4 Summary

In this chapter, upon categorizing materials based on their primary energy carriers into electron-dominated metals and phonon-dominated non-metals, I outlined some of the theoretical models for estimating their thermal conductivity. I discussed the differences in the thermal conductivity of materials at the bulk and nanoscale and reviewed the theory behind modeling nanoscale thermal transport. Further, I surveyed the differences between crystals and amorphous media from a nanoscale thermal transport perspective and showed the steps towards modeling their thermal conductivity.

# Chapter 3

# Metrology and Analysis

In this chapter, I will discuss the details of the thermometry technique that is used throughout this dissertation to measure the thermal properties of materials. I will outline some of the core concepts in TDTR experiments, such as thermoreflectivity and lock-in amplification, after providing a brief overview of the background and related works that led to the development of TDTR. Then, I provide a detailed solution to the heat diffusion equation and the following mathematical model for data acquisition. Further, I assess the accuracy of TDTR measurements and the possible uncertainties associated with TDTR experiments. Finally, I will give an overview of the interpretation of TDTR data and demonstrate how thermal properties such as thermal conductivity, thermal boundary conductance (TBC), heat capacity, and sound velocity can be extracted.

## 3.1 Background

Measurement of thermal transport properties dates back to the pioneering work of Joseph Fourier [80] in the early 1800's, and as yet, efforts are being made towards the development of a more affordable, versatile, user-friendly, and faster measurement technique for thermal conductivity. Contrary to electrical conductivity measurements such as 4-point probe, where all the equipment fit into a relatively small controller box, thermal conductivity measurements could be considerably more challenging depending on the material, characteristic length scale, temperature, and size of the sample. With the invention of the laser, as with every other scientific field, great breakthroughs were achieved in the field of thermometry. Taking advantage of changes in reflectivity of materials as a result of temperature perturbations, commonly referred to as thermoreflectivity, several laser-based techniques were introduced in the 1970's and 1980's using continuous wave (CW) laser source for heating and sensing. Later, with the emergence of ultrafast (sub-nanosecond) pulsed lasers, this technique soon became more popular for interrogating non-equilibrium electron-phonon interactions [81, 82], electronic band structure [83, 84] picosecond acoustics [85–87], and thermal transport properties [88, 89].

Among various thermometry techniques, an established laser-based metrology for determining the thermophysical properties of materials, from thin films to bulk, is ultrafast transient thermoreflectance (TTR), originally developed by Paddock and Eesley [88] in 1986 for measuring the thermal diffusivity of metallic films. Their technique works on the basis of changes in the thermoreflectivity of the material as a result of temperature fluctuations. Although the rate of change in reflectivity with temperature ($\partial R/\partial T$) could vary from one material to another, as long as the temperature perturbation is small ($<10\%$ of absolute temperature or $<10$ K, whichever is smaller [90]), a linear relation can be established between the changes in reflectivity and temperature:

$$\frac{\Delta R}{R_0} = \left(\frac{1}{R_0}\frac{\partial R}{\partial T}\right)\delta T = \beta \Delta T, \tag{3.1}$$

where $R_0$ is the reflectivity of the material at a base temperature and $\beta$ is coefficient of thermoreflectivity. The idea behind TTR is to optically deliver heat with a high power beam, *pump*, to the surface of the sample and then, using a second low power beam, *probe*, measure the changes in reflectivity of the sample as a function of time which can be related to the changes in temperature. Depending on how surface thermoreflectivity changes with respect to an applied laser power, using the heat diffusion equation, the thermal properties of material can be quantified.

Most TTR-based thermometry techniques require a thin ($\sim$100 nm) metallic layer on the surface of the sample such as aluminum, platinum, ruthenium or gold, to facilitate the conversion of optical energy to heat as well as provide a high coefficient of thermoreflectivity for detection purposes. The choice of transducer material depends on many factors such as its absorption and thermoreflectivity coefficient, thermal conductivity, heat capacity, interfacial thermal resistance, and the temperature at which measurements are taken. Typically, the transducer material is selected to ensure the highest sensitivity of the measurements to the parameter of interest.

Regardless of transducer property, the coefficient of thermoreflectivity for most materials is typically very small [91, 92] and falls on the order of $10^{-5}$ to $10^{-4}$ $\mathrm{K}^{-1}$. Furthermore, the surface temperature rise due to pump heating is only a few Kelvin which leads to a significantly low magnitude in the thermoreflectance signal ($\sim 10^{-6}$ V) from the probe beam. As a result, lock-in amplification is used to distinguish such a faint signal from the background noise in the system. For this, the pump beam is typically modulated with a sine or square wave function at frequencies ranging from a few Hertz to several MHz depending on the technique and implementation. Upon probing signals at the pump frequency and ignoring all other frequencies in the system using a lock-in amplification technique, it is possible to capture changes in the reflectivity of the sample due to pump heating.

Over the past two decades, TTR-based techniques have evolved into powerful methods to measure the thermal properties of thin films and bulk materials. Since the introduction of TTR, several metrology techniques have been developed on the basis of thermoreflectivity such as time- and frequency-domain thermoreflectance [93, 94], steady-state thermoreflectance [95], and nanosecond transient thermoreflectance [96] to name a few. The focus of this dissertation is on ultrafast time-domain thermoreflectance (TDTR) that not only is capable of thermal conductivity measurements from nanoscale to macroscale but also is capable of measuring thermal boundary conductance, heat capacity, and sound velocity in materials with reasonable accuracy.

## 3.2 Time-domain Thermoreflectance

In a typical two-tint TDTR setup, the output of a Nd:YAG CW laser is directed to a Ti-Sapphire oscillator that produces femtosecond laser pulses at repetition rate of 80 MHz. Other types of ultrafast laser sources have been integrated into TDTR setup, such as a dye laser with center wavelength of 632 nm [97] or Yb:doped fiber laser with center wavelength of 1030 nm [92]. Yet, the Ti-Sapphire oscillators are the most common and popular light source for TDTR due to their stability, beam shape, and ultrafast nature [90]. For optimum efficiency, Ti-Sapphire oscillators typically operate at a center wavelength around 800 nm with full width half maximum ranging from 10 to 16 nm.

The schematic of the two-tint TDTR setup used for the measurement of thermal properties in this dissertation is depicted in Fig. 3.1. A Faraday optical isolator is placed at the output of the oscillator in order to protect the laser from any scattered light or reflected beam going back to the oscillator. The laser beam is then split into a pump and a probe path using a polarizing beam splitter (PBS). The pump path is directed to an electro-optic modulator (EOM) with a modulation frequency of nearly 8.4 MHz, and the probe path is directed to a mechanical delay stage to capture the changes in temperature of the sample as a function of time. It is also possible to advance the pump instead of delaying the probe, which would require a different analysis. The advantage of this approach is the higher stability of the probed signal as the beam no longer passes through any moving optics.

The pump and probe beams, after passing through a 10X objective, are focused to spot sizes of 20 and 10 $\mu$m on the surface of the sample, respectively. Using a dichroic mirror, the pump and probe are spatially overlapped by maximizing the signal magnitude. The reflected probe is then directed towards a fast-response balanced photodetector to convert the optical response of the sample into electrical signals, which is then picked up by a digital lock-in amplifier (Zurich Instruments) that deconvolutes the signal from the background noise. Since the lock-in amplifier detects any periodic signal at the modulation frequency, it is consequential to ensure the reflected pump beam does not bleed to the photodetector. As previously stated, the thermoreflectivity coefficient $\partial R/\partial T$ is very small ($10^{-4}$) and even slightest amount of reflected pump beam (<0.01%) is sufficient to distort the TDTR signal. Hence, it is crucial to use appropriate optical approaches, such as spatial or spectral separation of pump and probe, to block the reflected pump beam from bleeding into the detector.

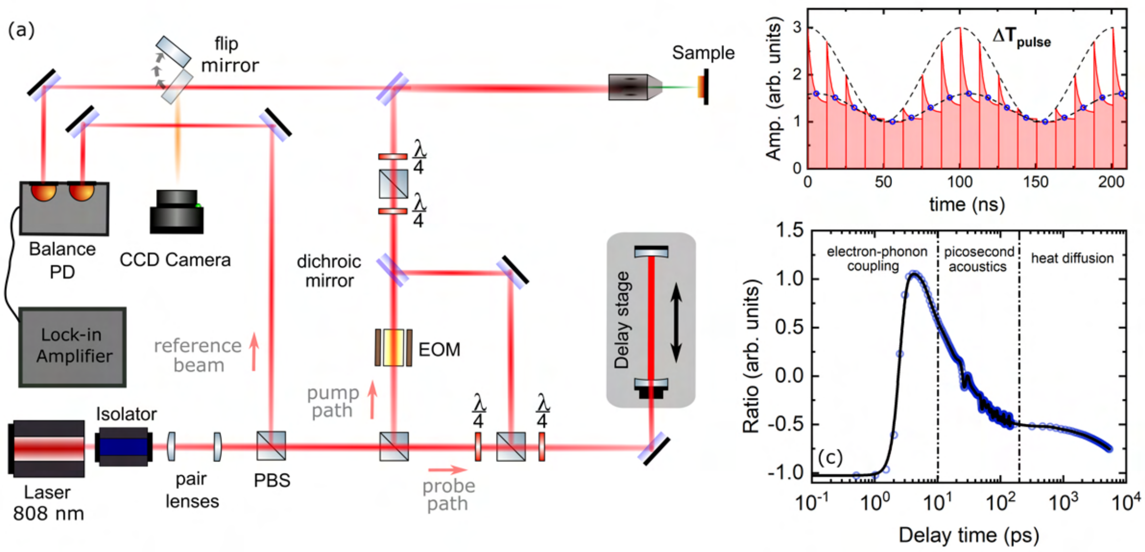

Figure 3.1: (a) The schematic of a typical two-tint TDTR setup, (b) Sine-wave modulation of pulsed laser with the corresponding steady-state and transient temperature rises, (c) the data acquired form TDTR for a 40 nm thick silicon telluride film with labels showing different thermal transport regimes.

As shown in Fig. 3.1(a), in addition to the reflected probe beam, a reference beam is also directed to the balance photodetector which allows for removal of any noise associated with the laser instabilities and would significantly improve the signal-to-noise ratio in TDTR data. A representative TDTR data set acquired for 80 nm Ru on 40 nm SiTe on a silicon substrate is shown in Fig. 3.1(c). Depending on the time scale, there are three main regimes in this plot and each enables extracting different information about the thermal properties of the system. In this regard, the ultrafast response of the material within the first few picoseconds ($<$10 ps) can be related to the non-equilibrium dynamics of electrons and their interaction with phonons to reach equilibrium. Typically, when the pump pulse hits the surface of the metallic transducer, it couples with its free electrons and moves them to an excited non-equilibrium state. Due to the relatively low heat capacity of electrons, their temperature at this state could be thousands of degrees higher than that of the lattice temperature. Over the first few picoseconds, the electrons dump their energy into the lattice and reach an equilibrium state which could be facilitated by high electron-phonon interaction, commonly referred to as *electron-phonon coupling*. The relatively rapid energy transfer between electrons and the lattice leads to formation of strain waves on the surface of the sample, which then propagate into the underlying layers at the speed of sound. In this regime from 10 to $\sim$200 ps, the TDTR signal allows investigation of sound velocity in different materials. In order to extract sound velocity, caution must be taken prior to sample fabrication to make sure the materials used in the multilayer stack have a significantly large acoustic mismatch for emergence of acoustic echoes from the interfaces in the TDTR signal. For more details about sound velocity measurements, refer to the *sound velocity* subsection at the end of this chapter. The third regime, from $\sim$200 to $\sim$5000 ps, is the heat diffusion regime at which the lattice cools down to room temperature. The rate of this decay in temperature depends on the underlying materials and allows extraction of thermal properties such as thermal conductivity, thermal boundary conductance, and heat capacity.

Thermal transport properties in TDTR experiments are typically determined by adjusting free parameters such as unknown thermal conductivity and thermal boundary conductance so that an optimized theoretical fit is achieved between the thermal model and the experimental data. The theoretical fit is obtained by solving the heat diffusion equation for a multilayer system consisting of at least two layers, transducer/substrate, or in the case of thin films transducer/film/substrate. More layers can be incorporated between the transducer and the substrate, but this would require sufficient information about the thermal properties of additional layers and would add to the complexity of interpreting the acquired data. It must be noted that TDTR measures thermal effusivity ($\alpha = \sqrt{\kappa C_v}$) which is a convolution of thermal conductivity and volumetric heat capacity. Therefore, from TDTR measurements, it is only possible to extract one of these parameters with an accurate knowledge of the other. Since the heat capacity for most materials at high temperatures does not change by much from bulk to nanoscale, commonly the free parameter in the TDTR model is thermal conductivity. In addition to heat capacity for the material of interest, there are many other input parameters (laser spot size, transducer thermal conductivity, heat capacity, and thickness) that go into the thermal model, which is crucial for an accurate measurement of thermal conductivity. The model that relates TDTR experimental data to the thermal properties requires two steps: first, solving the heat diffusion equation for the multilayer stack, and second, modeling the acquired data from the TDTR experiment. In the following, I summarize the details of the model that captures the thermal properties of individual layers in a multilayer stack from the TDTR experiment.

### 3.2.1 Solution to the Heat Diffusion Equation

In order to solve the heat diffusion equation for an anisotropic three-dimensional multilayer stack, it is more convenient to work in cylindrical coordinates due to the assumed cylindrical symmetry of the laser source. In this respect, the heat diffusion equation can be rewritten as:

$$C_v \frac{\partial T}{\partial t} = \frac{\eta \kappa_z}{r} \frac{\partial}{\partial r} \left( r \frac{\partial T}{\partial r} \right) + \kappa_z \frac{\partial^2 T}{\partial^2 r}, \tag{3.2}$$

where $C_v$ is the volumetric heat capacity, $\eta$ is the ratio for the in-plane thermal conductivity ($\kappa_r$) versus cross-plane thermal conductivity ($\kappa_z$). Assuming a prescribed temperature (T) and heat flux (q) for the uppermost layer ($z = 0$) which is the surface of the transducer, and bottom layer ($z = d$) which is the semi-infinite substrate, the boundary condition can be written as:

$$T(0,r,t) = T_{top}; \quad \left.\frac{\partial T(z,r,t)}{\partial z}\right|_{z=0} = -\frac{1}{\kappa_z} q_{top}, \tag{3.3}$$

$$T(d,r,t) = T_{bot}; \quad \left.\frac{\partial T(z,r,t)}{\partial z}\right|_{z=d} = -\frac{1}{\kappa_z} q_{bot}. \tag{3.4}$$

In order to simplify the parabolic partial differential equation of Eq. 3.2 to an ordinary differential equation, we can apply the Fourier and Hankel transform to the time variable $t$ and radial $r$ coordinate, $\mathrm{T}(z,r,t) \rightarrow \Theta(z,k,\omega)$, arriving at:

$$\frac{\partial^2 \Theta}{\partial^2 z} = \lambda^2 \Theta, \tag{3.5}$$

where $\Theta$ is the temperature in frequency-domain and $\lambda = 4\pi^2 k^2 \eta + i\omega C/\kappa_z$. The general solution to Eq. 3.5 can be written as:

$$\Theta = e^{\lambda z} B^+ + e^{-\lambda z} B^-, \tag{3.6}$$

where $B^+$ and $B^-$ are complex constants that can be determined based on the boundary conditions. Applying Fourier's law $Q = -\kappa_z (d\Theta/dz)$ to equation 3.6, the heat flux can be obtained as:

$$Q = \gamma(-e^{\lambda z} B^+ + e^{-\lambda z} B^-), \tag{3.7}$$

where $\gamma = \kappa_z \lambda$. Reformatting equation 3.6 and 3.7 into matrices we have:

$$\begin{bmatrix} \Theta \\ Q \end{bmatrix}_{i,z=L} = \begin{bmatrix} 1 & 1 \\ -\gamma_i & \gamma_i \end{bmatrix} \begin{bmatrix} e^{\lambda L} & 0 \\ 0 & e^{-\lambda L} \end{bmatrix}_i \begin{bmatrix} B^+ \\ B^- \end{bmatrix}_i = [N_i] \begin{bmatrix} B^+ \\ B^- \end{bmatrix}_i . \tag{3.8}$$

The complex constants $B^+$ and $B^-$ can be regarded as the material properties of the $i$th layer, which can be obtained from the temperature and heat flux boundary condition for the surface in equation 3.8:

$$\begin{bmatrix} B^{+} \\ B^{-} \end{bmatrix}_i = \frac{1}{2\gamma_i} \begin{bmatrix} \gamma_i & -1 \\ \gamma_i & 1 \end{bmatrix} \begin{bmatrix} \Theta \\ Q \end{bmatrix}_{i,z=0} = [M]_i \begin{bmatrix} \Theta \\ Q \end{bmatrix}_{i,z=0} . \tag{3.9}$$

In order to consider the heat flow across the interface between the layers, an additional matrix must be taken into account to relate heat flux and the temperature of the top layer to the bottom layer, which is defined as:

$$\begin{bmatrix} \Theta \\ Q \end{bmatrix}_{i+1,z=0} = \begin{bmatrix} 1 & -1/G \\ 0 & 1 \end{bmatrix}_i \begin{bmatrix} \Theta \\ Q \end{bmatrix}_{i,z=L} = [R]_i \begin{bmatrix} \Theta \\ Q \end{bmatrix}_{i,z=L} , \tag{3.10}$$

where G is the equivalent thermal conductance ($\kappa_z/d$) between the two layers. As a result, the heat flux and temperature of the top layers in the multilayer stack are related to the bottom-most layer (substrate) through:

$$\begin{bmatrix} \Theta \\ Q \end{bmatrix}_{i=n,z=L_n} = [N]_n[M]_n \cdots [R]_1[N]_1[M]_1 \begin{bmatrix} \Theta \\ Q \end{bmatrix}_{i=1,z=0} = \begin{bmatrix} A & B \\ C & D \end{bmatrix}_i \begin{bmatrix} \Theta \\ Q \end{bmatrix}_{i=1,z=0} . \tag{3.11}$$

Assuming an adiabatic boundary condition for the semi-infinite bottom layer, the heat flux goes to zero at distances far away from the interface $Q_{z\to\mathrm{inf}} = 0$, which yields $0 = C\Theta_{i=1,z=0} + DQ_{i=1,z=0}$. The temperature response of the layers at a single point in the multilayer stack can be related to the heat flux through the Green's function:

$$\hat{G}(k,\omega) = \frac{\Theta_{i=1,z=0}}{Q_{i=1,z=0}} = \frac{D}{C}. \tag{3.12}$$

Once above Green's function is obtained, one can readily acquire the thermal response of the multilayer stack via multiplication of $\hat{G}(k,\omega)$ with the heat source function in the frequency domain, which will be discussed in the subsequent subsection.

### 3.2.2 Signal Processing in TDTR Experiment

In this subsection, I review the details of modeling the surface temperature rise with respect to position and time as a result of the pump beam as well as the details of sensing the corresponding temperature rise with a probe beam based on the analytical solution presented in ref [90]. In order to make the math easier, we take the Hankel transform of position and the Fourier transform of time to perform the math in the Hankel transform and frequency domain. Since the laser pulses in TDTR are significantly shorter (<500 fs) than the pulse interval (12.5 ns), it is reasonable to assume an infinite series of Dirac delta functions for the heat flux deposited on the surface of the sample.

$$p_1(r,t) = \frac{2A_1}{\pi w_1^2}\exp\left(\frac{2r^2}{w_1^2}\right)e^{i\omega_0 t}\sum_{n=-\infty}^{\infty}\delta(t-nT_s-t_0), \tag{3.13}$$

where $A_1$ is average pump power, $w_1$ is the pump beam size measured at $1/e^2$ from the highest intensity assuming Gaussian distribution, $\omega_0$ is the modulation frequency, and $t_0$ is the arbitrary time delay for laser pulses. Taking the Hankel and Fourier transform for position and time, respectively, we can rewrite equation 3.13 as follows:

$$P_1(k,\omega) = A_1\exp(\pi^2k^2w_1^2/2)\omega_s\sum_{n=-\infty}^{\infty}\delta(\omega-\omega_0-n\omega_s)e^{in\omega_s t_0}. \tag{3.14}$$

Now, we can obtain the temperature rise on the surface by multiplying the thermal response function $\hat{G}$ with the input power:

$$\Theta(k,\omega) = P_1(k,\omega)\hat{G}(k,\omega). \tag{3.15}$$

In order to transfer the surface temperature rise back to cylindrical coordinates, we take the inverse Hankel transform and obtain the radial distribution of the temperature on the surface of the sample:

$$\Theta(r,\omega) = \int_0^{\infty} P_1(k,\omega)\hat{G}(k,\omega)J_0(2\pi kr)2\pi k dk. \tag{3.16}$$

Similarly, the inverse Fourier transform of the above equation gives the surface temperature response as a function of time. Now, in order to model sensing the temperature rise with the probe beam, we take a similar approach to pump temperature rise with the difference of adding the time delay term ($t_d$) to the equation:

$$p_2(r,\omega) = \frac{2A_2}{\pi w_2^2}\exp\left(\frac{2r^2}{w_2^2}\right)\sum_{m=-\infty}^{\infty}\delta(t - mT_s - t_0 - t_d). \tag{3.17}$$

Taking the Fourier transform of the above equation gives:

$$P_2(r,t) = \frac{2A_2}{\pi w_2^2}\exp\left(\frac{2r^2}{w_2^2}\right)\sum_{m=-\infty}^{\infty}\delta(\omega - m\omega_s)e^{in\omega_s t_0}. \tag{3.18}$$

Considering the weighted average of the temperature distribution within the probe beam in real space, we can arrive at the following equation:

$$\Delta\Theta(\omega) = \int_0^\infty \left[\frac{1}{2\pi}\int_{-\infty}^{\infty}\Theta(r,\zeta)P_2(r,\omega-\zeta)d\zeta\right]2\pi r dr. \tag{3.19}$$

Simplifying the above equation, we can rewrite the probed temperature profile in the frequency domain as:

$$\begin{aligned}\Delta\Theta(\omega) = A_1\int_0^\infty \sum_{\infty}^{n=-\infty}\delta(\omega-\omega_0)\hat{G}(k,\omega_0+n\omega_s)\exp(in\omega_s t_d)\\ \times\exp[-\pi^2k^2(w_1^2+w_2^2)/2]2\pi k dk.\end{aligned} \tag{3.20}$$

Now, taking the root mean square of the pump and probe beam sizes $w_0 = \sqrt{(w_1^2+w_2^2)/2}$ and considering the harmonic modulation of the pump beam with a frequency of $\omega$ we arrive at:

$$\Delta\Theta(\omega) = \delta(\omega-\omega_0)\sum_{n=-\infty}^{\infty}\Delta T(\omega_0 - n\omega_s)\exp(in\omega_s t_d). \tag{3.21}$$

By simply taking the inverse Fourier transform of the above equation, we convert the probed signal back to the time domain at a time delay of $t_d$:

$$\Delta R(t) = e^{i\omega_0 t} \sum_{n=-\infty}^{\infty} \Delta T(\omega_0 - n\omega_s)\exp(in\omega_s t_d). \tag{3.22}$$

The lock-in amplifier detects the in-phase and out-of-phase component of the TDTR signal ($\Delta R(t)$) at the pump modulation frequency at a specific delay time:

$$V_{in} = Re[\Delta R(t)] = \frac{1}{2}\sum_{n=-\infty}^{\infty} \Delta T(\omega_0 + n\omega_s) + \Delta T(-\omega_0 + n\omega_s)\exp(in\omega_s t_d), \tag{3.23}$$

$$V_{out} = Im[\Delta R(t)] = \frac{1}{2}\sum_{n=-\infty}^{\infty} \Delta T(\omega_0 + n\omega_s) - \Delta T(-\omega_0 + n\omega_s)\exp(in\omega_s t_d). \tag{3.24}$$

By reading the signal through the lock-in amplifier at various delay times, typically from -15 to ∼5000 ps (we need pre-zero data for phase correction, see ref. [98]), the TDTR measurement is completed. The in-phase signal $V_{in}$ is the response of the sample due to a single laser pulse, *impulse response*, and determines its corresponding temperature rise. The decay of $V_{in}$ can be directly related to the cooling rate of the surface and the corresponding thermal effusivity of the underlying layers. On the other hand, the out-of-phase signal $V_{out}$ is due to the pulse train accumulation which leads to the modulated heating response from the sample. Typically, for fitting purposes in the TDTR model, in order to get a cleaner data the ratio of in-phase versus out-of-phase signal $-V_{in}/V_{out}$ is used. The magnitude of the in-phase and out-of-phase components ($\sqrt{V_{in}^2 + V_{out}^2}$) can be related to the total changes in the reflectivity of the surface as a result of pump pulses.

## 3.3 Uncertainty

As with any other experimental technique, uncertainty analysis is an integral part of determining the measurement accuracy. In this section, I will discuss the possible sources of error and uncertainty associated with TDTR measurements. In general, the sources of error in experimental studies fall into three main categories; instrumental, procedural, and data analysis. With regards to TDTR, which is a laser-based technique where the laser beam passes through a variety of different instruments and optics, slight misalignment of the beam or malfunction of a device could lead to obvious or hidden errors in the measured data. For instance, one of the common procedural errors in TDTR measurements is neglecting pump and probe overlap, which is an integral part of the measurement and could throw off the results without the user noticing it. In order to minimize any instrumental or procedural error from the TDTR measurements, every day before taking any data, the system must be calibrated by measuring the thermal conductivity of standard calibration samples such as $Al_2O_3$ or amorphous $SiO_2$, and comparing the results against literature values. For our calibration, we take three scans at different locations on both $Al_2O_3$ and amorphous $SiO_2$ calibration samples and accept an average thermal conductivity within $\pm 3\%$ of the expected value. In the case where the measured thermal conductivity falls outside $\pm 3\%$ range, the system is checked to find the possible source of error. The measurement of calibration samples not only ensures the system is healthy and ready for use, but also, prevents any procedural error that the user could make.

Nonetheless, in TDTR experiments, the major source of uncertainty stems from misinterpreting the acquired data rather than taking unreliable data. In most cases, when the number of layers in the multilayer stack increases to more than three or the number of unknown properties are more than two, the interpretation of TDTR results requires more attention. In the following, I will discuss some of the analytical approaches that one can take to facilitate the interpretation of the acquired data and identify the effective parameters of the thermal model and possible sources of uncertainty.

### 3.3.1 Sensitivity Analysis

The typical unknown properties for TDTR experiments are thermal conductivity and thermal boundary conductance, which are treated as free parameters and are adjusted through the least squares minimization technique so that the difference between the model and experimental data is minimized. Depending on the properties of each layer in the multilayer stack, the thermal model is affected to a different extent by each parameter, such as spot size, film thickness, heat capacity, and thermal conductivity. In other words, the degree to which each parameter impact the fitting of data to the TDTR results varies. Sensitivity analysis can provide valuable insight into the strength of relationships between the parameters in the fit and measured signal. In order to identify the parameters that play an effective role in our thermal model, I turn to a mathematical equation originally introduced by Costescu et al. [99] commonly referred to as *sensitivity analysis*:

$$S_\zeta = \frac{\partial \ln R}{\partial \ln \zeta} = \frac{\zeta}{R}\frac{\partial R}{\partial \zeta}, \tag{3.25}$$

where $S_\zeta$ is the sensitivity coefficient, $R$ is the TDTR signal $R = -V_{in}/V_{out}$, and $\zeta$ is the target parameter for fitting. The magnitude of $S_\zeta$ for a specific parameter determines its impact on the TDTR signal. In other words, if $\zeta$ increases by 1%, the ratio signal $R$ will also increase by 1%. Similarly, for the case where the $S_\zeta = 0$, the signal $R$ is not affected by the parameter $\zeta$ and therefore, the measurement is insensitive to that parameter. For the measurement of a property, ideally the fitting parameter has the highest sensitivity and the sensitivity to other parameters such as thicknesses and spot sizes is the smallest. The sensitivity analysis provides a powerful tool for designing the TDTR experiment in a way that the highest sensitivity, and therefore, the highest accuracy is achieved for the target parameter.

In order to demonstrate the significance of sensitivity analysis in TDTR measurements, I turn to a common phase change material, $Ge_2Sb_2Te_4$ (GST), which will also be the focus of subsequent chapter. For this, I consider a 40 nm thick GST film between the ruthenium transducer and silicon substrate at different structural phases, amorphous, cubic, and hexagonal, with differing thermal conductivities. For this, we assume all of the phases possess almost identical properties other than their thermal conductivity, which is 0.16, 0.50, 1.30 W $\mathrm{m}^{-1}\mathrm{K}^{-1}$, respectively. The thermal resistance circuit is depicted in Fig. 3.2 (a-c). This is a great example to demonstrate the interplay of thermal conductivity and thermal boundary conductance due to sensitivity of the measurement. Figure 3.2 (d-f) shows the sensitivity of our measurements to thermal conductivity ($\kappa$) and TBC ($G_{\mathrm{GST/W}}$) at different structural phases. As can be seen, there is negligible sensitivity to TBC in the amorphous phase, which has the lowest thermal conductivity or thermal highest resistance. However, upon increasing thermal conductivity in the cubic phase, the resistance due to the film itself becomes comparable to that of the interfaces, and therefore, the sensitivity to TBC slightly increases. However, comparing the amorphous to the hexagonal phase, we can clearly observe that the sensitivity to TBC increases and is comparable to that of the thermal conductivity. In this case, it is almost impossible to differentiate the effect of thermal conductivity from that of the interface because the sensitivities to both of these parameters are very close. However, there are other ways around this, which I will discuss in the next section to distinguish thermal conductivity from that of the TBC in thin films.

### 3.3.2 Confidence Range

The sensitivity analysis provides a practical approach to determine the effectiveness of a parameter in our thermal model prior to taking any measurement. However, it does not provide any information about the quality of the fit to the experimental data or how much the fit deviates from the best-fit. In certain cases, it would be helpful to know how much a parameter changes the quality of a fit so that a confidence range, *error bars*, can be provided for the reported values. Typically, when the sensitivity of the measurement is low to the target property, such as sensitivity to the TBC in the amorphous phase of GST 3.2 (a), it is not possible to report a value for the TBC. However, the data acquired from TDTR allows us to provide a range of values instead of a single number based on the amount of

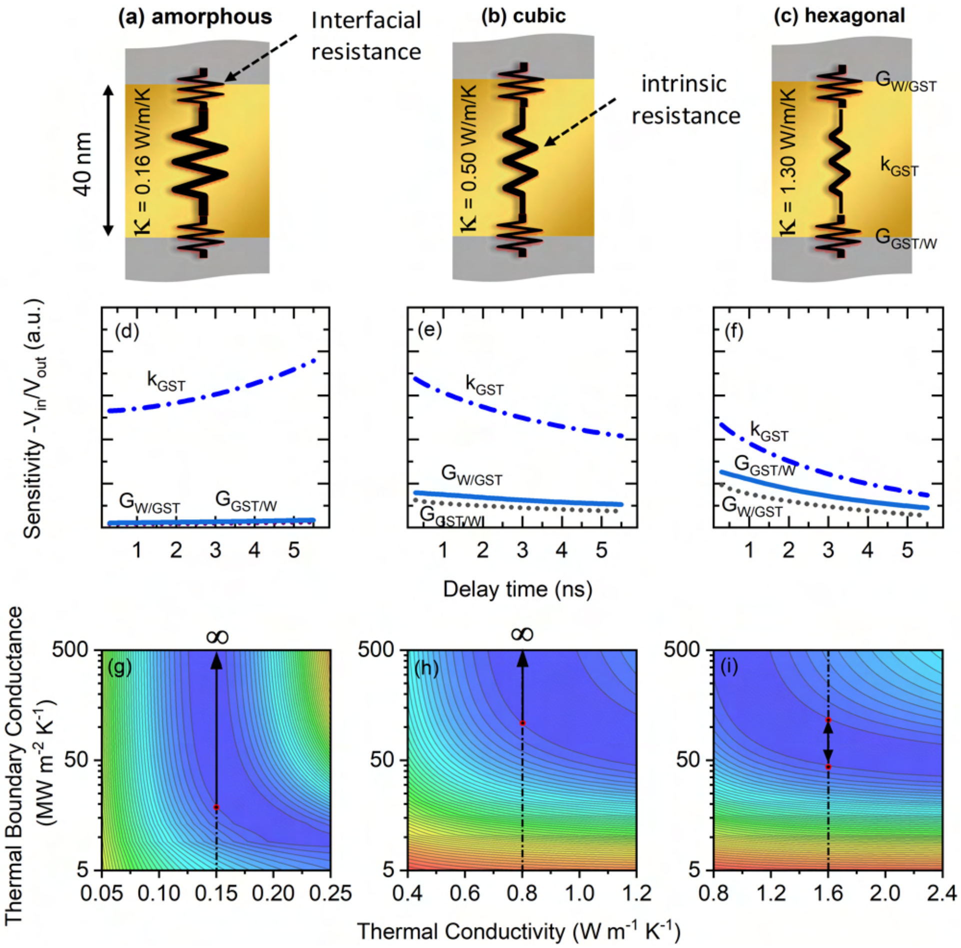

Figure 3.2: (a-c) Schematic of the layers studied showing amorphous, cubic, and hexagonal phase. (d-f) Sensitivity of thermal conductivity and top/bottom interfaces in a 40 nm thick GST as a function of delay time across different phases. (g-i) Residual contour showing the degree of deviation from the best-fit for $G_{GST/W}$ as a function of thermal conductivity in different phases of GST.

deviation from the best-fit. In other words, by changing the target parameter and looking at the quality of the fit to the experimental data, it can be realized that for certain values the fit is no longer acceptable. Generally, as long as the fit is within 2% of the best-fit, we consider it an acceptable fit.

This approach becomes very helpful for samples that have little sensitivity to the parameter of interest. Figures 3.2 (g-i) show the contour plots for thermal conductivity as a function of TBC in amorphous, cubic, and crystalline phases of GST. The colors in the plot from blue to red indicate the amount of deviation or residual value from the best-fit. According to Fig. 3.2 (g), for the amorphous phase where there is little sensitivity to the TBC, any values from 25 MW $m^{-2}K^{-1}$ to infinity would give a reasonable fit and for values less than 25 MW $m^{-1}K^{-1}$, the model does not produce a good fit to the data. This enables us to provide a lower bound to the TBC instead of reporting a specific value. On the other hand, as the sensitivity to TBC increases in the hexagonal phase, Fig. 3.2 (i), the range of which the TBC would still produce a good fit is only limited to 50-150 MW $m^{-2}K^{-1}$. This technique enables providing a reasonable range of values for thermal properties such that the sensitivity of TDTR measurements is small.

## 3.4 Thermal Properties

The complexity of data acquisition and data processing in TDTR experiments proves its worth by enabling measurement of several thermal properties such as in-plane and cross-plane thermal conductivity, thermal boundary conductance, heat capacity, and sound speed. Although TDTR is a relatively versatile approach for measuring thermal properties, when it comes to a sample with multiple unknown parameters, it imposes great challenges. As a result, in order to obtain accurate thermal properties, it is very important to have a comprehensive understanding of the parameters such as beam spot sizes as well as thickness, heat capacity, thermal boundary conductance, and thermal conductivity of each layer in the sample geometry. Ideally, other than the target property, all other parameters in the multilayer stack are accurately known. However, in reality, a complete knowledge of all parameters in the thermal model is less likely without detailed characterization, which is both costly and time-consuming. The solution to this problem is to design the sample architecture in such a way that the sensitivity of measurement to the target property is highest with a minimum sensitivity to other possible unknown parameters. In this section, I discuss the details of the analysis regarding the acquired data and show how various thermal properties can be obtained from TDTR data.

### 3.4.1 Thermal Conductivity

The most widely used application of TDTR is the measurement of thermal conductivity for materials ranging from tungsten diselenide $WSe_2$ with an ultralow thermal conductivity of 0.05 W $m^{-1}$ $K^{-1}$ [68–70] to diamond with ultrahigh thermal conductivity of $\sim$2000 W $m^{-1}$ $K^{-1}$ [38–40, 100]. In addition to bulk materials, TDTR has been established as a powerful technique to measure a wide variety of thin films down to a few nanometers. For this type of measurement, extra care is necessary as the measured thermal conductivity could be a convolution of intrinsic thermal conductivity and thermal boundary conductances. It must be noted that, depending on the thermal properties of the thin films and modulation frequency, TDTR could only measure a finite depth from the surface of the sample. The depth at which the heat pulses can penetrate through is commonly referred to as *thermal penetration depth* and can be estimated by the knowledge of thermal conductivity, heat capacity, and the modulation frequency, $d_{p,z} = \sqrt{\kappa_z / \pi f_{mod} C}$. Note, $d_{p,z}$ disregards the resistance from the interfaces, and therefore, if there are interfaces within this depth the actual penetration depth would be less than the calculated value. For films that are thinner than this depth, the TDTR measurements are sensitive not only to the transducer/film interface but also to the film/substrate interface, assuming only a three layer stack (transducer/film/substrate). Generally, in the case where the effect of intrinsic thermal conductivity is not distinguishable from that of the interfaces, an *effective* thermal conductivity is reported to demonstrate extrinsic properties such as interfaces could be effecting the reported value.

To demonstrate the influence of TBC on the thermal conductivity measurements for thin films, I use 20 and 160 nm of $Ge_2Sb_2Te_4$ (GST) sandwiched between 5 nm of tungsten layers, which is a relevant sample structure for the subsequent chapters of this dissertation. Figure 3.3(a) shows the acquired TDTR data with its corresponding theoretical fit for these two thicknesses. According to these measurements, the thermal conductivity of the 160 nm GST is $\sim$1.3 W $m^{-1}$ $K^{-1}$ while the effective thermal conductivity of the 20 nm sample is $\sim$0.3 W $m^{-1}$ $K^{-1}$. This four fold reduction in thermal conductivity is the result of additional resistance from the interface.

### 3.4.2 Thermal Boundary Conductance

Thermal boundary conductance (TBC) which is the inverse of a more widely used term, *interfacial thermal resistance*, determines the ability of an interface to conduct heat across. For interfaces where one side is a non-metal, the thermal conductance depends on a variety of different factors such as interfacial adhesion strength [101–107], spectral phonon overlap [108–110], interface roughness [111–113], compositional intermixing at the interface [114], and electron-phonon coupling [115, 116]. One of the major factors in determining the efficiency of thermal transport at an interface is how closely the energy states of phonons at the interface between the two materials overlap. For instance, taking a metal/non-metal interface as an example, it has been shown that better phonon spectrum overlap between Cu or Cr and $Al_2O_3$ as compared to Au and $Al_2O_3$ lead to more than three fold increase in TBC of metal/non-metal interfaces [108]. This also agrees with the seminal diffuse mismatch theory (DMM) [117] which states that the more similar the phononic spectra of the materials on either side of the interface (characterized by their phonon velocities and maximum phonon frequencies/Debye temperatures), the higher the energy transmission and resulting thermal boundary conductance [117–121]. As I will show in the next chapter, disordered interfaces generally have a higher TBC compared to abrupt, perfect interfaces. This is due to the emergence of additional vibrational modes in the case of an imperfect interface versus a perfect interface, which leads to a better spectral overlap of phonons between the two materials at the interface.

The fitting parameters in TDTR are typically the thermal conductivity of the substrate $\kappa_{sub}$ and TBC between the transducer and the substrate $G_{tansd/sub}$. In most cases, since there are different sensitivities to these parameters at different delay times, both of these values can be obtained from a single TDTR scan. This, however, is slightly more complicated when more layers are added between the transducer and the substrate. In this case, depending on the thickness of the film, the measurement may become sensitive to the back-side interface between the film and the substrate. In this scenario, there are three unknown parameters, $\kappa_{film}$, $G_{tansd/film}$, and $G_{film/sub}$, which requires either simplifying assumptions or additional measurements to identify some of these unknowns. Here, I discuss how thermal conductivity and the TBC can be obtained from TDTR measurements for cases where the number of unknowns in the multilayer stack is greater than two.

Figure 3.3(a) shows the acquired TDTR data with its corresponding theoretical fit for 20 and 160 nm of $Ge_2Sb_2Te_4$ (GST) that are sandwiched between 5 nm of tungsten layers. In order to find the GST intrinsic thermal conductivity and the associated TBC between GST and W ($G_{GST/W}$), I perform measurements on two thicknesses of GST. This is because the sensitivity of TDTR measurements to thermal conductivity and TBC varies with respect to thickness and, therefore, by measuring thermal conductance across various thicknesses, the intrinsic thermal conductivity can be differentiated from that of the TBC. According to the sensitivity analysis in Fig. 3.3 (b,c), for 20 nm GST, the sensitivity of the measurements to TBC is highest, whereas in the 160 nm thick GST, the sensitivity to TBC is negligible. Therefore, the intrinsic thermal conductivity of GST can be obtained from a 160 nm film where the influence of TBCs are minimum and the TBC can be obtained from a 20 nm film where there is more sensitivity to the TBC.

In the case of 20 nm thick GST, the existence of a thin GST layer increases the sensitivity of our measurements to $G_{GST/W}$ (Fig. 3.3(b)). To find $G_{GST/W}$, as depicted in Fig. 3.3(d), the effect of all other resistors in the series must be subtracted from the total resistance. For this, since the 20 nm GST film yield a relatively small resistance between the Ru and Si, we can treat the entire stack (W/GST/W) as an interfacial layer and using a two layer model, measure the thermal conductance across the Ru/Si interface. The penetration depth in TDTR measurement is on the order of $\sim$100 nm. The substrate is silicon which acts as a heat sink, and therefore the resistance due to this layer is negligible. This leaves us with seven resistors between Ru and Si, as depicted in the first schematic in Fig. 3.3(d).

Now, in order to deconvolute the thermal conductivity from that of the TBC, we need to know the intrinsic thermal conductivity of each layer as well as their corresponding

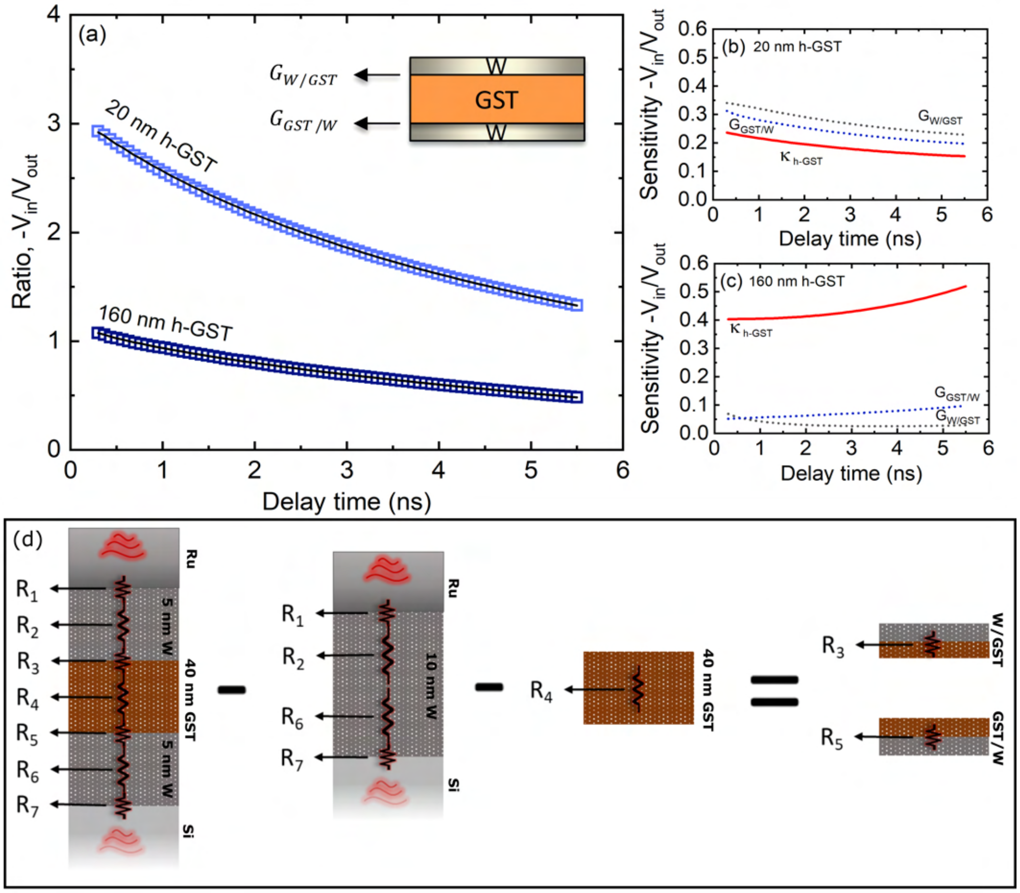

Figure 3.3: (a) Theoretical fit for 20 and 160 nm GST thickness, (b,c) Sensitivity to thermal conductivity and TBC on either side of GST layer for a 20 and 160 nm GST (d) Schematic representing the approach used in this dissertation to find the thermal boundary conductance between GST and W.

TBCs. For this, using a different set of samples, the thermal conductance across Ru/10 nm W/Si is measured to account for the intrinsic thermal conductivity of W, Ru/W, and W/Si interfaces. Next, assuming the intrinsic thermal conductivity of 20 nm thick GST film is similar to that of the 160 nm, we can subtract the resistance due to the 20 nm GST film from the total resistance. In order to mathematically derive an equation for estimating the TBC between GST and W, I assume each layer and interface introduces a resistance to the thermal transport from the transducer to the substrate similar to the schematic in Fig. 3.3 (d). The overall resistance of the stack between Ru and Si can be obtained from the following equation:

$$\begin{aligned} R_{\text{total}} &= R_{\text{W}} + R_{\text{GST}} + R_{\text{W}} \\ &\quad + R_{\text{Ru/W}} + R_{\text{W/GST}} + R_{\text{GST/W}} + R_{\text{W/Si}}, \end{aligned} \tag{3.26}$$

where $R$ represents the thermal resistance and is defined as the inverse of thermal conductance, $\text{R}_{\text{total}} = 1/\text{G}_{\text{total}}$. Due to the high thermal conductivity of W, the thermal resistance of the W layer compared to that of GST is negligible and can be dropped from Eq. 3.26. Additionally, due to electronic transport of heat between the metals, the interfacial thermal resistance between metal-metal interfaces such as Ru/W is negligible compared to other resistances in the stack. Furthermore, assuming the boundary conductance at the front and rear sides of the GST that are in contact with tungsten are identical ( $R_{\text{W/GST}} = R_{\text{GST/W}}$), Eq. 3.26 can be simplified to:

$$R_{\text{total}} = R_{\text{GST}} + 2R_{\text{W/GST}} + R_{\text{W/Si}}. \tag{3.27}$$

In the above equation, except for the $\text{R}_{\text{W/GST}}$, other parameters can be measured from TDTR. Considering that the thermal resistance is the inverse of the thermal conductance, by rearranging the terms in Eq. 3.27 we can obtain an equation for the thermal boundary conductance between GST and tungsten:

$$\text{TBC}_{\text{GST/W}} = \frac{2}{\left(\frac{1}{G_{\text{total}}} - \frac{d_{film}}{k_{160\text{ nm GST}}} - \frac{1}{G_{\text{Ru/10 nm W/Si}}}\right)}. \tag{3.28}$$

In this analysis, $\text{G}_{\text{total}}$ is the total thermal conductance across the multilayer stack of Ru/W/GST/W/Si and $d_{\text{film}}$ is the thickness of the GST film. The above expression allows direct extraction of TBC for cases where the sensitivity to the parameter of interest is low. Through this approach, multiple measurements on different sample geometries, we have been able to provide a reasonable approximation of the TBC between GST and tungsten. As I will show in the next chapter, this expression holds true across different temperatures and GST phases.

### 3.4.3 Heat Capacity

As stated earlier, TDTR measures the thermal effusivity ($\alpha = \sqrt{\kappa C_v}$) which is a convolution of thermal conductivity and volumetric heat capacity. As a result, with the knowledge of one, the other can be extracted from a single TDTR scan but not both. In other words, since the sensitivity to $\kappa$ and $C_v$ is relatively similar, one cannot use both of them as free parameters for fitting. Nonetheless, we can extract thermal conductivity and heat capacity by performing multiple scans at different modulation frequencies; by varying the modulation frequency at which the thin film is heated, the thermal decay varies from an effusivity regime to a purely diffusivity-dominated regime. In other words, these frequency-dependent TDTR experiments allow an independent measurement of both the volumetric heat capacity and thermal conductivity of GSST films without convolution from other thermophysical properties of the heterostructure. For this purpose, modulation frequencies in the range of 0.4-8.4 MHz are chosen, and the experiment is performed on a ~220 nm thick GSST in amorphous and crystalline phases. This thickness is chosen because the measurements would have the highest sensitivity to the thermal conductivity and volumetric heat capacity. Figure 3.4 shows the result of these variable modulation frequency measurements, where the intersection of our data at different frequencies corresponds to the volumetric heat capacity [122]. Based on these data, the volumetric heat capacities for the amorphous and annealed cases are determined to be 1.5 ± 0.1 and 1.8 ± 0.1 MJ $m^{-3}$ $K^{-1}$, respectively. This indicates that the heat capacity increases by 20% upon crystallization. Typically, the heat capacity largely depends on the atomic mass and the density of the materials.

According to the TEM measurements, there is a ~5% reduction in the thickness of GSST upon amorphous to crystalline phase transformation, which agrees with previous observations [16, 123]. Now, the fact that the heat capacity of GSST increases by 20% is surprising. There are two scenarios that could take place here. First, it is possible that due to strain effects from the substrate and the transducer layer, the film density does not change in the in-plane direction (i.e. only the thickness of the film changes). This means that the change in film thickness (∼5%) is comparatively equal to the change in density upon crystallization. This scenario is consistent with previous measurements of density in GST films where the changes in the thickness of the film are similar to the changes in the density [123]. However, if the 5% densification in the film occurs in all directions, xyz, then the change in the density is larger than the change in the thickness. Assuming isotropic change in all directions (∼5%), we can estimate the change in the film density $(d_{amorphous})^3/(d_{crystalline})^3$ to be ∼15%, which is comparable to our measurement of 20% change in the heat capacity. In any case, regardless of the scenarios discussed, the uncertainty associated with our measurements could also explain this disparity between the measurements and the expectations. This means, considering the error bars, the changes in the heat capacity can vary from minimum of 5% to a maximum of 30%, which is within the range of both scenarios.

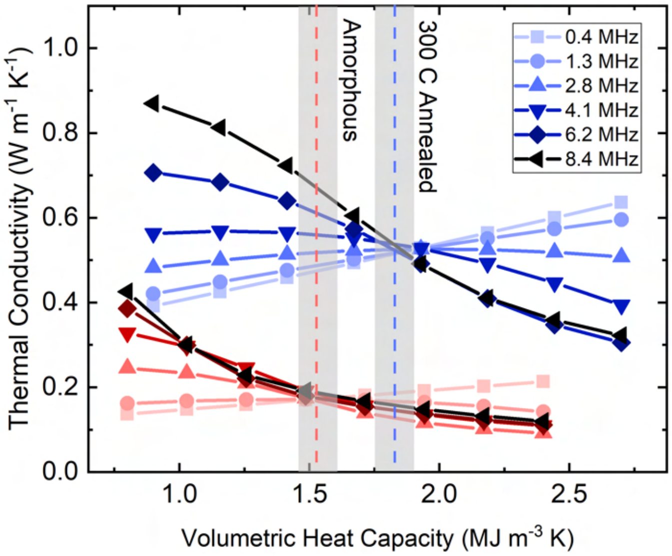

Figure 3.4: volumetric heat capacity for amorphous and crystalline phases of GSST measured with TDTR at different modulation frequencies. The gray area corresponds to uncertainty of the measurements.

### 3.4.4 Sound Velocity

Another important material property that can be obtained from TDTR measurements is the sound velocity of thin films. The measurement is similar to regular TDTR but with significantly higher temporal resolution, which is typically on the order of sub-picoseconds. In these measurements, similar to any transient thermoreflectance technique, the absorption of an ultrashort laser pulse launches a strain wave from the sample surface that propagates through the underlying layers at the speed of sound. Once these strain waves reach an interface between two different materials, depending on the acoustic impedance of the two materials defined as ($Z = \rho \times E$) where $\rho$ is density and $E$ is elastic modulus, the waves are partially reflected and the remainder is transmitted. The reflected waves from each interface travel all the way back to the surface and change the thermoreflectivity of the transducer. This results in qualitative "humps" and "troughs" superimposed on the TDTR thermal decay curve, as shown in Fig. 3.5 (a). For better clarity, the schematic in Fig. 3.5 (b) depicts the propagation of strain waves across different layers for the similar multilayer stack studied in previous subsections. As can be seen in Fig 3.5 (b) *i*, a strain wave is launched from the surface and travels across the Ru layer. Upon reaching the Ru/W interface, a lack of sufficient acoustic mismatch between Ru and W, allows the wave packet to completely pass through the interface without any interference (Fig 3.5 (b) *ii*). On the other hand, once the strain wave reaches the W/GST interface (Fig 3.5 (b) *iii*), as a result of large acoustic mismatch between W and GST, the wave is partially reflected and travels back to the surface and appears as upward "humps" in the residual plot. The other portion of the wave that passes the interface travels across the GST layer, and again, is partially reflected upon reaching the other GST/W interface, where the consequence of this reflection appears as downward "troughs" in the residual plot. Using the time it takes for the strain waves to travel across the film, the longitudinal sound velocity can be estimated.

The propagation of strain waves can be modeled using finite element (FE) simulations to ensure that our interpretation of the picosecond ultrasonic echoes are correct. In these simulations, the density, Poisson ratio, and longitudinal sound velocity are used as inputs to determine the location of echoes in time. As such, the solid lines in Fig. 3.5 (c) correspond to the simulation results, and the dotted line corresponds to the picosecond residuals. As can be seen in Fig. 3.5 (a), the "humps" and "troughs" in the residual plots agree well with the simulations. The agreement on the location of the echoes between the simulations and the experiment confirms that they are not an artifact of measurement and are directly related to the reflection of the strain waves from the interfaces.

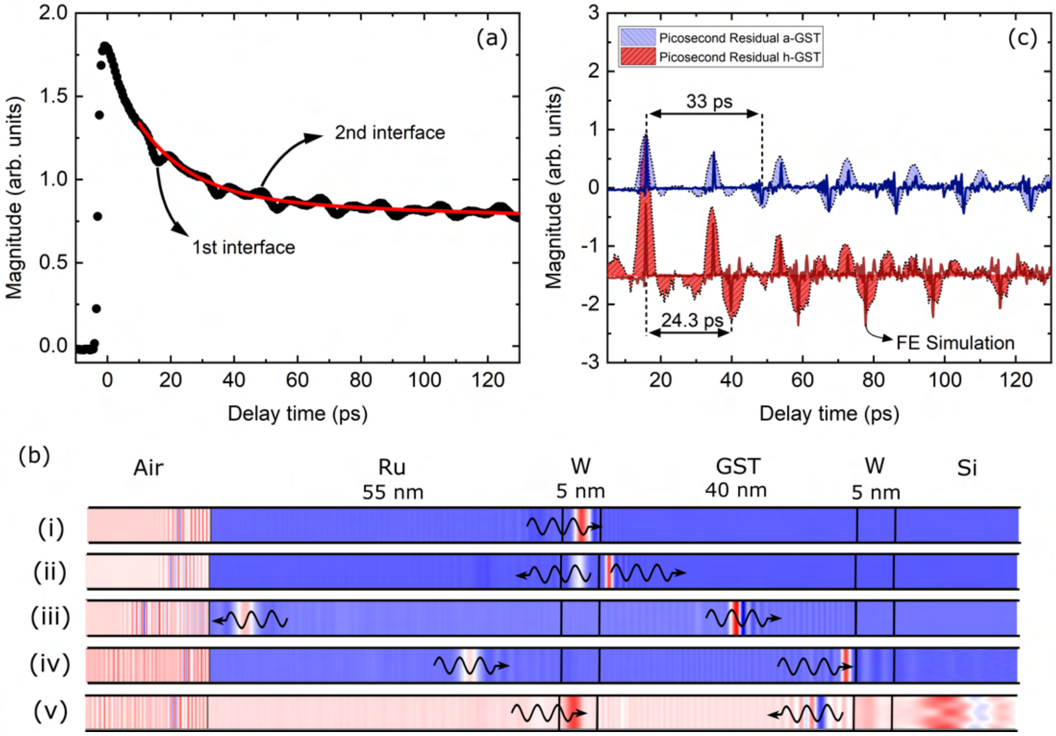

Figure 3.5: (a) Picosecond ultrasonic measurements for 40 nm of GST. The "troughs" and "humps" corresponds to the reflection of strain waves off of first interface (W/GST) and second interface (GST/W), respectively. (b) A representation of strain wave and how it propagates and reflects off of various interfaces. (c) Picosecond ultrasonic measurements subtracted from an exponential decay and the corresponding simulations data from COMSOL. The lines correspond to finite element simulation of strain wave propagation across different layers.

## 3.5 Summary

In this chapter, I reviewed some of the core concepts regarding the experimental technique, specifically TDTR, that is used in the subsequent chapters for the measurement of thermophysical properties and its pertinent data analysis. After briefly outlining the experimental and theoretical work that TDTR has been built upon, I discussed the mathematical details related to the TDTR experiment and evaluated the accuracy of its measurements through sensitivity analyses. Finally, I showed the application of TDTR to extract thermophysical properties of novel phase change materials such as thermal conductivity, thermal boundary conductance, heat capacity, and sound speed.

# Chapter 4

# Engineering Interfaces to Confine Heat

Phase change random access memory (PRAM) is a rapidly growing technology that not only offers advancements in storage-class memories but also enables in-memory data processing to overcome the von Neumann bottleneck. In PRAMs, data storage is driven by thermal excitation. However, there is limited research regarding PRAM thermal properties at length scales close to the memory cell dimensions. In this chapter, I present a new paradigm to manage thermal transport in memory cells by manipulating the interfacial thermal resistance between the phase change unit and its electrodes without incorporating additional insulating layers. My results indicate a substantial change in interfacial thermal resistance as GST transitions from cubic to hexagonal crystal structure, resulting in a factor of 4 reduction in the effective thermal conductivity. This reduction is attributed to a large increase in the interfacial thermal resistance as the PCM crystal structure transitions from cubic to hexagonal phase. Through molecular dynamics simulations, I provide some insight into the underlying mechanisms behind this increase. Further, finite element analyses reveal that interfacial resistance between PCM and its adjacent layer can reduce the reset current for 20 and 120 nm diameter devices by up to $\sim$40% and $\sim$50%, respectively. These thermal insights present a new opportunity to reduce power and operating currents in PRAMs.

## 4.1 Background

The growing demands for higher capacity memory devices and burgeoning data-intensive applications, such as artificial intelligence, have intensified efforts to beat the von Neumann computing bottleneck that separates processing from the storage unit. A promising alternative for transistor-based non-volatile memory devices is an emerging technology known as phase change random access memory (PRAM), which offers prospective gains in speed, device lifetime, and storage capacity, as well as in-memory storage and computing capabilities [33, 124]. The most widely used phase change material, germanium antimony telluride (GST), possesses a high electrical resistivity contrast between its amorphous and crystalline states, as well as sub-nanosecond switching times [125, 126]. This class of phase change materials can quickly switch phase between amorphous and crystalline states upon controlled thermal excitation. In PCMs, the transition from amorphous to crystalline and crystalline to amorphous are commonly referred to as *set* and *reset*, respectively. In devices utilizing phase change units, thermal transport plays a pivotal role as it dictates the efficiency of the set/reset process and overall power consumption.

One of the major limitations in PRAM devices is their high operating current, leading to excessive power consumption [127]. In order to mitigate thermal leakage during programming, Kim et al. [128] used a thermal barrier (2-20 nm of $C_{60}$) to isolate GST from directly contacting the electrode, showing a factor of three reduction in their set current ($I_{set}$). Although a lower power consumption in their device architecture offered performance gains, the relatively large thickness of the thermal barrier introduced additional electrical resistance, decreased bit density, and provided an additional source of degradation for the PCM over time. Later, Ahn et al. [129] proposed a much thinner insulating layer by using a single sheet of graphene (thickness $<1$ nm) as a thermal barrier to confine the heat inside the PRAM cell and showed that the $I_{reset}$ was reduced by 40% compared to the cells without a graphene barrier.

More recently, superlattice phase change memories have received a great deal of attention due to their unique capabilities offering lower power consumption, faster programming rate, higher retention time, and lower noise and drift in electrical resistance [19, 125, 130, 131]. Although earlier superlattice PRAMs consisted of GeTe/$Sb_2Te_3$ alternating stacks, it was soon realized that this configuration tends to intermix and transform into bulk GST at high annealing temperatures [132]. Nonetheless, the idea of superlattice PRAMs inspired researchers to look for alternative material configurations. Very recently, Shen et al. [130] and Ding et al. [19] showed that superlattice PRAMs with $TiTe_2/Sb_2Te_3$ layers have superior properties compared to bulk GST. Despite the fact that in superlattice PRAMs the interface is an integral component in the performance of these devices, its effect on the overall thermal transport is heretofore unknown and unstudied.

With all these previous works in mind, I am prompted to experimentally investigate the effect of interfacial thermal resistance on the performance of PRAM devices. For this purpose, the selected materials are amongst those that are widely used in PRAM devices: $Ge_2Sb_2Te_4$ (GST) as a phase change unit, tungsten (W) as an electrode, and silicon dioxide ($SiO_2$) and silicon nitride ($SiN_x$) as the insulating separators used to confine heat and current within the cell. My work focuses on identifying the critical parameters that influence thermal transport as the length scale of the phase change unit approaches that of the energy carriers' mean free paths. I assess the effect of GST film thickness on thermal transport across various phase transitions and determine the minimum thickness before which thermal transport transitions into a ballistic regime.

To date, the majority of studies investigating thermal transport in GST were performed on layers with thicknesses on the order of 200 nm [15, 133–135]. However, as Xiong et al. [136] demonstrated, in order to decrease power consumption and further the economic benefits of PRAM devices, the thickness of PCM layers should be on the order of 10 nm. In this respect, Kim et al. devised an operational PRAM device with cell dimensions as small as 7.5 nm × 17 nm [137]. In general, as the length scale of materials and interconnects in memory components shrink to dimensions less than energy carrier mean free paths, a number of additional mechanisms, such as electron tunneling [138–140] and thermal boundary resistances [112, 117, 141], may impact the performance of these devices [142]. In this chapter, I present evidence of ballistic transport of energy carriers across the PCM in a confined cell geometry as the characteristic length of the device is decreased to less than the mean free paths of the electrodes' carriers. To demonstrate this, I show that for tungsten electrodes there is a lower limit for the thickness of GST in memory cells before thermal transport transitions from a diffusive to a ballistic regime. I use this knowledge of carrier dynamics to experimentally identify an optimal thickness of phase change material based on a balance of thermal conductivity and crystallographic-phase-dependent thermal boundary conductances (TBC) in order to improve memory device performance.

In this chapter, in contrast to previous studies that were primarily focused on introducing additional layers between the electrode and GST to confine heat in the memory cell, I focus on the interfacial thermal resistance and thermal properties of the layers in contact with GST. First, I investigate the effect of materials adjacent to the PCM by comparing different materials from conductive electrodes to insulators as a spacer between PCM and other neighboring cells. Then, I show that, by intentionally engineering the phase and thickness of the phase change unit, the overall thermal resistance can be substantially increased, causing decreases in requirements for set/reset currents, without incorporating additional layers as a thermal barrier. Although the results presented here are for commonly used materials in PRAMs such as GST and W, I demonstrate that, through manipulation of the interfacial resistance between the phase change unit and the adjacent layer, the predicted reset current can be reduced by up to 40% and 50% for devices with lateral size of 20 and 120 nm in diameters, respectively. This chapter highlights the importance of engineering interfaces to allow for devices with increased performance.

## 4.2 Results

The thermal transport properties of the GST thin films, deposited via magnetron sputtering, were measured using TDTR as previously discussed in details. The surface of the samples are coated with an 80 nm ruthenium transducer. The input into our thermal model are volumetric heat capacity of Ru, *a*-GST, h-GST, and the Si substrate which is assumed to be 2.96, 1.3, 1.4, and 1.64 MJ $m^{-3}$ $K^{-1}$, respectively [143, 144]. The thermal conductivity of the transducer layer is determined to be 54 W $m^{-1}$ $K^{-1}$ based on 4-point probe electrical resistivity measurements and extracting thermal conductivity using Wiedemann-Franz law and the thickness of each layer is confirmed via transmission electron microscopy (TEM).

### 4.2.1 Suppressing Thermal Leakage through Electrode Design

In PRAM devices, efficiency is strongly tied to the materials surrounding the GST and how efficiently heat is localized to the memory cell. For instance, it has been shown that the majority of heat generated in the memory cell is lost through the bottom electrode [145–147]. Thus, the thermal conductivity of the electrodes and thermal conductance across their interfaces are crucial for controlling temperature and optimizing the operating conditions of PCMs. A common electrode material for the PCM is titanium nitride (TiN), which has a range of thermal conductivities and electrical resistivities, depending on the deposition process ranging from (8-63 W $m^{-1}$ $K^{-1}$) and (13.5-150 $\mu\Omega$ cm), respectively [146, 148–152]. The mechanical strength of TiN, coupled with its moderate thermal conductivity, make it appealing for electrode applications. In this section, I evaluate improvement of thermal confinement within the memory cell by introducing a carbon-based electrode that has a low intrinsic thermal conductivity, over an order of magnitude lower than that of TiN, as well as low thermal boundary conductance with an appreciable electrical conductivity.

For this, I begin with measuring the thermal conductivity of $CN_x$ thin films at different thicknesses for as-deposited amorphous and annealed cases. The total thermal resistance, $R$, measured across the Ru/$CN_x$/Si interface as a function of $CN_x$ film thickness are shown in Fig. 4.1 which allow us to measure the intrinsic thermal conductivity of the $CN_x$ independent of the interfaces. The intrinsic thermal conductivity of thin films can be extracted from the data in Fig. 4.1 by applying a linear fit to the total thermal resistance as a function of film thickness, where the inverse of its slope $(\Delta R/\Delta d)^{-1}$ corresponds to the thermal

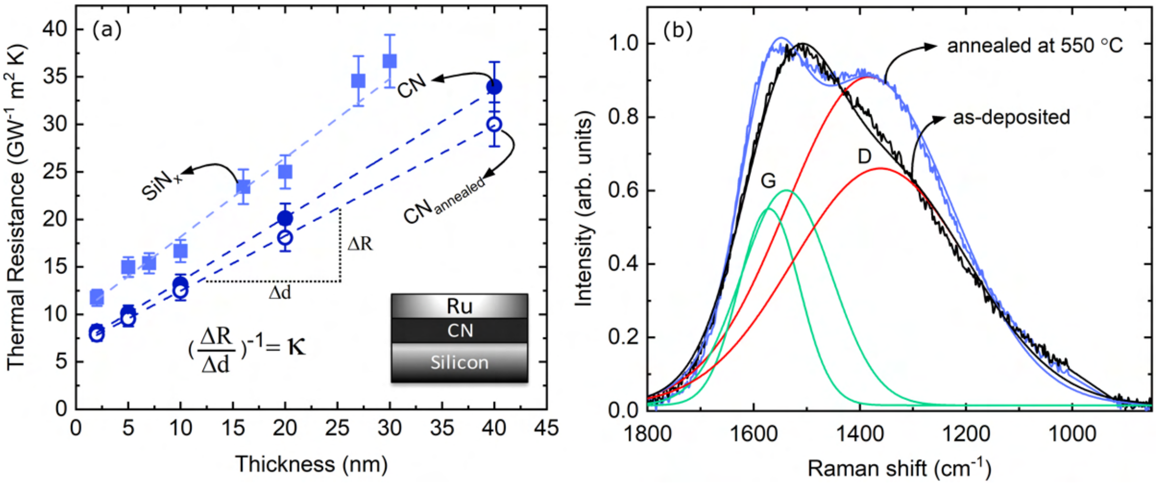

Figure 4.1: Carbon nitride, CN$_x$, thermal characterization. (a) Room temperature measurements of thermal resistance as a function of thickness for SiN$_x$ (squares), as-deposited CN$_x$ (solid circles), and 400 °C annealed CN$_x$ (open circles). The inverse of linear fit slope corresponds to the thermal conductivity of each material. (b) Raman spectra for 30 nm CN$_x$ film in as-deposited and 550°C annealed cases.

conductivity. This approach yields thermal conductivity of $1.47 \pm 0.09$ W m$^{-1}$ K$^{-1}$ for the as-deposited CN$_x$ and $1.72 \pm 0.1$ W m$^{-1}$ K$^{-1}$ for the annealed films. For comparison, I measure the intrinsic thermal conductivity of SiN$_x$ as $\sim$1.20 W m$^{-1}$ K$^{-1}$, derived from the same slope analysis, in good agreement with SiN$_x$ fabricated under similar conditions [153, 154]. These CN$_x$ films exhibit thermal conductivities typical of amorphous materials, and are over an order of magnitude lower than that of the commonly used TiN electrode. These results demonstrate promise using CN$_x$ as a heat confining low thermal conductivity electrode.

To understand the possible microscopic mechanisms leading to the enhancement in electrical and thermal conductivity upon annealing, Raman spectroscopy is performed and compare the Raman spectra for CN$_x$ at different annealing temperatures. Although CN$_x$ maintains its amorphous structure, based on the Raman spectra, the density of the defective regions decreases by annealing at high temperatures [155]. I attribute the $\sim$0.2 W m$^{-1}$ K$^{-1}$ gain in thermal conductivity of the CN$_x$ as a result of annealing to an increase in electrical conduction. The electrical resistivity of as-deposited CN$_x$ at room temperature is above 120 mΩ cm. This implies that the contribution of electrons to thermal conduction is negligible compared to the phononic contribution. However, upon annealing to 400 °C, the electrical resistance drops to nearly 5 mΩ cm, which corresponds to an electronic thermal conductivity of $\sim$0.15 W m$^{-1}$ K$^{-1}$ according to the Wiedemann Franz law formalism. As a result, I posit the increase in electrical contribution to thermal conductivity is the driving factor leading to the enhancement of total thermal conductivity and reduction of thermal resistance from annealing $CN_x$.

### 4.2.2 Thermal Conductance across $CN_x$/PCM/$CN_x$

After characterizing the thermal properties of $CN_x$ film, in this subsection I discuss the effect of thermal conductance when $CN_x$ is adjacent to PCM and compare its results with common conductive metals such as tungsten (W) and common insulators such as $SiN_x$. For this, two sets of samples with GST thicknesses of 10 nm and 40 nm are fabricated. The GST layers are sandwiched between 5 nm films of W, $CN_x$, and $SiN_x$ spacers. The samples are grown on a silicon substrate with 80 nm of Ru on top for TDTR measurements (80 nm Ru/5 nm Spacer/10 nm GST/5 nm Spacer/Silicon substrate). The exact thicknesses for each layer has been confirmed via TEM micrographs. From TEM images, it is observed that an approximately 3 nm amorphous region at the surface of the silicon substrate which is present in all samples and is attributed to the ion milling cleaning procedure prior to film deposition.

Figure 4.2 shows the thermal conductance between Ru and Si (across the various thin films in between and their corresponding interfaces) at elevated temperatures. For the case of the W spacer, the thermal conductance is the highest. This implies that W would result in a large thermal leakage which increases the power consumption in the PRAM device. Although W is a better electrical conductor than $CN_x$ and allows for more efficient Joule heating in the GST, it also allows for substantial thermal loss that is detrimental to the performance of the device. On the contrary, $CN_x$ has a lower electrical conductivity compared to W but proves to be a better choice from a thermal transport perspective due to its low

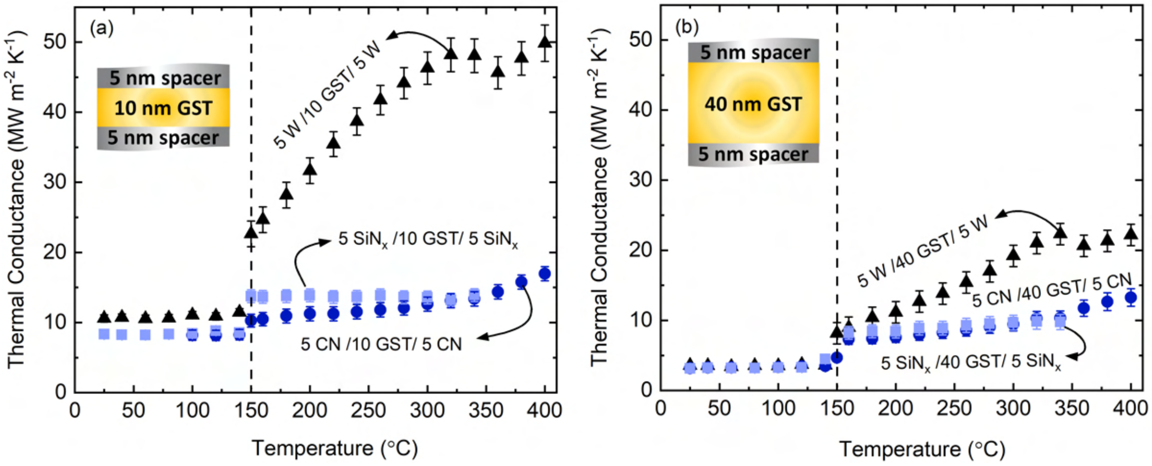

Figure 4.2: Thermal conductance for various spacer compositions. Thermal conductance of $Ge_2Sb_2Te_5$ sandwiched between 5 nm of W (triangles), $SiN_x$ (squares), and $CN_x$ (circles) spacers as a function of temperature for (a) 10 nm GST and, (b) 40 nm of GST. Experimental data is not available for $SiN_x$ above 340°C due to film delamination. Below 150°C, the error bars are smaller than the symbols.

thermal conductivity. To support this, the thermal conductance measurements reported in Fig. 4.2 show significantly lower thermal conductance for $CN_x$ spacers and indicates the promise of $CN_x$ as a potential electrode material to confine heat in the GST more efficiently than W, particularly at elevated temperatures. Although the comparison drawn between W and $CN_x$ electrodes can only be quantified if used in a device, the results presented here pave the way for future studies on $CN_x$ electrodes. Furthermore, even though $CN_x$ is used for electrode applications and $SiN_x$ is used as an insulator, in the thin film GST regime (10 nm), $CN_x$/GST/$CN_x$ shows a lower thermal conductance up to nearly 340 °C. Considering the higher thermal conductivity of $CN_x$, this observation indicates that the interfacial conductance between GST/$CN_x$ is lower than that of GST/$SiN_x$ which results in a lower overall thermal conductance. At temperatures above 340 °C, for the $CN_x$ spacer, thermal conductance is suppressed by almost a factor of three compared to the W spacer. This observation implies that $CN_x$ can serve as an efficient heat barrier in phase change memory cells. Furthermore, Fig. 4.2(a) shows that at the crystallization temperature ($\sim$ 150 °C), unlike W and $SiN_x$ spacers, $CN_x$ spacers do not exhibit as large a change in the thermal conductance and yields almost 30% lower conductance than that of the $SiN_x$ which is an insulator. This is particularly crucial during the set process where the GST temperature rises above its crystallization temperature for a longer duration. Figure 4.2(b) shows the conductance for a similar set of samples with a thicker GST layer (40 nm). As a result of the increased thickness, the measured conductance for all cases is lower than that of 10 nm GST. In this regime, the total conductance from the Ru to the Si is dominated by the GST film itself rather than the interfaces or the spacers. As a result of this thickness effect, the thermal conductance for $CN_x$/GST/$CN_x$ and $SiN_x$/GST/$SiN_x$ is nearly identical up to 340 °C.

### 4.2.3 Interfacial Conductance at Room Temperature

In previous subsection, I demonstrated that the interface between $CN_x$ and GST leads to lower conductances compared to $SiN_x$ up to 300 °C. This can be justified by considering the higher atomic mismatch at the interface and less overlap in the corresponding density of states between $CN_x$ and GST versus $SiN_x$ and GST. This highlights the effect of thermal conductance and lead me to follow this hypothesis if it is possible to engineer the interfaces with a common electrode material such as tungsten. In order to investigate this, I perform several measurements at room temperature to determine at what GST thickness the effect of interfaces become appreciable in the thermal transport. A pictorial representation of the configuration of layers used in this study is given in Fig. 4.3 (a) along with the corresponding TEM images for amorphous (*a*-GST) and hexagonal (h-GST) phases. In order to distinguish the effect of interfaces from that of the layers, it is often instructive to idealize material stacks as a series of thermal resistors comprised of the resistances at interfaces and the intrinsic resistance of the materials, similar to the schematic shown in Fig. 4.3 (c). The measured thermal resistance, is the total resistance between the Ru and Si including all the resistances involved in the multilayer stack. Using different thicknesses of *a*-GST, which varies the relative contribution of each resistor to the overall measured conductance, allow us to assess the relative contribution of each thermal resistance to the overall device thermal transport.

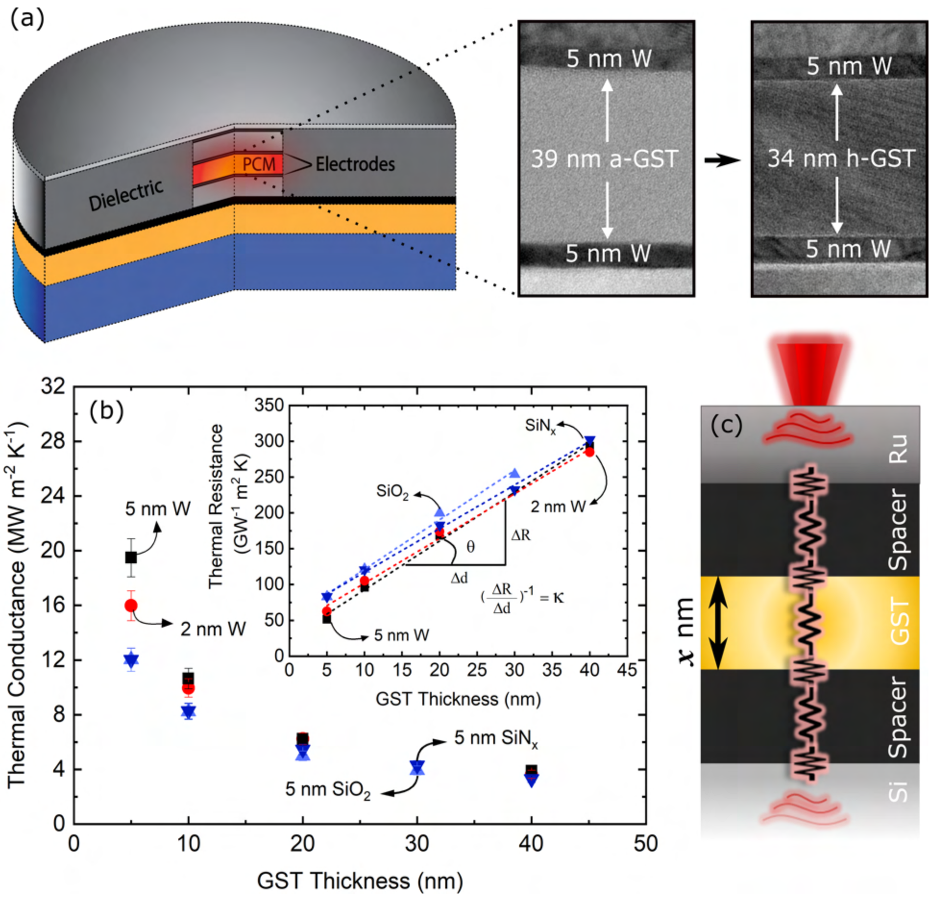

Figure 4.3: (a) Schematic of a confined phase change memory cell along with corresponding TEMs for a 40 nm *a*-GST and h-GST film sandwiched between 5 nm tungsten spacers, (b) thermal conductance across Ru/spacer/GST/spacer/Si for different spacer compositions as a function of GST thickness. The inset shows thermal resistance as a function of thickness where the inverse of the slope for the fitted line corresponds to the *a*-GST thermal conductivity. The average thermal conductivity estimated for *a*-GST is $0.15 \pm 0.02$ W $m^{-1}$ $K^{-1}$. The error bars are calculated based on 7% uncertainty in the Ru transducer thickness, and (c) a schematic of the thermal resistances in series for the multilayer configurations studied here.

Figure 4.3 (b) shows the thermal conductance between Ru and Si, including all intermediate layers (spacer/ *a*-GST/spacer), as a function of *a*-GST thickness. The spacers are W (2 and 5 nm), amorphous $SiO_2$ (5 nm), and amorphous $SiN_x$ (5 nm), where the spacers' thicknesses are identical on either side of the *a*-GST. As the thickness of *a*-GST increases, the effect of the spacers on the overall thermal transport becomes negligible owing to the fact that the *a*-GST layer becomes the dominant resistor. Based on Fig. 4.3 (b), for thicknesses greater than $\sim$10 nm, thermal conductance is largely governed by the *a*-GST layer regardless of the adjacent material, whereas for thicknesses less than 10 nm, the effect of materials adjacent to the GST and therefore TBC become appreciable. Note, for $SiN_x$ and $SiO_2$ spacers, their thermal conductances are similar and lower than that of W. This is expected as the thermal conductivities of $SiN_x$ and $SiO_2$ are similar and more than an order of magnitude lower than that of W [156]. However, it is important to note that the thermal conductance of the stack with the 5 nm W spacer is greater than that with 2 nm spacer. This is contrary to expectations when considering diffusive thermal transport processes, where thermal conductance decreases linearly with an increase in thickness of the material. The observed reduction in thermal conductance for 2 nm W is attributed to the boundary scattering of electrons and phonons. Similar thermal boundary conductance dependencies on the thickness of intermediate layer have been observed across Au/Ti/sapphire [103], Au/Cr/sapphire, and Au/Cu/sapphire [108] interfaces. The thermal conductivity of *a*-GST is determined from these measurements by fitting a linear regression to the slope of the measured thermal resistance as a function of thickness, depicted in the inset of 4.3 (b). The thermal conductivity of *a*-GST is determined to be 0.15 ± 0.02 W $m^{-1}$ $K^{-1}$, in good agreement with previously reported values [15, 133, 157].

### 4.2.4 Interfacial Conductance at Elevated Temperature.

Above, I showed that the effects of materials adjacent to GST and the corresponding TBC are only appreciable for *a*-GST when the thickness is less than 10 nm. However, as the *a*-GST film changes phase, its intrinsic thermal conductivity increases by almost an order of magnitude which reduces the resistance due to the GST layer. This implies that thermal transport in the crystalline phase should be more dramatically affected by the TBC than in the amorphous phase. Therefore, it is crucial to understand the effects of thermal transport across W/GST interfaces as GST undergoes phase transitions. TDTR measurements are taken as a function of temperature using a resistive heating stage that allows us to measure the thermal conductivity of GST and the thermal boundary conductance at the h-GST/W interface from room temperature up to 400 °C, thereby, capturing the thermal properties of GST in all of phases (i.e., amorphous, cubic and hexagonal).

Figure 4.4 (a) shows the thermal conductivity of 40 nm and 160 nm thick *a*-GST layers that are heated under nominally identical conditions across various temperatures. In this figure, the solid symbols correspond to the thermal conductivity of *a*-GST when heated from room temperature up to 400 °C, whereas the hollow symbols correspond to the thermal conductivity of h-GST when cooled down from 400 °C to room temperature. The solid circles denoting the 160 nm film in Fig. 4.4 (a) show a clear transition from *a*-GST to c-GST, and c-GST to h-GST at approximately 150 °C and 340 °C, respectively, in good agreement with reported literature values [15, 158, 159]. The enhancement of thermal conductivity in the crystalline phase is attributed to the dissolution of disordered vacancy clusters and increasing order in the crystalline phase [160, 161]. After the sample reaches 400 °C and the GST is fully transformed into the hexagonal phase, its thermal conductivity is measured as the sample is cooled down to room temperature, shown as hollow circles in Fig. 4.4 (a). The thermal conductivity of the 160 nm h-GST decreases slightly over temperature as a result of reduced electronic contribution to the thermal conductivity [160].

On the other hand, for the 40 nm thick GST, the measurement of intrinsic thermal conductivity in the crystalline phase is increasingly difficult as the effects of interfacial thermal resistance interfere with thermal conductivity measurements as opposed to the 160 nm case as discussed in previous chapter. For this reason, I report the effective thermal conductivity ($k_{\mathrm{eff}} = G_{\mathrm{Ru/W/GST/W/Si}} \times d_{\mathrm{GST}}$), depicted as solid diamonds, which incorporates both the

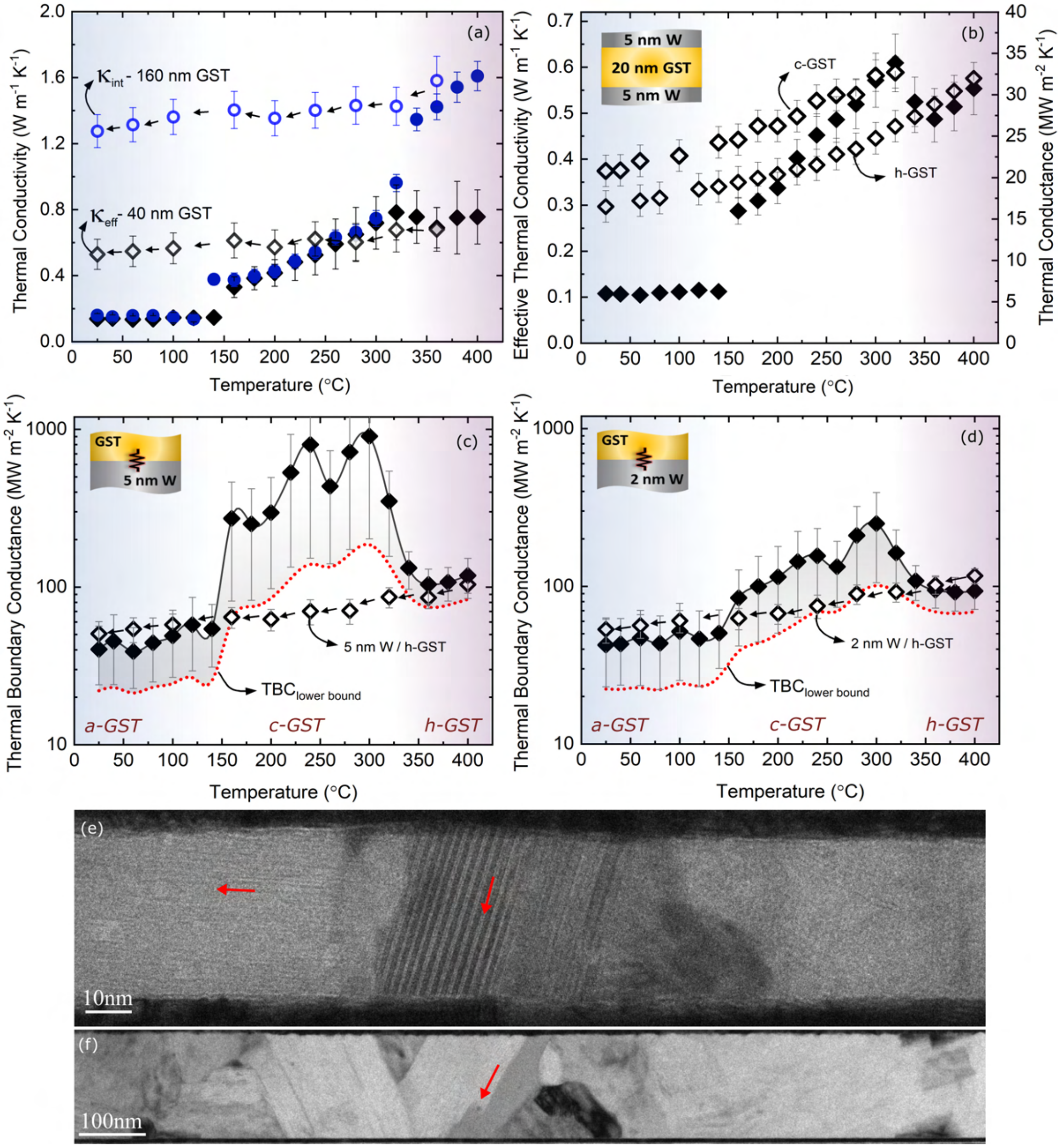

Figure 4.4: Thermal properties of GST thin films and interfaces across different phases. (a) Thermal conductivity of GST layer sandwiched between 5 nm W spacers for 40 nm (diamonds) and 160 nm (circles) GST films. The solid symbols correspond to the thermal conductivity of GST as it transitions through different phases upon heating and hollow symbols correspond to the thermal conductivity of h-GST upon cooling. (b) Effective thermal conductivity for 20 nm thick GST film as a function of temperature across different phases of GST upon heating and cooling when annealed to 300 and 400 °C. (c,d) Thermal boundary conductance for as-deposited GST upon heating and h-GST upon cooling with 5 and 2 nm W spacer, respectively. The error bars are calculated based on 7% uncertainty in the GST film thickness. (e,f) Bright field images of 40 nm and 160 nm GST films at 400 °C.

effects of the intrinsic thermal conductivity of GST and the associated TBCs. The effective thermal conductivity for the 40 nm thick GST sample follows a similar trend to that of 160 nm film up to 300 °C, except for the slight upward shift in crystallization temperature to 150 °C. The agreement of thermal conductivity up to 300 °C between the two thicknesses is due to negligible effect of TBC on thermal transport in the amorphous and cubic phase. However, upon transformation from c-GST to h-GST, the TBC at the h-GST/W interface considerably decreases. As a result, it is observed that the effective thermal conductivity for the 40 nm GST film deviates from the 160 nm GST in the hexagonal phase. Above 300 °C, we no longer measure the intrinsic thermal conductivity of the h-GST layer but, instead, a convolution of the h-GST thermal conductivity and the h-GST/W TBCs. The effective thermal conductivity for the 40 nm sample plateaus near $\sim$0.8 W m$^{-1}$ K$^{-1}$, almost a factor of two lower than the thermal conductivity measured for 160 nm h-GST. This difference is even more pronounced when the samples are cooled down to room temperature where the thermal conductivity for 40 and 160 nm are $\sim$0.5 and $\sim$1.3 W m$^{-1}$ K$^{-1}$. In order to ensure the observed reduction in the effective thermal conductivity is not due to any microstructural changes in the film, I present extensive TEM with *in situ* heating to compare the quality of the crystals for both thicknesses. Although defects, such as stacking faults, occur in the hexagonal phase as is shown in Fig. 4.4 (e,f), no significant microstructural anomalies was identified between the two cases that explains such a significant reduction in the 40 nm thick GST film. The TEM results imply that the intrinsic thermal conductivity in both cases remains unaltered and, therefore, the observed discrepancy must be related to extrinsic effects such as TBC. This finding indicates that, contrary to what is generally assumed, total thermal transport does not necessarily increase with the increase in thermal conductivity of GST.

To further support my hypothesis regarding the effect of TBC on thermal transport in h-GST, I measure the total thermal conductance across the Ru/W/GST/W/Si film stack for a 20 nm thick GST layer. For this thickness regime, the Kapitza length, defined as the thermal conductivity divided by the TBC and represents the thickness of a material in which thermal boundary conductances can influence the overall thermal transport of a system, is comparable to the thickness of the film and, as a result, the effect of interfaces in the TDTR measurements are more pronounced compared to the 40 nm film. For this thickness, the thermal conductances as a function of temperature are depicted in Fig. 4.4 (b) in solid diamonds, which follow the same trend observed in effective thermal conductivity of 40 nm film with a more pronounced drop at the transition from c-GST to h-GST. This is clear evidence for the opposite trend of TBC to that of the thermal conductivity for c-GST to h-GST transition. In order to compare the TBC for c-GST vs. h-GST, I take another 20 nm thick *a*-GST sample and heat it up to 320 °C where the GST film becomes fully cubic. By cooling the sample down to room temperature, I measure the thermal conductance in the cubic phase as a function of temperature. Once the thermal conductance over the temperature range of interest was measured, the same sample is again heated up to 400 °C to transform the c-GST into hexagonal phase and its thermal conductance was remeasured upon cooling (hollow diamonds). As shown in Fig. 4.4 (b), a higher thermal conductance is obtained in c-GST than that of the h-GST phase across the entire temperature range. This is contrary to expectations as the thermal conductivity in h-GST is nearly two times higher than the c-GST, however, due to relatively poor thermal transport at the interfaces, a lower thermal conductance is measured. Based on the results presented here, it can be concluded that the TBC between h-GST and W is lower than that of the c-GST and W.

In this respect, due to the significant impact of TBC on thermal transport of thin film GST, it is important to study how it changes across various phases. Figure 4.4 (c,d) shows the TBC between GST and two different thicknesses of W. The TBC in h-GST is significantly suppressed compared to c-GST. A similar reduction in TBC has been experimentally and theoretically observed at GST/metal interfaces at the cubic to hexagonal phase transition which were attributed to the formation of a 2 nm interfacial layer [162] and increased electron-phonon contribution to the interfacial resistance [163]. According to the TEM images, an additional interfacial layer is not observed after cubic to hexagonal phase transition. Considering the reduction of structural disorder upon annealing GST to higher temperatures [160, 161], I use a simplistic model via molecular dynamics simulations and demonstrate that a change in atomic-scale disorder at the interface from c-GST to h-GST can, in fact, be another possible reason behind the suppression of thermal transport. Disorder and defects at interfaces are well known to influence the TBC, and have in fact been computationally and experimentally shown to enhance TBC [164–167]. To this end, as will be shown in the next subsection my molecular dynamics simulations suggest that interfacial disorder plays a stronger role in the reduction of TBC than changes in the GST crystal structure and phonon density of states. It must be noted that in my molecular dynamics simulations, I am using Lennard-Jones potential that is not developed to predict the thermal properties of W or GST. However, the simplicity of these potentials allows us to assess my hypotheses to general classes of materials, thus providing means to broadly study our posits of the origin of reduction in TBC across the cubic to hexagonal phase transition. In Fig. 4.4 (c,d) the dotted line represents the minimum limit to the TBC by assuming the worst case scenario for the effective parameters based on 10% uncertainty, which in many cases is far higher than measured uncertainty. Lack of sensitivity in the amorphous and cubic phases causes the reported range of TBC (best-fit to minimum-limit) to be quite broad, but as the GST transitions to hexagonal and gains more sensitivity to TBC, this range contracts. The hollow diamonds in Fig. 4.4 (c,d) shows the TBC for h-GST which decreases by almost a factor of two as the sample is cooled down from 400 °C to room temperature. Figures 4.4 (c,d) again demonstrate that the TBC for 5 nm W is higher than that of 2 nm W, especially in the crystalline phase where the effect of TBC is more pronounced.

### 4.2.5 Effect of Disorder at the Interface

As the GST undergoes cubic to hexagonal phase transition, not only does the lattice structure change, but also do the electronic structure and the bonding. Obviously, the variation of several properties in GST makes it exceedingly difficult to pinpoint the exact underlying reasons behind the observed reduction in TBC. Nonetheless, in order to provide more insight into the role of crystal structure and interfacial disorder on the observed transition in TBC, I carry out a series of molecular dynamics simulations on the TBC across cubic and hexagonal interfaces that have equivalent average masses to W and GST using a 6-12 Lennard-Jones (LJ) potential. Lennard-Jones is a 2-body potential; therefore, the only free parameter is the distance between the atoms, and this enables creating different lattice structures using the same potential. This enables studying the role of crystal structure and disorder on TBC without making any assumptions regarding changes in the bonding character for different cases. This highlights the advantages of conducting these molecular dynamics simulations using the LJ potential. Additionally, the simplicity of these potentials allows us to assess my hypotheses to general classes of materials, thus providing means to broadly study the posits of the origin of reduction in TBC across the crystalline phase transitions.

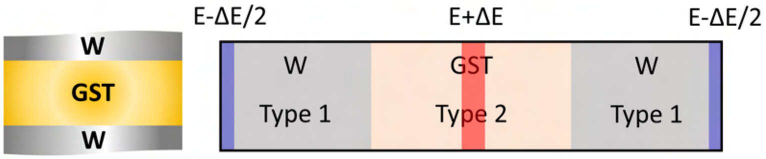

Figure 4.5: Molecular dynamics simulations configuration. Simulation set up and the location of heat baths for the molecular dynamic calculations.

Since LJ potential is used to describe W and GST films, in order to avoid misrepresentation, I call the section that represents W as *type 1* and the section that represents GST as *type 2*. With that in mind, I use parameters provided by Filippova et al. [168] for solid tungsten at room temperature ($\varepsilon$= 1.451420 eV and $\sigma$ = 2.50374 nm). For the atoms in type 2 (GST), I could use a LJ potential with softer bonding energy compared to that of tungsten to represent soft nature of bonding in GST, yet, to keep the model as simple as possible, I use the same potential across all atom types in the GST and W. This allows us to only survey the effect of changes in the lattice structure. Thus, the only parameters that are different between type 1 (W) and type 2 (GST) are average atomic masses and number density. The atomic mass for type 1 is similar to that of W (183.84 u) and for type 2 is

Table 4.1: Thermal boundary conductance (TBC) and resistance (TBR) across the interface between different lattice structures. Disordered FCC/FCC and FCC/HCP interfaces are the cases where the initial phase of the atoms in type 2 were amorphous, however, during the course of simulation nucleated near the interfaces and transformed into a polycrystalline structure.

| Interface | TBC (MW $m^{-2}$ $K^{-1}$) | TBR ($GW^{-1}$ $m^2$ K) |
|---|---|---|
| ordered FCC/FCC | 838 | 1.193 |
| disordered FCC/FCC | 1600 | 0.625 |
| ordered FCC/HCP | 1045 | 0.957 |
| disordered FCC/HCP | 2700 | 0.370 |

the arithmetic average of $Ge_2Sb_2Te_4$ (112.4 u). The number density for W and GST in our model is calculated to be $\sim 6.6 \times 10^{28}$ $m^{-3}$ and $\sim 2.7 \times 10^{28}$ $m^{-3}$ which stays relatively constant across all phases. A schematic of the molecular dynamic simulation set up is depicted in 4.5. For computational efficiency, a cutoff distance of 5.5 Å is used. For estimating the TBC at the interface between type 1 and type 2, I use a simulation box of 300 Å length with cross section area of $50 \times 50$ $\text{Å}^2$. In order to investigate the effect of disorder at the interface, I used a melt-quench technique to amorphize type 2 (GST) atoms. However, due to ordered interface of type 1, the amorphous structure nucleates near interface and turns into a thin FCC layer at the type-1/type-2 interface. I refer to this nucleated region as a disordered crystalline region which shows a higher TBC as compared to the *ordered* crystalline interfaces. The summary of the calculated TBC between different lattice structure are presented in Table 4.1.

Our results suggest that a change in phase from cubic to HCP does not significantly change the thermal boundary conductance. However, structural disorder at the interface could play an important role in the reduction of TBC from the cubic to HCP phase in the measured data across the W/GST/W interfaces. This is consistent with previous computational and experimental observations regarding the effect of disorder at the interface on the enhancement of TBC [164–167]. Tian et al. [164] used a theoretical approach - atomistic Green's function - and showed that the interface roughness in Si/Ge can increase phonon transmission compared to an ideal sharp interface. They concluded that this effect is even

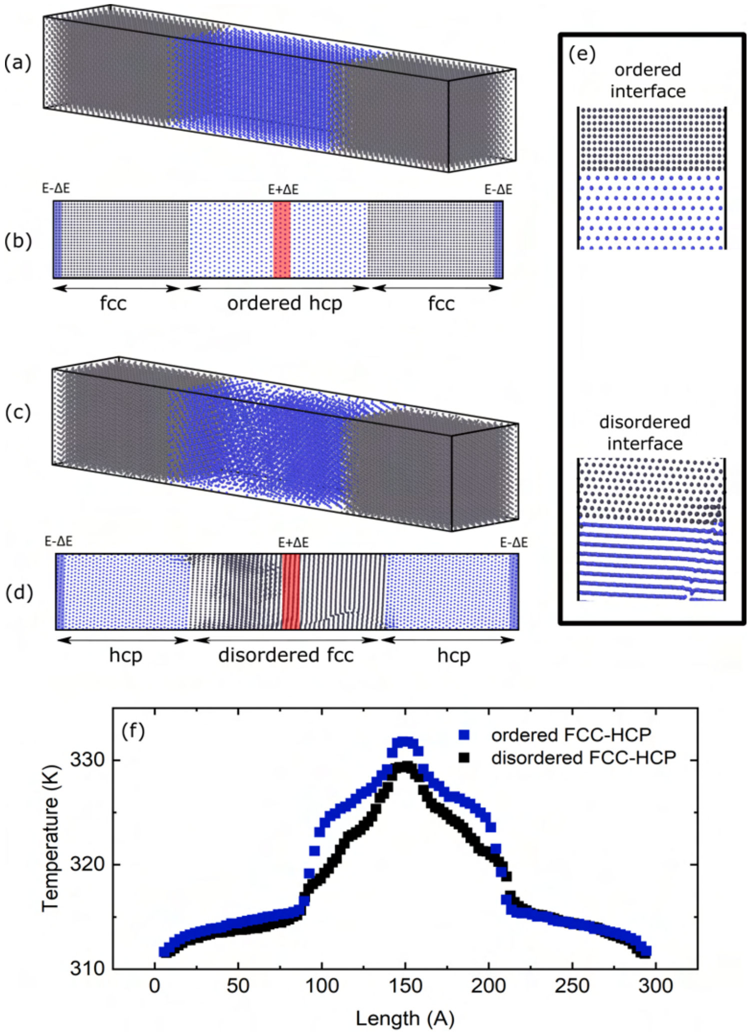

Figure 4.6: Molecular dynamics simulation results for the system size of 50×50×300 $\text{Å}^3$. (a,b) 3D and 2D visualization of the atomic arrangement in the simulation after 6 ns for cubic/hexagonal/cubic structure. (c,d) 3D and 2D visualization of the atomic arrangement in the simulation after 6 ns for hexagonal/disordered fcc/hexagonal structure. (e) The quality of interface after 6 million timesteps for interfaces with different quality. (f) Temperature profile along the simulation box when $\Delta E = 1.5$ eV/ps is added and subtracted from the hot and cold region depicted in red and blue.

more pronounced if the acoustic mismatch between the materials at the interface is large, which is the case for GST and W. Several molecular dynamics simulations [165, 169] have shown that compositionally disordered interfaces show higher TBCs than sharp interfaces. In addition, Gorham et al. [166] experimentally showed that TBC can increase across ion irradiated interfaces of Al/native oxide/Si with sufficiently high ion dose due to compositional mixing and point defect formation. With respect to these previous works on the effect of disorder at the interface supported by MD simulations, I hypothesize that one driving factor for the reduction in TBC from cubic to hexagonal phase could be due to the reduction of disorder rather than structural phase transition.

### 4.2.6 Ballistic Thermal Transport Regime

Figure 4.7(a, b) shows the thermal conductance across Ru/W/GST/W/Si as a function of temperature for 5 nm and 40 nm thick GST film with different spacers (2 nm W, 5 nm W, and 5 nm $SiN_x$). The thermal conductance for a 10 nm W control is also plotted to clarify that the TBC at Ru/W and W/Si interfaces are relatively constant and sufficiently large compared to GST intrinsic thermal conductivity and GST/W interface. In Fig. 4.7(a), a linear trend is observed for thermal conductance of 5 nm GST film as a function of temperature after the crystallization onset ($>$ 150 °C) for W spacer. This is in contrast with the trend observed in Fig. 4.7(b) for 40 nm thick GST where the thermal conductance plateaus above 300 °C. In a fully diffusive thermal transport regime, the effect of reduced TBC in h-GST must be even more noticeable for 5 nm GST where the effect of intrinsic thermal conductivity is minimum. To explain this, it has been shown that as the thickness of the GST layer decreases to ultra-thin, the onset of crystallization increases to higher temperatures [170]. As a result, it is tempting to attribute this increase to a crystallization lag where at 300-400 °C range the film is gradually transitioning to h-GST. To assess this hypothesis, I can predict the total thermal conductance of the Ru/ 5 nm W/5 nm GST/ 5 nm W/Si stack at different phases using thermal conductivity and TBC measured in the previous section. Using a series resistors model, I calculate the stack total thermal conductance at 400 °C

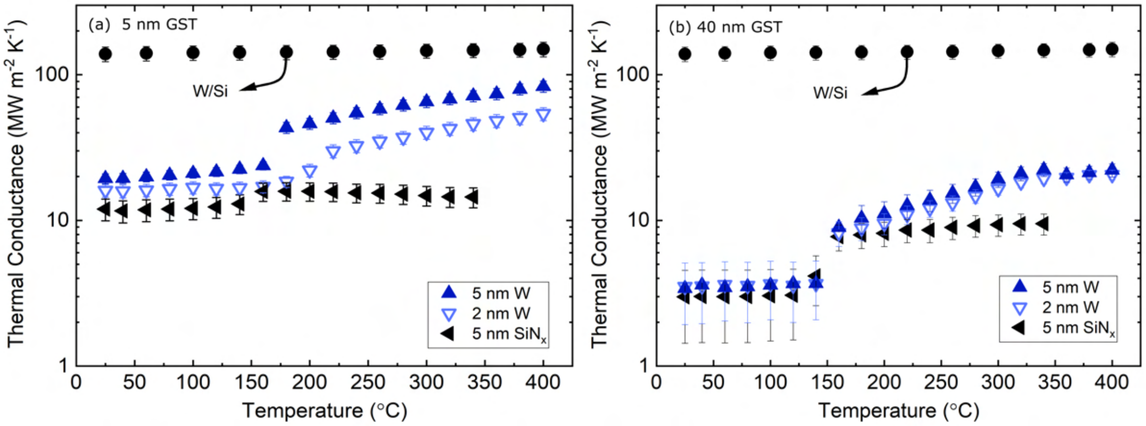

Figure 4.7: Thermal conductance behavior of thin GST films in the ballistic and diffusive regime. Thermal conductance for (a) 5 nm and (b) 40 nm thick GST in contact with different spacers. The error bars are calculated based on 7% uncertainty in the GST film thickness. Experimental data are not available for SiN$_x$ above 340 °C due to film delamination.

to be 43 ± 5 MW m$^{-2}$ K$^{-1}$ which is almost a factor 2 lower than the measured value of 83 ± 7 MW m$^{-2}$ K$^{-1}$. It is noteworthy to mention that the TBC for GST/W and W/GST interfaces alone, is 59 ± 7 MW m$^{-2}$ K$^{-1}$, which is significantly lower than the measured thermal conductance for the entire stack. The fact that almost a factor of two higher thermal conductance for h-GST at 400 °C is measured cannot be explained within the diffusive thermal transport limit. On the other hand, it has been shown that in bulk tungsten the average electron mean free paths before scattering with phonons at room temperature can be as long as 19.1 nm [171]. Additionally, due to tungsten high lattice thermal conductivity (∼46 W m$^{-1}$ K$^{-1}$)[171], it has phonons with long mean free paths relative to other metals [172]. From this, I conservatively estimate the phonon mean free path in tungsten to be on the order of $\lambda = 3k_\mathrm{p}/Cv = (3 \times 46)/(2.58\times10^6 \times 5174) = 10.3$ nm. Since the thickness of 5 nm GST is within the range of the phonons' and electrons' mean free paths, I attribute this enhancement in thermal conductance to ballistic transport of energy carriers emitted from the top W spacer to the bottom W spacer.

I further study this hypothesis by measuring the thermal conductance of a similar multilayer system in which I replace the W spacer with amorphous SiN$_x$. The SiN$_x$ spacer is widely used as a dielectric in electronic devices due to its high electrical and thermal resistivity [156]. As a result, I expect the contribution of phonons and electrons to thermal conductance in $SiN_x$ to be negligible compared to that of W spacer. As shown in Fig. 4.7(a) the thermal conductance across the Ru/$SiN_x$/5 nm GST/$SiN_x$/Si stack is relatively constant across all temperatures, which gives further credence to my hypothesis regarding ballistic electron/phonon transport leading to increased thermal conductance in the 5 nm GST films between W contacts. In this case, no significant enhancement is observed in thermal conductance after the crystallization temperature. This suggests that, due to the absence of long-wavelength electrons and phonons in amorphous $SiN_x$, there is no ballistic transportation from the top $SiN_x$ to the bottom $SiN_x$ layer.

## 4.3 GST Morphology at Different Phases.

In order to confirm phase transformation and the quality of the crystal structure associated with each phase, TEM is performed on the 40 and 160 nm GST with *in situ* heating (Figs. 4.8 (a)-(f)). The transition from diffuse rings in the selected area diffraction (SADP) to sharp diffraction rings denotes the transformation from *a*-GST to polycrystalline cubic GST (c-GST), as shown in Figs. 4.8 g and h, respectively. This is in agreement with previous results showing that GST transforms from an amorphous phase to a face-centered cubic (FCC) lattice at $\sim$155 °C [173–175]. The 160 nm GST film thickness was measured as 160, 152, and 149 nm at 25, 240, and 400 °C, respectively, and similarly the 40 nm GST film thickness as 38.7, 36.9, and 33.7 nm at 25, 240, and 400 °C. On average, the thickness of GST films change by $\sim$5% and $\sim$6%, at the transition from amorphous to cubic and cubic to hexagonal, respectively, which are comparable to the values of 6.5% and 8.2% reported elsewhere [123]. The grain size for c-GST ranges from 10-20 nm in both films. When the films transform to the hexagonal phase, there are highly faulted grains that span the thickness of the films, as shown in Fig. 4.8 (c). A few differences in the lateral (i.e., in-plane) grain size were observed between the 40 and 160 nm films. In the 160 nm film, the lateral size of the smaller grains is approximately 50 nm, whereas in the 40 nm film, the size varied from 50 to 100 nm. Large faulted grains in the 160 nm film are ∼100-200 nm wide, but only about 100 nm wide in the 40 nm film. The cross-plane dimension of the grains in the 40 nm film are often that of the film thickness (i.e., 40 nm), while there is a range in the 160 nm film.

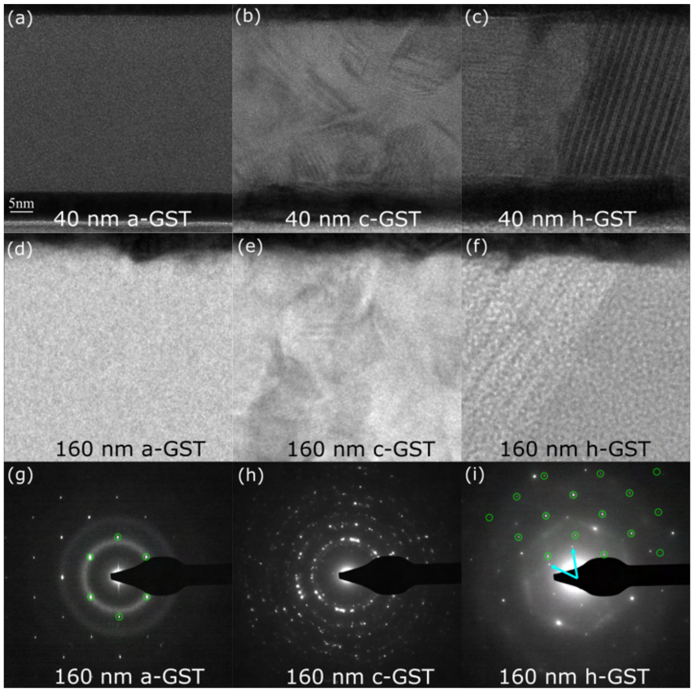

Figure 4.8: Transmission electron microscopy of different GST phases. Bright-field images of the: (a-c) 40 nm and (d-f) 160 nm GST thin films at: (a,d) 25 °C, (b,e) 240 °C and (c,f) 400 °C, showing a sequence of phase transformations from amorphous to cubic to hexagonal GST, respectively. Selected area diffraction patterns (SADP) of the 160 nm film at: (g) 25, (h) 240, and (i) 400°C, reflecting the phase transformations and microstructures observed in the BF images. In the inner ring of (g) and the top half of (i), the green circles indicate Bragg spots in the [110] zone axis of the Si substrate, and blue arrows in (i) show $\{100\}$ primitive reciprocal-lattice vectors of h-GST in a [001] zone axis. Diffuse streaks in (i) extending through the $\{2\bar{1}0\}$ Bragg spots are due to the transnational shear faults seen in (c) and (f).

The SADP from GST at 400 °C (Fig. 4.8 (i)) displays a single GST [001] zone axis and the [110] zone axis of the Si substrate, due to the much larger grain size compared to 240 °C (Fig. 4.8 (h)). Diffuse streaks emanate from the $\{2\bar{1}0\}$ Bragg spots as a result of the faulted grain. Highly faulted structures have been observed in a variety of chalcogenides including Ge-Sb-Te compounds [176–181]. The large, faulted grains grew laterally by growth ledges that often nucleate at the W/GST interface. The growth ledges then propagate along the h-GST/c-GST interface, consuming smaller grains as they move. Crystalline GST is composed of van der Waals coupled building blocks, each of which contains five Te layers separated by either a Ge or Sb anion layer [176, 177, 182, 183]. By shifting each nine-layer building block by a partial lattice vector, the c-GST becomes h-GST and vice versa. Recent literature suggests that the weak bonding between the sesqui-chalcogenides building blocks, such as $Sb_2Te_3$, significantly exceeds those of van der Waals forces and, therefore, possess more of a metavalent bond nature [180, 184]. As a result of the weak bonding between the blocks, there is a low energy barrier to passing partial dislocations that transform the lattice and cause faults. Faulted grains in the 160 nm sample were primarily at an angle to the film normal as seen in Fig 4.8 (f). The same was observed for the 40 nm film, such as on the right side of Fig 4.8 (c) in addition to grains whose building blocks/faults were parallel to the film normal, as on the left side of Fig. 4.8 (c).

## 4.4 Discussion

As the memory cell dimension in PRAM devices shrinks and progress towards superlattice structures, it is essential to account for the parameters that are not conventionally considered in thick regime such as interfacial thermal resistance and ballistic thermal transport. In superlattice PRAMs, due to existence of several interfaces in a single cell, engineering the interfacial resistance can substantially improve the performance of the device. For superlattice structures, the TBR at $GeTe/Sb_2Te_3$ interface is reported [185] to be around 3.4 $m^2$ K $GW^{-1}$. This work, in addition to reporting a significantly higher TBR between h-GST and W, $\sim$10 $m^2$ K $GW^{-1}$, demonstrates how judiciously engineering the interface between GST and its adjacent material can reduce the reset current. To demonstrate the effect of TBR on thermal transport, I show that for a 20 nm thick GST film the effective thermal conductivity can be reduced by a factor of 4 due to the increased interfacial resistance in h-GST. My work shows that interfacial resistance is only effective in reducing

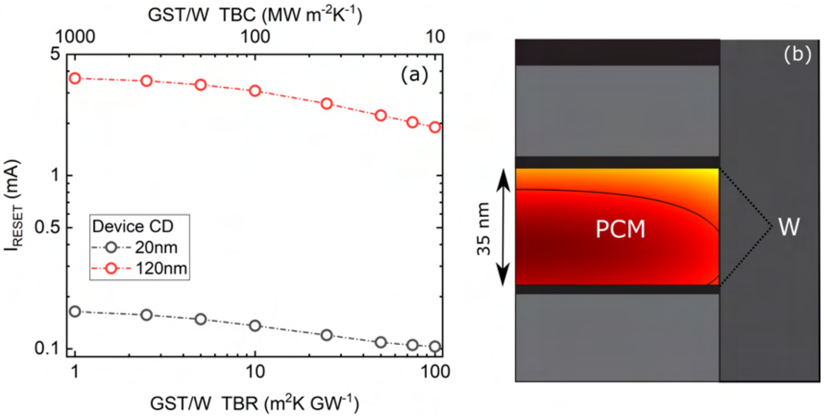

Figure 4.9: The effect of thermal boundary resistance on reset current for a confined memory cell geometry. (a) Simulation results for the reset current as a function of thermal boundary resistance (TBR) between GST and its neighboring materials for two different device lateral sizes, (b) Schematic for the PRAM configuration and its corresponding temperature gradient.

thermal transport when the GST thicknesses is less than 40 nm. On the other hand, there is a limitation on reducing the thickness of the GST layer before the thermal transport transitions into a ballistic regime. According to my results, as the thickness of GST reaches ∼5 nm, ballistic transport of phonons/electrons from the top W electrode to the bottom electrode increases the thermal transport by almost a factor of two. To prevent this ballistic transport effect, it is important to choose interlayers that have carriers with short mean free paths. In the previous subsection, I demonstrated that materials such as carbon nitride with short mean free path energy carriers can serve as a better electrode than tungsten when the device dimension reaches below 10 nm. For the specific layer configuration studied here, W/GST/W, the GST thickness at which electrode engineering has the biggest impact in efficiency optimization is approximately 20 nm. For thinner GST thicknesses, ballistic thermal transport limits thermal confinement and at larger thicknesses, bulk properties of the GST will play a larger role and as a result the effect of TBR between GST and the electrode diminishes.

Earlier, I demonstrated that by reducing the W thickness from 5 to 2 nm, thermal conductance can be moderately suppressed. In order to demonstrate the effect of W layer thickness on PRAM device performance, computational models are used for a PRAM device in

Table 4.2: The impact of parameters such as thermal conductivity ($k_{GST}$), thermal boundary resistance between GST and dielectric ($TBR_{GST/d}$) or GST and tungsten ($TBR_{GST/W}$), tungsten electrode thickness ($d_W$) extracted from the empirical measurements on the reset current ($I_{reset}$) for devices with lateral size of 20 and 120 nm.

| | | | | | |
|---|---|---|---|---|---|
| $k_{GST}$ (W $m^{-1}$ $K^{-1}$) | 0.8 | k(T) | k(T) | k(T) | k(T) |
| $TBR_{GST/d}$ ($GW^{-1}$ $m^2$ K) | 10 | 10 | 41 | 41 | 41 |
| $TBR_{GST/W}$ ($GW^{-1}$ $m^2$ K) | 10 | 10 | 10 | TBR(T) | TBR(T) |
| $d_W$ (nm) | 5 | 5 | 5 | 5 | 2 |
| $I_{reset}$ ($\mu$A) 20 nm device | **183** | **186** | **137** | **133** | **127** |
| $I_{reset}$ ($\mu$A) 120 nm device | **3.35** | **3.40** | **3.09** | **3.07** | **2.88** |

confined cell geometry. For this, a 35 nm thick GST unit is sandwiched between identical W layers (2 or 5 nm), and connected to TaN electrodes. The cell geometry is a cylinder confined by dielectric materials; the simulation is repeated for two different cell dimensions with lateral size of 20 nm and 120 nm diameter in order to compare thermal transport in small and large devices. The simulations are carried out by using finite-element simulation package COMSOL Multiphysics. Table 4.2 summarizes the step-by-step simulation process as we progressively add measured parameters into the simulation. My simulations demonstrate that thinning the W layer from 5 nm to 2 nm, taking 35% reduction in thermal conductance into account, leads to reset current ($I_{reset}$) drop from 133 $\mu$A to 127 $\mu$A for the 20 nm device and from 3.07 mA to 2.88 mA for the 120 nm device, corresponding to 4.5% and 6.2% reduction in reset current, respectively. Although manipulating W thickness leads to a modest reduction in the reset current, it should be noted that this is achieved through practical changes in an interface that is not typically optimized for its thermal properties. Further optimization along these lines could lead to larger improvements. In order to demonstrate this, simulations are extended to account for a range of TBR between the phase change unit and the adjacent electrode. It is expected that the TBR between GST and most materials to fall in the range of 1-100 $m^2$ K $GW^{-1}$ [186]. The result of simulations for reset current as a function TBR between PCM/electrode and the cell configuration for a 120 nm confined cell is presented in Fig. 4.9 (a) and (b), respectively. These predictions suggest that the reset current can be reduced up to ∼40% and ∼50% depending on the device lateral size if the TBR changes from 1 to 100 $m^2$ K $GW^{-1}$. In superlattice structures where there are multiple interfaces, the reset current can be even further reduced. Boniardi et al. [187] observed nearly 60% reduction in set and reset current for (GeTe/$Sb_2Te_3$)/$Sb_2Te_3$ superlattice compared to bulk GST, which they attributed to increased thermal resistance in the superlattices from the period interfaces as compared to the GST. These results highlight the importance of interfacial engineering on thermal confinement of PCM memory cells.

## 4.5 Summary

In this chapter, I demonstrated that as the length scale of phase change materials decrease to the dimensions on the order of carriers' mean free paths, the mechanism of heat transport drastically differs from its bulk. I showed carbon nitride would be a suitable electrode for GST with low thermal conductivity 1.72 ± 0.1 W $m^{-1}$ $K^{-1}$, and moderate electrical resistivity of 5-10 mΩ cm. Based on my observations, at temperatures ranging from 150-340 °C, $CN_x$ confine heat better than an insulating material, $SiN_x$, due to high $CN_x$/GST interfacial thermal resistance which can be qualitatively explained from the existence of larger atomic mismatch at the interface of $CN_x$/GST. In addition, according to my results, as the GST transition from one crystallographic phase to another, the interfacial resistance changes. The TBR for *a*-GST/W, c-GST/W, and h-GST/W interfaces are measured to be approximately 25 ± 5, 3 ± 1.5, 10 ± 2 $m^2$ K $GW^{-1}$, respectively. My molecular dynamics simulations results suggest that a change in phase from cubic to hexagonal does not significantly alter the thermal boundary conductance. However, structural disorder at the interface plays an important role in the reduction of TBC from the cubic to the hexagonal phase. Overall, the interfacial resistance for a 20 nm thick GST film results in a factor of 4 reduction in the effective thermal conductivity from ∼1.3 to ∼0.3 W $m^{-1}$ $K^{-1}$ at room temperature. My work illustrated that the thermal boundary resistance can be employed to substantially suppress heat transport in phase change units. Finite element simulations are used to elucidate the effect of TBR on the reset current for two different cell sizes. According to these simulations, the TBR can lead up to 40% and 50% reduction in reset current. The results presented in this work improve our knowledge of thermal transport mechanism in ultra-thin phase change units and enable us to design PRAM devices with superior performance.

# Chapter 5

# Effect of Selenium Substitutions on Energy Transport of Ge-Sb-Te

In previous chapter, the energy transport processes in a well-known phase change material Ge-Sb-Te was investigated. In this chapter, I examine a novel phase change material that is particularly developed for photonic and optical devices. The quaternary alloy, $Ge_2Sb_2Se_4Te$, is one of the most promising material candidates for application in photonic circuits due to its broadband transparency and large optical contrast in the infrared spectrum. In this chapter, I investigate the thermal properties of $Ge_2Sb_2Se_4Te$ and show that upon substituting tellurium with selenium, the thermal transport transitions from an electron dominated to a phonon dominated regime. By implementing an ultrafast mid-infrared spectroscopy technique that allows for direct monitoring of electronic and vibrational energy carrier lifetimes, I show that this reduction in thermal conductivity is a result of a drastic change in electronic lifetimes of $Ge_2Sb_2Se_4Te$, leading to a transition from an electron-dominated to a phonon-dominated thermal transport mechanism upon selenium substitution. In addition to thermal conductivity measurements, I provide an extensive study on the thermophysical properties of $Ge_2Sb_2Se_4Te$ thin films such as thermal boundary conductance and sound velocity from room temperature to 400 °C across varying thicknesses.

## 5.1 Background

Modern computing relies on the processing of information by constantly shuttling the data back and forth between the storage and the processing units [188]. This computing architecture, known as von Neumann, leads to huge traffic jams between the memory and processor, incurring considerable costs in terms of latency and energy [20, 189]. With growing demand for data-centric technologies such as artificial intelligence and machine learning, there is a global effort to find alternative computing paradigms to supersede the traditional von Neumann architecture [17–19]. Biologically-inspired neuromorphic computing is one of the more promising alternatives to transistor-based technologies that not only offers significantly higher degree of connectivity between the memory nodes leading to faster computation and less power consumption, but also allows for simultaneous storage and processing of information within the memory cell [190, 191]. Chalcogenide-based phase change materials (PCMs) have been an indispensable component in the development of this technology due to their large properties contrast at different phases [192]. With the emergence of these materials, several works have demonstrated that neuromorphic computing is possible both in the realm of nanoelectronics and nanophotonics [23, 29].

In chalcogenide-based PCMs, thermal excitation can induce reversible solid-state phase transitions between amorphous and crystalline states [124, 138]. This phase transition is non-volatile and leads to large contrasts in the electrical [193], optical [194], and thermal properties [16]. Germanium antimony telluride, Ge-Sb-Te (GST), is the most popular and the most studied chalcogenide-based PCMs due to its phase stability [138], large property contrast [30], and fast switching rate [127, 195]. Although GST has been successfully implemented into a number of different applications from thermal camouflage [14] to reconfigurable metalenses [196], its properties are not optimized for photonic devices. For instance, in nanophotonic devices such as optical memories and reconfigurable meta-optics, both phases of GST suffer from large optical losses [194] which limits its implementation.

Recently, a class of phase change materials, $Ge_2Sb_2Se_4Te$ (GSST), has emerged which offers superior properties in regards to photonic applications, such as broadband transparency for the wavelengths in the range of 1–18.5 $\mu$m, significant refractive index contrast ($\Delta n$) between the phases with low optical loss contrast ($\Delta k$) leading to a large figure of merit ($\Delta n/\Delta k$), and improved thermal stability [197–199]. Despite the growing interest for integration of GSST into optical and photonic devices, such as reconfigurable metasurfaces, its thermal properties remain unknown.

Understanding the thermal transport properties of PCMs is of critical importance to design and modeling of active photonic devices based on PCMs. Switching PCM in photonic devices is customarily performed using micro-heaters made of metals [198, 200], doped Si [201–203], transparent conductive oxides [204, 205], and graphene [206, 207]. In all cases, the heater design must meet several requirements to enable reversible PCM switching, including sufficient heating temperature to trigger phase transition, rapid quench rate to facilitate re-amorphization, and maximal temperature uniformity to ensure device longevity [208]. To fulfill these requirements, extensive thermal modeling of the micro-heaters must be carried out. Thermal properties of the heater materials, in particular the PCMs, are therefore essential for their applications in photonics.

In this chapter, I investigate the thermal properties of GSST across phase transition for thicknesses ranging from 20-220 nm. Specifically, I report on the thermal conductivity, longitudinal sound speed, and volumetric heat capacity of GSST in amorphous and crystalline phases (see Table 5.1). I find that although GSST is a close cousin to typical GST compositions, their respective heat transport mechanisms in crystalline phase are fundamentally different. In particular, I show that upon substituting Te with Se in GST, the thermal transport is dominated by vibrational carriers rather than electrons across different phases. These results are understood from a series of ultrafast time-domain spectroscopy methods that allow for direct investigation of electrons and phonons scattering rates in these materials. Specifically, through various ultrafast mid-infrared experiments, a drastic reduction in the electronic lifetimes of GSST is observed in comparison to its GST counterpart. This increased electron scattering rate in GSST is attributed to the presence of an additional atomic species that introduces both intrinsic mass scattering as well as a change in the local bonding environment of the material system.

## 5.2 Results

The GSST films were prepared using thermal evaporation from a single $Ge_2Sb_2Se_4Te$ source. Bulk starting material of $Ge_2Sb_2Se_4Te$ was synthesized using a standard melt quench technique from high-purity (99.999%) raw elements. The film deposition was performed using a custom-designed system (PVD Products, Inc.) following previously established protocols [194]. Stoichiometries of the films were confirmed using wavelength-dispersive spectroscopy (WDS) on a JEOL JXA-8200 SuperProbe Electron Probe Micro-analyzer (EPMA) to be within 2% (atomic fraction) deviation from target compositions.

### 5.2.1 Microstructure

In order to confirm compositional homogeneity across the film thickness, energy-dispersive X-ray spectroscopy (EDS) is used in a scanning transmission electron microscope (TEM). STEM-EDS was performed using a 400 pA beam current and the results are shown in Fig. 5.1. The annular darkfield image in Fig. 5.1(a) shows multiple equiaxed and non-equiaxed grains. The composition of the various grains do not have differing compositions in any-way correlated to the morphologies in the darkfield signal, as shown in Fig. 5.1(b-e). A compositional gradient is present across the thickness of the films, as shown in Fig. 5.1(h). The gradient may in part be from X-ray absorption affects that are thickness dependent or could be a result of growth conditions. It is striking that such a large gradient is present, and the gradient may explain the preferential non-equiaxed grain morphology being present at the bottom of the film and not the top.

To investigate the atomic structure of GSST thin-films before and after phase transformation, selected area electron diffraction is performed in a transmission electron microscope on amorphous and crystalline samples that are nominally 20 and 150 nm thick

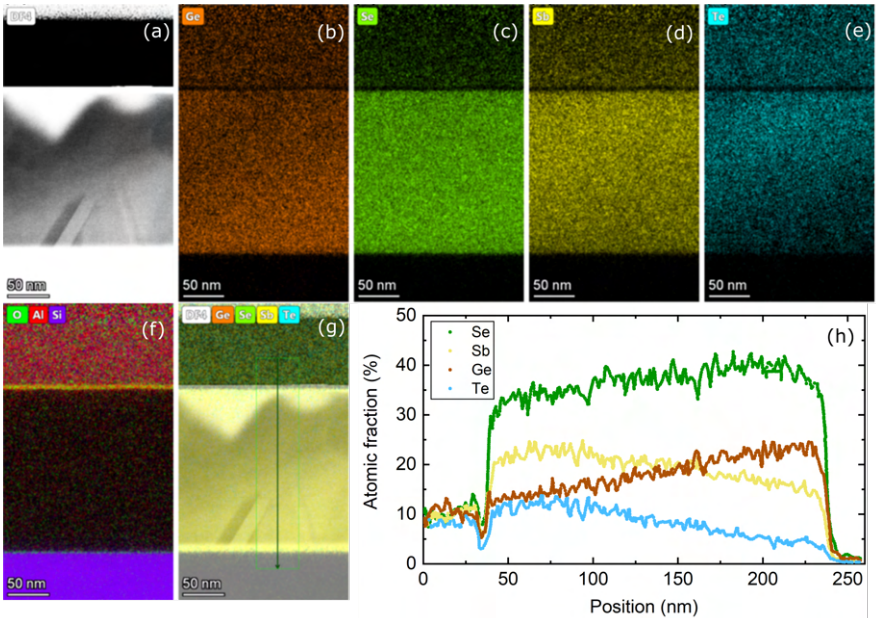

Figure 5.1: STEM-EDS spectrum image with (a) diffraction contrast from an annular dark-field detector showing multiple grains with uniform (b) Ge, (c) Se, (d) Sb, and (e) Te compositions. Observation of signatures of other elements in the Al transducer is associated with the noise in the system and artifact of measurement. The Si and Al layers are shown in (f) along with thin oxides present at each interface. The composite image of (a-e) is shown in (g), where a line profile is indicated. The quantitative compositions along the line profile are shown in (h).

as shown in Fig. 5.2. Each of the four diffraction patterns shows a high-intensity, single crystalline, [110] zone-axis Si diffraction pattern from the oriented substrate. In addition to the Si substrate pattern, the diffraction patterns of the amorphous sample have diffuse rings which result from short- and medium-range order and a lack of long-range order. The lack of other diffraction peaks demonstrates that the samples are purely amorphous and lack any crystalline structure. Diffraction patterns from the 150 nm crystalline sample (Fig. 5.2d) exhibits many Bragg diffraction peaks, in addition to the single crystalline substrate diffraction pattern, indicating the existence of many nanometer sized crystalline grains. Diffuse rings from an amorphous GSST material are still present in this 150 nm selected area diffraction pattern (Fig. 5.2d), which could suggest incomplete crystallization or minor damage from sample preparation; similar observations are found in the 20 nm crystalline GSST film. A ~5% thickness reduction is measured upon crystallization in both 20 and 150 nm films indicating densification of GSST after the phase transformation, similar to previous observations in GST [16, 123].

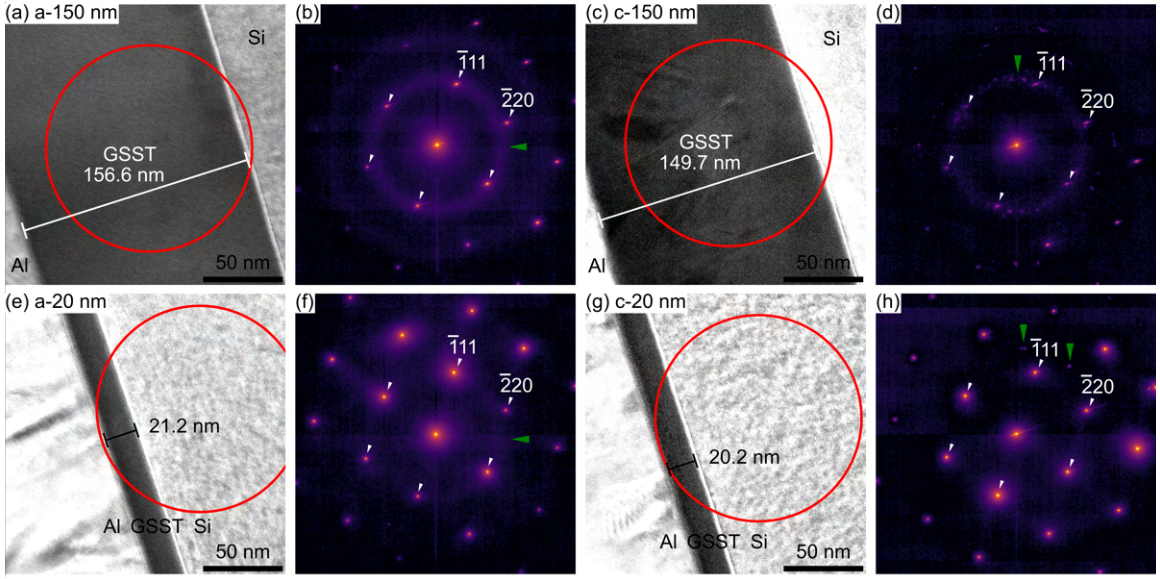

Figure 5.2: The structure and thickness variation in GSST upon phase transformation. Bright-field TEM images and their corresponding diffraction patters of 20 nm (a,b) amorphous and (c,d) crystalline films and 150 nm (e,f) amorphous and (g,h) crystalline films. Red circles indicate the selected area where diffraction patterns are acquired. In all cases the selected area aperture includes the Si substrate. In diffraction patterns (b,d,f,h), white arrows indicate first-order reflections from the Si substrate and the green arrows point to the first-order GSST (b,f) amorphous ring, (d) polycrystalline ring, and isolated reflections.

### 5.2.2 Sound Velocity

The thermophysical properties of these PCMs are measured using time-domain thermoreflectance (TDTR), an optical pump-probe thermometry technique that is capable of measuring thermal properties of thin films such as thermal conductivity, thermal boundary conductance, specific heat, and sound speed. The details regarding measurement technique and the thermal model that relates the experimental data to thermal properties of the films studied here are discussed in detail elsewhere [93, 209, 210]. In Chapter 3, I demonstrate the measurement of heat capacity of GSST in both amorphous and crystalline phases and in the following I talk about the sound velocity measurements.

Table 5.1: The thermal properties of GSST studied here in amorphous and crystalline phases for 150 nm GSST.

| GSST Phase | Thermal Conductivity ($\mathrm{W\ m^{-1}\ K^{-1}}$) | Specific Heat ($\mathrm{MJ\ m^{-3}\ K^{-1}}$) | Density ($\mathrm{g\ cm^{-3}}$) | Sound Speed ($\mathrm{m\ s^{-1}}$) |
|---|---|---|---|---|
| amorphous | 0.20 ± 0.02 | 1.5 ± 0.1 | 5.27[206] | 2300 ± 100 |
| crystalline | 0.48 ± 0.06 | 1.8 ± 0.1 | 5.53[1] | 2750 ± 150 |

[i] considering 5% densification upon amorphous-to-crystalline phase transformation.

The longitudinal sound velocity in GSST is measured via picosecond acoustics, the details of which are given in chapter 3. In these measurements, the pump pulse launches strain waves on the surface of the sample that propagate through the underlying layers with the speed of sound. These strain waves, upon reaching an interface between the two materials, depending on the acoustic mismatch, are partially reflected and partially transmitted. The reflected portion of the waves travel all the way back to the surface and can be detected by the probe beam with picosecond resolution. Figure 5.3(a) shows the corresponding peaks and troughs due to reflection from the Al/GSST and GSST/Si interfaces for 20 and 150 nm thick GSST. By measuring the time between these two peaks and the knowledge of film thicknesses, the sound velocity can be obtained. Using this technique, I measure the sound velocity in GSST for the two different phases at various thicknesses as shown in Fig. 5.3(b). It can be observed that although the sound velocity in amorphous GSST remains relatively constant across different thicknesses, in the crystalline phase it converges to that of the amorphous phase as the thickness of GSST film decreases. Similar behavior has also been observed in GST thin films as discussed in previous chapter. Although identifying the underlying reasons behind this reduction is beyond the scope of this dissertation, I hypothesize that it is due to partial crystallization of GSST near the interfaces for the thinner films.

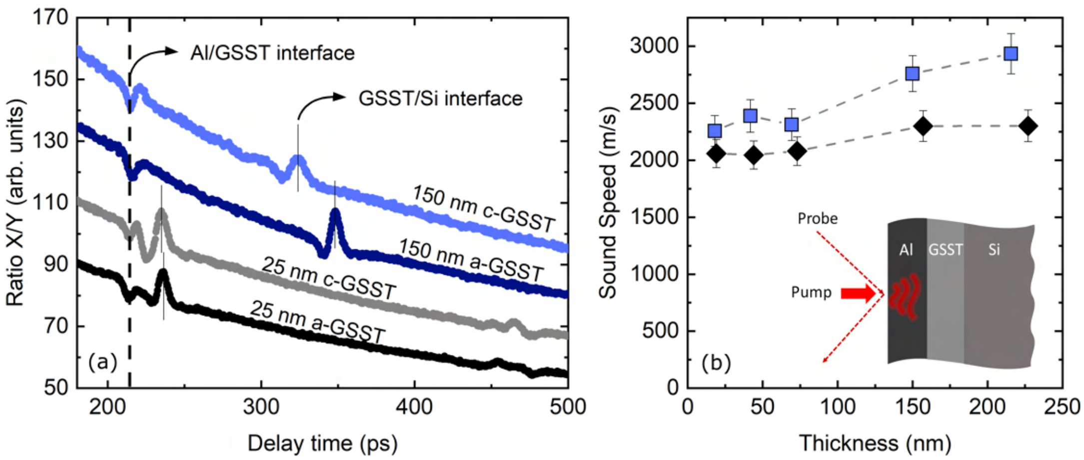

Figure 5.3: (a) Picosecond acoustics measurements and the corresponding echoes from the interfaces, (b) sound speed for different thicknesses of GSST in amorphous (black diamonds) and crystalline (blue squares) phase. The uncertainty is calculated based on 10% variation in GSST film thickness.

### 5.2.3 Thermal Conductivity

For investigating the thermal transport in GSST, I begin my experiments by measuring the room temperature properties. For this, different thicknesses of GSST films are deposited on silicon substrate with 7 nm $Al_2O_3$ interlayer between GSST and the Pt transducer to avoid any diffusion or possible reaction. Although $Al_2O_3$ is very thin, TDTR experiments are very sensitive to the transducer properties and since $Al_2O_3$ has a heat capacity close to that of Pt, the effect of its heat capacity may interfere with measured thermal conductivity. In order to account for this and show that this layer, *in fact*, does not impact the TDTR results, I use a 4-layer model and treat $Al_2O_3$ as a separate layer instead of an interface and fit for thermal conductivity of GSST and its interfacial conductance with $Al_2O_3$. Nonetheless, as shown in Fig. 5.4, if the heat capacity of $Al_2O_3$ changes by a factor of two which is unlikely, it has minimal impact on the measured thermal conductivity. Although variations in the heat capacity result in a change in the Y-axis intercept (interfacial thermal resistance), it does not change the slope of the fitted line. This is because due to the large interfacial resistance between $Al_2O_3$ and GSST, the effect of heat capacity is negligible. This agrees with my thermal conductivity measurements as a function of temperature which will be discussed in the following, where I observe no change in the thermal conductivity for the 20 nm thick GSST film. The fact that no chance in thermal conductivity of 20 nm is observed across phase transition is attributed to the interfacial thermal resistance between $Al_2O_3$ and the GSST which is the dominant resistor in the multilayer stack.

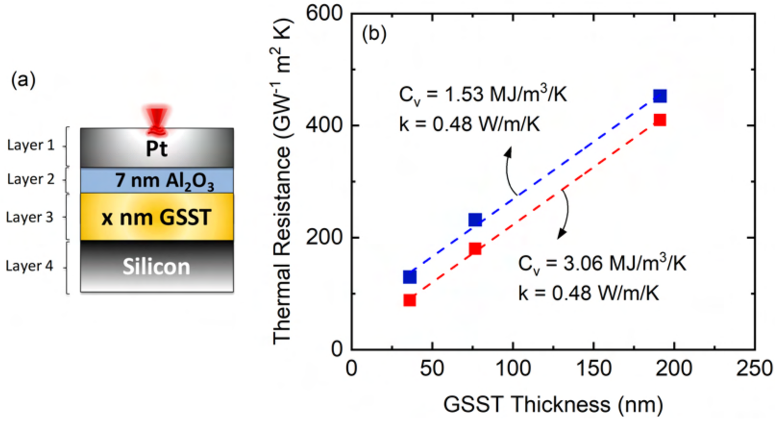

Figure 5.4: (a) The schematic showing the configuration of the layers in the thermal conductivity measurements. (b) Thermal resistance as a function of GSST thickness assuming two different specific heat for the $Al_2O_3$.

Now that I showed the addition of $Al_2O_3$ interlayer does not impact the thermal conductivity measurements, the thickness series samples are divided into two categories; as-deposited amorphous and annealed (300°C) crystalline samples. The thickness of GSST films studied here are selected in the range of 20-220 nm which capture both of its thin film and bulk-like thermal properties. Similar to previous chapter, the total thermal resistance across transducer-substrate (Pt/$Al_2O_3$/GSST/Si) is measured that incorporate the resistance due to all interfaces and interlayers. By solely changing the thickness of GSST film, the relative contribution of GSST to the resistance of the stack can be varied and hence its thermal conductivity can be determined independent of other extraneous resistances such as interfaces and $Al_2O_3$ layer. Figure 5.5(a) shows the thermal resistance as a function of the GSST thickness where the inverse of the linear fit to the experimental data corresponds to the thermal conductivity of the GSST. According to this, thermal conductivity of the GSST at room temperature for the as-deposited amorphous and 300 °C annealed crystalline phases are 0.20 and 0.48 W m$^{-1}$ K$^{-1}$, respectively.

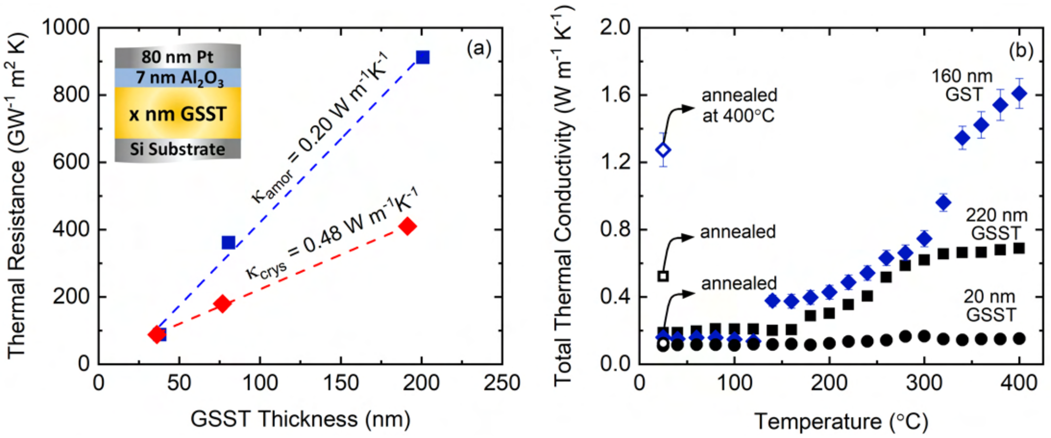

Figure 5.5: (a) GSST thermal resistance as a function of thickness in amorphous and crystalline (annealed at 300°C) phases. The inverse of linear fit to the experimental data corresponds to the thermal conductivity in each phase. (b) Thermal conductivity of as-deposited GSST with thicknesses of 20 nm (solid circles) and 220 nm (solid squares) as a function of temperature. The thermal conductivity GST (solid diamonds) is shown for comparison.

In order to understand the thermal transport mechanisms across amorphous-to-crystalline phase transition in GSST, the thermal conductivity is measured at elevated temperatures using a resistive heating stage. For this, I perform the measurement on the thinnest (20 nm) and the thickest (220 nm) samples where there are variable sensitivities to the interfacial thermal conductance and thermal conductivity. For the case of 20 nm thick GSST, due to small resistance from the film itself, the resistance from the interfaces would dominate the thermal transport. Figure 5.5(b) shows the thermal conductivity of 20 nm thick GSST as a function of temperature. According to this plot, the thermal conductivity of 20 nm GSST does not show a noticeable change across its crystalline phase transition, or at higher temperatures. Although this might lead one to conjecture that the phase transformation did not take place due to the reduced thickness of the film, it is confirmed that the phase transformation does in-fact occur via both Raman and TEM measurements. This behavior is very similar to the previous chapter discussion regarding the effect of thermal boundary conductance where I demonstrated that the thermal conductivity of the 20 nm GST can be reduced by a factor of four compared to thick films (160 nm) due to the dominance of interfacial resistance. Similarly here, for the case of GSST, the temperature-independent thermal conductivity of the 20 nm GSST is attributed to the dominance of interfacial thermal resistance. With the knowledge of thermal conductivity, the TBC between $Al_2O_3$ and crystalline GSST can be estimated to be 20 MW $m^{-2}$ $K^{-1}$. Note, I do not report a TBC for the amorphous phase as the measurements do not have sufficient sensitivity to it [16, 211].

As shown in Fig. 5.5(b), the thermal conductivity in the amorphous phase is approximately 0.18 W $m^{-1}$ $K^{-1}$, in strong agreement with the value obtained from the linear fit to the thickness series in the previous section. For the 220 nm GSST, it is observed that the thermal conductivity remains constant with increasing temperature up to the onset of crystallization and shows a modest increase upon phase transition at $\sim$180 °C. This is consistent with previous measurements for the temperature at which the phase transformation occurs in GSST [194]. After phase transformation, the thermal conductivity gradually increases with temperature up to $\sim$280 °C after which the thermal conductivity reaches a constant value of $\sim$0.65 W $m^{-1}$ $K^{-1}$ up to 400 °C. For comparison, I plot the thermal conductivity data for 160 nm GST which represent the intrinsic thermal conductivity of GST independent of interfaces similar to 220 nm GSST. By comparing the thermal conductivity of GST vs. GSST as a function of temperature, we observe that the thermal conductivity is significantly suppressed in the crystalline phase by more than a factor of two.

### 5.2.4 Electron Contribution to Thermal Transport in GSST

In order to investigate how thermal properties of GST change upon Se substitution from a pure vibrational mode perspective, disregarding the contribution from electrons, both Se and Te are 2-coordinated elements, and therefore, Se substitutions should not alter the degree of connectivity and bonding network in the system, leaving minimal impact on the thermal conductivity from a topological perspective [62]. However, the insertion of Se as an additional element is expected to increase the scattering rate. At the same time, Se is a lighter element compared to Te and should lead to an increase in thermal conductivity. As a result of these competing events and to gain a deeper understanding of the dominant phonon scattering mechanisms in GSST, I turn to analytical models that provide an estimation for the thermal conductivity based on kinetic theory of gases. Since the thermal conductivity of crystalline phase is the focus of this discussion, I refer to the phonon-mediated minimum limit [64]. Hence, according to Cahill and Pohl [67], the minimum scattering length of vibrational carriers, in this case phonons, is on the order of one half of their wavelength:

$$\kappa_{\min,\mathbf{P}} = 1.21\ k_B\, n^{2/3}\, v_g, \tag{5.1}$$

where $k_B$ is the Boltzmann constant, $v_g$ is the average sound speed of the material, and $n$ is the number density. The average sound velocity is calculated with respect to the longitudinal ($v_{LA}$) and transverse ($v_{TA}$) modes as: $v_g^2 = \frac{1}{3}\left(2v_{\mathrm{TA}}^2 + v_{\mathrm{LA}}^2\right)$. Assuming density of 6.20 and 5.53 g cm$^{-3}$, and sound speed of 2800 and 2750 m s$^{-1}$ for crystalline phases [16, 206], the minimum limit to the thermal conductivity of the GST and GSST is calculated to be 0.36 and 0.38 W m$^{-1}$ K$^{-1}$, respectively. Based on this, from a pure phononic perspective, the thermal conductivity of GST with its higher mean atomic mass is almost similar to that of the GSST. However, from previous studies, it is known that the thermal conductivity of GST in hexagonal phase is primarily dominated by the electronic contribution due to metal-insulator transition [15, 160, 212]. As a result, it is conjectured that the observed reduction in thermal conductivity of GSST could be related to the suppressed contribution of electrons rather than phonons. To investigate this, the electronic contribution in thermal conductivity is estimated by using the Wiedemann-Franz (W-F) formalism that related electrical resistivity to the thermal conductivity:

$$k_{\mathrm{e}} = LT/\rho \tag{5.2}$$

where $L$ is the Lorenz number $2.44 \times 10^{-8}$ W $\Omega$ K$^{-2}$, $T$ is the absolute temperature, and $\rho$ is the electrical resistivity. Based on previously measured electrical resistivity for GST and GSST as a function of temperature [194], I plot the electronic contribution in thermal conductivity in Fig. 5.6(a). According to these calculations, due to higher resistivity of the GSST across all phases compared to GST, the electronic contribution in thermal conductivity for the crystalline phase is suppressed by more than an order of magnitude. Figure 5.6(b) shows the electronic contribution of thermal conductivity as a function of temperature at different annealing temperatures. According to this plot, the electronic contribution increases for higher annealing temperatures and reaches a maximum of 0.16 W $m^{-1}$ $K^{-1}$ at 383 °C. Based on this, the electronic contribution in thermal conductivity of GSST at 383 °C is approximately 25% which reduces to 5% near room temperature.

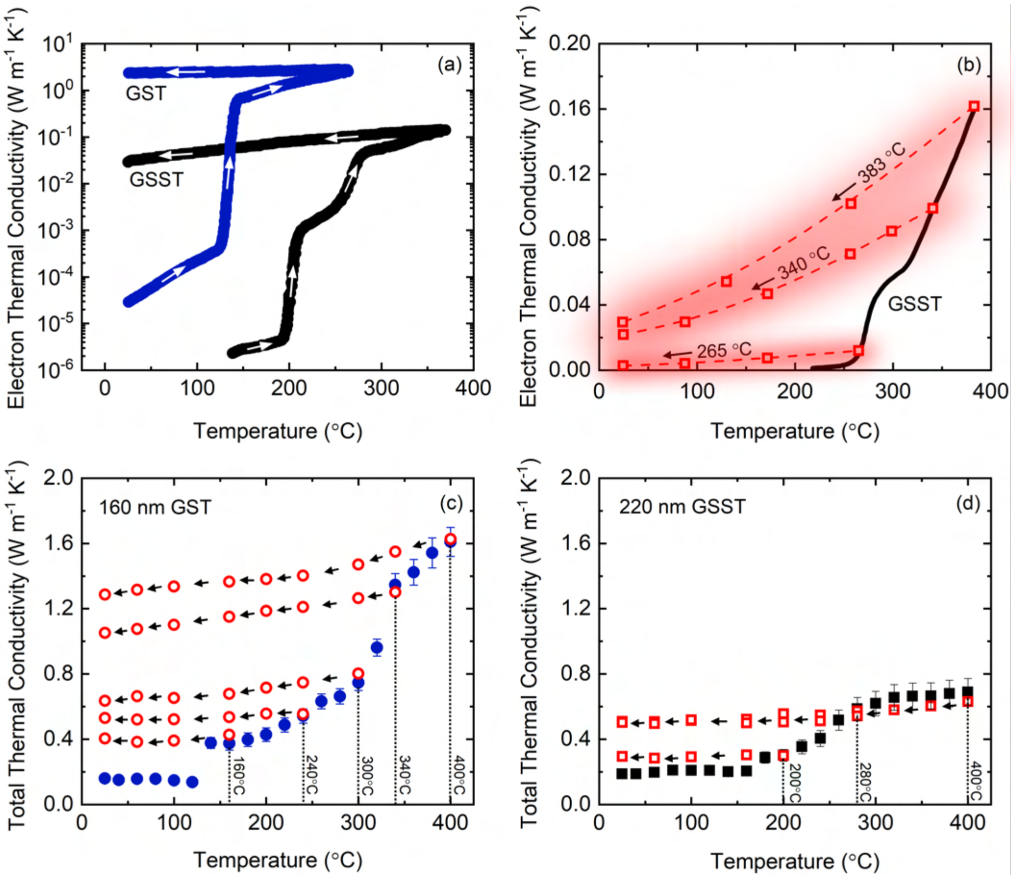

Figure 5.6: Electron contribution to the thermal conductivity for (a) GST and GSST upon heating and phase transformation obtained from W-F. (b) Electron thermal conductivity of GSST as a function of temperature upon cooling at various annealing temperatures obtained from W-F. The shaded area shows 25% uncertainty associated with Lorenz number. Measured total thermal conductivity from TDTR for (c) 160 nm GST and (d) 220 nm GSST upon heating (solid symbols), and their corresponding thermal conductivity upon cooling (hollow symbols) at different annealing temperatures. The vertical dotted lines show the annealing temperatures.

In order to experimentally investigate the contribution of electrons in thermal conductivity using thermal conductivity measurements, the GST and GSST are annealed at different temperatures and their thermal conductivities are measured upon cooling. Since electronic contribution in GST changes significantly as a result of metal-insulator transition [160] upon heating, it is expected that the thermal conductivity trend as a function of temperature changes for higher annealing temperatures. For this purpose, an as-deposited GST sample is heated to temperatures close and above the phase transition, and by cooling the samples down, its thermal conductivity is recorded (hollow circles in Fig. 5.6(c)). The solid circles in Fig. 5.6(c) show the thermal conductivity of as-deposited GST upon heating, whereas, the hollow circles show the thermal conductivity of GST at different annealing temperatures upon cooling. According to these results, for annealing temperatures of 160 °C and 240 °C, the thermal conductivity remains constant upon cooling to room temperature. However, when the annealing temperature raises above 300 °C, the thermal conductivity trend begins to increase with temperature (decrease upon cooling). This change in the trend of thermal conductivity as a function of temperature cannot be explained from a pure phononic perspective. This is because in crystalline systems, the thermal conductivity either decreases with temperature due to increase in the anaharmonic interactions or in the case of 2D or defective crystals it follows the heat capacity (i.e. constant above the Debye temperature). The increase in thermal conductivity due to heat capacity is ruled out because not only Ge-Sb-Te-based PCMs are typically soft materials but also the constant thermal conductivity trend for annealing up to 240 °C, indicate room temperature is well above the Debye temperature of the GST. According to these, the increase in thermal conductivity of GST can only be related to the enhancement in the electronic contribution. Considering the metal-insulator transition in GST near 300 °C, this is a reasonable deduction. On the other hand, repeating the same procedure for the GSST, yields a different behavior. As can be seen in Fig. 5.6(d) the thermal conductivity for the annealed cases remain constant with temperature for all annealing temperatures. Considering the high electrical resistivity of GSST compared to GST, this supports the conclusion that the thermal conductivity of GSST is reduced due to suppression of electronic contribution.

### 5.2.5 Mid-Infrared Vibrational Spectroscopy

So far, using Wiedemann-Franz law and thermal conductivity data, I showed that the reduction in thermal conductivity of GSST could be related to the suppressed electronic contribution. Nonetheless, although W-F approximation provides a reasonable qualitative insight into the contribution of electrons in thermal conductivity, the Lorenz number has been shown to vary with temperature on multiple occasions, and is well-known to deviate from its standard value under conditions of increased inelastic electronic collisions (e.g., “vertical processes”) [74, 76, 213–215]. As a result, I turn to additional experimental measurements to verify this. For this, I provide a direct measurement of both the electron and phonon lifetimes in the crystalline phases of GST and GSST through ultrafast mid-infrared spectroscopy [216, 217].

To further investigate the varying scattering mechanisms that give rise to changes in the thermal conductivity of these chalcogenide-based PCMs, I turn to mid-infrared (MIR) pump-probe spectroscopy to directly monitor the lifetime of electronic and vibrational energy carriers in these materials. Described in more details elsewhere [216, 217], the GST and GSST films are excited with sub-picosecond 520 nm pump pulses, thus inducing a non-equilibrium state in the film of interest. At varying time delays, a tunable-wavelength MIR probe pulse interrogates the change in reflectivity of the film due to the change in either carrier concentration or temperature [218]. At wavelengths near interband transitions (e.g., band gap) in the films, this modulated reflectivity becomes dominated by the electronic response of the material system and is indicative of changes in the electronic density of states [217]. In contrast, for wavelengths far from such transitions, the response becomes dominated by changes in the vibrational density of states, and is thus a strong indication of the change in lattice temperature [217]. The decay time of these subsystems is indicative of their relative populations; where the electron response is dictated by both the subsystem temperature and excited-state number density [219]. As such, the reported decay times between GST and GSST are indicative of a convolution of recombination processes as well as intrinsic carrier scattering rates.

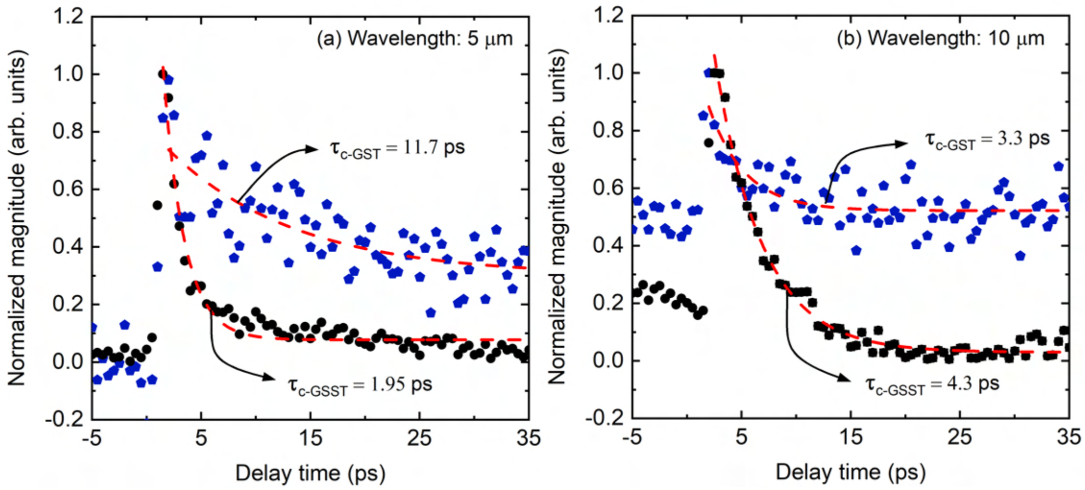

Figure 5.7: Modulated reflectivity data for the mid-infrared ultrafast spectroscopy measurements for probe wavelengths of (a) 5 microns and (b) 10 microns. The higher energy (lower wavelength) probe beam preferentially interrogates the electronic density of states upon pump excitation, demonstrating a greatly suppressed electronic lifetime of GSST compared to its GST counterpart. In contrast, the lower energy (higher wavelength) probe response is indicative of the materials' lattice response, and demonstrates similar decay times for both GST and GSST, indicating similar vibrational lifetimes for the two material systems. Note, the decay time is obtained by fitting an exponential decay to the data and the large variation in the experimental data for the GST stems from its thinner film thickness and different deposition technique.

The results of this ultrafast MIR spectroscopy is shown for two select probe wavelengths in Fig. 5.7. For the higher energy probe beam (probe wavelength of 5 $\mu$m, Fig. 5.7(a)), large increased decay rate of the ultrafast signal in the c-GSST ($\tau$ = 1.95 ps) film is observed compared to the c-GST ($\tau$ = 11.7 ps) counterpart. In other words, the electron decay time/scattering rate is greatly increased in GSST relative to GST films. The origin of this enhanced relaxation time can be attributed to inelastic electron scattering with high frequency nuclear motion (e.g., high frequency phonons) that are introduced from the addition of Se to the crystal basis; similar effects have been demonstrated, experimentally [216, 220] and computationally [221–223], in other metallic systems following the incorporation of lighter atoms. While this observed suppression of the electron lifetime in GSST likely invalidates the use of L = L0 in the W-F analysis of electronic thermal conductivity, it further supports our posit that electrons in GSST do not significantly contribute to its energy transport/thermal conductivity when compared to its GST counterpart. In contrast, for probe wavelengths that dominantly interrogate the vibrational states in the films of interest, relatively similar scattering times, 3.3 and 4.3 ps, for both GST and GSST are observed, respectively. In other words, the phonon lifetimes of the two material systems are comparable, which, at least qualitatively, supports the similarity in their comparable lattice contributions to thermal conductivity.

## 5.3 Summary

In this chapter, I unraveled some of the thermal properties of $Ge_2Sb_2Se_4Te$, an emerging phase change material with superior properties for photonic applications. I showed that the thermal conductivity of the GSST as a function of temperature in amorphous phase remains constant around $\sim$0.18 W m$^{-1}$ K$^{-1}$ up to the phase transition temperature at 180 °C. Upon phase transition and raising the temperature to 400 °C, the thermal conductivity increases to $\sim$0.65 W m$^{-1}$ K$^{-1}$. Based on the results presented in this chapter, the thermal conductivity of GSST is more than a factor of 2 lower than its close cousin GST. This reduction in thermal conductivity is attributed to strong suppression of electronic contribution in thermal conductivity of crystalline GSST which could potentially enables better confinement of heat near the memory cell, leading to less power consumption. Yet, the sluggish crystallization of GSST would require an order of magnitude longer pulse duration for crystallization that would overwhelm the power consumption in these materials.

# Chapter 6

# Towards Ultralow Thermal Conductivity in Amorphous Solids

Thus far, I have discussed the impact of phase transformation on the energy transport of chalcogenide-based phase change materials. In this chapter, I focus on a different integral component in the memory cell architecture, commonly referred to as the selector device. In PRAM, these devices are typically selected from amorphous chalcogenide alloys due to their large non-linearities in optical and electrical properties as well as low vibrational thermal conductivities. Since lower thermal conductivity in these devices leads to better performance of the memory cell, I introduce a novel mechanism to suppress the thermal transport in a representative amorphous chalcogenide system, silicon telluride (SiTe), by nearly an order of magnitude via systematically tailoring the cross-linking network among the atoms. As such, I experimentally demonstrate that in fully dense amorphous SiTe the thermal conductivity can be reduced to as low as $0.10 \pm 0.01$ W $m^{-1}$ $K^{-1}$ for high tellurium content with a density nearly twice that of amorphous silicon. Using ab-initio simulations integrated with lattice dynamics, the ultralow thermal conductivity of SiTe is attributed to the suppressed contribution of extended modes of vibration, namely propagons and diffusons. This leads to a large shift in the mobility edge - a factor of five - towards lower frequency and the localization of nearly 42% of the modes. This localization is the result of reductions in coordination number and a transition from an over-constrained to an under-constrained atomic network.

## 6.1 Background

In recent years, there have been numerous efforts to synthesize materials with ultralow thermal conductivities, a crucial parameter in the development of thermoelectric materials, memory devices, and thermal barrier coatings [69, 224–226]. It has been generally believed that amorphous solids possess the lowest thermal conductivity possible[53]. Nonetheless, with advances in nanofabrication, several studies have shown that thermal conductivity of crystalline materials can be significantly lower than amorphous material, by suppressing the mean free paths of the vibrational modes. For instance, disordered layered and cage-like crystal structures as well as superatomic clusters with complex unit cell proved to be an effective approach for increasing the anharmonicity of the system, leading to ultralow thermal conductivities. [69, 70, 224–228] More than a decade ago, Chiritescu et al. [68] found that by sequentially stacking extremely thin bilayers of W and Se (0.66 nm thick), the thermal conductivity of $WSe_2$ at room temperature can drop to the record value of $\sim$0.05 W $m^{-1}$ $K^{-1}$, six fold lower than the corresponding minimum limit prediction. Although using weak Van der Waals interaction between the bilayers is a brilliant approach to impede the propagation of heat, the integration of 2D materials into actual devices is limited due to their large anisotropic properties. For instance, in $WSe_2$, the in-plane thermal conductivity is 30 times higher than the cross-plane thermal conductivity [229].

Amorphous solids are a suitable choice for device fabrication due to their isotropic properties, yet, manipulating their atomic structure to reach values below the minimum limit is more complicated, as it is already in their highest disordered state. Thus, a question remains: how can the thermal conductivity of a fully dense amorphous solid be further reduced? One approach is to introduce chemical heterogeneity. For example, in amorphous alloys, in addition to atomic mass mismatch, disruptions in the bond structure or atomic network can significantly impede the propagation of vibrational energy. Prior works have demonstrated that the thermal conductivity of amorphous thin films can be strongly reduced by breaking the number of linkers that connect the atoms through varying the stoichiometry of a given material. For instance, Ghossoub et al. [230] showed that network connectivity in $a$-$CF_x$ can be manipulated by changing the fluorine concentration, resulting in nearly a factor of two reduction in thermal conductivity. Later, King et al. [231] illustrated that by introducing hydrogen impurities into amorphous SiC, the connectivity between the atoms transitions from a rigid to a percolated network, resulting in a reduction of thermal conductivity by nearly an order of magnitude. In a similar study, Braun et al. [232] showed that by altering hydrogen concentration in $a$-SiC:H and $a$-SiO:H, the thermal conductivity can be suppressed by a factor of two. In all of these studies, changing the number of bonds between constituent elements is achieved by introducing an additional impurity like fluorine or hydrogen to the baseline amorphous composition.

The insertion of impurities not only changes the physical properties of the original material but also introduces chemical complexities to the system. For instance, as shown in Fig. 6.1(a), increasing the hydrogen concentration in $a$-SiO:H reduces the density by more than a factor of two and also changes the nature of the bonding with the addition of hydrogen-terminated dangling bond sites. These large variations in density and bonding properties are directly proportional to the associated thermal transport, making it difficult to exclusively pinpoint the effect of bond percolation on thermal conductivity.

Unlike previous studies where the reduction of thermal conductivity is achieved through increasing the scattering rate of heat carriers, in this chapter, using different compositions of SiTe binary alloys, I demonstrate how vibrational modes can come to a complete halt and become fully localized to achieve ultralow thermal conductivities. According to ab-initio molecular dynamics (AIMD) simulations, for high tellurium content SiTe, not only is the contribution of propagons to thermal conductivity subdued, but also the mobility edge shifts by a factor of five to lower frequencies, leading to the localization of 42% of the modes and ultralow thermal conductivities in these amorphous alloys. This is achieved in contrast

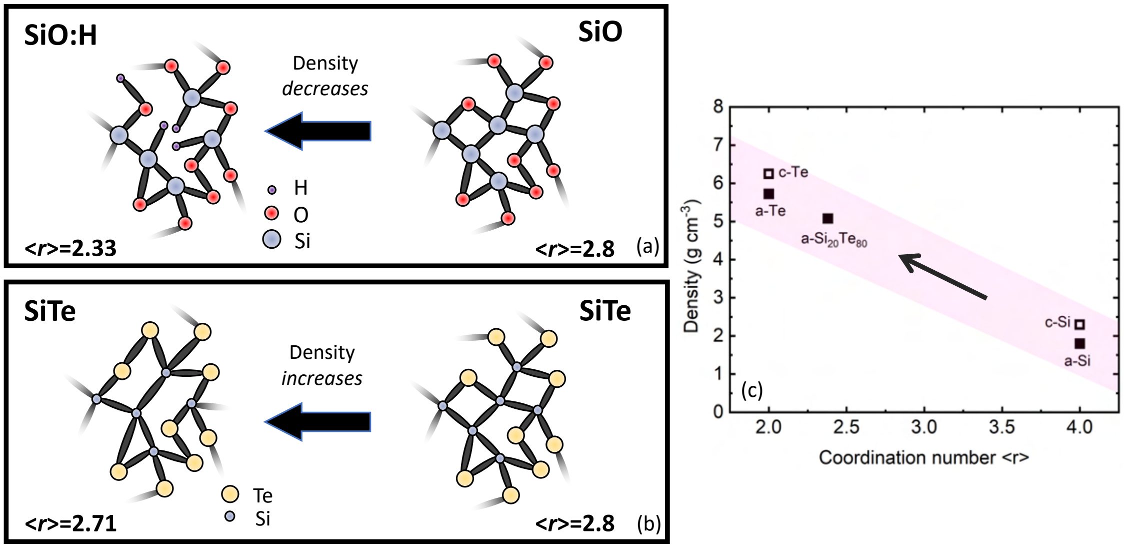

Figure 6.1: Schematic of atomic bonding network showing reductions in coordination number upon addition of (a) hydrogen to silicon oxide, (b) more tellurium to silicon telluride. (c) Density as a function of coordination number for amorphous silicon telluride composition.

with previous studies where reductions in thermal conductivity follow reductions in mass density from bond termination and networking. Here, depending on the composition of the SiTe system, ultralow thermal conductivities can be achieved while increasing the mass density (see Fig. 6.1 (b,c)). This is a consequence of the differing network coordinations of silicon and tellurium and the resulting vibrational localization that ensues from creating a solid solution of these two differently coordinated elements. To the best of my knowledge, not only is this work the first to show how vibrational modes can become fully localized in an amorphous medium, but it also represents the first systematic demonstration of how thermal transport changes across different topological network regimes: under-constrained, stress-free, and over-constrained.

## 6.2 Results

In IV-VI and V-VI chalcogenide alloys, as the concentration of one constituent changes relative to another, depending on the number of covalent bonds per element, the mean atomic coordination number changes. This leads to a natural evolution of the atomic network that will directly affect the physical properties of the amorphous alloy. According to glass theory, disordered media are categorized into (i) flexible polymeric glasses consisting of long chains of randomly oriented atoms with low melting temperatures, (ii) stress-free amorphous structures with optimal glass formation properties, and (iii) rigid amorphous solids consisting of a tightly interconnected network of atoms with high melting temperatures. Inspired by Maxwell's mathematical model for truss structures, Phillips [233] proposed that when the number of local bonding constraints, $n_c$, on an atom equals the number of degrees of freedom, the atomic structure is stress-free. For a three-dimensional network, this occurs when $n_c = 3$ and the mean coordination number, $\langle r_m \rangle$, is 2.40, which is generally referred to as the *rigidity* threshold; below this rigidity threshold, the material behaves like a polymeric glass, which is classified as under-constrained, while above this limit, the material is rigid and classified as over-constrained.

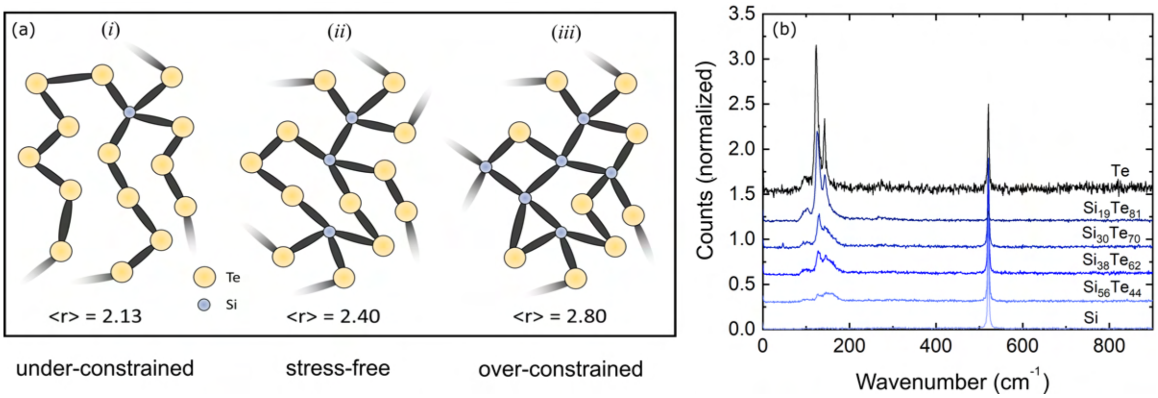

Figure 6.2: (a) Schematics of amorphous networks with a total of 15 atomic sites for different Te to Si ratios representing various topological regimes: (*i*) under-constrained network, (*ii*) stress-free network, and (*iii*) over-constrained network. (b) Raman spectra for SiTe at different Te concentrations. The sharp silicon peak is the effect of the substrate and is not associated with the thin film properties.

The schematic in Fig. 6.2(a) illustrates different possibilities of network topology based on the silicon to tellurium ratio in amorphous SiTe. It has been shown that in chalcogenide glasses, as the structure transitions from an over-constrained to an under-constrained network, additional low frequency vibrational modes emerge [234–236]. To detect any signature of these additional vibrational modes, Raman spectroscopy on SiTe samples with different concentrations of tellurium are performed. As presented in Fig. 6.2(b), in thin film SiTe, the spectra nearly look identical for all tellurium concentrations and no considerable shift in the location of the peak or emergence of additional peaks are detected.

### 6.2.1 Characterization

To study the effect of the atomic network in amorphous materials on the thermal conductivity, thin films of silicon telluride $Si_xTe_{1-x}$ and selenium telluride $Se_xTe_{1-x}$ with different compositions are deposited via magnetron sputtering, using both co-sputtering and nano-laminate techniques, as required to achieve the desired composition. As discussed in previous chapters, the thermal properties are tied to the atomic structure, specifically, ordered vs.$\sim$ disordered. For instance, it has been shown that the thermal conductivity of crystalline GeTe is almost an order of magnitude higher than the amorphous phase [237, 238]. Various spectroscopy techniques, such as X-ray fluorescence (XRF), X-ray diffraction (XRD), Raman, and transmission electron microscopy (TEM) are employed to characterize the films compositions, structures, vibrational energies, and thicknesses.

Table 6.1 shows the structural details of the films studied in this dissertation. The compositions, thicknesses, and atomic structure are confirmed by XRF, TEM, and XRD, respectively. Figure 6.3 shows the XRD result for as-deposited pure Te and $a$-$Si_{25}Te_{75}$ on a $SiO_2$ substrate and 3-5 nm carbon capping layer. For comparison, the XRD measurements of $a$-$Si_{17}Te_{83}$ is presented from the literature [239]. For bulk $a$-$Si_xTe_{100-x}$ alloy ($10 \leq x \leq 28$), it was shown that after annealing for 2 hours at 494 K, excess Te starts to crystallize while the remaining material stays amorphous. Then, upon annealing at 575 K for another 2 hours, the remainder of amorphous phase crystallize into hexagonal $SiTe_2$ phase [239]. According to this study, the XRD patterns across all compositions for $10 \leq x \leq 28$ are identical. The sharp peaks in Fig. 6.3 for the pure Te films demonstrate that the structure of the film is polycrystalline. The peaks for pure Te sample agree well with the 494 K annealed sample where only Te has been crystallized. On the other hand, for $Si_{25}Te_{75}$

Table 6.1: The SiTe compositions studied with the corresponding deposition technique and thicknesses.

| Nominal composition | Deposition | Si% XRF (± 3%) | Te% XRF (± 3%) | Thickness TEM (± 1 nm) | Structure TEM/XRD |
|---|---|---|---|---|---|
| Te | co-sputter | 0 | 100 | 30 | crys |
| $Si_{10}Te_{90}$ | co-sputter | 11 | 89 | 30 | amor |
| $Si_{20}Te_{80}$ | co-sputter | 19 | 81 | 44 | amor/crys |
| $Si_{20}Te_{80}$ | nano-laminate | 38 | 62 | 41 | amor/crys |
| $Si_{30}Te_{70}$ | co-sputter | 34 | 66 | 37 | amor/crys |
| $Si_{40}Te_{60}$ | nano-laminate | 53 | 47 | 41 | amor/crys |
| $Si_{50}Te_{50}$ | nano-laminate | 56 | 44 | 47 | amor/crys |
| $Si_{70}Te_{47}$ | nano-laminate | 65 | 36 | 45 | amor/crys |
| Si | co-sputter | 100 | 0 | 26 | amor |

sample, it does not yield any sharp peak that is indicative of crystallization.

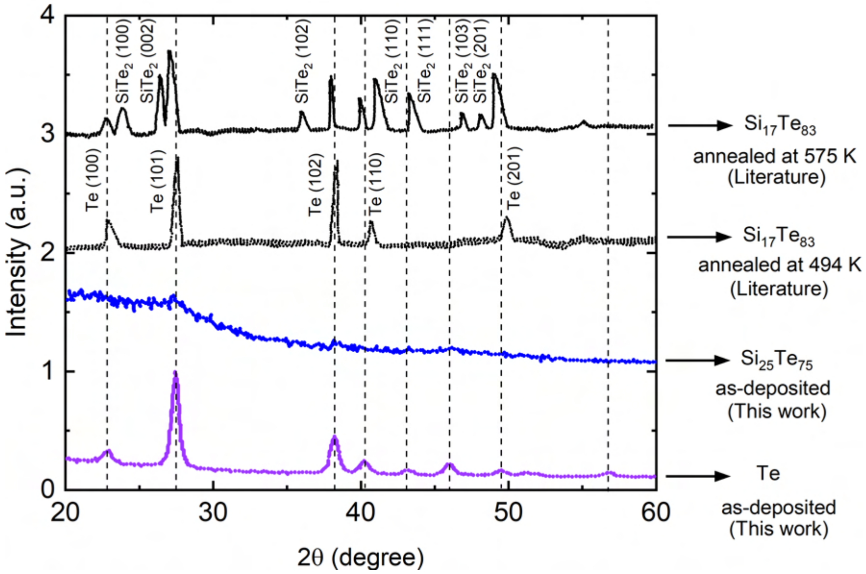

Figure 6.3: Comparison in X-ray diffraction of amorphous $Si_{25}Te_{75}$ used in this study against literature. XRD results are from samples with $SiO_2$ substrate and 3-5 nm carbon coating

Given that, tellurium is an element with a low glass transition temperature and, as a result, compositions with high Te content are prone to crystallization during the deposition process. This prompted me to look in more depth into the atomic structure of the films under investigation. Considering the films' thickness (<40 nm) and the low glass-transition temperature for these samples (400-500 K), implementing atomic-scale structural characterization without damaging the films is exceedingly challenging. Although XRD measurements for the high Te content samples do not show any substantial peaks that indicate crystallinity, the TEM and EELS micrographs for all SiTe compositions except $Si_{11}Te_{89}$ composition, depict Te rich crystallites on the order of 2-5 nm embedded in an amorphous $SiO_x$ matrix. Observations of oxygen signatures and phase segregation in the SiTe films are perplexing. The crystallization could be the result of ion bombardment during the sample preparation process. This is not an unreasonable speculation, especially when it is observed that during the TEM imaging/mapping, the electron beam causes further segregation in the region of mapping, which indicates that the electron beam has sufficient energy to induce phase transformations. Apart from this, I should mention that although the TEM results indicate an entirely different morphology between $Si_{11}Te_{89}$ (uniform, homogeneous amorphous structure) and $Si_{19}Te_{81}$ (segregated regions with Te rich crystallites in an amorphous $SiO_x$ matrix), their measured thermal conductivity value is identical. This is another indication that the films might have been damaged during the sample prep process. In short, despite the fact that segregation and ordered regions in some of the SiTe samples are observed, I posit that these are artifacts of sample preparation and are not intrinsic to the films.

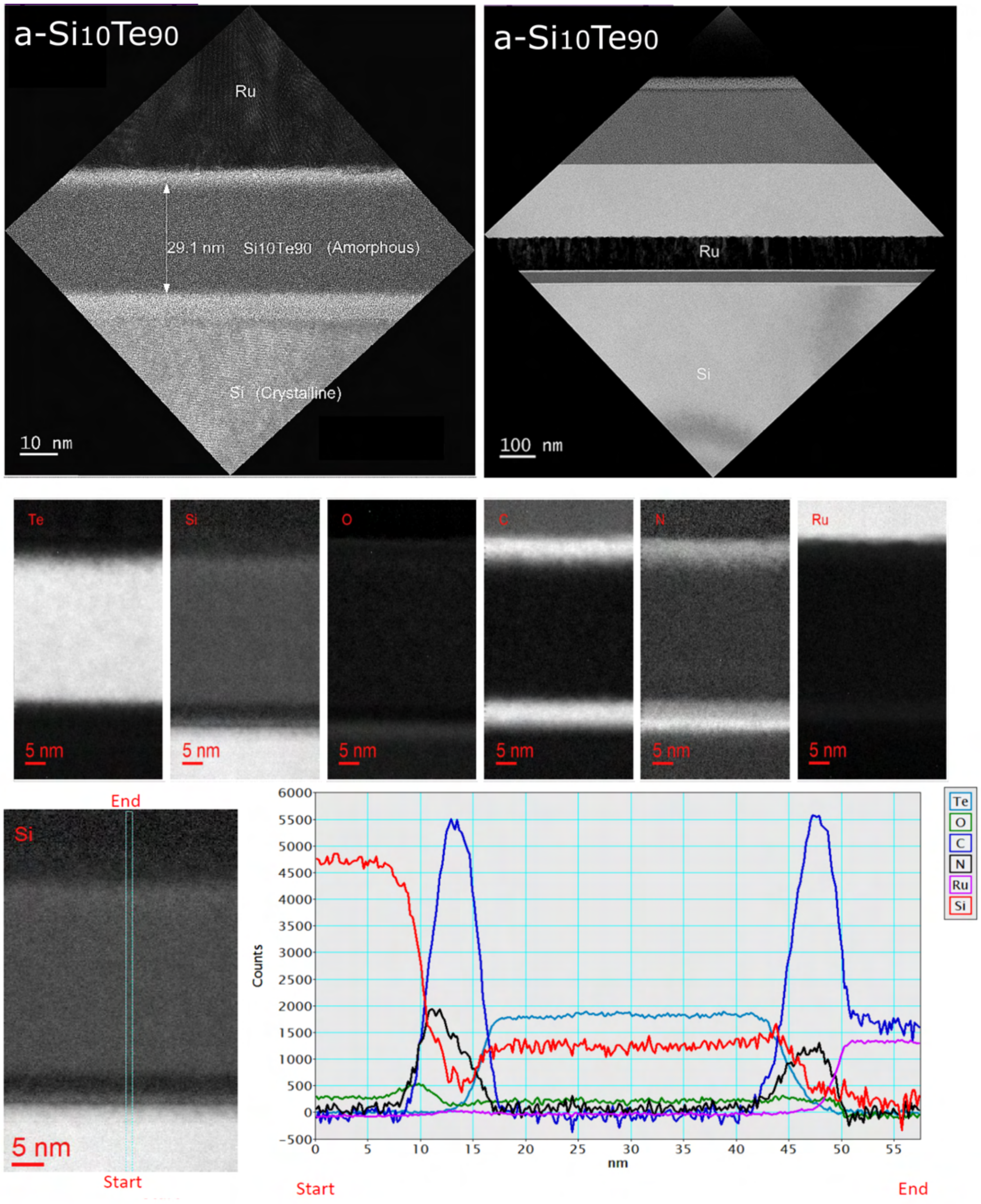

Figure 6.4: TEM micrographs for the sample with nominal composition of *a*-$\text{Si}_{10}\text{Te}_{90}$. According to these results the film is uniformly amorphous. Little oxygen is in *a*-$\text{Si}_{10}\text{Te}_{90}$, however, the oxygen level in the *a*-$\text{Si}_{10}\text{Te}_{90}$ is similar that in Si substrate, so the oxygen could be from air exposure after FIB-cut.

### 6.2.2 Ultralow Thermal Conductivity

The cross-plane thermal properties of the SiTe alloys were measured using time-domain thermoreflectance (TDTR) with the multilayer stack as depicted in Fig. 6.5(a). Figure 6.5(b) shows an exemplary TDTR thermal decay curve as a function of pump delay time for the 40 nm $a$-$Si_{19}Te_{81}$ sample. The inset shows the first few picoseconds of this prototypical TDTR decay curve where the troughs and peaks correspond to the reflection of acoustic waves from the Ru/$CN_x$ and $CN_x$/Si interfaces, respectively. By calculating the time between these *echoes* and with the knowledge of the film thicknesses obtained from TEM, the longitudinal sound speed of the SiTe films are measured.

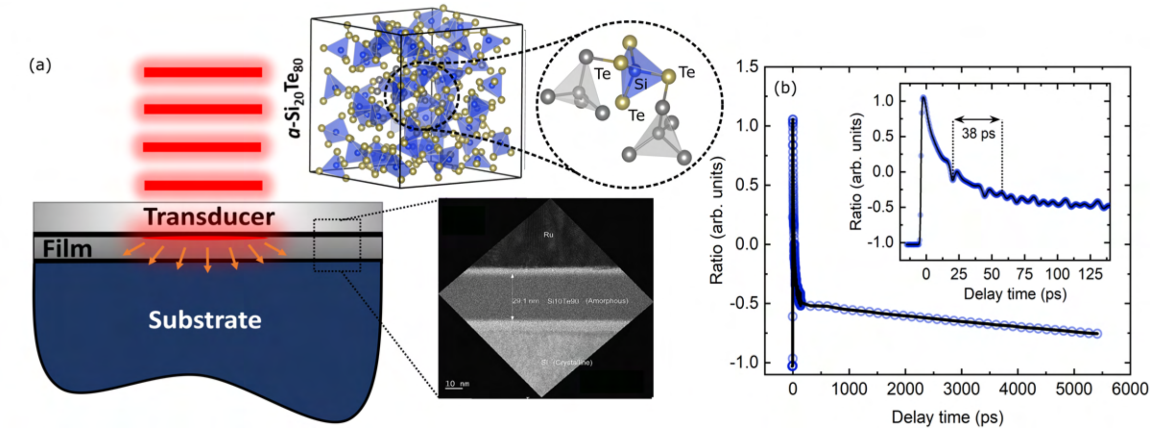

Figure 6.5: (a) Illustration of TDTR measurement geometry, the corresponding layers studied micrograph, and the atomic structure of $a$-$Si_{20}Te_{80}$ with 300 atoms forming randomly oriented tetrahedrons where each Si is bonded to 4 Te atoms. (b) Representative TDTR data for 40 nm thick $a$-$Si_{19}Te_{81}$. The inset shows the picosecond acoustic measurements where the distance between the troughs and the peaks in the measured TDTR data are related to the time it takes for acoustic waves traveling at the speed of sound to transverse the $a$-$Si_{19}Te_{81}$ film.

In the thermal analysis, the model assumes three effective layers in the direction of heat flow i.e. Ru transducer, SiTe film, and the substrate. Figures 6.6(a,b) demonstrate the sensitivity of measurements to parameters such as thickness (d), specific heat (C), thermal conductivity (k), and the thermal boundary conductance (G) for a 5 and 40 nm thick $Si_{20}Te_{80}$ film, respectively. The subscripts indicate the layer number which are labeled as L1, L2, and L3 in the schematics in Figs. 6.6(d,e). These calculations suggest that the

TDTR experiment is mostly sensitive to thickness of the first and second layers. As a result, the uncertainty is estimated by varying the thickness of the SiTe film ($d_2$) by 10%. Another important parameter that needs to be taken into account for estimating the thermal conductivity of the film, is thermal boundary conductance (TBC) at its top and bottom interfaces. As can be seen in Fig. 6.6(a), due to extremely low thermal conductivity of of $Si_{20}Te_{80}$ films, the sensitivity to its thermal conductivity is much higher than the thermal boundary conductance, even for a 5 nm thick film. Therefore, in the thermal model, the TBC is assumed to be infinity for the $G_{1/2}$ and $G_{2/3}$ interfaces and the only free parameter that is fitted for is the thermal conductivity of the $Si_xTe_{1-x}$ layer which is the main source of thermal resistance in the stack. Using a different set of samples, the thermal conductance across Ru/ 10 nm $CN_x$/Si is measured and then was subtracted from the measured thermal conductivity to account for the boundary resistances. However, since the resistance of the $Si_{20}Te_{80}$ is large, subtracting the effect of $CN_x$ layer as the interface has negligible effect on the measured thermal conductivity. A representative experimental data and its corresponding theoretical fit is demonstrated in Fig. 6.6(c) for a 5 and 40 nm thick $Si_{20}Te_{80}$ film. As can be seen, although unrealistic values for the TBC is assumed, due to their negligible sensitivity, the model perfectly fits to the experimental data.

To ensure the accuracy of approach taken to analyse the TDTR data and extract the thermal conductivity, a thin film thickness series in the range of 5-40 nm is made and measured. Then, by applying a linear fit to the thermal resistance data, similar to previous chapters, the thermal conductivity can be obtained independent of the TBCs. This approach is applied to 2 different sample configurations with different interlayers to ensure the accuracy of measurements and negligible impact of TBC on the thermal conductivity measurements. Based on these two sample configurations, the thermal conductivity of the $Si_{20}Te_{80}$ film is measured to be $0.1 \pm 0.01$ W $m^{-1}$ $K^{-1}$, in perfect agreement with the three layer thermal model fit for the 40 nm thick film. The uncertainty is calculated by varying the thickness of the film by $\pm 10\%$.

Now, in order to understand the effects of atomic network and coordination number on

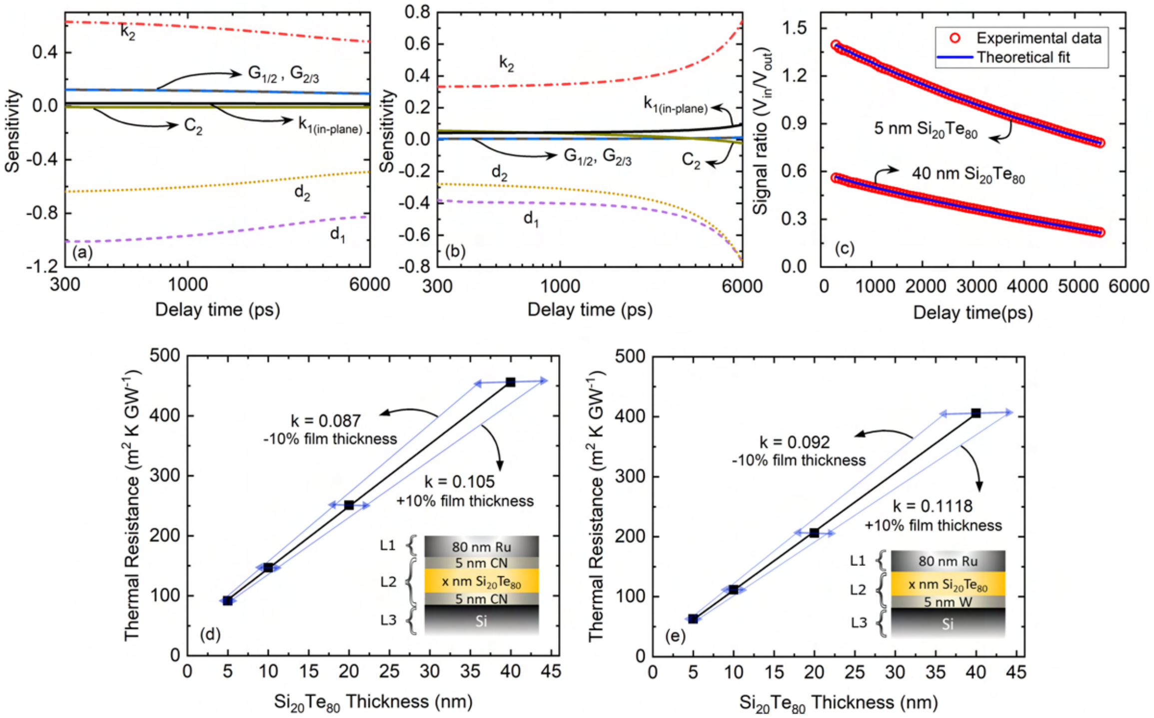

Figure 6.6: Sensitivity of TDTR measurements to parameters such as thermal conductivity, k, thermal boundary conductance, G, specific heat, H, and layers thickness, d, for (a) 5 and (b) 40 nm thick $Si_{20}Te_{80}$, (c) a representative fit to the experimental data for a 5 and 40 nm thick $Si_{20}Te_{80}$. (d,e) thermal conductivity of $Si_{20}Te_{80}$ for different samples configurations, obtained by applying a linear fit to the thermal resistance as a function of thickness.

the thermal transport, amorphous SiTe and SeTe alloys with different Te concentration is measured. It must be noted that, different content of Te in SiTe changes the mean coordination number in the range of $2 < \langle r_m \rangle < 4$ while different content of Te in SeTe lead to a constant mean coordination number $\langle r_m \rangle = 2$. This two separate configurations facilitate pinpointing the effect of coordination and bonding network on their thermal transport. Figure 6.7(a) shows the thermal conductivity of amorphous SiTe and SeTe alloys as a function of Te atomic percentage at room temperature. In SeTe, as shown in red diamonds, the coordination numbers for both Se and Te are identical $\langle r_{\text{Te}} \rangle = \langle r_{\text{Se}} \rangle = 2$, therefore, the relative atomic concentration does not alter the total bonding network and the thermal conductivity remains relatively constant with increasing the Te content. Thus, in spite of the existence of a relatively large atomic mismatch between Se and Te, the changes in thermal conductivity for these under-constrained ($< \langle r_m \rangle < 2.4$) amorphous alloys are negligible.

To further investigate the effect of atomic mass mismatch on thermal conductivity, I perform molecular dynamics simulations on amorphous Si with different concentration of heavy-Si atoms (with atomic mass similar to Te) which will be discussed in more details in the subsequent subsection. The inset in Fig. 6.7(a) shows the results of these simulations. Similar to the thermal conductivity behavior in SeTe alloy, the thermal conductivity of Si-HeavySi modestly decreases from $\sim$1.0 W m$^{-1}$ K$^{-1}$ in amorphous Si to $\sim$0.50 W m$^{-1}$ K$^{-1}$ in *a*-Si at 50-90% heavy-Si concentrations. On the other hand, in the amorphous SiTe alloys, as the Te concentration in SiTe increases, the thermal conductivity drops to as low as $\sim$0.10 $\pm$ 0.01 W m$^{-1}$ K$^{-1}$ and stays relatively constant for Te content ranging from 70% to 90%. The measured thermal conductivity for $\sim$26 nm amorphous silicon film with no tellurium is analogous to values reported previously [240] for films of comparable thicknesses (0.8 $\pm$ 0.2 W m$^{-1}$ K$^{-1}$). For the pure Te film, the thermal conductivity suddenly increases to 0.23 $\pm$ 0.04 W m$^{-1}$ K$^{-1}$ compared to other high content Te composition. As was discussed in the previous subsection, TEM micrographs as well as XRD reveal that the Te film is not amorphous, but rather polycrystalline. It is not uncommon for Te to crystallize during growth or post-processing as tellurium has a low glass-transition temperature, $T_g$, which makes it extremely difficult to deposit in its amorphous state[241]. The measured thermal conductivity for Te film is less than those reported in the literature [242–244], which report in the range of 0.43-3.0 W m$^{-1}$ K$^{-1}$, suggesting that some degree of disorder is present in the Te films.

My cryogenic thermal conductivity measurements are shown in Fig. 6.7(b) which reveal that the thermal conductivities of pure Te and a-SiTe samples follow an amorphous-like trend. Typically, in materials with high degree of disorder the thermal conductivity as a function of temperature basically follows the heat capacity trend, and plateau above the Debye temperature. This behavior in crystals is an indication of a high concentration of disorder. Of course, the samples studied in this chapter are supposed to be “amorphous” which means should have the highest degree of disorder, yet, in previous subsection we observed that in samples such as Te, the film is polycrystalline. This amorphous-like trend of thermal conductivity not only is another evidence to the amorphous nature of the films but also could explain the reason behind the low thermal conductivity of the polycrystalline Te film compared to the literature values.

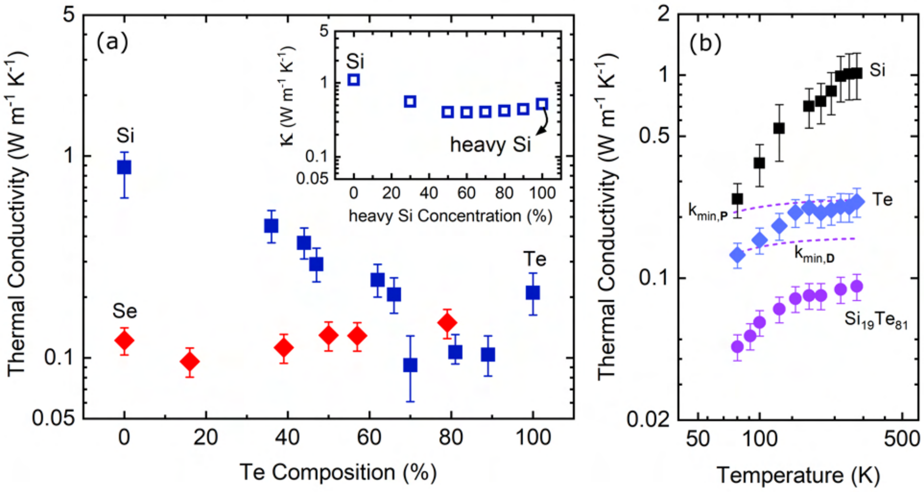

Figure 6.7: (a) The measured thermal conductivity as a function of tellurium concentration in amorphous SiTe and SeTe. The inset shows the NEMD simulation results for thermal conductivity of Si (28 u), heavy Si (127 u), and their alloy. (b) Thermal conductivity of amorphous silicon, tellurium, and $Si_{19}Te_{81}$ as a function of temperature.

In order to investigate how the thermal conductivity of $Si_{20}Te_{80}$ changes at high temperature, I performed in-situ high temperature thermal conductivity measurements. For this, a resistive heating stage is used while passing nitrogen gas through the chamber and incrementing the temperature of the sample every 10 minutes by 20°C. Figure 6.8 shows the thermal conductivity at elevated temperature up to 300°C before the sample starts to delaminate. According to these measurement, the thermal conductivity of $Si_{20}Te_{80}$ remains constant at elevated temperatures.

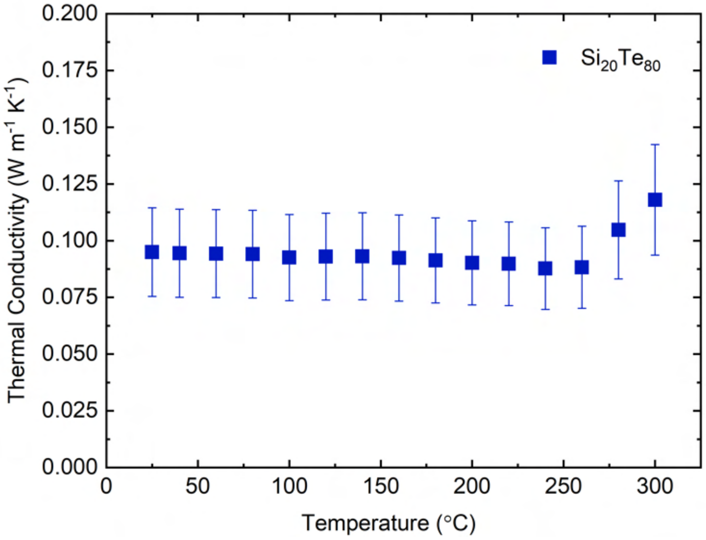

Figure 6.8: Thermal conductivity of 20 nm thick $Si_{20}Te_{80}$ from room temperature up to 300 °C. The film started to delaminate for temperatures above 300 °C. The uncertainty is calculated by assuming 10% variations in the $Si_{20}Te_{80}$ film thickness.

### 6.2.3 Minimum Limit Models

Although the increased mass density of high content Te alloys and the large atomic mass mismatch between Si and Te could partly explain the reductions observed in thermal conductivity, as discussed earlier, they are not the primary reason behind such a dramatic reduction in thermal conductivity. In order to understand such a strong reduction in thermal conductivity of SiTe alloys at high tellurium content, I use existing theoretical approaches to estimate the minimum limit to the thermal conductivity which is derived in the context of phonons ($\kappa_{\mathrm{min,\mathbf{P}}}$) and diffusons ($\kappa_{\mathrm{min,\mathbf{D}}}$). According to Cahill and Pohl [67], a lower limit to the thermal conductivity of materials is estimated based on the collective atomic vibrations, i.e. phonons, derived from the kinetic theory of gases:

$$\kappa_{\mathrm{min,\mathbf{P}}} = 1.21 k_B n^{2/3} v_g, \tag{6.1}$$

where $k_B$ is the Boltzmann constant, $v_g$ is the average sound velocity in the material, and $n$ is the number density. The average sound velocity can be written in terms of the longitudinal

($v_{LA}$) and transverse ($v_{TA}$) sound velocities as: $v_g^2 = \frac{1}{3}\left(v_{\mathrm{TA1}}^2 + v_{\mathrm{TA2}}^2 + v_{\mathrm{LA}}^2\right)$. In this work, for consistency, I assume that transverse sound velocity is 60% of the longitudinal mode, $v_T = 0.6v_L$. For $\mathrm{Si_{19}Te_{81}}$, using picosecond acoustics measurements, I measure a longitudinal sound velocity of $v_L = 2150 \pm 100$ m s$^{-1}$, which is in good agreement with previously reported values ($v_L = 2030$ m s$^{-1}$) for the sound velocity of a thicker SiTe film [245]. Other parameters that are used as an input to calculate the minimum limit such as number density and sound velocities across different compositions are given in Table 6.2. Using these parameters, I determine a minimum thermal conductivity of 0.24 W m$^{-1}$ K$^{-1}$ for $\mathrm{Si_{19}Te_{81}}$ at room temperature. This estimate for the minimum thermal conductivity, however, is still more than a factor of two higher than the measured thermal conductivity of $\mathrm{Si_{19}Te_{81}}$ (0.10 W m$^{-1}$ K$^{-1}$). In fact, for nearly all compositions of SiTe studied in this work, Eq. 6.1 over-predicts the measured thermal conductivities, as shown in Fig. 6.9. This discrepancy increases as the SiTe coordination number decreases and the alloy transitions into an under-constrained network.

Although phonon-mediated minimum limit to thermal conductivity has served as a successful approach to predict the thermal conductivity of disordered crystals and amorphous materials, several recent works have experimentally measured values well below this limit. This has motivated others to model the thermal conductivity in amorphous solids as a form of energy hopping between localized vibrational eigenstates. According to Allen and Feldman [71] (AF), a large portion of heat in disordered solids is transferred by harmonic coupling of quantized vibrations that are neither propagating nor localized. These delocalized non-propagating vibrational modes, *diffusons*, carry heat by interactions with other vibrational modes with length scales on the order of the vibrational wavelength. According to AF theory, the thermal conductivity due to diffuson contribution can be approximated by:

$$\kappa_{AF} = \frac{1}{V}\sum_{i=1}^{N} C(\omega_i)D(\omega_i), \tag{6.2}$$

where $V$ is the system volume, $\omega_i$ is frequency of $i$th mode, $C(\omega_i)$ and $D(\omega_i)$ are the frequency dependant specific heat and mode diffusivity, respectively. Based on the AF formalism, Agne et al. [65] suggested a modified minimum limit model for heat transport in disordered solids that relies on the concept of diffusons rather than phonons. They argued that in a disordered solid, the lower bound to thermal conductivity occurs when the thermal transport is entirely driven by diffusons. This approach, albeit the heat transfer carrier length scale being fundamentally different from those modeled in Eq. 6.1, leads to a similar functional form for the thermal conductivity of disordered materials:

$$\kappa_{\mathrm{min},\mathbf{D}} \approx 0.76 P k_B n^{2/3} \nu_g, \tag{6.3}$$

where $P$ is the probability of successful energy transfer between the atoms. According to this diffuson-mediated minimum model, in one period of oscillation, each vibrating carrier will make two attempts to transfer energy where $P$ is the probability of a successful energy transfer. In the high temperature limit and maximum diffusivity where $P = 1$, the calculated thermal conductivity is ∼37% lower than the phonon minimum limit model. By applying this diffuson-mediated minimum limit model to $\mathrm{Si}_{19}\mathrm{Te}_{81}$, thermal conductivity of 0.14 W $\mathrm{m}^{-1}$ $\mathrm{K}^{-1}$ is calculated, which is in a better agreement with the measured value. However, considering the fact that this model is supposed to set the lower bound to thermal conductivity, it still predicts 40% higher thermal conductivity than the measured value.

The dashed line in Fig. 6.8(b) shows the theoretical minimum limit based on diffuson-mediated thermal conductivity for $a$-$\mathrm{Si}_x\mathrm{Te}_{1-x}$. In the high temperature limit and maximum diffusivity where $P$ = 1, the calculated diffuson-mediated thermal conductivity is ∼37% lower than the phonon minimum limit model. Figure 6.8(b) demonstrates that the measured thermal conductivity of $a$-$\mathrm{Si}_{19}\mathrm{Te}_{81}$ is well below the minimum limit calculations for both existing models. This implies that the thermal transport mechanism in high Te content $\mathrm{Si}_x\mathrm{Te}_{1-x}$ is dominated by other atomistic properties that impede the transfer of energy beyond those accounted for in the minimum limit models.

To resolve this discrepancy between the models and the experimental data, I revisit the earlier assumption that was made in the diffuson-mediated thermal conductivity, which assumes 100% of attempts to transfer energy are successful between diffusons. In the case

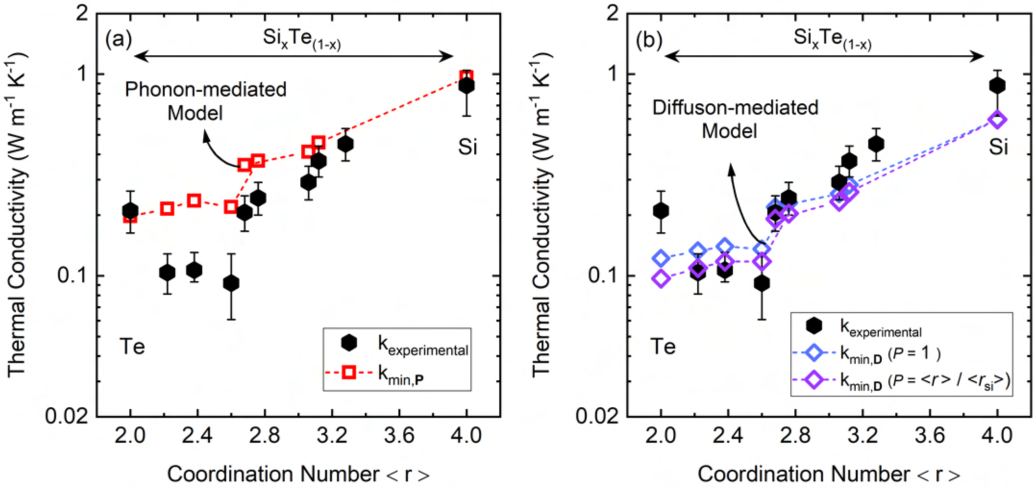

Figure 6.9: Thermal conductivity of SiTe as a function of coordination number measured by TDTR (solid hexagons) and the corresponding (a) phonon-mediated minimum limit (hollow squares), and (b) the diffuson-mediated thermal conductivity (hollow diamonds). The uncertainty is calculated based on 10% variation in thickness of SiTe film. The sample corresponding to data point for $a$-Si$_{30}$Te$_{70}$ and $< \langle r_m \rangle = 2.6$ was deposited in a different run and therefore has a larger uncertainty.

of Si$_x$Te$_{1-x}$ composition, since the coordination number decreases by increasing the Te concentration, the alloy transitions from an over-constrained to an under-constrained network. This reduction in the number of bonds per atom eliminates the number of pathways through which diffusons can interact, and leads to a reduction in the probability of their successful energy transfer. The calculated coordination number of these alloys is based on the measured relative atomic percentages assuming Si and Te as 4- and 2-coordinate elements, respectively. This time, for calculating $\kappa_{\text{min},\mathbf{D}}$, I assume $P$ changes with respect to mean coordination number of each composition. For this, I use a model proposed by Xi et al. [72] showing a power law dependence between mean coordination number and thermal conductivity (k$\propto P^{1/3}$). By normalizing each coordination number with respect to pure Si, i.e., $P = \langle r_{\text{m}} \rangle / \langle r_{\text{max}} \rangle = \langle r_{\text{Si}_\text{x}\text{Te}_{1-\text{x}}} \rangle / \langle r_{\text{Si}} \rangle$. Using this assumption, $P$ changes from 1 for Si ($\langle r_{Si} \rangle = 4$) to $\sim$0.8 for Te ($\langle r_{Te} \rangle = 2$). By applying this condition, the diffuson-mediated model predicts a thermal conductivity in better agreement with the measured values for the SiTe alloys as shown in 6.8(b). With the varying coordination number in SiTe with composition, these results imply that the nature of the vibrational modes contributing to thermal

Table 6.2: The longitudinal $v_{long}$, total sound speed $v_g$, number density n, coordination number $< r >$, and probability of successful transfer $P$ for different amorphous chalcogenide compositions used in thermal conductivity estimation.

| Composition | $v_{long}$ ($\mathrm{m.s^{-1}}$) | $v_g$ ($\mathrm{m.s^{-1}}$) | $n \times 10^{28}$ ($\mathrm{m^{-3}}$) | $< r >$ | $P$ | $\kappa_{\min,\mathbf{P}}$ ($\mathrm{W.m^{-1}.K^{-1}}$) | $\kappa_{\min,\mathbf{D}}$ ($\mathrm{W.m^{-1}.K^{-1}}$) |
|---|---|---|---|---|---|---|---|
| Se | 1840 [a] | 1221 | 3.68 | 2.00 | 0.79 | 0.22 | 0.11 |
| Te | 1840 [b] | 1238 | 2.50 | 2.00 | 0.79 | 0.20 | 0.10 |
| $Si_{11}Te_{89}$ | 1980 | 1333 | 3.00 | 2.22 | 0.82 | 0.21 | 0.11 |
| $Si_{19}Te_{81}$ | 2150 | 1447 | 3.05 | 2.38 | 0.84 | 0.24 | 0.12 |
| $Si_{30}Te_{70}$ | 1968 | 1324 | 3.12 | 2.60 | 0.87 | 0.22 | 0.11 |
| $Si_{34}Te_{66}$ | 3290 | 2215 | 3.19 | 2.68 | 0.88 | 0.35 | 0.19 |
| $Si_{38}Te_{62}$ | 3153 | 2122 | 3.15 | 2.76 | 0.88 | 0.37 | 0.21 |
| $Si_{53}Te_{47}$ | 3523 | 2372 | 3.35 | 3.06 | 0.91 | 0.41 | 0.24 |
| $Si_{56}Te_{44}$ | 3874 | 2608 | 3.39 | 3.12 | 0.92 | 0.45 | 0.26 |
| Si | 6310 [c] | 4248 | 4.99 | 4.00 | 1.00 | 0.96 | 0.61 |

[a] see Ref. [246].
[b] Assuming amorphous tellurium sound speed is similar to that of selenium [246].
[c] see Ref. [247].

conductivity in SiTe amorphous films becomes more spatially localized as the coordination number is reduced below the rigidity threshold and the SiTe atomic network transitions away from the over-constrained regime.

### 6.2.4 Molecular Dynamics Simulations

While the theoretical models discussed above provide reasonable qualitative insight into the thermal transport mechanisms in the amorphous SiTe alloys, I turn to molecular dynamics and lattice dynamic simulations to gain a deeper understanding of the mechanism that drives the ultralow thermal conductivity of $Si_{19}Te_{81}$. In order to exclusively investigate the effect of mass scattering on a-SiTe alloy, non-equilibrium molecular dynamics (NEMD) and equilibrium molecular dynamics (NMD) simulations were performed by randomly substituting the mass of Si with that of Te (127 u) at different compositions. For both techniques, Stillinger-Weber interatomic potential that has been widely used to characterize the thermal properties of Si is selected. The simulation procedure and details of these techniques are given elsewhere [248–250]. Figure 6.10 (a) demonstrates the temperature profile across the simulation box. For these simulations, two heat bath are assigned at the beginning and in the middle of the simulation box and periodic boundary condition are applied to all directions. The temperature of the hot and cold regions are set to 550 and 450 K, respectively. By measuring the heat flux transferred between these two heat baths, the thermal conductivity of the $a$-Si$_{20}$-heavySi$_{80}$ is determined from Fourier's law to be $\sim$0.50 W m$^{-1}$ K$^{-1}$. These simulations are in good agreement with my EMD Green-Kubo calculations as shown in Fig. 6.10 (b). The calculated thermal conductivity for $a$-Si$_{20}$-heavySi$_{80}$ is a factor 5 higher than the measured thermal conductivity of $a$-Si$_{20}$Te$_{80}$. Therefore, it can be concluded that the large atomic mass mismatch between Si and Te and corresponding alloy scattering cannot alone explain the ultralow thermal conductivity of this material.

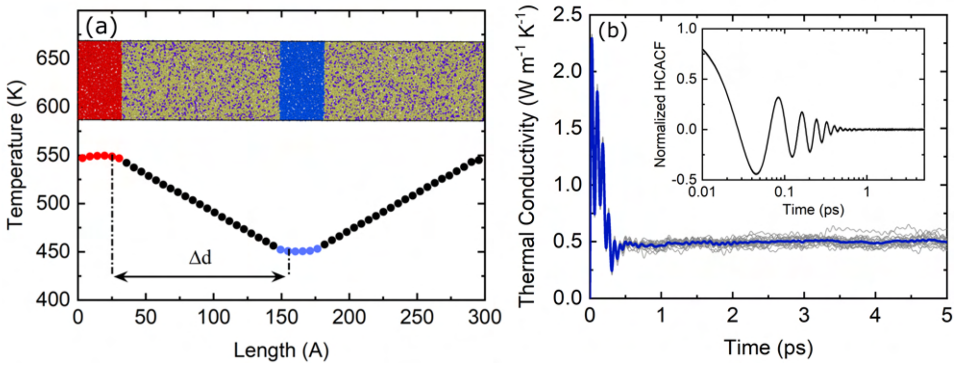

Figure 6.10: Thermal conductivity for $a$-Si$_{20}$-heavySi$_{80}$ from (a) non-equilibrium and (b) equilibrium molecular dynamic calculations. Both method result in thermal conductivity of $\sim$0.50 W m$^{-1}$ K$^{-1}$. The heavySi mass in these simulations is similar to that of the Te.

In order to understand the ultralow thermal conductivity in $a$-Si$_{19}$Te$_{81}$, it is necessary to evaluate the contribution of each fundamental energy carriers to the thermal conductivity; propagons, diffusons, and locons. In a-Si, Seyf and Henry [251] showed that a small defect concentration ($\sim$10%) leads to a dramatic decrease in the population of propagons. Given the large concentration of Te in $a$-Si$_{19}$Te$_{81}$, it is very likely that low-frequency propagons scatter with the impurities and have a negligible contribution to the total thermal conductivity. For this, I turn my attention to medium-frequency heat carrying diffusons and high-frequency locons (fully localized modes). Locons are vibrational excitations with vibrational amplitudes that decay exponentially from the center of excitation, and normally have high frequencies. The frequency above which vibrational modes are fully localized is known as the mobility edge. The inverse participation ratio (IPR) determines the degree of localization of modes and is given by:

$$IPR = \frac{\Sigma_i^N \left(\Sigma_{\alpha=1}^3 u_{i\alpha}^2\right)^2}{\left(\Sigma_{i=1}^N \left(\Sigma_{\alpha=1}^3 u_{i\alpha}^2\right)\right)^2}, \tag{6.4}$$

where $N$ is the number of atoms and $u_{i\alpha}$ is the eigenvector component for atom $i$ in the direction $\alpha$. For a mode that is fully localized on a single atomic site, IPR=1, and for a fully delocalized mode that spans all atoms, IPR=1/$N$. While it is not possible to define a precise IPR value for the transition of modes from diffusons to locons, for this work, locons are defined as modes where the eigenvector is spread across 20% or less of the atoms in the supercell (60 atoms, IPR$\geq$0.01667). This convention has been used in a number of previous studies[252–254] and serves as a reasonable cutoff for comparison with other works.

Figures 6.11(a-c) show the vibrational density of states (DOS), mode diffusivity, and IPR for amorphous Si, respectively. The thermal conductivity in *a*-Si is dominated by low-frequency propagons and diffusons. However, since negligible contribution from propagons to thermal conductivity of SiTe films with high Te contents is assumed, I only focus on diffusons contribution which is $\sim$0.88 W m$^{-1}$ K$^{-1}$ at room temperature for *a*-Si. Based on the calculated mobility edge, it is found that locons make up less than 4% of modes in *a*-Si which is in agreement with previous studies [59]. This indicates that almost all modes in *a*-Si are active in transferring heat. The small percentage of locons could be a result of the over-constrained bonding network in *a*-Si. This means that the reduction of mean coordination number in SiTe, should increase the number of localized states.

To assess the assumption that coordination number, i.e. number of constraint on an atom, can lead to localization, I turn to another familiar amorphous structure, *a*-SiO$_2$. The mean coordination number for this structure is 2.67, which is lower than *a*-Si and based on our assumption, should have a larger percentage of locons than *a*-Si. This composition also has a similar coordination number and atomic structure to *a*-SiTe$_2$. For instance, the *a*-SiO$_2$ structure consists of randomly oriented tetrahedrons where each Si is bonded to 4 oxygen atoms and each tetrahedron shares an oxygen atom with another tetrahedron (Si-O-Si). Given these similarities, a major difference between *a*-SiO$_2$ and *a*-SiTe$_2$ is the large atomic mass difference between oxygen and tellurium. In order to facilitate comparison between *a*-SiO$_2$ and *a*-SiTe$_2$ alloy, the oxygen mass ($m_O = 16$ amu) are replaced with heavy-oxygen ($m_{Te} = 127.6$ amu). I use a *a*-Si$^{127}$O$_2$ taxonomy for the modified SiO$_2$ to avoid confusion with the real system.

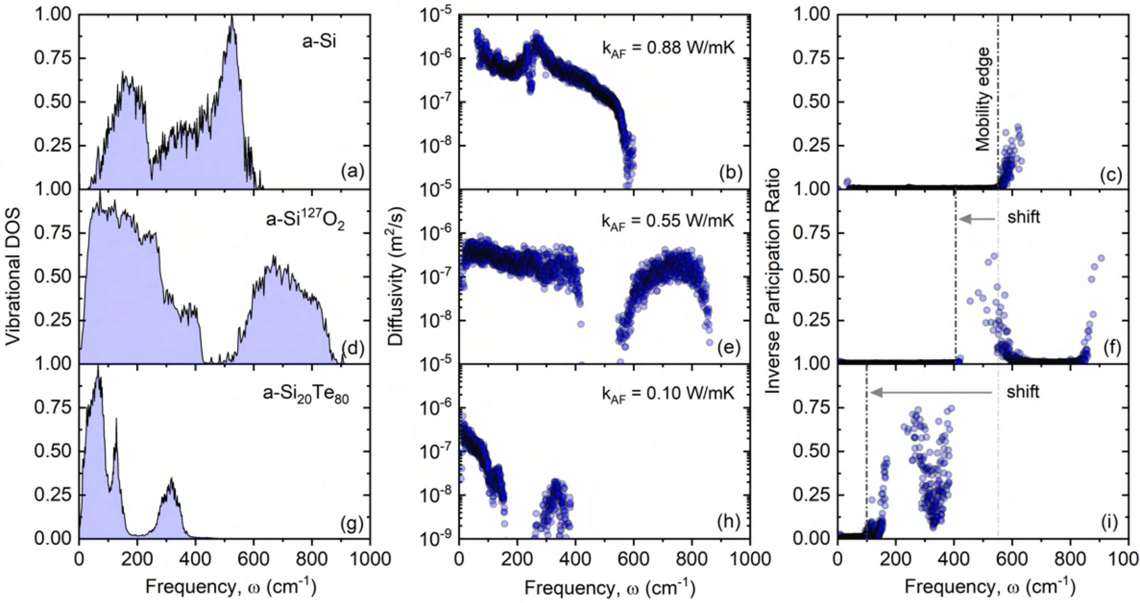

Figure 6.11: (a,d,g) Vibrational density of states (DOS), (b,e,h) mode diffusivity, and (c,f,i) inverse participation ratio (IPR) for *a*-Si, *a*-Si$^{127}$O$_2$, and *a*-Si$_{20}$Te$_{80}$, respectively. The corresponding thermal conductivity are given for each system. The shift in the mobility edge with respect to the *a*-Si is depicted by an arrow.

Another notable difference between *a*-SiO$_2$ and *a*-SiTe$_2$ systems is the bond enthalpy which is significantly higher for Si-O ($\sim$450 kJ/mol) compared to Si-Te ($\sim$220 kJ/mol) and Si-Si ($\sim$225 kJ/mol)[255]. This indicates that strong Si-O bonds would favor high frequency modes. As can be seen in Fig. 6.11(d), the *a*-Si$^{127}$O$_2$ structure has modes with frequencies higher than *a*-Si. The emergence of these higher frequency modes is attributed to the artifact of an improper interatomic potential. As a result of this, the Si-$^{127}$O bonds in our modified *a*-Si$^{127}$O$_2$ are shorter than Si-Te, leading to the appearance of high frequency modes observed in DOS calculations. Nevertheless, these high frequency modes are localized and do not contribute to thermal conductivity. Figure 6.11(f) shows that the mobility edge is shifted to ~400 cm$^{-1}$ compared to *a*-Si and the percentage of locons has increased to ~10%. The AF thermal conductivity for *a*-Si$^{127}$O$_2$ system is estimated to be ~0.55 W m$^{-1}$ K$^{-1}$.

In order to further investigate the effect of coordination number on the localization of modes, I consider Si$_{20}$Te$_{80}$ composition with a coordination number of 2.4 at the rigidity threshold. For this structure, it is assumed that *a*-Si$_{20}$Te$_{80}$ consists of randomly oriented Si-Te tetrahedrons where the tetrahedrons do not share a Te atom (Si-Te-Te-Si). Using force constants derived from ab-initio calculations, the DOS, diffusivity and IPR are reported for *a*-Si$_{20}$Te$_{80}$ alloy in Figs. 6.11(g-i). According to my calculations, in this composition not only is the effective frequency range reduced, but also based on the IPR calculation, nearly 42% of the modes are localized. It is found that locons begin to appear for frequencies greater than 89 cm$^{-1}$ and above 102 cm$^{-1}$ all vibrational modes act as locons and do not contribute to thermal transport. This includes the large vibrational peak centered at 125 cm$^{-1}$ due to tellurium motion and the higher optical band from 250 cm$^{-1}$ to 400 cm$^{-1}$ due primarily to silicon atoms. According to the IPR calculation, the mobility edge is shifted from 550 to 102 cm$^{-1}$, more than a factor of five to lower frequencies. The thermal conductivity due to diffuson contribution in *a*-Si$_{20}$Te$_{80}$ is calculated to be $0.10 \pm 0.005$ W m$^{-1}$ K$^{-1}$ in excellent agreement with measured value. The uncertainty is calculated by changing the broadening factor by 50%.

Figures 6.12(a-c) show the thermal conductivity accumulation as a function of vibrational frequency at 300 K. The calculated thermal conductivity for *a*-Si is comparable to those calculated by Larkin and McGaughey [61]. It is observed that for all cases, beyond the mobility edge limit where the modes are fully localized, the thermal conductivity stays constant. This is expected since the locons contribution to total thermal conductivity is negligible. This also indicates that in *a*-$Si_{20}Te_{80}$, a great deal of modes (42%) are localized leading to ultralow thermal conductivity. The delocalized and localized modes are visualized in 6.12(d,e) by showing the eigenvectors for modes at frequency below (41 $cm^{-1}$) and above (290 $cm^{-1}$) the mobility edge. The amplitude of eigenvectors for localized frequency are strongly suppressed compared to delocalized modes. The large amplitude for eigenvector observed in some of the modes are indicative of strong localization showing the energy associated with these modes are confined in a small geometric region. Figures 6.12(f,g) indicate the population of eigenvectors based on their amplitude. According to these figures, for a frequency below the mobility edge, the amplitude of the eigenvectors are uniformly spread out from 0 to $\sim$15. Whereas for frequency above the mobility edge, due to the effect of localization, the amplitude of a large number of modes drastically decreases to below 2.

The thermal properties of chalcogenide materials across different topological constraint regimes have been previously investigated for bulk silicon telluride and arsenic selenide [256, 257]. In stark contrast to the results presented in this chapter, the authors observe a peak for thermal diffusivity and conductivity at the rigidity threshold. Philip and Madhusoodanan [256] reported a thermal diffusivity of $\sim$0.06 $cm^2/s$ for bulk a-$Si_{20}Te_{80}$ which is more than a factor two higher than the amorphous silicon [258]. This could indicates that either their sample is not entirely amorphous or there is a large concentration of impurities. This discrepancy between the bulk and thin films, however, is not surprising as the defects such as impurities are common in bulk systems.

A close material cousin to SiTe is the well-known thermoelectric/phase-change material, GeTe, that has been extensively studied before both in terms of electrical and thermal properties. Although several studies reported the thermal conductivity of GeTe in amorphous phase at different tellurium concentrations [237, 259–261], depending on the deposition process and thermometery technique, the values range from 0.1-0.23 W $m^{-1}$ $K^{-1}$. The absence of a unique investigation on the thermal properties of GeTe with respect to the

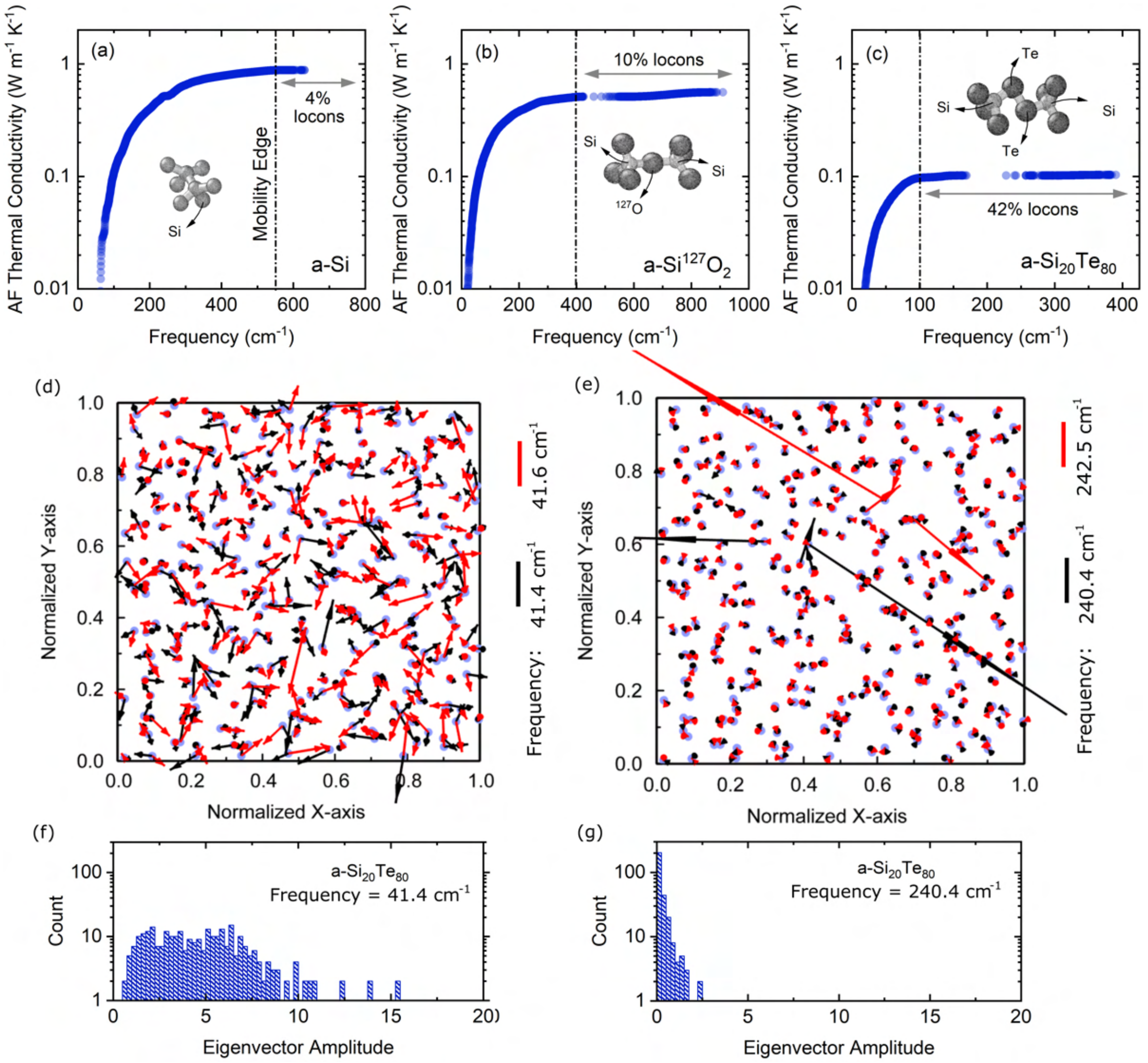

Figure 6.12: Allen-Feldman thermal conductivity accumulation as a function of vibrational mode frequency for (a) *a*- with inset showing Si-Si bond between two tetrahedrons, (b) *a*-$Si^{127}O_2$ with inset showing Si-$^{127}$O-Si bond between two tetrahedrons, and (c) *a*-$Si_{20}Te_{80}$ with inset showing Si-Te-Te-Si bond between two tetrahedrons. Two-dimensional visualization for the spatial component of the eigenvectors at (d) delocalized, 41 $cm^{-1}$, and (e) localized, 290 $cm^{-1}$, frequencies in *a*-$Si_{20}Te_{80}$. The few high amplitude eigenvectors in localized frequency are an indication of strong localization showing the energy associated with these modes are confined in a small geometric region. (f,e) Histogram indicating the population of modes based on their eigenvector amplitude at delocalized and localized frequencies.

coordination number makes it difficult to compare any trend in this composition against that of SiTe. However, due to the structural similarity between SiTe and GeTe, I use the model for *a*-$Si_{20}Te_{80}$ and replace the Si atomic mass with that of Ge (*a*-$^{78}Si_{20}Te_{80}$) and calculate its diffusivity and thermal conductivity. Since GeTe has a higher average atomic mass, one would expect to observe a lower thermal conductivity compared to SiTe. However, according to my calculations, the thermal conductivity for heavier $a$-$^{78}Si_{20}Te_{80}$ does not change and remains similar to $a$-$Si_{20}Te_{80}$. This demonstrates that the low frequency heat carrying modes are not influenced by mass scattering in these unique topological chalcogenide phases.

### 6.2.5 Amorphous $Ge_{20}Te_{80}$ vs. $Si_{20}Te_{80}$

GeTe alloy is a well-known phase-change/thermoelectric material which has been extensively studied in terms of its thermal properties. Similar to silicon, germanium is a 4-coordinated element and forms a short range ordered tetrahedron upon mixing with Te. Atomic structure of SiTe studied here in many cases such as coordination number and radial distribution function resembles that of the GeTe. Figure 6.13 shows the radial distribution function for a-$^{78}Si_{20}Te_{80}$ where the mass of silicon atoms are replaced by that of germanium and $a$-$Ge_{20}Te_{80}$ from ref. [262]. Due to similarities between GeTe and SiTe, it is interesting to investigate how much atomic masses of the constituent elements in $a$-$Si_{20}Te_{80}$ would change the thermal properties. For this, the simulations for $a$-$Si_{20}Te_{80}$ is repeated while changing the silicon mass to that of germanium, $a$-$^{78}Si_{20}Te_{80}$. The result for this modified alloy system is presented in Fig. 6.14. As can be seen, due to higher average atomic mass, the frequency of the modes have dropped from $\sim$400 cm$^{-1}$ to $\sim$300 cm$^{-1}$. However, this has negligible impact on the thermal conductivity of the $a$-$^{78}Si_{20}Te_{80}$. As discussed in the manuscript, this is because all the modes above $\sim$100 cm$^{-1}$ are localized and do not contribute to heat transfer. Although the force constants in $a$-$^{78}Si_{20}Te_{80}$ has not been developed for $a$-$Ge_{20}Te_{80}$ alloy system, the estimated thermal conductivity is in good agreement with experimentally reported values that spans from 0.1 to 0.23 W m$^{-1}$ K$^{-1}$ [237, 259–261].

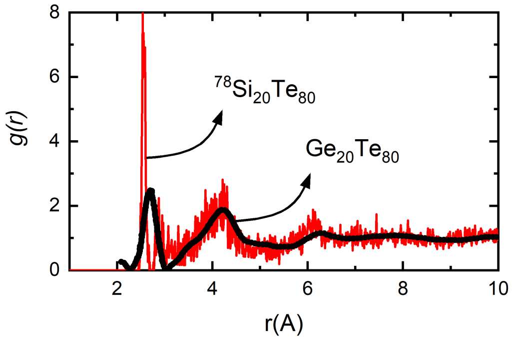

Figure 6.13: Comparison between $a$-$^{78}$Si$_{20}$Te$_{80}$ with 300 atom supercell and $a$-Ge$_{20}$Te$_{80}$ Ref. [262] radial distribution function.

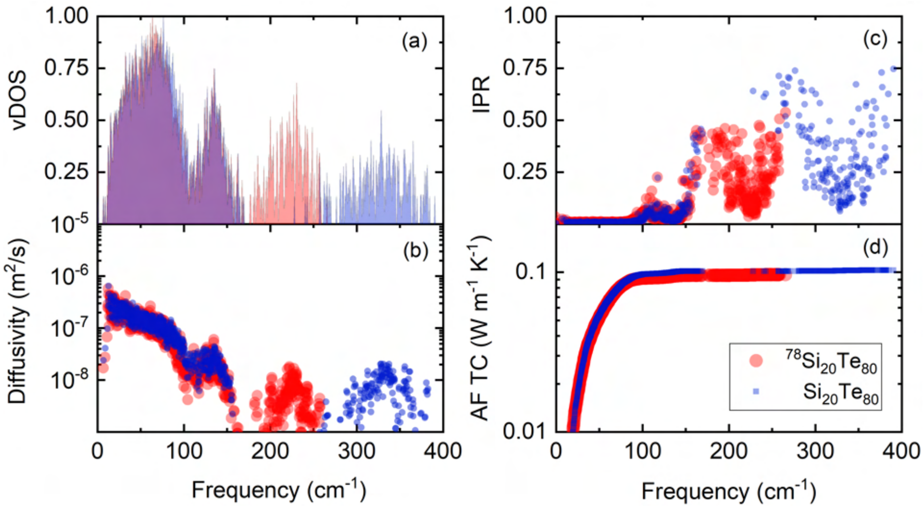

Figure 6.14: (a) Vibrational density of states (vDOS) for $a$-Si$_{20}$Te$_{80}$ and $a$-$^{78}$Si$_{20}$Te$_{80}$ (similar mass to $a$-GeTe) obtained from force constant calculation on 300 atom supercell (b) diffusivity of modes calculated from AF formalism, (c) inverse participation ratio calculated from vibrational mode eigenvectors (d) Accumulative thermal conductivity as a function of modes frequency.

## 6.3 Summary

In this chapter, I experimentally demonstrated that through manipulating the coordination number in amorphous silicon telluride (SiTe) alloys, the thermal conductivity can reach an ultralow value of ∼0.1 W m$^{-1}$ K$^{-1}$. It is observed that the thermal conductivity decreases with coordination number in SiTe and reaches its minimum near the rigidity threshold where the coordination number is 2.2-2.6 with tellurium concentration of 90-70%. The ultralow thermal conductivity of *a*-$Si_{20}Te_{80}$ is attributed to the strong localization of heat carrying modes evident by a large shift in mobility edge - a factor of five - towards lower frequencies.

# Chapter 7

# Bidirectional Thermal Conductivity Switching

In this chapter, I investigate the mechanism of crystalline-to-crystalline phase transformations. Through experimental measurements, I demonstrate that manipulating phonon scattering rate can switch thermal conductivity of antiferroelectric $PbZrO_3$ bidirectionally by -10% and +25% upon applying electrical and thermal excitation, respectively. For this, in order to apply a rapid thermal excitation and raise the temperature of the sample hundreds of degrees above room temperature, I integrate an additional heater beam with TDTR pump-probe. Further, through extensive characterization and modeling, I delve into the underlying reasons behind bidirectional thermal switching of $PbZrO_3$. I will show that bidirectional thermal conductivity switching in $PbZrO_3$ occurs as a result of separate phase transformation mechanisms that alter the phonon scattering rate in different manners. The goal of this chapter is to demonstrate that $PbZrO_3$ can serve as a fast ($<$1 second), repeatable, simple trigger, and reliable thermal switch with a net switching ratio of nearly 38% from $\sim$1.20 to $\sim$1.65 W m$^{-1}$ K$^{-1}$.

## 7.1 Background

Dynamic control over heat flow in solid-state materials has a wide range of applications from the nanoscale, where enhanced temperature stabilization in electronic devices [263, 264] and boosted efficiency of thermoelectric generators [265, 266] have been demonstrated, to the macroscale, where thermal control systems are mandatory for many space-exploration technologies [8, 9, 12]. The ability to change the thermal conductivity ($k$) of a material "on-demand" has gained significant traction in recent years, with research efforts focused on materials and mechanisms that enable large on/off switching ratios ($k_{high}/k_{low}$), fast modulation between the two states ($<$ seconds), and trigger mechanisms that can be easily accessed in solid-state architectures (e.g., no moving parts). With developments in materials science and thermometry techniques, several material systems have been discovered with thermal-switching behavior under different stimuli such as electrical [267], thermal [41], electrochemical [268, 269], optical [270], magnetic [271], strain [272], and even hydration [273]. Although some of these materials provide large switching ratios (up to an order of magnitude), their complicated trigger mechanisms and the associated switching timescale limit their applications. For instance, most recently Lu et al. [268] demonstrated the thermal conductivity of $SrCoO_{2.5}$ can be bidirectionally tuned by nearly $10\pm4$-fold via electrochemically oxygenating and hydrogenating the film. Although their reported switching ratio is significant, it occurs over a time span of several minutes and degrades over multiple switching cycles. In addition, the use of a liquid/gel electrolyte for enforcing the electrochemical reaction adds further complication to integrating the thermal switch into many device architectures.

A promising class of material candidates for dynamic thermal conductivity switching that have recently received considerable attention due to their fast, repeatable, and well-integrated trigger mechanism are ferroelectric (FE) perovskites, such as lead zirconate titanate $PbZr_{1-x}Ti_xO_3$ (PZT) and lead titanate $PbTiO_3$ (PTO) [267, 274, 275]. In these FE materials, the application of a sufficiently large electric field alters the ferroelectric domain structure and the corresponding domain wall population densities. The thermal conductivity of these FE solids is dominated by phonons and any variations in their domain wall density could potentially impact their scattering rate and change their thermal conductivity. In this regard, it has been shown that in ferroelectric $BiFeO_3$ the thermal boundary conductance between the domains is lower than that of grain boundaries and results in strong scattering of vibrational modes [276]. Later, Ihlefeld et al. [267] showed the thermal conductivity of $PbZr_{0.3}Ti_{0.7}O_3$ / $PbZr_{0.7}Ti_{0.3}O_3$ bilayers, deposited on silicon substrates moderately decreases by 11% upon application of electric field; their observation was attributed to an increase in domain wall density and a corresponding increase in the phonon-boundary scattering rate. In a different approach, Foley et al. [277] showed the thermal conductivity of suspended PZT membranes could be increased by 13% with electric field biasing. In this geometry, the ferroelectric film is not mechanically clamped to the substrate, which allows the domain size to increase and *reduce* the phonon-boundary scattering rate. In another work, Langenberg et al. [272] showed thermal conductivity of epitaxially grown PTO with high domain wall density is 61% lower than that of the single-domain film. More recently, through first-principles simulations, Liu et al. [278] showed that the thermal conductivity of PTO can be bidirectionally tuned by applying electric fields of opposite polarities. Although, they attributed the bidirectional thermal switching to a combined change in the unit-cell structure and domain-wall response, previous experimental works on ferroelectric materials such as PZT as well as the current study, found that the thermal conductivity changes uni-directionally upon application of electric field of opposite polarities [267, 277].

Despite the large focus on investigating the thermal conductivity of PZT with varying conditions, its antiferroelectric (AFE) end-member, lead zirconate $PbZrO_3$ (PZO), has received much less attention. In this material, a sufficient electric field will transition the antiferroelectric phase (orthorhombic space group *Pbam*) to a ferroelectric phase (rhombhohedal space group *R*3*m*), where there is a volume expansion, reduction in the unit-cell size from 8 formula units to 6, and the possibility of altering the populations of ferroelastic domains [279]. Furthermore, these ferroelastic domains within antiferroelectric PZO may directly impact phonon scattering rates. In addition to the AFE-to-FE phase transition, PZO undergoes another phase transition upon heating, transitioning from antiferroelectric to paraelectric (PE), where the lattice structure goes from 8 formula units to 1 (cubic space group $Pm\bar{3}m$), and thus may be expected to reduce the phonon scattering rate and lead to higher thermal conductivities.

The application of PZO in functional devices relies heavily on the ability to maintain and regulate the material's temperature; for example, both the pyroelectric [280] and electrocaloric [281, 282] efficiency of PZO are highly temperature-sensitive quantities. In this work, I aim to fill this void in literature by investigating both the temperature-dependent thermal conductivity as well as the electric-field dependence of PZO thin films in both polycrystalline and epitaxial embodiments. In particular, I demonstrate how the thermal conductivity of an antiferroelectric solid, PZO, can be bidirectionally switched between low- and high-thermal conductivities using electrical and thermal excitation, respectively. I show that the thermal conductivity of PZO decreases by 10% via domain restructuring during electrical biasing and can be increased by up to 25% upon heating; the combination of these mechanisms allows for thermal conductivity switching of $\sim$38%, which is significantly larger than previously reported switching in PZT and PTO [267, 274, 277].

## 7.2 Results

The results presented in this chapter are categorized into two separate sections. In the first section I discuss the sample preparation plus its corresponding characterizations and in the second section I present the thermal conductivity measurements and interpretation of the experimental data.

### 7.2.1 Sample Preparation

Epitaxial PZO thin films were grown to a thickness of 60 nm on a 15 nm $SrRuO_3$-buffered $DyScO_3$ (110) substrate using established pulsed laser deposition (PLD) proce-

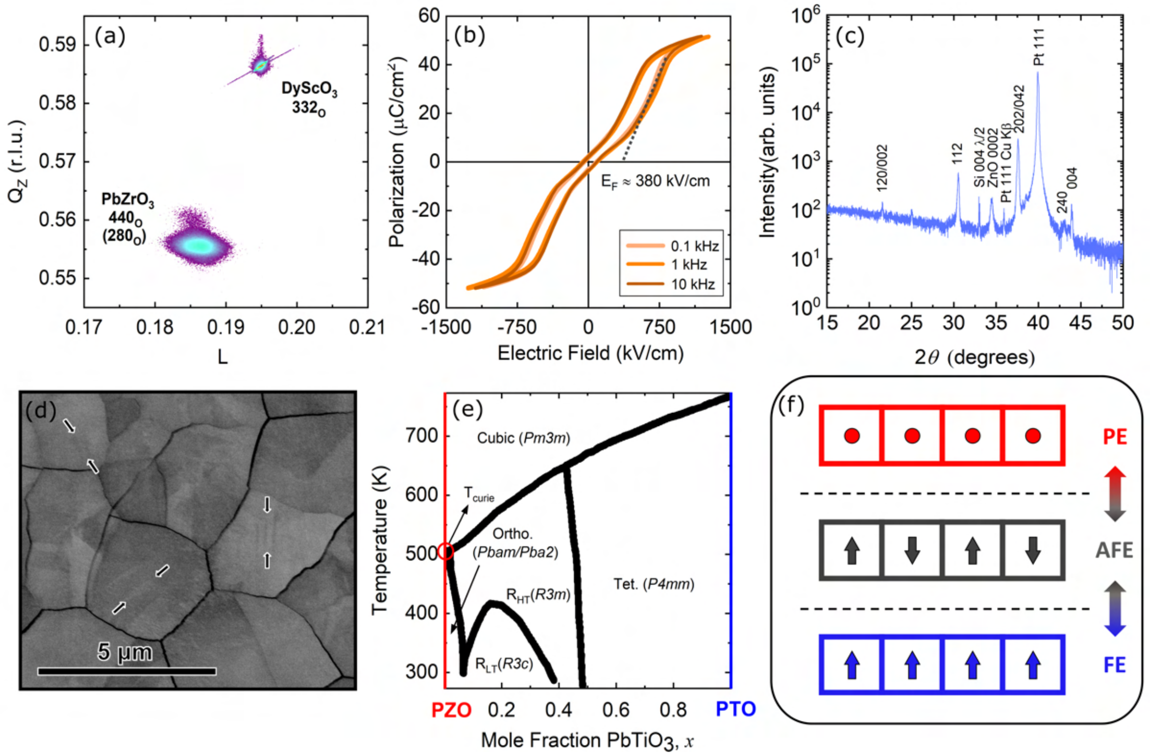

Figure 7.1: Structural phase transformations in PZO upon electrical and thermal stimuli. (a) Reciprocal space map of the $PbZrO_3$ 440/$280_O$ and $DyScO_3$ $332_O$ reflections demonstrating epitaxial growth and the presence of ferroelastic domains in the epitaxial film. (b) Polarization-electric field hysteresis response for the epitaxial $PbZrO_3$ film showing antiferroelectric switching. (c) $2\theta$-$\omega$ XRD pattern for the polycrystalline $PbZrO_3$ film. (d) Channeling-contrast backscatter electron micrograph of the polycrystalline $PbZrO_3$ film. The arrows indicate the locations of clearly resolved ferroelastic domains. (e) Phase diagram for lead zirconate titanate ($PbZr_{1-x}Ti_xO_3$, PZT) recreated from Ref [283]. (f) schematic of dipole orientation across antiferroelectric to ferroelectric (AFE-to-FE) and antiferroelectric to paraelectric (AFE-to-PE) phase transitions.

dures detailed in a previous work by Gao et al. [284]. 25 $\mu$m diameter with thickness of 80 nm $SrRuO_3$ contacts were patterned on the PZO film to serve as electrical contacts and transducers for thermal measurements. In addition, polycrystalline PZO films were prepared to a thickness of 300 nm via chemical solution deposition (CSD) on a 100 nm Pt/40 nm ZnO/300 nm $SiO_2$/(001) Si substrate. Au and Al transducer metals were deposited on the polycrystalline PZO with thicknesses of 80 nm via e-beam evaporation. Figure 7.1(a) shows a reciprocal space map taken on the epitaxial film. The film is $(120)_O$ oriented where $O$ denotes orthorombic phase (i.e., the film $[120]_O$ is parallel to the substrate normal

$[110]_O$) and exhibits (expected) 90° structural domains as indicated by the presence of $440_O$ and $280_O$ diffraction peaks. A polarization-electric field, P(E), hysteresis loop is shown for this film in Fig. 7.1(b) and reveals antiferroelectric response with an AFE-to-FE transition at ∼380 kV/cm. Figure 7.1(c) shows the $2\theta$-$\omega$ XRD pattern for the polycrystalline film. The film is phase-pure without pyrochlore or PbO secondary phases. The higher intensity of the $202/042_O$ reflection suggests that the film has a preferred crystallographic texture. A channeling-contrast backscatter scanning electron micrograph of the polycrystalline film is shown in Fig. 7.1(d). The average grain size is 3.3 $\mu$m and some ferroelastic stripe domains were observed, as indicated by the arrows. The ferroelastic domain wall spacing varies, but appears to be on the order of 200 nm and are much larger than those in the bilayer PZT films in a prior study on thermal conductivity switching [267]. Figure 7.1(e) shows the phase diagram for lead zirconate titanate ($PbZr_{1-x}Ti_xO_3$, PZT) [283]. According to this diagram, the PZO would undergo an antiferroelectric to paraelectric phase transition at elevated temperature near ∼500 K. The schematic in Fig. 7.1(f) shows the orientation of dipoles across two various phase transition in PZO upon electrical (AFE-to-FE) and thermal (AFE-to-PE) excitation.

### 7.2.2 Temperature Rise due to Optical Heating

For rapid heating of PZO, I implement an additional laser beam into the TDTR system to rapidly deliver large thermal energy locally. For estimating the temperature profile due to laser heating, a precise knowledge of parameters such as heater spot size, deposited power, surface absorption, and the thermal properties of the underlying layers are necessary. For measuring the heater beam size, chalcogenide-based phase-change material $Ge_2Sb_2Te_4$ (GST) is used that undergoes a structural phase transition under thermal excitation. The phase transition from an amorphous to a crystalline phase is initiated at nearly 150 °C where its thermal conductivity increases by almost a factor of three and upon further heating can change by almost an order of magnitude [16, 195]. By initiating this temperature-induced phase transition in GST with the optical heating source, a permanent spatially-dependent thermal conductivity pattern is formed. I then characterize this pattern, and thus determine the laser-heating profile, using a recently-developed thermal conductivity mapping technique [285]. For this, I take a sample with a 40-nm-thick amorphous GST film deposited on a silicon substrate and shine the heater laser with 740 mW power on its surface, which is coated with 60 nm of ruthenium (60 nm Ru/5 nm W/40 nm GST/5 nm W/Si). Subsequently, upon spatially mapping the thermal conductivity of the heated region and based on the changes in thermal conductivity [286], the spot size of the heater laser can be determined. The result of thermal conductivity map (Fig. 7.2(a)) shows a change from $\sim$0.15 W m$^{-1}$ K$^{-1}$ at the unheated area to $\sim$1 W m$^{-1}$ K$^{-1}$ at the center of the beam. By fitting a Gaussian distribution to the thermal conductivity data, Fig. 7.2(b),the heater diameter are determined to be 7.6 $\mu$m at 1/e$^2$. To further assess this critical aspect of laser-heating calibration, I also perform knife-edge measurement to determine the beams spot sizes which a good agreement between the two methods is found.

In order to estimate the temperature distribution profile as a result of laser heating, I turn to finite-element simulations using COMSOL Multiphysics. For this, a 2D axisymetric configuration is considered in cylindrical coordinates (Fig. 7.2(c)) with an adiabatic boundary condition at the top surface and open boundary condition at the side and the bottom of the computational domain. In order to ensure the domain size is sufficiently large, I choose the height and the radius of the simulation domain to be 30× the heater size. In order to ensure the size and grid independence of the simulations, I perform simulations at larger domain size (100×) and finer mesh and find negligible change in the results ($<$0.1%). A Gaussian-shaped beam is selected for the heat source with diameter similar to the measured value (7.6 $\mu$m). In order to verify my simulation results, I select a commonly used material for calibration, quartz (c-$SiO_2$), and experimentally measure its thermal conductivity as a function of laser power. I then use my model to estimate the temperature gradient across the sample. It must be noted that the probe beam in this study is not sufficiently smaller than the heater laser to allow constant properties assumption in the probed region. Therefore, the measured thermal conductivity is a weighted average of the thermal conductivity

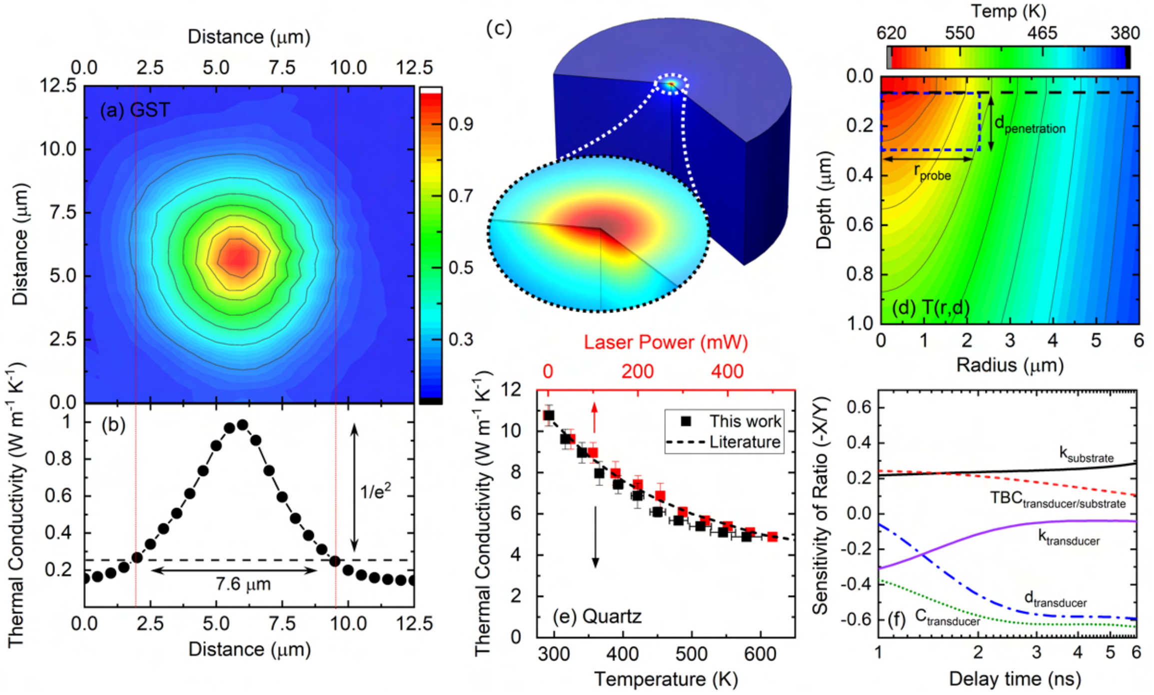

Figure 7.2: Thermal conductivity and temperature profile as a result of localized heating source from a laser beam. (a) Thermal conductivity map for a blanket coated sample with 60 nm ruthenium on 40 nm thick phase change material ($Ge_2Sb_2Te_4$) on silicon substrate exposed to heater laser with 740 mW. (b) Thermal conductivity profile of phase change material as a function of distance. (c) Simulation domain for Al/Quatrz and its corresponding temperature rise, (d) 2D temperature profile in the quartz and the region probed by TDTR beam, (e) Thermal conductivity of quartz as a function of temperature and laser power. The x-axis and y-axis uncertainty is calculated based on standard deviations in temperature of probed volume and thermal conductivity measurement of 3 different spots, respectively. (f) Sensitivity analysis for the 80 nm SRO-transducer/60 nm PZO/15 nm SRO/DSO-substrate configuration for parameters such as thermal conductivity, $k$, volumetric heat capacity, $C$, thermal boundary conductance, TBC, and thickness, d.

gradient in the probed volume. To correctly account for this, I assume a cylindrical probed volume with radius and height similar to that of the probe and the thermal penetration depth of the probe beam ($d_p = \sqrt{k/\pi f C}$), with $k$ as the thermal conductivity, $f$ as the modulation frequency, and $C$ as the volumetric heat capacity. The probed region is demonstrated as the blue dashed rectangular in Fig. 7.2(d). Using this approach, the thermal conductivity of quartz as a function of the mean temperature within probed region is presented in Fig. 7.2(e), which shows reasonable agreement with the literature.

### 7.2.3 Reciprocal Space Mapping

To confirm a phase transformation upon heating, reciprocal space map measurements have been performed on the epitaxial $PbZrO_3$ film from 300 to 523 K, as show in Fig. 7.3. Example data collected around the $DyScO_3$ 332 reflection is shown below as well as the $PbZrO_3$ $450_O$ reflection. The intensity of the $450_O$ reflection decreases with increasing temperature as the displacements of oxygen and lead ions from their lattice positions increase with temperature. It should be noted that the displacements, particularly of lead, have been shown to be much larger than typical thermal displacements and lead to local disorder [287]. The $450_o$ reflection is one that is not present in the cubic phase and is due to large orthorhombic unit cell of the antiferroelectric phase. Likewise, the $PbZrO_3$ $440_O$ and $280_O$ orthorhombic reflections visible between 300 and 423 K merge to a single $013_c$ (where $c$ denotes cubic) reflection between 473 and 523 K, which further confirms transition to the higher symmetry cubic structure at elevated temperatures. The return of the $450_O$ reflection and splitting of the $440_O$ and $280_O$ reflections after cooling to room temperature emphasizes the reversibility of the AFE-to-PE phase transformation. As a result, the structural evolution from 300 to 523 K in $PbZrO_3$ is a reversible transition from the antiferroelectric to the paraelectric phase, consistent with thermal conductivity measurements presented in the subsequent section.

The structural phase transition upon heating (AFE-to-PE) in PZO results in a higher symmetry crystal structure and should lead to less phonon-phonon scattering [288]. As a result, one would expect to observe an increase in the PZO thermal conductivity upon transitioning into the paraelectric phase. Although there is extensive research on the origin on the antiferroelectricity in PZO [289–291], the effect of field and thermal perturbation on its thermal conductivity is limited in the literature. Motivated by this, I am prompted to investigate how electric field and temperature affect the PZO thermal conductivity. In the following, I will first demonstrate how the thermal conductivity of the PZO changes upon application of electric field. Then I present the temperature-dependent thermal conductivity data for epitaxial and polycrystalline samples using resistive heating. Once it is shown that

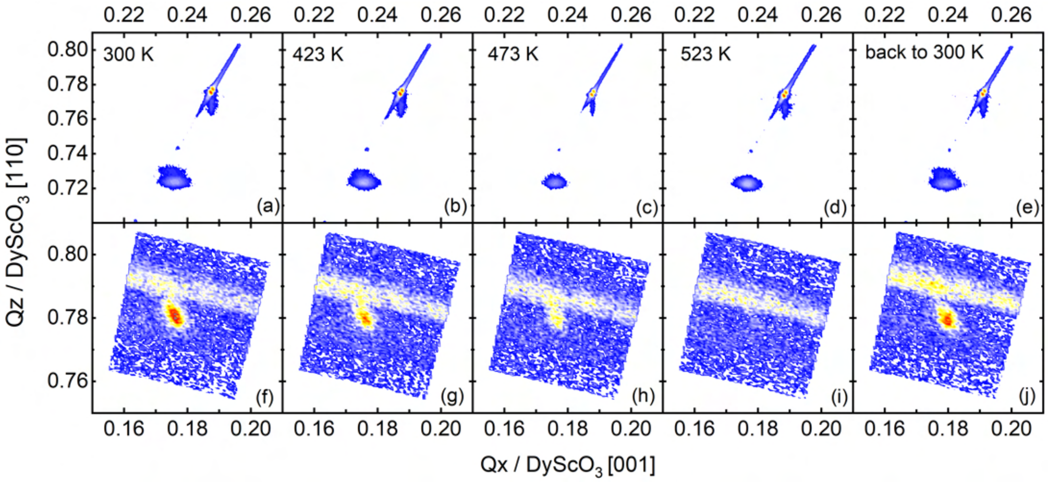

Figure 7.3: Reciprocal space maps at different temperatures to confirm antiferroelectric to paraelectric (AFE-to-PE) phase transition. (a)-(e) show maps collected about the $DyScO_3$ 332 reflection and (f)-(j) show maps collected for the $PbZrO_3$ $450_o$ reflection. The $450_o$ reflection disappears between 473 and 523 K while the $440_o$ and $280_o$ reflections merge to a single peak above 423 °C. These data confirm that the antiferroelectric to paraelectric transformation in epitaxial $PbZrO_3$ occurs between 473 and 523 K. The streak denoted as the PEEK dome in (f)-(j) is a reflection from the protective dome on the hot stage and not part of the sample stack.

the thermal conductivity of the PZO increases with temperature, I turn to laser heating experiment and show thermal conductivity dependence with respect to the laser power. Finally, I will show how the electric field and optical heating can be used to switch the thermal conductivity of PZO between various states.

## 7.3 Thermal Conductivity Measurements

In order to determine the thermal conductivity of epitaxial PZO from TDTR data, a two-layer model (transducer-substrate) is considered, where the 60 nm PZO film is treated as an interfacial layer. Figure 7.2(f) shows the sensitivity of these measurements to various parameters considering a two-layer model. According to this, the TDTR measurements are highly sensitive to the volumetric heat capacity and the thickness of the transducer. The volumetric heat capacity of the transducer is obtained from literature and the uncertainty is calculated based on the transducer thickness. To increase sensitivity of the measurements to the thermal conductivity of PZO film, additional measurements are performed on 300 nm polycrystalline PZO as a function of temperature. For consistency in the analyses of the results between field and thermal effects, constant values for heat capacity and transducer thickness are assumed as a function of temperature and fit for the thermal boundary conductance ($\mathrm{TBC}_{\mathrm{transducer/substrate}}$) and substrate thermal conductivity ($\mathrm{k}_{\mathrm{substrate}}$) as a function of varying laser power; note, as the volumetric heat capacity of both the SRO transducer and DSO substrate increase with temperature [292, 293], this method likely leads to a slight underprediction of the increase observed in thermal conductivity upon heating.

### 7.3.1 Substrate Effects

In this subsection, I show that the thermal conductivity measurement of 60 nm thick PZO is independent of changes in the thermal conductivity of substrate. Clearly, temperature variations can lead to changes the thermal conductivity of substrate and create a fictitious increase or decrease in the thermal conductivity measurements. I investigate this by separately measuring the thermal conductivity of DSO substrate as a function of temperature. Figure 7.4(a) shows the experimental data with its corresponding theoretical fit at room and elevated temperatures. As depicted in Fig. 7.4(b), the thermal conductivity of DSO substrate slightly decreases at high temperatures which is in great agreement with previous studies [293]. This indicates that, if the measured thermal conductivity of PZO was affected by the substrate, a reduction in the thermal conductivity must be observed. As will be shown in the subsequent subsection, unlike DSO, the thermal conductivity of PZO increases with temperature which is an indicative of the independence of the measurements from that of the substrate. The increase in thermal conductivity of PZO is further supported by the measurement of a thicker film (300 nm) polycrystalline PZO that was deposited on a Si substrate. Similarly, identical substrates were used in a previous study for PZT films and no spurious increases in thermal conductivity were observed.

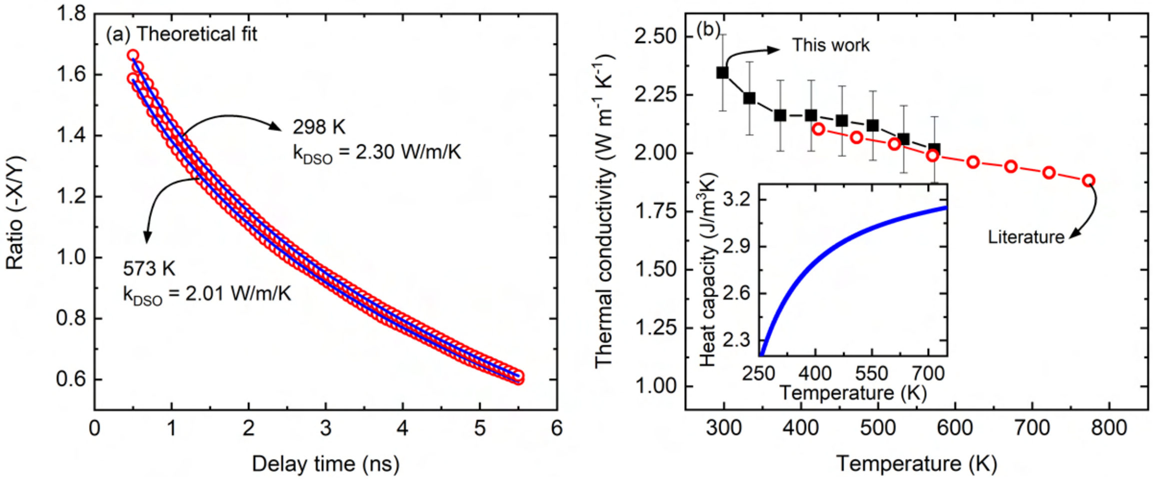

Figure 7.4: (a) Experimental data and the theoretical fit for thermal conductivity measurements at room temperature and 573 K. (b) Thermal conductivity of DSO substrate as a function of temperature. The uncertainty is calculated based on 10% variations in the transducer thickness. The inset shows the heat capacity of DSO estimated using equation provided in Ref. [293]

.

### 7.3.2 Electrical Biasing

As discussed earlier, the switching behavior in thermal conductivity has been observed previously in $PbZr_{0.3}Ti_{0.7}O_3$/ $PbZr_{0.7}Ti_{0.3}O_3$ ferroelectric bilayers which was attributed to the formation of new ferroelastic domains under applied electric field leading to increases in the domain-boundary density [267]. The changes in the domain boundary populations are on the order of hundreds of nanoseconds and enables ultrafast switching of these materials [294]. The increased boundary area between the domains results in a greater phonon-boundary scattering leading to a reduction in thermal conductivity upon the application of an electric field. As shown in Fig. 7.1(b), with the application of fields greater than $\sim$380 kV cm$^{-1}$, the AFE phase of the epitaxial film transforms into a ferroelectric phase. The same field required for that transformation is the onset of the decrease in thermal conductivity, which suggests that the decrease is related to the phase transition. It is postulated that upon transitioning to the ferroelectric phase, new ferroelastic domains form with an accompanying increase in ferroelastic domain boundary area, which increase the phonon scattering rates and decreases thermal conductivity. This is consistent with the decrease observed in thermal conductivity of PZO upon application of electric field similar to those of PZT and may be expected because the film is clamped to a mechanically rigid substrate.

In order to determine the effects of electrical bias on thermal conductivity, an electric field is applied across 60 nm of PZO deposited on a $DyScO_3$ (DSO) substrate and its thermal conductivity is measured as a function of voltage. For applying electric field in the cross-plane direction across the PZO, the film is deposited on 15 nm of $SrRuO_3$ which serves as the bottom electrode, and subsequent to PZO deposition, circular electrical contacts (80 nm of $SrRuO_3$) are deposited on top of the PZO layer to serve as the top electrode (see inset in Fig. 7.7c). These results are presented in Fig. 7.7(a) showing that the thermal conductivity drops by nearly 10% upon applying positive/negative electric field and immediately returns to its original state after removing the electric field. This is consistent with what one would expect for an antiferroelectric material which returns to its original non-polar state upon elimination of electric field.

In order to provide some insight into the observed changes in thermal conductivity as a function of electric field, I use a Callaway-type model [295] that is widely used to estimate the thermal conductivity of crystalline materials [39, 40, 296–299]. Using this, I provide an estimation for thermal conductivity of PZO with respect to electric field:

$$\kappa = \frac{k_\mathrm{B}}{2\pi^2 v} \int_{k_\mathrm{B}\Theta_\mathrm{D}/\hbar}^{0} \tau \frac{\hbar^2 \omega^2}{k_\mathrm{B}^2 T^2} \frac{e^{\hbar\omega/k_\mathrm{B}T}}{(e^{\hbar\omega/k_\mathrm{B}} - 1)^2} \omega^2 d\omega, \tag{7.1}$$

where $k_B$ and $\hbar$ are the Boltzmann's and Planck's constants, respectively, $v$ is the speed of sound, $\Theta_D$ is the Debye temperature, $\tau$ is relaxation time, $\omega$ is the vibrational modes frequency, and T is temperature. The relaxation time from different scattering mechanism such as Umklapp, defect, and boundary scattering can be estimated via Matthiessen's rule:

$$\tau^{-1} = A\omega^4 + B\omega^2 T e^{-C/T} + v/d, \tag{7.2}$$

where $d$ is the scattering length scale, and *A, B,* and *C*, are the scattering coefficients for impurity scattering (A$\omega^4$) and Umklapp scattering (B$\omega^2$ Texp$^{(-C/T)}$). Pertinent to this study, since the domain wall density increases upon electrical biasing, the scattering length scale (*d*) is adjusted to match the thermal conductivity measurements. For this, the scattering length scale are set to the same size as the domains in PZO and fit *A, B,* and *C* to the experimental data as a function of temperature as shown in Fig. 7.5. According to Gao et al. [284], the antiferroelectric domains in PZO film are oriented at 90°and display correlation lengths on the order of 3 and 30 nm for the [$\bar{1}$01] and [101] orientations, respectively. Assuming $d$ = 3 and 30 nm, I fit for *A, B,* and *C*. Once, these scattering coefficients are determined, it is calculated how much the scattering length scale *d* must change upon electrical biasing to match the experimental observations. According to these calculations, in order to reduce the thermal conductivity of PZO by ∼10% for 3 and 30 nm domain size, *d* must change by 18% and 20%, respectively. This degree of change in scattering length scale is not far from reason, and in fact, is comparable to previously reported values (10%) regarding percentage of change in the domain wall density for ferroelectric materials [267].

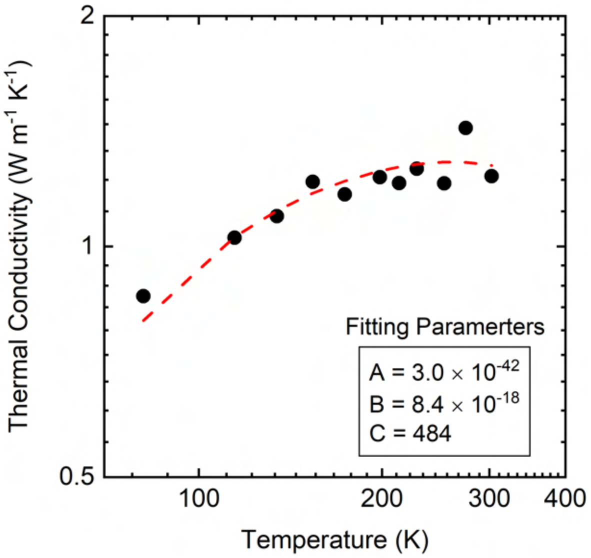

Figure 7.5: Measured thermal conductivity of PZO as a function of temperature. The dashed shows the Callaway-type model's fit for the domain size of 3 nm.

With regards to the disagreement in the measured thermal conductivity between the bulk and thin film samples, I should mention that I contacted several vendors to purchase high-quality PZO in bulk and we found it impossible to find a company that makes 100% high quality bulk PZO with no porosity and defects. Nonetheless, to investigate our hypothesis regarding the existence of porosity and impurities in our bulk PZO, SEM and EDS measurements were performed on the bulk sample. A comparison between the bulk and the epitaxial PZO is presented in Fig. 7.6. According to these results, we found that not only a significant degree of porosity exists in our measured bulk PZO as depicted in following figure but also, traces of Ti impurities and non-stoichiometry is present in the bulk sample. Pure $PbZrO_3$ should be 20 mole percent Pb, but this ceramic was closer to 19 mole%. On the other hand, the PZO films made for this study are epitaxially grown and the balance of Pb vaporization and Pb flux during growth results in improved stoichiometry films. Furthermore, the epitaxial films have a very high degree of crystallinity and crystal perfection. In the light of these evidences, it is impossible to compare our thermal conductivity results for thin films with that of the bulk ceramics to which we have access. This discussion is added to the Supporting information.

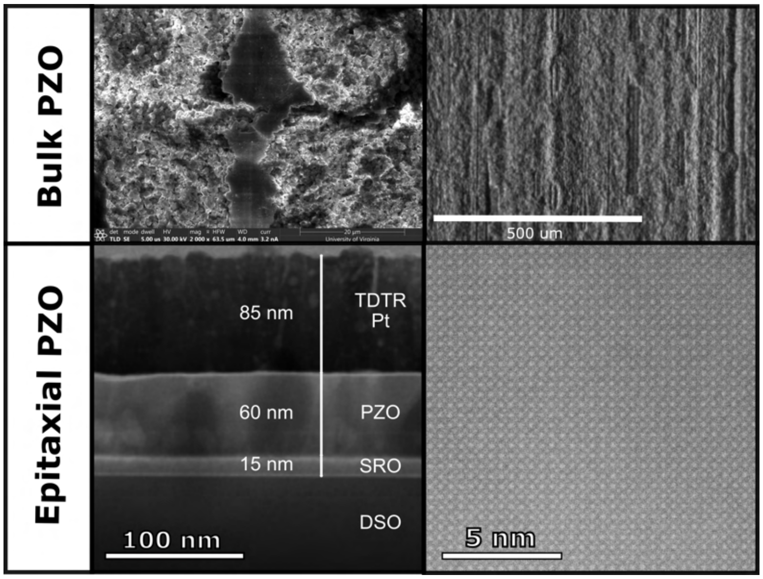

Figure 7.6: Microstructure in bulk and epitaxial PZO. The bulk PZO shows a large porosity as well as non-stoichiometric compound in its structure.

### 7.3.3 Resistive Heating

Figure 7.7(b) shows the thermal conductivity of the epitaxial and polycrystalline PZO samples as a function of temperature. For these measurements, constant properties at room temperature are assumed with specific heat of 2.52 MJ $m^{-3}$ $K^{-1}$ for polycrystalline PZO taken from Ref. [300]. The thermal conductivity of PZO follows a glass-like behavior at low temperatures and plateaus above 200 K. Above room temperature, the thermal conductivity gradually increases with temperature up to $\sim$500 K where the PZO transitions from an AFE-to-PE phase leading to an increase in thermal conductivity from $\sim$1.30 to $\sim$1.65 W $m^{-1}$ $K^{-1}$. This trend is observed across multiple samples with different microstructures, thicknesses, and transducers as presented in Fig. 7.7(b). The smoothly increasing thermal conductivity is unusual for a highly crystalline material and shows that the complex octahedral tilts and lead ion displacements in $PbZrO_3$ lead to high phonon scattering rates. Upon transitioning to the cubic phase, the material becomes globally cubic; the octahedral tilts cease to exist. This cubic symmetry leads to an increase in the thermal conductivity. The increase in thermal conductivity, however, is likely smaller than one would anticipate for such a dramatic change in crystal symmetry (i.e. an 8X reduction in unit cell volume). The existence of local lead-ion disorder, which occurs on the lengths scales of phonon wavelengths, impacts the overall achievable thermal conductivity in the cubic phase.

This increase in thermal conductivity is related to the structural transition to a higher symmetry crystal structure in the PZO. As shown in the previous section, the complex orthorhombic unit cell of PZO at room temperature transforms into a cubic unit cell above the phase-transition temperature. This transition into a simpler, higher symmetry cubic crystal structure reduces the number of atoms (N) in the conventional unit cell and, as a result, leads to less phonon scattering [288]. In addition to reciprocal space mapping, the phase transition in PZO for both epitaxial and polycrystalline is confirmed using scanning transmission electron microscopy (STEM). The lower magnification image shown in Fig. 7.7 (d) shows the layers in the epitaxial PZO sample. High-resolution Z-contrast images and selected-area diffraction patterns (SADP) as presented in Figs. 7.7(e,f) show that the

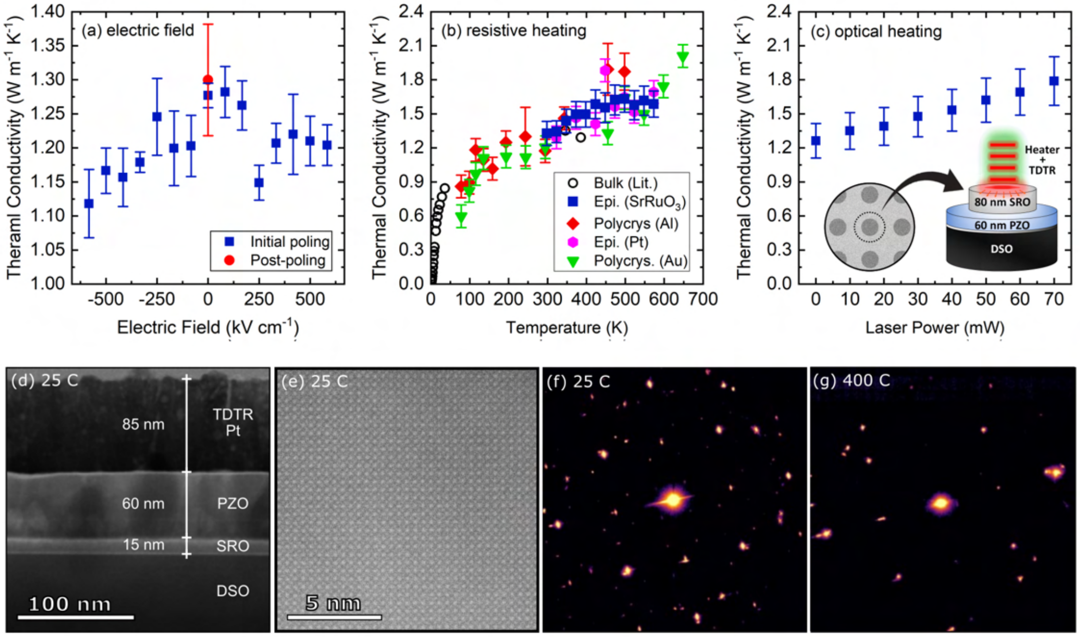

Figure 7.7: Thermal conductivity of PZO upon phase transformation as a result of electric field and thermal stimuli. (a) Thermal conductivity as a function of electric field for PZO measured at room temperature. (b) Thermal conductivity as a function of temperature measured on a resistive heating stage. The uncertainty in **a,b** is based on standard deviation across multiple scans. (c) Thermal conductivity as a function of laser power. The uncertainty in **c** is calculated based on 10% variations in the transducer thickness and the inset shows the schematic of the layer configuration studied here. (d) Annular bright-filed STEM image showing the corresponding layers in the epitaxial PZO at room temperature, (e) and the high resolution TEM showing the high degree of order in the studied sample. Selected area diffraction patterns of epitaxial PZO at (f) 25°C and (g) 400°C showing that the PZO film has undergone a phase transition from orthorombic space group *Pbam* to cubic $Pm\bar{3}m$.

grains are oriented with pseudo-cubic axes out-of-plane. Ordered reflections occurring in the room temperature SADP that indicate the presence of octahedral rotations disappear when the sample is heated to 400°C, as shown in Fig. 7.7 (f,g). The disappearance of the ordered reflections confirms the AFE-to-PE phase transition. In contrast to the AFE-to-PE phase transition observed here, thermal conductivity measurements on bulk commercial PZO using transient plane source technique show no change in thermal conductivity above room temperature which is due to existence of porosity and impurity in the bulk sample.

### 7.3.4 Optical Heating

High-temperature measurements are repeated using a focused laser source to locally heat the PZO and measure the thermal properties within the laser-heated region. For this experiment, I use epitaxial 60 nm PZO and perform the experiment on the SRO contacts. Unlike resistive stage heating where the entire sample is raised to the temperature of interest, laser heating creates a temperature gradient across the sample where the maximum temperature is on the surface and at the center of the focused laser spot. The existence of a temperature gradient in the heated area is closer to an actual device configuration and allows us to capture a more realistic change in thermal conductivity. Given that, after measuring the thermal conductivity as a function of laser power, similar to resistive heating, a gradual increase in thermal conductivity with laser power is observed. This gradual increase is consistent with the static temperature measurements where the continuously increase thermal conductivity with temperature was observed.

In order to determine the temperature rise in the case of PZO film, I turn to analytical model developed by Braun et al. [301]. The input parameters that goes into the model are absorption coefficient of the transducer $SrRuO_3$ at wavelength of 532 nm, the beam size (12 um), delivered power, and the multilayer stack properties. According to the literature, for 100 nm $SrRuO_3$ the absorption is near 80% [302]. Although the absorption of $SrRuO_3$ depends on the deposition process and the quality of the film, I take 80% as the upper limit for the absorption of $SrRuO_3$. Furthermore, the measured power is before the laser passes a few mirrors and the objective. Assuming 10% power drop from the measured point to the surface of the sample, the estimated temperature rises within the probed region for the 20, 40, and 60 mW is approximately 135, 271, and 406 K. This agrees with the observed trend in Fig. 7.8(b) in the main manuscript. Since the beam profile is Gaussian, there is a Gaussian temperature rise on the surface of the sample. This results in a formation of a temperature gradient in the in-plane direction.

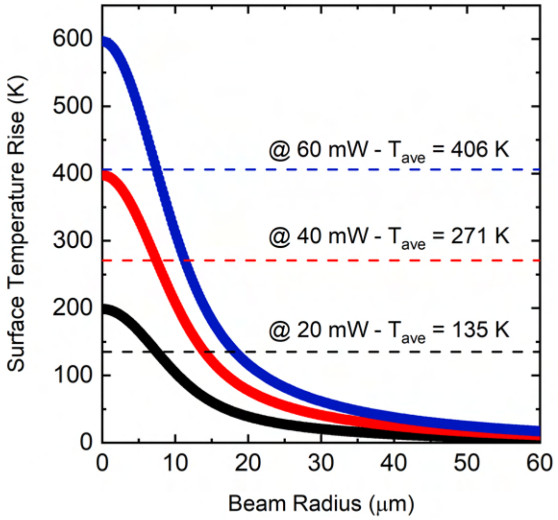

Figure 7.8: Temperature rise profile as a function of probe beam radius due to a Gaussian CW heater beam at different powers.

### 7.3.5 Thermal Conductivity Switching

So far, I demonstrated that the thermal conductivity of PZO decreases upon exposure to electric field and increases upon raising the temperature to the Curie temperature. Now, I demonstrate how these field and thermal effects can be used in tandem to create a bidirectional thermal conductivity switch. For this, electrical and optical excitation are periodically applied to the 60-nm-thick epitaxial PZO sample and switch the material between a low- and high-thermal conductivity states. Figures 7.9(a and b) show the switching mechanism in real time when the PZO is under periodic electric field and heating, respectively. For an electric field amplitude of 670 kV $\text{cm}^{-1}$ the thermal conductivity can be periodically decreased by nearly 10%. On the other hand, upon applying optical heating using a laser with spot size of 12 $\mu$m in diameter, the PZO thermal conductivity increases by nearly 25%. Figures 7.9(c, d) show this transition is repeatable for a number of cycles. Although switching thermal conductivity using electric field shows some drift from one cycle to another, this due to low sensitivity of the measurements to the film thermal conductivity rather than inherent changes in the film as a result of cycling or differing domain structures upon each field cycle. On the other hand, a small decay in thermal conductivity of PZO is observed as well as reflectivity signal after multiple switching cycles with the laser source, which is attributed to gradual degradation in the SRO transducer due to heating cycles.

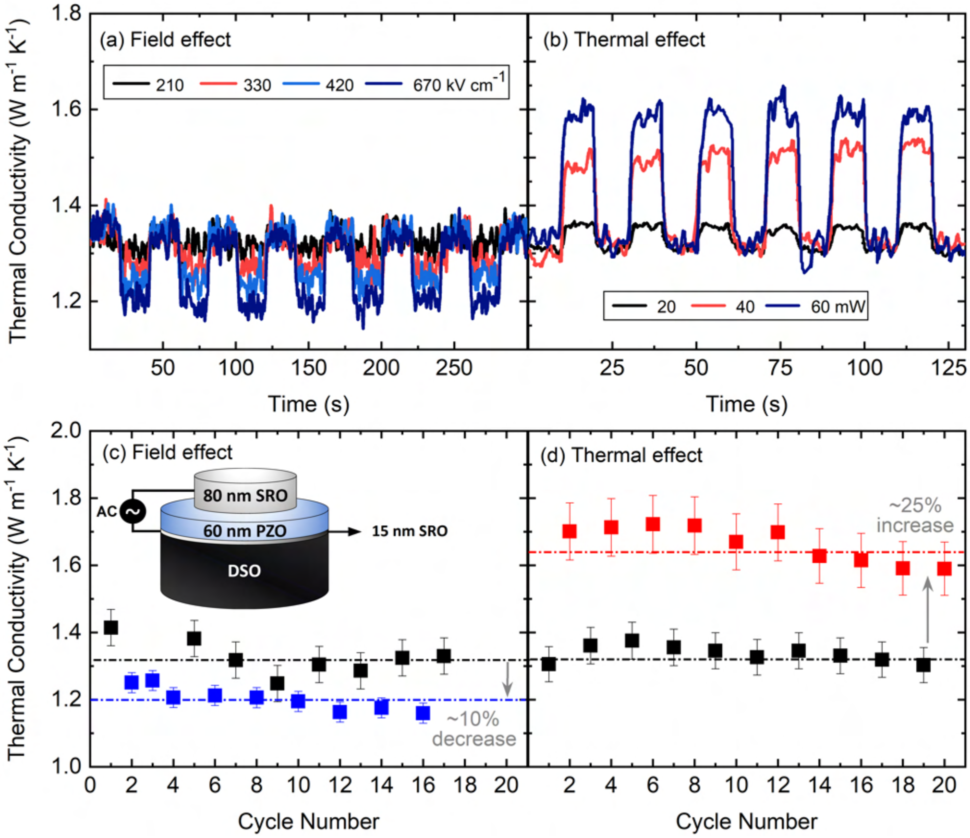

Figure 7.9: Real time switching of epitaxial PZO to high and low thermal conductivity using electrical and thermal stimuli. Switching thermal conductivity of PZO as a function of time measured at 500 ps delay time for (a) electric fields of 210, 330, 420, and 670 kV cm$^{-1}$, and (b) heater laser powers of 20, 40, and 60 mW. (c,d) Repeatability of switching thermal conductivity upon applying maximum electric field and laser power before damaging the sample. The dashed lines represent the weighted average of the data points corresponding to that line. These measurements were performed at a single location on the sample. The uncertainty is calculated based on 10% change in transducer thickness.

## 7.4 Summary

In this chapter, I demonstrated the thermal conductivity of antiferroelectric PZO can be bidirectionally switched by -10% and +25% upon application of electric field and thermal excitation, respectively. Similar to ferroelectric materials where application of electric field increases the domain wall density and reduces the thermal conductivity, it is observed that the thermal conductivity of antiferroelectric PZO decreases upon applying electrical bias. In addition, taking advantage of relatively low Curie temperature in PZO ($\sim$220°C) and upon using optical heating, orthorhombic to cubic phase transition can be triggered in PZO, which leads to higher crystal symmetry and increase in thermal conductivity. According to the results presented in this chapter, the net thermal conductivity switching ratio in PZO is around 38%.

# Chapter 8

# Concluding Remarks and Future Outlook

The human brain consumes as much energy as is needed to power a domestic light bulb, and yet, it is capable of outperforming state-of-the-art supercomputers by orders of magnitude both in energy efficiency and volume [303–305]. Consuming less energy not only reduces the computational costs but also eliminates complications such as heat generation and the formation of hot spots that deteriorate the device's performance and lifetime. Thus, it is important to design memories and processors with lower power consumption. Recently, it was shown that chalcogenide-based phase change materials are suitable candidates for constructing power-efficient phase-change random access memories (PRAM) or artificial neuromorphic systems [306]. In phase-change memory devices, the primary source of power consumption is the programming current that is used to induce phase transition. In the last decade, a number of breakthroughs on this front have pushed PCMs as the most promising technology for next-generation memory devices. Multiple approaches have been proposed to tackle the large power consumption in PCMs: (i) reducing the volume of the phase change unit [136], (ii) reducing the number of elements in the PCM composition [307], (iii) confining the motion of atoms to a single direction [125], and (iv) minimizing the thermal leakage from the memory cell to the surrounding materials [129].

In this dissertation, I attempted to tackle the power consumption issue in PRAM devices from a nanoscale thermal transport perspective. I demonstrated that through the use of low thermal conductivity electrodes such as $CN_x$, thermal leakage in memory devices can be greatly suppressed compared to conventional tungsten electrodes. The trade-off for using $CN_x$ electrode is higher electrical resistivity and potentially durability compared to tungsten. In addition to electrode materials design, I showed that through engineering the interfacial thermal conductance, heat can be efficiently isolated within the memory cell without the incorporation of any additional thermal barrier between the electrode and PCM. Further, I investigated the effect of partial substitution of selenium for tellurium in $Ge_2Sb_2Te_4$ on thermal properties and demonstrated that the energy transport transitions from an electron-dominated to a phonon-dominated regime. Another material that plays an important role in the thermal isolation of the memory cell is the selector device. Through detailed modeling, simulations, and experiments, I showed the specific composition of silicon telluride $a$-$Si_{20}Te_{80}$ has one of the lowest measured thermal conductivities amongst amorphous solids. Finally, using the knowledge gained from my previous work on phase change materials, I was able to lead a multi-institutional research collaboration for developing the first solid-state bidirectional thermal switch material using antiferroelectric lead zirconate ($PbZrO_3$). In the following, I will briefly discuss the major findings as a result of my Ph.D. work.

## 8.1 Summary and Major Findings

In chapter 2, the fundamental concepts and theoretical models concerning nanoscale thermal transport by conduction were presented. I reviewed the derivation of thermal conductivity for crystals and amorphous media based on the kinetic theory of gases. Further, the accuracy of the widely used Wiedemann-Franz law that relates the thermal conductivity of metals to their electrical conductivity is examined. These simple, yet insightful approximations have provided a powerful means in the subsequent chapters to interpret the experimental results. In chapter 5, for example, the Wiedemann-Franz formalism guided me to gain a better understanding of the mechanism of thermal transport in optical phase change materials and show that upon partial substitution of selenium with tellurium atoms, the thermal transport transitions from an electron-dominated to a phonon-dominated regime. Similarly, the thermal conductivity derived for amorphous and crystalline materials was used in chapters 6 and 7 to shed light on the mechanism of thermal transport across phase transformation.

In chapter 3, the details regarding the thermometry technique, in particular time-domain thermoreflectance, that has been employed throughout this dissertation and the pertinent data analysis were discussed. I reviewed some of the core concepts that enable the measurement of thermal properties at the nanoscale, such as thermoreflectivity and lock-in amplification. After presenting a step-by-step solution to the heat diffusion equation for a multilayer stack in the cylindrical coordinate, the details of signal processing and data acquisition were outlined. In addition, I presented some results related to the subsequent chapter to demonstrate the capabilities of TDTR in terms of thermal property measurements.

In chapter 4, energy transport processes across phase transformation in one of the most widely used phase change materials, $Ge_2Sb_2Te_4$, are investigated. The primary focus of this chapter is to develop techniques and methods to isolate heat within the memory cell in order to decrease power consumption. In this regard, in addition to a thorough study regarding the thermophysical properties of $Ge_2Sb_2Te_4$, I explored the ways thermal transport in memory cells can be manipulated by taking advantage of interfacial thermal conductance. This was accomplished by first identifying the length scale at which interfacial thermal transport plays a dominant role, and then determining the extent to which interfaces can suppress thermal transport. For instance, it was shown that the effective thermal conductivity of 20 nm $Ge_2Sb_2Te_4$ can be suppressed by a factor of four from 1.2 W m$^{-1}$ K$^{-1}$ in the thick film regime to 0.30 W m$^{-1}$ K$^{-1}$ due to the effect of resistances at the interfaces. Further, I demonstrated that as the thickness of $Ge_2Sb_2Te_4$ reaches below the carriers' mean free paths, the thermal transport transitions from a diffusive to a ballistic regime. For the case of 5 nm thick $Ge_2Sb_2Te_4$ sandwiched between tungsten electrodes, I showed that thermal conductance is almost a factor of two higher in the ballistic regime. The understanding obtained from this chapter would pave the way for more efficient and durable phase change memory devices.

In chapter 5, I investigated the extent to which the thermal transport mechanism changes as the tellurium atoms $Ge_2Sb_2Te_4$ are substituted by selenium. Using theoretical approximations such as phonon-mediate minimum limit, I demonstrated that the thermal conductivity of $Ge_2Sb_2Te_4$ in the crystalline phase is not expected to noticeably change upon Se substitution. Nonetheless, experimental measurements reveal that although thermal conductivity of the amorphous phase does not significantly change by substitution of Se, the thermal conductivity in the crystalline phase is a factor of two lower than that of the $Ge_2Sb_2Te_4$. Through theoretical models and experimental approaches, I showed that the electrons' contribution to the thermal conductivity of $Ge_2Sb_2Se_4Te$ is substantially suppressed. Since the optical bandgap of selenium is significantly larger than that of tellurium, this leads to reduced electron mobility in $Ge_2Sb_2Te_4$ and consequently lower electrical resistivity. I further supported this by a series of ultrafast mid-infrared pump-probe measurements that interrogated the electron and phonon relaxation times and showed a drastic reduction in the electronic lifetimes of $Ge_2Sb_2Se_4Te$, driving the thermal transport into a phonon-dominated regime.

In chapter 6, the thermal properties of the selector device, which is an integral component in phase-change memory architecture are investigated. For improved efficiency of the memory devices, materials with lower thermal conductivity are suitable candidates for this application. For this, a novel mechanism that leads to ultralow thermal conductivities in amorphous solids has been identified. I showed that through manipulating the atomic connectivity network in amorphous structures, the thermal transport in a representative amorphous alloy, silicon telluride $a$-$Si_{20}Te_{80}$ can be strongly suppressed. I show that existing predictive models for the thermal conductivity of amorphous media significantly over-predict the thermal conductivity of $a$-$Si_{20}Te_{80}$. However, the predictions from ab-initio molecular dynamics (AIMD) simulations, integrated with lattice dynamics calculations, show excellent agreement with experimental measurements. The ultralow thermal conductivity of $a$-$Si_{20}Te_{80}$ is attributed to reductions in coordination number and a transition from over-constrained to under-constrained glass network leading to strong localization of heat carriers, namely propagons and diffusons. As a result of the reduced number of pathways at which modes can interact with one another, a large shift in the mobility edge - a factor of five - towards lower frequency and the localization of nearly 42% of the vibrational modes is observed.

Chapter 7 was primarily focused on thermal transport across crystalline-to-crystalline phase transformations. Through experimental measurements, it was demonstrated that the thermal conductivity of antiferroelectric lead zirconate ($PbZrO_3$) can be *bidirectionally switched* by -10% and +25% upon applying electrical and thermal excitation, respectively; in other words, the heat flux can be either increased or decreased on-demand. This unique phenomenon is found to be enabled by an independent manipulation of the phonon scattering rates through differing external stimuli. Specifically, it was found that the antiferroelectric domains of $PbZrO_3$, and their corresponding domain wall densities, can be increased through electrical stimuli, leading to higher scattering of phonons. In addition, upon thermal stimuli, the crystal undergoes a structural phase transition from a low-symmetry orthorhombic to a high-symmetry cubic crystal structure, leading to less phonon scattering. As such, it was demonstrated that the thermal conductivity of $PbZrO_3$ can be tuned with a net switching ratio of 38% from $\sim$1.2 to $\sim$1.65 W $m^{-1}$ $K^{-1}$. To the best of my knowledge, not only did this chapter report the largest solid-state switching ratio in a purely phonon-dominated crystalline solid, but it is also the first to show an increasing thermal conductivity trend at the high-temperature limit for a highly ordered crystal.

## 8.2 Future Outlook and Opportunities

- **Thermal Transport in Phase Change Heterostructure**- In chapter 4 and 5, the details regarding the thermal transport of commonly used phase change materials in a homogeneous film structure (homostructure) were discussed. However, recently, it has been realized that confining the motion of atoms in one direction by forming a phase change heterostructure (TiTe/$Sb_2Te_3$) not only reduces the power consumption, but also significantly reduces the drift in collected signal between different switching cycles and improves the overall retention time. One important question that has not been addressed in these emerging phase change materials is the effect of interfaces on the overall thermal transport. For instance, what would be the optimum interface density for the best performance in these devices? What would be the optimum thickness for the bilayers? Or is there any size effect associated with each individual bilayer? As was shown in chapter 4, when the thickness of GST is around 5 nm, the thermal transport moves away from diffusive and transitions into a ballistic regime, which leads to higher thermal conductances. An in-depth thermal characterization in order to measure the interfacial thermal resistance as well as the thermal conductivity of each bilayer would greatly facilitate designing the next generation of these interfacial phase change materials.

- **Thermal Transport across Threshold Switching**- Silicon telluride $a$-$Si_{20}Te_{80}$ that was discussed in chapter 6 is a type of Ovonic threshold switch that undergo an electronic phase transition as a result of applied electric field. In this transition, the electrical resistivity of the material changes by orders of magnitudes, which has been the subject of investigation for decades. Although the changes in its electrical properties are an established research area, it is unclear how this phase transition would impact thermal properties. The obvious question here is: what is the thermal conductivity after threshold switching? The hypothesis around this question is that, if this transition is purely driven by electrons and the lattice structure remains intact, then depending on how much the electrical resistivity changes, it may or may not impact the thermal properties. Besides, this is all based on the assumption that after the phase transition, the material stays as an Ohmic and obeys the Wiedemann-Franz law. The experiment to measure the thermal conductivity of threshold switches upon phase transition is extremely challenging. For these types of measurements, a sample geometry that requires lithography to create small circuits is required. In addition, the circuit electrical pathways must align with the thermal conductivity measurement direction so that the changes in the electrical resistivity can be captured. On top of all these, the sample cannot be held above transition for an extended period of time (typically $<$100 ms) which requires the use of a modulated electrical field in order to avoid damaging the film. Although the experiment is challenging, the measurement of thermal properties after the threshold switching could potentially answer a decades-long question about the origin of threshold switching.

- **Mechanism of Threshold Switching**- The origin of threshold switching has been the subject of debates for the past few decades. With recent advancements in tunable wavelength pump-probe spectroscopy, a technique similar to TDTR, various vibrational modes and their lifetime from electrons to phonons can be detected with respect to the probe wavelength with sub-picosecond temporal resolution. This allows us to exclusively differentiate the effects of electronic changes from those of the lattice. To explain threshold switching, two competing models, electronic-assisted and thermally-assisted phase transition, have been relatively successful in providing some insight into the underlying mechanism. The electronic-assisted theory describes the phase transition in the context of energy hopping between the trap states within the defects in the atomic structure. According to this, the glassy network of chalcogenides gives rise to the formation of multiple localized defects where the conduction requires energy hopping between these localized trap states. Upon application of an electric field, these localized electrons hop between the trap states and move to the conduction band and lead to large changes in the electrical resistivity of the material. In order to probe these trap state in *a*-$Si_{20}Te_{80}$, the film can be directly (no transducer) excited by a pump beam and using a probe beam at different wavelength, the changes in the thermoreflectivity of material can be related to its electronic band structure. Since the bandgap of *a*-$Si_{20}Te_{80}$ is around 0.8 eV, a probe wavelength from 600 nm to 2000 nm can detect the band gap and any potential trap states associated within it.

# Bibliography

[1] R. P. Feynman, “Plenty of room at the bottom,” in *APS Annual Meeting*, 1959.

[2] G. Chen, *Nanoscale energy transport and conversion: a parallel treatment of electrons, molecules, phonons, and photons*. Oxford University Press, 2005.

[3] P. Ball, “Semiconductor technology looks up,” *Nature Materials*, vol. 21, no. 2, pp. 132–132, 2022.

[4] R. M. Pettit, W. Ge, P. Kumar, D. R. Luntz-Martin, J. T. Schultz, L. P. Neukirch, M. Bhattacharya, and A. N. Vamivakas, “An optical tweezer phonon laser,” *Nature Photonics*, vol. 13, no. 6, pp. 402–405, 2019.

[5] L. Anderegg, L. W. Cheuk, Y. Bao, S. Burchesky, W. Ketterle, K.-K. Ni, and J. M. Doyle, “An optical tweezer array of ultracold molecules,” *Science*, vol. 365, no. 6458, pp. 1156–1158, 2019.

[6] R. Erni, M. D. Rossell, C. Kisielowski, and U. Dahmen, “Atomic-resolution imaging with a sub-50-pm electron probe,” *Physical Review Letters*, vol. 102, no. 9, p. 096101, 2009.

[7] E. R. Hoglund, D.-L. Bao, A. O’Hara, S. Makarem, Z. T. Piontkowski, J. R. Matson, A. K. Yadav, R. C. Haislmaier, R. Engel-Herbert, J. F. Ihlefeld, *et al.*, “Emergent interface vibrational structure of oxide superlattices,” *Nature*, vol. 601, no. 7894, pp. 556–561, 2022.

[8] D. G. Gilmore and M. Donabedian, *Spacecraft thermal control handbook: cryogenics*, vol. 2. AIAA, 2002.

[9] A. E. Jahromi and D. F. Sullivan, “A piezoelectric cryogenic heat switch,” *Review of Scientific Instruments*, vol. 85, no. 6, p. 065118, 2014.

[10] Y. Li, W. Li, T. Han, X. Zheng, J. Li, B. Li, S. Fan, and C.-W. Qiu, “Transforming heat transfer with thermal metamaterials and devices,” *Nature Reviews Materials*, vol. 6, no. 6, pp. 488–507, 2021.

[11] M. Elzouka and S. Ndao, “High temperature near-field nanothermomechanical rectification,” *Scientific Reports*, vol. 7, no. 1, pp. 1–8, 2017.

[12] A. Hamed, M. Elzouka, and S. Ndao, "Thermal calculator," *International Journal of Heat and Mass Transfer*, vol. 134, pp. 359–365, 2019.

[13] M. Wuttig, "Towards a universal memory?," *Nature Materials*, vol. 4, no. 4, pp. 265–266, 2005.

[14] Y. Qu, Q. Li, L. Cai, M. Pan, P. Ghosh, K. Du, and M. Qiu, "Thermal camouflage based on the phase-changing material GST," *Light: Science & Applications*, vol. 7, no. 1, pp. 1–10, 2018.

[15] H.-K. Lyeo, D. G. Cahill, B.-S. Lee, J. R. Abelson, M.-H. Kwon, K.-B. Kim, S. G. Bishop, and B.-k. Cheong, "Thermal conductivity of phase-change material $Ge_2Sb_2Te_5$," *Applied Physics Letters*, vol. 89, no. 15, p. 151904, 2006.

[16] K. Aryana, J. T. Gaskins, J. Nag, D. A. Stewart, Z. Bai, S. Mukhopadhyay, J. C. Read, D. H. Olson, E. R. Hoglund, J. M. Howe, *et al.*, "Interface controlled thermal resistances of ultra-thin chalcogenide-based phase change memory devices," *Nature Communications*, vol. 12, no. 1, pp. 1–11, 2021.

[17] P. A. Merolla, J. V. Arthur, R. Alvarez-Icaza, A. S. Cassidy, J. Sawada, F. Akopyan, B. L. Jackson, N. Imam, C. Guo, Y. Nakamura, *et al.*, "A million spiking-neuron integrated circuit with a scalable communication network and interface," *Science*, vol. 345, no. 6197, pp. 668–673, 2014.

[18] W. Zhang and M. Wuttig, "Phase change materials and superlattices for non-volatile memories," *Phys. Status Solidi RRL*, vol. 13, p. 1900130, 2019.

[19] K. Ding, J. Wang, Y. Zhou, H. Tian, L. Lu, R. Mazzarello, C. Jia, W. Zhang, F. Rao, and E. Ma, "Phase-change heterostructure enables ultralow noise and drift for memory operation," *Science*, vol. 366, no. 6462, pp. 210–215, 2019.

[20] Z. Wang, H. Wu, G. W. Burr, C. S. Hwang, K. L. Wang, Q. Xia, and J. J. Yang, "Resistive switching materials for information processing," *Nature Reviews Materials*, pp. 1–23, 2020.

[21] D. Ielmini and H.-S. P. Wong, "In-memory computing with resistive switching devices," *Nature Electronics*, vol. 1, no. 6, pp. 333–343, 2018.

[22] J. Feldmann, N. Youngblood, C. D. Wright, H. Bhaskaran, and W. Pernice, "All-optical spiking neurosynaptic networks with self-learning capabilities," *Nature*, vol. 569, no. 7755, pp. 208–214, 2019.

[23] A. Sebastian, M. Le Gallo, R. Khaddam-Aljameh, and E. Eleftheriou, "Memory devices and applications for in-memory computing," *Nature Nanotechnology*, vol. 15, no. 7, pp. 529–544, 2020.

[24] C. D. Wright, Y. Liu, K. I. Kohary, M. M. Aziz, and R. J. Hicken, "Arithmetic and biologically-inspired computing using phase-change materials," *Advanced Materials*, vol. 23, no. 30, pp. 3408–3413, 2011.

[25] A. Sebastian, M. Le Gallo, and E. Eleftheriou, "Computational phase-change memory: Beyond von neumann computing," *Journal of Physics D: Applied Physics*, vol. 52, no. 44, p. 443002, 2019.

[26] Q. Xia and J. J. Yang, "Memristive crossbar arrays for brain-inspired computing," *Nature Materials*, vol. 18, no. 4, pp. 309–323, 2019.

[27] C. Ríos, M. Stegmaier, P. Hosseini, D. Wang, T. Scherer, C. D. Wright, H. Bhaskaran, and W. H. Pernice, "Integrated all-photonic non-volatile multi-level memory," *Nature Photonics*, vol. 9, no. 11, pp. 725–732, 2015.

[28] C. Rios, P. Hosseini, C. D. Wright, H. Bhaskaran, and W. H. Pernice, "On-chip photonic memory elements employing phase-change materials," *Advanced Materials*, vol. 26, no. 9, pp. 1372–1377, 2014.

[29] J. Feldmann, N. Youngblood, M. Karpov, H. Gehring, X. Li, M. Stappers, M. Le Gallo, X. Fu, A. Lukashchuk, A. S. Raja, *et al.*, "Parallel convolutional processing using an integrated photonic tensor core," *Nature*, vol. 589, no. 7840, pp. 52–58, 2021.

[30] M. Wuttig and N. Yamada, "Phase-change materials for rewriteable data storage," *Nature Materials*, vol. 6, no. 11, pp. 824–832, 2007.

[31] W. Wełnic and M. Wuttig, "Reversible switching in phase-change materials," *materials today*, vol. 11, no. 6, pp. 20–27, 2008.

[32] M. Wuttig, H. Bhaskaran, and T. Taubner, "Phase-change materials for non-volatile photonic applications," *Nature Photonics*, vol. 11, no. 8, pp. 465–476, 2017.

[33] W. Zhang, R. Mazzarello, M. Wuttig, and E. Ma, "Designing crystallization in phase-change materials for universal memory and neuro-inspired computing," *Nature Reviews Materials*, vol. 4, no. 3, pp. 150–168, 2019.

[34] W. Zhang and E. Ma, "Unveiling the structural origin to control resistance drift in phase-change memory materials," *Materials Today*, 2020.

[35] E. Bozorg-Grayeli, J. P. Reifenberg, M. Asheghi, H.-S. P. Wong, and K. E. Goodson, "Thermal transport in phase change memory materials," *Annual Review of Heat Transfer*, vol. 16, 2013.

[36] A. J. Bullen, K. E. O'Hara, D. G. Cahill, O. Monteiro, and A. Von Keudell, "Thermal conductivity of amorphous carbon thin films," *Journal of Applied Physics*, vol. 88, no. 11, pp. 6317–6320, 2000.

[37] M. Shamsa, W. Liu, A. Balandin, C. Casiraghi, W. Milne, and A. Ferrari, "Thermal conductivity of diamond-like carbon films," *Applied Physics Letters*, vol. 89, no. 16, p. 161921, 2006.

[38] D. Onn, A. Witek, Y. Qiu, T. Anthony, and W. Banholzer, “Some aspects of the thermal conductivity of isotopically enriched diamond single crystals,” *Physical Review Letters*, vol. 68, no. 18, p. 2806, 1992.

[39] J. Olson, R. Pohl, J. Vandersande, A. Zoltan, T. Anthony, and W. Banholzer, “Thermal conductivity of diamond between 170 and 1200 k and the isotope effect,” *Physical Review B*, vol. 47, no. 22, p. 14850, 1993.

[40] L. Wei, P. Kuo, R. Thomas, T. Anthony, and W. Banholzer, “Thermal conductivity of isotopically modified single crystal diamond,” *Physical Review Letters*, vol. 70, no. 24, p. 3764, 1993.

[41] K. Aryana, Y. Zhang, J. A. Tomko, M. S. B. Hoque, E. R. Hoglund, D. H. Olson, J. Nag, J. C. Read, C. Ríos, J. Hu, *et al.*, “Suppressed electronic contribution in thermal conductivity of ge2sb2se4te,” *Nature Communications*, vol. 12, no. 1, pp. 1–9, 2021.

[42] A. Ward, D. Broido, D. A. Stewart, and G. Deinzer, “Ab initio theory of the lattice thermal conductivity in diamond,” *Physical Review B*, vol. 80, no. 12, p. 125203, 2009.

[43] X. Xu, Q. Zhang, M. Hao, Y. Hu, Z. Lin, L. Peng, T. Wang, X. Ren, C. Wang, Z. Zhao, *et al.*, “Double-negative-index ceramic aerogels for thermal superinsulation,” *Science*, vol. 363, no. 6428, pp. 723–727, 2019.

[44] X. Qian, J. Zhou, and G. Chen, “Phonon-engineered extreme thermal conductivity materials,” *Nature Materials*, pp. 1–15, 2021.

[45] A. A. Balandin, S. Ghosh, W. Bao, I. Calizo, D. Teweldebrhan, F. Miao, and C. N. Lau, “Superior thermal conductivity of single-layer graphene,” *Nano Letters*, vol. 8, no. 3, pp. 902–907, 2008.

[46] D. Ghosh, I. Calizo, D. Teweldebrhan, E. P. Pokatilov, D. L. Nika, A. A. Balandin, W. Bao, F. Miao, and C. N. Lau, “Extremely high thermal conductivity of graphene: Prospects for thermal management applications in nanoelectronic circuits,” *Applied Physics Letters*, vol. 92, no. 15, p. 151911, 2008.

[47] A. A. Balandin, “Thermal properties of graphene and nanostructured carbon materials,” *Nature Materials*, vol. 10, no. 8, pp. 569–581, 2011.

[48] M. Fujii, X. Zhang, H. Xie, H. Ago, K. Takahashi, T. Ikuta, H. Abe, and T. Shimizu, “Measuring the thermal conductivity of a single carbon nanotube,” *Physical Review Letters*, vol. 95, no. 6, p. 065502, 2005.

[49] B. Kumanek and D. Janas, “Thermal conductivity of carbon nanotube networks: A review,” *Journal of Materials Science*, vol. 54, no. 10, pp. 7397–7427, 2019.

[50] J.-P. Salvetat, J.-M. Bonard, N. Thomson, A. Kulik, L. Forro, W. Benoit, and L. Zuppiroli, “Mechanical properties of carbon nanotubes,” *Applied Physics A*, vol. 69, no. 3, pp. 255–260, 1999.

[51] E. Saether, S. Frankland, and R. B. Pipes, “Transverse mechanical properties of single-walled carbon nanotube crystals. part i: determination of elastic moduli,” *Composites Science and Technology*, vol. 63, no. 11, pp. 1543–1550, 2003.

[52] Z. Ni, H. Bu, M. Zou, H. Yi, K. Bi, and Y. Chen, “Anisotropic mechanical properties of graphene sheets from molecular dynamics,” *Physica B: Condensed Matter*, vol. 405, no. 5, pp. 1301–1306, 2010.

[53] D. G. Cahill and R. Pohl, “Heat flow and lattice vibrations in glasses,” *Solid State Communications*, vol. 70, no. 10, pp. 927–930, 1989.

[54] T. Feng and X. Ruan, “Quantum mechanical prediction of four-phonon scattering rates and reduced thermal conductivity of solids,” *Physical Review B*, vol. 93, no. 4, p. 045202, 2016.

[55] T. Feng, L. Lindsay, and X. Ruan, “Four-phonon scattering significantly reduces intrinsic thermal conductivity of solids,” *Physical Review B*, vol. 96, no. 16, p. 161201, 2017.

[56] S. Li, Q. Zheng, Y. Lv, X. Liu, X. Wang, P. Y. Huang, D. G. Cahill, and B. Lv, “High thermal conductivity in cubic boron arsenide crystals,” *Science*, vol. 361, no. 6402, pp. 579–581, 2018.

[57] K. Chen, B. Song, N. K. Ravichandran, Q. Zheng, X. Chen, H. Lee, H. Sun, S. Li, G. A. G. U. Gamage, F. Tian, *et al.*, “Ultrahigh thermal conductivity in isotope-enriched cubic boron nitride,” *Science*, vol. 367, no. 6477, pp. 555–559, 2020.

[58] P. Klemens, “The scattering of low-frequency lattice waves by static imperfections,” *Proceedings of the Physical Society. Section A*, vol. 68, no. 12, p. 1113, 1955.

[59] P. B. Allen, J. L. Feldman, J. Fabian, and F. Wooten, “Diffusons, locons and propagons: Character of atomie yibrations in amorphous si,” *Philosophical Magazine B*, vol. 79, no. 11-12, pp. 1715–1731, 1999.

[60] P. B. Allen and J. Kelner, “Evolution of a vibrational wave packet on a disordered chain,” *American Journal of Physics*, vol. 66, no. 6, pp. 497–506, 1998.

[61] J. M. Larkin and A. J. McGaughey, “Thermal conductivity accumulation in amorphous silica and amorphous silicon,” *Physical Review B*, vol. 89, no. 14, p. 144303, 2014.

[62] K. Aryana, D. A. Stewart, J. T. Gaskins, J. Nag, J. C. Read, D. H. Olson, M. K. Grobis, and P. E. Hopkins, “Tuning network topology and vibrational mode localization to achieve ultralow thermal conductivity in amorphous chalcogenides,” *Nature Communications*, vol. 12, no. 1, pp. 1–9, 2021.

[63] P. B. Allen and J. L. Feldman, “Thermal conductivity of glasses: Theory and application to amorphous si,” *Physical Review Letters*, vol. 62, no. 6, p. 645, 1989.

[64] D. G. Cahill, S. K. Watson, and R. O. Pohl, “Lower limit to the thermal conductivity of disordered crystals,” *Physical Review B*, vol. 46, no. 10, p. 6131, 1992.

[65] M. T. Agne, R. Hanus, and G. J. Snyder, “Minimum thermal conductivity in the context of diffuson-mediated thermal transport,” *Energy & Environmental Science*, vol. 11, no. 3, pp. 609–616, 2018.

[66] Z. Chen and C. Dames, “An anisotropic model for the minimum thermal conductivity,” *Applied Physics Letters*, vol. 107, no. 19, p. 193104, 2015.

[67] D. G. Cahill and R. O. Pohl, “Lattice vibrations and heat transport in crystals and glasses,” *Annual review of physical chemistry*, vol. 39, no. 1, pp. 93–121, 1988.

[68] C. Chiritescu, D. G. Cahill, N. Nguyen, D. Johnson, A. Bodapati, P. Keblinski, and P. Zschack, “Ultralow thermal conductivity in disordered, layered wse$_2$ crystals,” *Science*, vol. 315, no. 5810, pp. 351–353, 2007.

[69] J. C. Duda, P. E. Hopkins, Y. Shen, and M. C. Gupta, “Exceptionally low thermal conductivities of films of the fullerene derivative pcbm,” *Physical Review Letters*, vol. 110, no. 1, p. 015902, 2013.

[70] X. Wang, C. D. Liman, N. D. Treat, M. L. Chabinyc, and D. G. Cahill, “Ultralow thermal conductivity of fullerene derivatives,” *Physical Review B*, vol. 88, no. 7, p. 075310, 2013.

[71] P. B. Allen and J. L. Feldman, “Thermal conductivity of disordered harmonic solids,” *Physical Review B*, vol. 48, no. 17, p. 12581, 1993.

[72] Q. Xi, J. Zhong, J. He, X. Xu, T. Nakayama, Y. Wang, J. Liu, J. Zhou, and B. Li, “A ubiquitous thermal conductivity formula for liquids, polymer glass, and amorphous solids,” *Chinese Physics Letters*, vol. 37, no. 10, p. 104401, 2020.

[73] R. Franz and G. Wiedemann, “Ueber die wärme-leitungsfähigkeit der metalle,” *Annalen der Physik*, vol. 165, no. 8, pp. 497–531, 1853.

[74] R. Makinson, “The thermal conductivity of metals,” in *Mathematical Proceedings of the Cambridge Philosophical Society*, vol. 34, pp. 474–497, Cambridge University Press, 1938.

[75] X. Zheng, D. Cahill, P. Krasnochtchekov, R. Averback, and J.-C. Zhao, “High-throughput thermal conductivity measurements of nickel solid solutions and the applicability of the wiedemann–franz law,” *Acta Materialia*, vol. 55, no. 15, pp. 5177–5185, 2007.

[76] Q. Zheng, A. B. Mei, M. Tuteja, D. G. Sangiovanni, L. Hultman, I. Petrov, J. E. Greene, and D. G. Cahill, "Phonon and electron contributions to the thermal conductivity of v n x epitaxial layers," *Physical Review Materials*, vol. 1, no. 6, p. 065002, 2017.

[77] C. Kittel, "Introduction to solid state physics, john wiley & sons," *Inc., Sixth edition,(New York, 1986)*, 2005.

[78] M. Thesberg, H. Kosina, and N. Neophytou, "On the lorenz number of multiband materials," *Physical Review B*, vol. 95, no. 12, p. 125206, 2017.

[79] S. Lee, K. Hippalgaonkar, F. Yang, J. Hong, C. Ko, J. Suh, K. Liu, K. Wang, J. J. Urban, X. Zhang, *et al.*, "Anomalously low electronic thermal conductivity in metallic vanadium dioxide," *Science*, vol. 355, no. 6323, pp. 371–374, 2017.

[80] J. B. J. Fourier, G. Darboux, *et al.*, *Théorie analytique de la chaleur*, vol. 504. Didot Paris, 1822.

[81] H. Elsayed-Ali, T. Norris, M. Pessot, and G. Mourou, "Time-resolved observation of electron-phonon relaxation in copper," *Physical Review Letters*, vol. 58, no. 12, p. 1212, 1987.

[82] S. Brorson, A. Kazeroonian, J. Moodera, D. Face, T. Cheng, E. Ippen, M. Dresselhaus, and G. Dresselhaus, "Femtosecond room-temperature measurement of the electron-phonon coupling constant $\gamma$ in metallic superconductors," *Physical Review Letters*, vol. 64, no. 18, p. 2172, 1990.

[83] J. Weaver, D. W. Lynch, C. Culp, and R. Rosei, "Thermoreflectance of v, nb, and paramagnetic cr," *Physical Review B*, vol. 14, no. 2, p. 459, 1976.

[84] E. Colavita, A. Franciosi, D. W. Lynch, G. Paolucci, and R. Rosei, "Thermoreflectance investigation of the antiferromagnetic and paramagnetic phases of cr," *Physical Review B*, vol. 27, no. 3, p. 1653, 1983.

[85] C. Thomsen, H. Maris, and J. Tauc, "Picosecond acoustics as a non-destructive tool for the characterization of very thin films," *Thin Solid Films*, vol. 154, no. 1-2, pp. 217–223, 1987.

[86] H.-N. Lin, R. Stoner, H. Maris, and J. Tauc, "Phonon attenuation and velocity measurements in transparent materials by picosecond acoustic interferometry," *Journal of applied physics*, vol. 69, no. 7, pp. 3816–3822, 1991.

[87] G. Tas and H. J. Maris, "Electron diffusion in metals studied by picosecond ultrasonics," *Physical Review B*, vol. 49, no. 21, p. 15046, 1994.

[88] C. A. Paddock and G. L. Eesley, "Transient thermoreflectance from thin metal films," *Journal of Applied Physics*, vol. 60, no. 1, pp. 285–290, 1986.

[89] W. Capinski, H. Maris, T. Ruf, M. Cardona, K. Ploog, and D. Katzer, "Thermal-conductivity measurements of gaas/alas superlattices using a picosecond optical pump-and-probe technique," *Physical Review B*, vol. 59, no. 12, p. 8105, 1999.

[90] P. Jiang, X. Qian, and R. Yang, "Tutorial: Time-domain thermoreflectance (tdtr) for thermal property characterization of bulk and thin film materials," *Journal of Applied Physics*, vol. 124, no. 16, p. 161103, 2018.

[91] Y. Wang, J. Y. Park, Y. K. Koh, and D. G. Cahill, "Thermoreflectance of metal transducers for time-domain thermoreflectance," *Journal of Applied Physics*, vol. 108, no. 4, p. 043507, 2010.

[92] R. Wilson, B. A. Apgar, L. W. Martin, and D. G. Cahill, "Thermoreflectance of metal transducers for optical pump-probe studies of thermal properties," *Optics express*, vol. 20, no. 27, pp. 28829–28838, 2012.

[93] D. G. Cahill, "Analysis of heat flow in layered structures for time-domain thermoreflectance," *Review of scientific instruments*, vol. 75, no. 12, pp. 5119–5122, 2004.

[94] A. J. Schmidt, R. Cheaito, and M. Chiesa, "A frequency-domain thermoreflectance method for the characterization of thermal properties," *Review of scientific instruments*, vol. 80, no. 9, p. 094901, 2009.

[95] J. L. Braun, D. H. Olson, J. T. Gaskins, and P. E. Hopkins, "A steady-state thermoreflectance method to measure thermal conductivity," *Review of Scientific Instruments*, vol. 90, no. 2, p. 024905, 2019.

[96] C. Yuan, W. M. Waller, and M. Kuball, "Nanosecond transient thermoreflectance method for characterizing anisotropic thermal conductivity," *Review of Scientific Instruments*, vol. 90, no. 11, p. 114903, 2019.

[97] W. S. Capinski and H. J. Maris, "Improved apparatus for picosecond pump-and-probe optical measurements," *Review of Scientific Instruments*, vol. 67, no. 8, pp. 2720–2726, 1996.

[98] B. Sun and Y. K. Koh, "Understanding and eliminating artifact signals from diffusely scattered pump beam in measurements of rough samples by time-domain thermoreflectance (tdtr)," *Review of Scientific Instruments*, vol. 87, no. 6, p. 064901, 2016.

[99] R. M. Costescu, M. A. Wall, and D. G. Cahill, "Thermal conductance of epitaxial interfaces," *Physical Review B*, vol. 67, no. 5, p. 054302, 2003.

[100] R. Wilson and D. G. Cahill, "Limits to fourier theory in high thermal conductivity single crystals," *Applied Physics Letters*, vol. 107, no. 20, p. 203112, 2015.

[101] M. D. Losego, M. E. Grady, N. R. Sottos, D. G. Cahill, and P. V. Braun, "Effects of chemical bonding on heat transport across interfaces," *Nature Materials*, vol. 11, no. 6, p. 502, 2012.

[102] C. B. Saltonstall, C. A. Polanco, J. C. Duda, A. W. Ghosh, P. M. Norris, and P. E. Hopkins, "Effect of interface adhesion and impurity mass on phonon transport at atomic junctions," *Journal of Applied Physics*, vol. 113, no. 1, p. 013516, 2013.

[103] D. H. Olson, K. M. Freedy, S. J. McDonnell, and P. E. Hopkins, "The influence of titanium adhesion layer oxygen stoichiometry on thermal boundary conductance at gold contacts," *Applied Physics Letters*, vol. 112, no. 17, p. 171602, 2018.

[104] J. Duda, C.-Y. Yang, B. Foley, R. Cheaito, D. Medlin, R. Jones, and P. Hopkins, "Influence of interfacial properties on thermal transport at gold: silicon contacts," *Applied Physics Letters*, vol. 102, no. 8, p. 081902, 2013.

[105] P. E. Hopkins, M. Baraket, E. V. Barnat, T. E. Beechem, S. P. Kearney, J. C. Duda, J. T. Robinson, and S. G. Walton, "Manipulating thermal conductance at metal–graphene contacts via chemical functionalization," *Nano Letters*, vol. 12, no. 2, pp. 590–595, 2012.

[106] B. M. Foley, S. C. Hernandez, J. C. Duda, J. T. Robinson, S. G. Walton, and P. E. Hopkins, "Modifying surface energy of graphene via plasma-based chemical functionalization to tune thermal and electrical transport at metal interfaces," *Nano Letters*, vol. 15, no. 8, pp. 4876–4882, 2015.

[107] S. Walton, B. Foley, S. Hernández, D. Boris, M. Baraket, J. Duda, J. Robinson, and P. Hopkins, "Plasma-based chemical functionalization of graphene to control the thermal transport at graphene-metal interfaces," *Surface and Coatings Technology*, vol. 314, pp. 148–154, 2017.

[108] M. Jeong, J. P. Freedman, H. J. Liang, C.-M. Chow, V. M. Sokalski, J. A. Bain, and J. A. Malen, "Enhancement of thermal conductance at metal-dielectric interfaces using subnanometer metal adhesion layers," *Physical Review Applied*, vol. 5, no. 1, p. 014009, 2016.

[109] C. A. Polanco, R. Rastgarkafshgarkolaei, J. Zhang, N. Q. Le, P. M. Norris, and A. W. Ghosh, "Design rules for interfacial thermal conductance: Building better bridges," *Physical Review B*, vol. 95, no. 19, p. 195303, 2017.

[110] D. Saha, X. Yu, M. Jeong, M. Darwish, J. Weldon, A. J. Gellman, and J. A. Malen, "Impact of metal adhesion layer diffusion on thermal interface conductance," *Physical Review B*, vol. 99, no. 11, p. 115418, 2019.

[111] P. E. Hopkins, L. M. Phinney, J. R. Serrano, and T. E. Beechem, "Effects of surface roughness and oxide layer on the thermal boundary conductance at aluminum/silicon interfaces," in *International Heat Transfer Conference*, vol. 49415, pp. 313–319, 2010.

[112] P. E. Hopkins, "Thermal transport across solid interfaces with nanoscale imperfections: effects of roughness, disorder, dislocations, and bonding on thermal boundary conductance," *ISRN Mechanical Engineering*, vol. 2013, 2013.

[113] S. Merabia and K. Termentzidis, “Thermal boundary conductance across rough interfaces probed by molecular dynamics,” *Physical Review B*, vol. 89, no. 5, p. 054309, 2014.

[114] P. E. Hopkins, P. M. Norris, and R. J. Stevens, “Influence of inelastic scattering at metal-dielectric interfaces,” *Journal of Heat Transfer*, vol. 130, no. 2, p. 022401, 2008.

[115] A. Majumdar and P. Reddy, “Role of electron–phonon coupling in thermal conductance of metal–nonmetal interfaces,” *Applied Physics Letters*, vol. 84, no. 23, pp. 4768–4770, 2004.

[116] X. Wu and T. Luo, “Effect of electron-phonon coupling on thermal transport across metal-nonmetal interface—a second look,” *EPL (Europhysics Letters)*, vol. 110, no. 6, p. 67004, 2015.

[117] E. T. Swartz and R. O. Pohl, “Thermal boundary resistance,” *Reviews of modern physics*, vol. 61, no. 3, p. 605, 1989.

[118] R. J. Stevens, A. N. Smith, and P. M. Norris, “Measurement of thermal boundary conductance of a series of metal-dielectric interfaces by the transient thermoreflectance technique,” *Journal of Heat Transfer*, vol. 127, no. 3, pp. 315–322, 2005.

[119] P. M. Norris and P. E. Hopkins, “Examining interfacial diffuse phonon scattering through transient thermoreflectance measurements of thermal boundary conductance,” *Journal of Heat Transfer*, vol. 131, no. 4, p. 043207, 2009.

[120] R. Cheaito, J. T. Gaskins, M. E. Caplan, B. F. Donovan, B. M. Foley, A. Giri, J. C. Duda, C. J. Szwejkowski, C. Constantin, H. J. Brown-Shaklee, *et al.*, “Thermal boundary conductance accumulation and interfacial phonon transmission: Measurements and theory,” *Physical Review B*, vol. 91, no. 3, p. 035432, 2015.

[121] A. Giri, S. W. King, W. A. Lanford, A. B. Mei, D. Merrill, L. Li, R. Oviedo, J. Richards, D. H. Olson, J. L. Braun, *et al.*, “Interfacial defect vibrations enhance thermal transport in amorphous multilayers with ultrahigh thermal boundary conductance,” *Advanced Materials*, vol. 30, no. 44, p. 1804097, 2018.

[122] J. Liu, J. Zhu, M. Tian, X. Gu, A. Schmidt, and R. Yang, “Simultaneous measurement of thermal conductivity and heat capacity of bulk and thin film materials using frequency-dependent transient thermoreflectance method,” *Review of Scientific Instruments*, vol. 84, no. 3, p. 034902, 2013.

[123] W. K. Njoroge, H.-W. Wöltgens, and M. Wuttig, “Density changes upon crystallization of $Ge_2Sb_{2.04}Te_{4.74}$ films,” *Journal of Vacuum Science & Technology A: Vacuum, Surfaces, and Films*, vol. 20, no. 1, pp. 230–233, 2002.

[124] H.-S. P. Wong, S. Raoux, S. Kim, J. Liang, J. P. Reifenberg, B. Rajendran, M. Asheghi, and K. E. Goodson, “Phase change memory,” *Proceedings of the IEEE*, vol. 98, no. 12, pp. 2201–2227, 2010.

[125] R. Simpson, P. Fons, A. Kolobov, T. Fukaya, M. Krbal, T. Yagi, and J. Tominaga, "Interfacial phase-change memory," *Nature Nanotechnology*, vol. 6, no. 8, p. 501, 2011.

[126] F. Rao, K. Ding, Y. Zhou, Y. Zheng, M. Xia, S. Lv, Z. Song, S. Feng, I. Ronneberger, R. Mazzarello, *et al.*, "Reducing the stochasticity of crystal nucleation to enable subnanosecond memory writing," *Science*, vol. 358, no. 6369, pp. 1423–1427, 2017.

[127] D. Loke, T. Lee, W. Wang, L. Shi, R. Zhao, Y. Yeo, T. Chong, and S. Elliott, "Breaking the speed limits of phase-change memory," *Science*, vol. 336, no. 6088, pp. 1566–1569, 2012.

[128] C. Kim, D.-S. Suh, K. H. Kim, Y.-S. Kang, T.-Y. Lee, Y. Khang, and D. G. Cahill, "Fullerene thermal insulation for phase change memory," *Applied Physics Letters*, vol. 92, no. 1, p. 013109, 2008.

[129] C. Ahn, S. W. Fong, Y. Kim, S. Lee, A. Sood, C. M. Neumann, M. Asheghi, K. E. Goodson, E. Pop, and H.-S. P. Wong, "Energy-efficient phase-change memory with graphene as a thermal barrier," *Nano Letters*, vol. 15, no. 10, pp. 6809–6814, 2015.

[130] J. Shen, S. Lv, X. Chen, T. Li, S. Zhang, Z. Song, and M. Zhu, "Thermal barrier phase change memory," *ACS Applied Materials & Interfaces*, vol. 11, no. 5, pp. 5336–5343, 2019.

[131] Y. Saito, K. V. Mitrofanov, K. Makino, P. Fons, A. V. Kolobov, J. Tominaga, F. Uesugi, and M. Takeguchi, "Chalcogenide materials engineering for phase change memory and future electronics applications: from sb-te to bi-te," *physica status solidi (RRL)–Rapid Research Letters*, 2020.

[132] J. Momand, R. Wang, J. E. Boschker, M. A. Verheijen, R. Calarco, and B. J. Kooi, "Interface formation of two-and three-dimensionally bonded materials in the case of GeTe–$Sb_2Te_3$ superlattices," *Nanoscale*, vol. 7, no. 45, pp. 19136–19143, 2015.

[133] W. Risk, C. Rettner, and S. Raoux, "Thermal conductivities and phase transition temperatures of various phase-change materials measured by the $3\omega$ method," *Applied Physics Letters*, vol. 94, no. 10, p. 101906, 2009.

[134] Z. Li, J. Lee, J. P. Reifenberg, M. Asheghi, R. G. Jeyasingh, H.-S. P. Wong, and K. E. Goodson, "Grain boundaries, phase impurities, and anisotropic thermal conduction in phase-change memory," *IEEE electron device letters*, vol. 32, no. 7, pp. 961–963, 2011.

[135] E. A. Scott, E. Ziade, C. B. Saltonstall, A. E. McDonald, M. A. Rodriguez, P. E. Hopkins, T. E. Beechem, and D. P. Adams, "Thermal conductivity of $(Ge_2Sb_2Te_5)_{1-x}C_x$ phase change films," *Journal of Applied Physics*, vol. 128, no. 15, p. 155106, 2020.

[136] F. Xiong, A. D. Liao, D. Estrada, and E. Pop, "Low-power switching of phase-change materials with carbon nanotube electrodes," *Science*, vol. 332, no. 6029, pp. 568–570, 2011.

[137] I. Kim, S. Cho, D. Im, E. Cho, D. Kim, G. Oh, D. Ahn, S. Park, S. Nam, J. Moon, *et al.*, "High performance PRAM cell scalable to sub-20nm technology with below 4F2 cell size, extendable to DRAM applications," in *2010 Symposium on VLSI Technology*, pp. 203–204, IEEE, 2010.

[138] S. Raoux, F. Xiong, M. Wuttig, and E. Pop, "Phase change materials and phase change memory," *MRS bulletin*, vol. 39, no. 8, pp. 703–710, 2014.

[139] F. Xiong, M.-H. Bae, Y. Dai, A. D. Liao, A. Behnam, E. A. Carrion, S. Hong, D. Ielmini, and E. Pop, "Self-aligned nanotube–nanowire phase change memory," *Nano Letters*, vol. 13, no. 2, pp. 464–469, 2013.

[140] G. W. Burr, R. S. Shenoy, K. Virwani, P. Narayanan, A. Padilla, B. Kurdi, and H. Hwang, "Access devices for 3D crosspoint memory," *Journal of Vacuum Science & Technology B, Nanotechnology and Microelectronics: Materials, Processing, Measurement, and Phenomena*, vol. 32, no. 4, p. 040802, 2014.

[141] E. A. Scott, J. T. Gaskins, S. W. King, and P. E. Hopkins, "Thermal conductivity and thermal boundary resistance of atomic layer deposited high-k dielectric aluminum oxide, hafnium oxide, and titanium oxide thin films on silicon," *APL Materials*, vol. 6, no. 5, p. 058302, 2018.

[142] E. Bozorg-Grayeli, J. Reifenberg, K. Chang, M. Panzer, and K. Goodson, "Thermal conductivity and boundary resistance measurements of GeSbTe and electrode materials using nanosecond thermoreflectance," in *Thermal and Thermomechanical Phenomena in Electronic Systems (ITherm), 2010 12th IEEE Intersociety Conference on*, pp. 1–7, IEEE, 2010.

[143] G. T. Furukawa, M. L. Reilly, and J. S. Gallagher, "Critical analysis of heat—capacity data and evaluation of thermodynamic properties of ruthenium, rhodium, palladium, iridium, and platinum from 0 to 300k. a survey of the literature data on osmium.," *Journal of Physical and Chemical Reference Data*, vol. 3, no. 1, pp. 163–209, 1974.

[144] P. Zalden, K. S. Siegert, S. Rols, H. E. Fischer, F. Schlich, T. Hu, and M. Wuttig, "Specific heat of (gete) x (sb2te3) 1–x phase-change materials: The impact of disorder and anharmonicity," *Chemistry of Materials*, vol. 26, no. 7, pp. 2307–2312, 2014.

[145] G. W. Burr, M. J. Breitwisch, M. Franceschini, D. Garetto, K. Gopalakrishnan, B. Jackson, B. Kurdi, C. Lam, L. A. Lastras, A. Padilla, *et al.*, "Phase change memory technology," *Journal of Vacuum Science & Technology B, Nanotechnology and Microelectronics: Materials, Processing, Measurement, and Phenomena*, vol. 28, no. 2, pp. 223–262, 2010.

[146] E. Bozorg-Grayeli, J. P. Reifenberg, M. A. Panzer, J. A. Rowlette, and K. E. Goodson, "Temperature-dependent thermal properties of phase-change memory electrode materials," *IEEE Electron Device Letters*, vol. 32, no. 9, pp. 1281–1283, 2011.

[147] S. Harnsoongnoen and C. Sa-ngiamsak, "Confined-chalcogenide phase-change memory with thin metal oxide interlayer for low reset current operation," in *2009 6th International Conference on Electrical Engineering/Electronics, Computer, Telecommunications and Information Technology*, vol. 1, pp. 440–443, IEEE, 2009.

[148] J. P. Reifenberg, K.-W. Chang, M. A. Panzer, S. Kim, J. A. Rowlette, M. Asheghi, H.-S. P. Wong, and K. E. Goodson, "Thermal boundary resistance measurements for phase-change memory devices," *IEEE Electron Device Letters*, vol. 31, no. 1, pp. 56–58, 2009.

[149] B. Saha, Y. R. Koh, J. P. Feser, S. Sadasivam, T. S. Fisher, A. Shakouri, and T. D. Sands, "Phonon wave effects in the thermal transport of epitaxial tin/(al, sc) n metal/semiconductor superlattices," *Journal of Applied Physics*, vol. 121, no. 1, p. 015109, 2017.

[150] W. Ren, B. Liu, Z. Xu, J. Xu, A. He, L. Jiang, X. Jing, Y. Xiang, B. Zhang, J. Ren, *et al.*, "Pvd tin for bottom electrode of phase change memory," *ECS Transactions*, vol. 60, no. 1, pp. 533–538, 2014.

[151] J. Wu, M. Breitwisch, S. Kim, T. Hsu, R. Cheek, P. Du, J. Li, E. Lai, Y. Zhu, T. Wang, *et al.*, "A low power phase change memory using thermally confined tan/tin bottom electrode," in *2011 International Electron Devices Meeting*, pp. 3–2, IEEE, 2011.

[152] L. Wang, S. Gong, C. Yang, and J. Wen, "Towards low energy consumption data storage era using phase-change probe memory with tin bottom electrode," *Nanotechnology Reviews*, vol. 5, no. 5, pp. 455–460, 2016.

[153] A. Marconnet, M. Panzer, S. Yerci, S. Minissale, X. Wang, X. Zhang, L. Dal Negro, and K. Goodson, "Thermal conductivity and photoluminescence of light-emitting silicon nitride films," *Applied Physics Letters*, vol. 100, no. 5, p. 051908, 2012.

[154] J. L. Braun, C. H. Baker, A. Giri, M. Elahi, K. Artyushkova, T. E. Beechem, P. M. Norris, Z. C. Leseman, J. T. Gaskins, and P. E. Hopkins, "Size effects on the thermal conductivity of amorphous silicon thin films," *Physical Review B*, vol. 93, no. 14, p. 140201, 2016.

[155] I. Childres, L. A. Jauregui, W. Park, H. Cao, and Y. P. Chen, "Raman spectroscopy of graphene and related materials," *New developments in photon and materials research*, vol. 1, 2013.

[156] J. T. Gaskins, P. E. Hopkins, D. R. Merrill, S. R. Bauers, E. Hadland, D. C. Johnson, D. Koh, J. H. Yum, S. Banerjee, B. J. Nordell, *et al.*, "Investigation and review of the thermal, mechanical, electrical, optical, and structural properties of atomic layer deposited high-k dielectrics: Beryllium oxide, aluminum oxide, hafnium oxide, and aluminum nitride," *ECS Journal of Solid State Science and Technology*, vol. 6, no. 10, p. N189, 2017.

[157] J. Lee, Z. Li, J. P. Reifenberg, S. Lee, R. Sinclair, M. Asheghi, and K. E. Goodson, "Thermal conductivity anisotropy and grain structure in ge2sb2te5 films," *Journal of Applied Physics*, vol. 109, no. 8, p. 084902, 2011.

[158] J. P. Reifenberg, M. A. Panzer, S. Kim, A. M. Gibby, Y. Zhang, S. Wong, H.-S. P. Wong, E. Pop, and K. E. Goodson, "Thickness and stoichiometry dependence of the thermal conductivity of GeSbTe films," *Applied Physics Letters*, vol. 91, no. 11, p. 111904, 2007.

[159] J. Lee, E. Bozorg-Grayeli, S. Kim, M. Asheghi, H.-S. Philip Wong, and K. E. Goodson, "Phonon and electron transport through ge2sb2te5 films and interfaces bounded by metals," *Applied Physics Letters*, vol. 102, no. 19, p. 191911, 2013.

[160] T. Siegrist, P. Jost, H. Volker, M. Woda, P. Merkelbach, C. Schlockermann, and M. Wuttig, "Disorder-induced localization in crystalline phase-change materials," *Nature Materials*, vol. 10, no. 3, pp. 202–208, 2011.

[161] W. Zhang, A. Thiess, P. Zalden, R. Zeller, P. Dederichs, J.-Y. Raty, M. Wuttig, S. Blügel, and R. Mazzarello, "Role of vacancies in metal–insulator transitions of crystalline phase-change materials," *Nature Materials*, vol. 11, no. 11, pp. 952–956, 2012.

[162] J.-L. Battaglia, V. Schick, C. Rossignol, A. Kusiak, I. Aubert, A. Lamperti, and C. Wiemer, "Thermal resistance at al-ge2sb2te5 interface," *Applied Physics Letters*, vol. 102, no. 18, p. 181907, 2013.

[163] D. Campi, E. Baldi, G. Graceffa, G. Sosso, and M. Bernasconi, "Electron–phonon interaction and thermal boundary resistance at the interfaces of ge2sb2te5 with metals and dielectrics," *Journal of Physics: Condensed Matter*, vol. 27, no. 17, p. 175009, 2015.

[164] Z. Tian, K. Esfarjani, and G. Chen, "Enhancing phonon transmission across a si/ge interface by atomic roughness: First-principles study with the green's function method," *Physical Review B*, vol. 86, no. 23, p. 235304, 2012.

[165] T. S. English, J. C. Duda, J. L. Smoyer, D. A. Jordan, P. M. Norris, and L. V. Zhigilei, "Enhancing and tuning phonon transport at vibrationally mismatched solid-solid interfaces," *Physical Review B*, vol. 85, no. 3, p. 035438, 2012.

[166] C. S. Gorham, K. Hattar, R. Cheaito, J. C. Duda, J. T. Gaskins, T. E. Beechem, J. F. Ihlefeld, L. B. Biedermann, E. S. Piekos, D. L. Medlin, *et al.*, "Ion irradiation of the native oxide/silicon surface increases the thermal boundary conductance across aluminum/silicon interfaces," *Physical Review B*, vol. 90, no. 2, p. 024301, 2014.

[167] A. Giri and P. E. Hopkins, "A review of experimental and computational advances in thermal boundary conductance and nanoscale thermal transport across solid interfaces," *Advanced Functional Materials*, vol. 30, no. 8, p. 1903857, 2020.

[168] V. Filippova, S. Kunavin, and M. Pugachev, “Calculation of the parameters of the lennard-jones potential for pairs of identical atoms based on the properties of solid substances,” *Inorganic Materials: Applied Research*, vol. 6, no. 1, pp. 1–4, 2015.

[169] A. Giri, P. E. Hopkins, J. G. Wessel, and J. C. Duda, “Kapitza resistance and the thermal conductivity of amorphous superlattices,” *Journal of Applied Physics*, vol. 118, no. 16, p. 165303, 2015.

[170] T. Chong, H. Koon, *et al.*, “Thickness dependent nano-crystallization in ge2sb2te5 films and its effect on devices,” *Japanese Journal of Applied Physics*, vol. 46, no. 4S, p. 2211, 2007.

[171] D. Choi, C. S. Kim, D. Naveh, S. Chung, A. P. Warren, N. T. Nuhfer, M. F. Toney, K. R. Coffey, and K. Barmak, “Electron mean free path of tungsten and the electrical resistivity of epitaxial (110) tungsten films,” *Physical Review B*, vol. 86, no. 4, p. 045432, 2012.

[172] Y. Chen, J. Ma, and W. Li, “Understanding the thermal conductivity and lorenz number in tungsten from first principles,” *Physical Review B*, vol. 99, no. 2, p. 020305, 2019.

[173] J. Koenig, H. Boettner, J. Tomforde, and W. Bensch, “Thermoelectric properties of phase-change materials,” in *2007 26th International Conference on Thermoelectrics*, pp. 390–393, IEEE, 2007.

[174] C. Luo, H. Ryll, C. H. Back, and F. Radu, “X-ray magnetic linear dichroism as a probe for non-collinear magnetic state in ferrimagnetic single layer exchange bias systems,” *Scientific Reports*, vol. 9, no. 1, pp. 1–9, 2019.

[175] L. Adnane, F. Dirisaglik, A. Cywar, K. Cil, Y. Zhu, C. Lam, A. Anwar, A. Gokirmak, and H. Silva, “High temperature electrical resistivity and seebeck coefficient of ge2sb2te5 thin films,” *Journal of Applied Physics*, vol. 122, no. 12, p. 125104, 2017.

[176] J. L. Da Silva, A. Walsh, and H. Lee, “Insights into the structure of the stable and metastable (gete) m (sb 2 te 3) n compounds,” *Physical Review B*, vol. 78, no. 22, p. 224111, 2008.

[177] J.-J. Wang, J. Wang, H. Du, L. Lu, P. C. Schmitz, J. Reindl, A. M. Mio, C.-L. Jia, E. Ma, R. Mazzarello, *et al.*, “Genesis and effects of swapping bilayers in hexagonal $GeSb_2Te_4$,” *Chemistry of Materials*, vol. 30, no. 14, pp. 4770–4777, 2018.

[178] W. Wełnic, J. A. Kalb, D. Wamwangi, C. Steimer, and M. Wuttig, “Phase change materials: From structures to kinetics,” *Journal of Materials Research*, vol. 22, no. 9, pp. 2368–2375, 2007.

[179] A. Lotnyk, U. Ross, T. Dankwort, I. Hilmi, L. Kienle, and B. Rauschenbach, “Atomic structure and dynamic reconfiguration of layered defects in van der waals layered ge-sb-te based materials,” *Acta Materialia*, vol. 141, pp. 92–96, 2017.

[180] A. M. Mio, P. M. Konze, A. Meledin, M. Küpers, M. Pohlmann, M. Kaminski, R. Dronskowski, J. Mayer, and M. Wuttig, “Impact of bonding on the stacking defects in layered chalcogenides,” *Advanced Functional Materials*, 2019.

[181] M. Behrens, A. Lotnyk, J. W. Gerlach, I. Hilmi, T. Abel, P. Lorenz, and B. Rauschenbach, “Ultrafast interfacial transformation from 2d-to 3d-bonded structures in layered ge–sb–te thin films and heterostructures,” *Nanoscale*, vol. 10, no. 48, pp. 22946–22953, 2018.

[182] R. Wang, F. R. Lange, S. Cecchi, M. Hanke, M. Wuttig, and R. Calarco, “2d or not 2d: strain tuning in weakly coupled heterostructures,” *Advanced Functional Materials*, vol. 28, no. 14, p. 1705901, 2018.

[183] J. Wang, I. Ronneberger, L. Zhou, L. Lu, V. L. Deringer, B. Zhang, L. Tian, H. Du, C. Jia, X. Qian, *et al.*, “Unconventional two-dimensional germanium dichalcogenides,” *Nanoscale*, vol. 10, no. 16, pp. 7363–7368, 2018.

[184] Y. Cheng, O. Cojocaru-Mirédin, J. Keutgen, Y. Yu, M. Küpers, M. Schumacher, P. Golub, J.-Y. Raty, R. Dronskowski, and M. Wuttig, “Understanding the structure and properties of sesqui-chalcogenides (ie, v2vi3 or pn2ch3 (pn= pnictogen, ch= chalcogen) compounds) from a bonding perspective,” *Advanced Materials*, vol. 31, no. 43, p. 1904316, 2019.

[185] K. L. Okabe, A. Sood, E. Yalon, C. M. Neumann, M. Asheghi, E. Pop, K. E. Goodson, and H.-S. P. Wong, “Understanding the switching mechanism of interfacial phase change memory,” *Journal of Applied Physics*, vol. 125, no. 18, p. 184501, 2019.

[186] J. P. Reifenberg, D. L. Kencke, and K. E. Goodson, “The impact of thermal boundary resistance in phase-change memory devices,” *IEEE Electron Device Letters*, vol. 29, no. 10, pp. 1112–1114, 2008.

[187] M. Boniardi, J. E. Boschker, J. Momand, B. J. Kooi, A. Redaelli, and R. Calarco, “Evidence for thermal-based transition in super-lattice phase change memory,” *physica status solidi (RRL)–Rapid Research Letters*, vol. 13, no. 4, p. 1800634, 2019.

[188] J. Von Neumann, “First draft of a report on the edvac,” *IEEE Annals of the History of Computing*, vol. 15, no. 4, pp. 27–75, 1993.

[189] B. Sun, T. Guo, G. Zhou, S. Ranjan, Y. Jiao, L. Wei, Y. N. Zhou, and Y. A. Wu, “Synaptic devices based neuromorphic computing applications in artificial intelligence,” *Materials Today Physics*, p. 100393, 2021.

[190] W. W. Koelmans, A. Sebastian, V. P. Jonnalagadda, D. Krebs, L. Dellmann, and E. Eleftheriou, “Projected phase-change memory devices,” *Nature Communications*, vol. 6, no. 1, pp. 1–7, 2015.

[191] S. Nandakumar, M. Le Gallo, I. Boybat, B. Rajendran, A. Sebastian, and E. Eleftheriou, "A phase-change memory model for neuromorphic computing," *Journal of Applied Physics*, vol. 124, no. 15, p. 152135, 2018.

[192] P. Guo, A. M. Sarangan, and I. Agha, "A review of germanium-antimony-telluride phase change materials for non-volatile memories and optical modulators," *Applied Sciences*, vol. 9, no. 3, p. 530, 2019.

[193] T. Nirschl, J. Philipp, T. Happ, G. W. Burr, B. Rajendran, M.-H. Lee, A. Schrott, M. Yang, M. Breitwisch, C.-F. Chen, *et al.*, "Write strategies for 2 and 4-bit multi-level phase-change memory," in *2007 IEEE International Electron Devices Meeting*, pp. 461–464, IEEE, 2007.

[194] Y. Zhang, J. B. Chou, J. Li, H. Li, Q. Du, A. Yadav, S. Zhou, M. Y. Shalaginov, Z. Fang, H. Zhong, *et al.*, "Broadband transparent optical phase change materials for high-performance nonvolatile photonics," *Nature Communications*, vol. 10, no. 1, pp. 1–9, 2019.

[195] K. Aryana, J. Gaskins, J. Nag, J. Read, D. Olson, M. Grobis, and P. Hopkins, "Thermal properties of carbon nitride toward use as an electrode in phase change memory devices," *Applied Physics Letters*, vol. 116, no. 4, p. 043502, 2020.

[196] K. Chaudhary, M. Tamagnone, X. Yin, C. M. Spägele, S. L. Oscurato, J. Li, C. Persch, R. Li, N. A. Rubin, L. A. Jauregui, *et al.*, "Polariton nanophotonics using phase-change materials," *Nature Communications*, vol. 10, no. 1, pp. 1–6, 2019.

[197] H. Wang, T. Guo, Y. Xue, S. Lv, D. Yao, Z. Zhou, S. Song, and Z. Song, "The phase change memory features high-temperature characteristic based on Ge-Sb-Se-Te alloys," *Materials Letters*, vol. 254, pp. 182–185, 2019.

[198] Y. Zhang, C. Fowler, J. Liang, B. Azhar, M. Y. Shalaginov, S. Deckoff-Jones, S. An, J. B. Chou, C. M. Roberts, V. Liberman, *et al.*, "Electrically reconfigurable non-volatile metasurface using low-loss optical phase-change material," *Nature Nanotechnology*, vol. 16, no. 6, pp. 661–666, 2021.

[199] S. Abdollahramezani, O. Hemmatyar, H. Taghinejad, A. Krasnok, Y. Kiarashinejad, M. Zandehshahvar, A. Alù, and A. Adibi, "Tunable nanophotonics enabled by chalcogenide phase-change materials," *Nanophotonics*, vol. 9, no. 5, pp. 1189–1241, 2020.

[200] Y. Wang, P. Landreman, D. Schoen, K. Okabe, A. Marshall, U. Celano, H.-S. P. Wong, J. Park, and M. L. Brongersma, "Electrical tuning of phase-change antennas and metasurfaces," *Nature Nanotechnology*, vol. 16, no. 6, pp. 667–672, 2021.

[201] J. Zheng, Z. Fang, C. Wu, S. Zhu, P. Xu, J. K. Doylend, S. Deshmukh, E. Pop, S. Dunham, M. Li, *et al.*, "Nonvolatile electrically reconfigurable integrated photonic switch enabled by a silicon pin diode heater," *Advanced Materials*, vol. 32, no. 31, p. 2001218, 2020.

[202] H. Zhang, L. Zhou, L. Lu, J. Xu, N. Wang, H. Hu, B. A. Rahman, Z. Zhou, and J. Chen, "Miniature multilevel optical memristive switch using phase change material," *ACS Photonics*, vol. 6, no. 9, pp. 2205–2212, 2019.

[203] C. Ríos, Q. Du, Y. Zhang, C.-C. Popescu, M. Y. Shalaginov, P. Miller, C. Roberts, M. Kang, K. A. Richardson, T. Gu, *et al.*, "Ultra-compact nonvolatile photonics based on electrically reprogrammable transparent phase change materials," *arXiv preprint arXiv:2105.06010*, 2021.

[204] K. Kato, M. Kuwahara, H. Kawashima, T. Tsuruoka, and H. Tsuda, "Current-driven phase-change optical gate switch using indium–tin-oxide heater," *Applied Physics Express*, vol. 10, no. 7, p. 072201, 2017.

[205] H. Taghinejad, S. Abdollahramezani, A. A. Eftekhar, T. Fan, A. H. Hosseinnia, O. Hemmatyar, A. E. Dorche, A. Gallmon, and A. Adibi, "Ito-based microheaters for reversible multi-stage switching of phase-change materials: towards miniaturized beyond-binary reconfigurable integrated photonics," *Optics Express*, vol. 29, no. 13, pp. 20449–20462, 2021.

[206] C. Ríos, Y. Zhang, M. Y. Shalaginov, S. Deckoff-Jones, H. Wang, S. An, H. Zhang, M. Kang, K. A. Richardson, C. Roberts, *et al.*, "Multi-level electro-thermal switching of optical phase-change materials using graphene," *Advanced Photonics Research*, vol. 2, no. 1, p. 2000034, 2021.

[207] J. Zheng, S. Zhu, P. Xu, S. Dunham, and A. Majumdar, "Modeling electrical switching of nonvolatile phase-change integrated nanophotonic structures with graphene heaters," *ACS applied materials & interfaces*, vol. 12, no. 19, pp. 21827–21836, 2020.

[208] Y. Zhang, C. Ríos, M. Y. Shalaginov, M. Li, A. Majumdar, T. Gu, and J. Hu, "Myths and truths about optical phase change materials: A perspective," *Applied Physics Letters*, vol. 118, no. 21, p. 210501, 2021.

[209] A. J. Schmidt, X. Chen, and G. Chen, "Pulse accumulation, radial heat conduction, and anisotropic thermal conductivity in pump-probe transient thermoreflectance," *Review of Scientific Instruments*, vol. 79, no. 11, p. 114902, 2008.

[210] P. E. Hopkins, J. R. Serrano, L. M. Phinney, S. P. Kearney, T. W. Grasser, and C. T. Harris, "Criteria for cross-plane dominated thermal transport in multilayer thin film systems during modulated laser heating," *Journal of Heat Transfer*, vol. 132, no. 8, p. 081302, 2010.

[211] J. A. Tomko, D. H. Olson, A. Giri, J. T. Gaskins, B. F. Donovan, S. M. O'Malley, and P. E. Hopkins, "Nanoscale wetting and energy transmission at solid/liquid interfaces," *Langmuir*, vol. 35, no. 6, pp. 2106–2114, 2019.

[212] K. Siegert, F. Lange, E. Sittner, H. Volker, C. Schlockermann, T. Siegrist, and M. Wuttig, "Impact of vacancy ordering on thermal transport in crystalline phase-change materials," *Reports on Progress in Physics*, vol. 78, no. 1, p. 013001, 2014.

[213] W. S. Williams, “High-temperature thermal conductivity of transition metal carbides and nitrides,” *Journal of the American Ceramic Society*, vol. 49, no. 3, pp. 156–159, 1966.

[214] W. S. Williams, “The thermal conductivity of metallic ceramics,” *Jom*, vol. 50, no. 6, pp. 62–66, 1998.

[215] S. Mason, D. Wesenberg, A. Hojem, M. Manno, C. Leighton, and B. Zink, “Violation of the wiedemann-franz law through reduction of thermal conductivity in gold thin films,” *Physical Review Materials*, vol. 4, no. 6, p. 065003, 2020.

[216] J. A. Tomko, E. L. Runnerstrom, Y.-S. Wang, W. Chu, J. R. Nolen, D. H. Olson, K. P. Kelley, A. Cleri, J. Nordlander, J. D. Caldwell, *et al.*, “Long-lived modulation of plasmonic absorption by ballistic thermal injection,” *Nature Nanotechnology*, vol. 16, no. 1, pp. 47–51, 2021.

[217] J. A. Tomko, S. Kumar, R. Sundararaman, and P. E. Hopkins, “Temperature dependent electron–phonon coupling of au resolved via lattice dynamics measured with sub-picosecond infrared pulses,” *Journal of Applied Physics*, vol. 129, no. 19, p. 193104, 2021.

[218] E. L. Radue, J. A. Tomko, A. Giri, J. L. Braun, X. Zhou, O. V. Prezhdo, E. L. Runnerstrom, J.-P. Maria, and P. E. Hopkins, “Hot electron thermoreflectance coefficient of gold during electron–phonon nonequilibrium,” *Acs Photonics*, vol. 5, no. 12, pp. 4880–4887, 2018.

[219] A. Sabbah and D. M. Riffe, “Femtosecond pump-probe reflectivity study of silicon carrier dynamics,” *Physical Review B*, vol. 66, no. 16, p. 165217, 2002.

[220] D. H. Olson, M. G. Sales, J. A. Tomko, T.-F. Lu, O. V. Prezhdo, S. J. McDonnell, and P. E. Hopkins, “Band alignment and defects influence the electron–phonon heat transport mechanisms across metal interfaces,” *Applied Physics Letters*, vol. 118, no. 16, p. 163503, 2021.

[221] Y.-S. Wang, X. Zhou, J. A. Tomko, A. Giri, P. E. Hopkins, and O. V. Prezhdo, “Electron–phonon relaxation at au/ti interfaces is robust to alloying: Ab initio nonadiabatic molecular dynamics,” *The Journal of Physical Chemistry C*, vol. 123, no. 37, pp. 22842–22850, 2019.

[222] T.-F. Lu, Y.-S. Wang, J. A. Tomko, P. E. Hopkins, H.-X. Zhang, and O. V. Prezhdo, “Control of charge carrier dynamics in plasmonic au films by tio x substrate stoichiometry,” *The journal of physical chemistry letters*, vol. 11, no. 4, pp. 1419–1427, 2020.

[223] X. Zhou, M. V. Tokina, J. A. Tomko, J. L. Braun, P. E. Hopkins, and O. V. Prezhdo, “Thin ti adhesion layer breaks bottleneck to hot hole relaxation in au films,” *The Journal of chemical physics*, vol. 150, no. 18, p. 184701, 2019.

[224] L.-D. Zhao, S.-H. Lo, Y. Zhang, H. Sun, G. Tan, C. Uher, C. Wolverton, V. P. Dravid, and M. G. Kanatzidis, "Ultralow thermal conductivity and high thermoelectric figure of merit in snse crystals," *Nature*, vol. 508, no. 7496, p. 373, 2014.

[225] W. Lee, H. Li, A. B. Wong, D. Zhang, M. Lai, Y. Yu, Q. Kong, E. Lin, J. J. Urban, J. C. Grossman, *et al.*, "Ultralow thermal conductivity in all-inorganic halide perovskites," *Proceedings of the National Academy of Sciences*, vol. 114, no. 33, pp. 8693–8697, 2017.

[226] A. Giri, A. Z. Chen, A. Mattoni, K. Aryana, D. Zhang, X. Hu, S.-H. Lee, J. J. Choi, and P. E. Hopkins, "Ultralow thermal conductivity of two-dimensional metal halide perovskites," *Nano Letters*, 2020.

[227] W.-L. Ong, E. S. O'Brien, P. S. Dougherty, D. W. Paley, C. F. Higgs III, A. J. McGaughey, J. A. Malen, and X. Roy, "Orientational order controls crystalline and amorphous thermal transport in superatomic crystals," *Nature Materials*, vol. 16, no. 1, pp. 83–88, 2017.

[228] J. L. Braun, C. M. Rost, M. Lim, A. Giri, D. H. Olson, G. N. Kotsonis, G. Stan, D. W. Brenner, J.-P. Maria, and P. E. Hopkins, "Charge-induced disorder controls the thermal conductivity of entropy-stabilized oxides," *Advanced Materials*, vol. 30, no. 51, p. 1805004, 2018.

[229] A. Mavrokefalos, N. T. Nguyen, M. T. Pettes, D. C. Johnson, and L. Shi, "In-plane thermal conductivity of disordered layered w se 2 and (w) x (w se 2) y superlattice films," *Applied Physics Letters*, vol. 91, no. 17, p. 171912, 2007.

[230] M. G. Ghossoub, J.-H. Lee, O. T. Baris, D. G. Cahill, and S. Sinha, "Percolation of thermal conductivity in amorphous fluorocarbons," *Physical Review B*, vol. 82, no. 19, p. 195441, 2010.

[231] S. W. King, J. Bielefeld, G. Xu, W. A. Lanford, Y. Matsuda, R. H. Dauskardt, N. Kim, D. Hondongwa, L. Olasov, B. Daly, *et al.*, "Influence of network bond percolation on the thermal, mechanical, electrical and optical properties of high and low-k a-sic: H thin films," *Journal of Non-Crystalline Solids*, vol. 379, pp. 67–79, 2013.

[232] J. L. Braun, S. W. King, A. Giri, J. T. Gaskins, M. Sato, T. Fujiseki, H. Fujiwara, and P. E. Hopkins, "Breaking network connectivity leads to ultralow thermal conductivities in fully dense amorphous solids," *Applied Physics Letters*, vol. 109, no. 19, p. 191905, 2016.

[233] J. C. Phillips, "Topology of covalent non-crystallien solids i: Short-range order in chalcogenide alloys," *Journal of Non-Crystalline Solids*, vol. 34, p. 153, 1979.

[234] X. Feng, W. Bresser, and P. Boolchand, "Direct evidence for stiffness threshold in chalcogenide glasses," *Physical Review Letters*, vol. 78, no. 23, p. 4422, 1997.

[235] D. Selvanathan, W. Bresser, P. Boolchand, and B. Goodman, "Thermally reversing window and stiffness transitions in chalcogenide glasses," *Solid state communications*, vol. 111, no. 11, pp. 619–624, 1999.

[236] H. M. Flores-Ruiz, G. G. Naumis, and J. Phillips, "Heating through the glass transition: a rigidity approach to the boson peak," *Physical Review B*, vol. 82, no. 21, p. 214201, 2010.

[237] R. Fallica, E. Varesi, L. Fumagalli, S. Spadoni, M. Longo, and C. Wiemer, "Effect of nitrogen doping on the thermal conductivity of gete thin films," *physica status solidi (RRL)–Rapid Research Letters*, vol. 7, no. 12, pp. 1107–1111, 2013.

[238] E. Bosoni, D. Campi, D. Donadio, G. Sosso, J. Behler, and M. Bernasconi, "Atomistic simulations of thermal conductivity in gete nanowires," *Journal of Physics D: Applied Physics*, vol. 53, no. 5, p. 054001, 2019.

[239] S. Asokan, G. Parthasarathy, and E. Gopal, "Crystallization studies on bulk sixte100-x glasses," *Journal of non-crystalline solids*, vol. 86, no. 1-2, pp. 48–64, 1986.

[240] J. L. Braun, C. H. Baker, A. Giri, M. Elahi, K. Artyushkova, T. E. Beechem, P. M. Norris, Z. C. Leseman, J. T. Gaskins, and P. E. Hopkins, "Size effects on the thermal conductivity of amorphous silicon thin films," *Physical Review B*, vol. 93, p. 140201, 2016.

[241] B. Bureau, S. Danto, H. L. Ma, C. Boussard-Plédel, X. H. Zhang, and J. Lucas, "Tellurium based glasses: A ruthless glass to crystal competition," *Solid State Sciences*, vol. 10, no. 4, pp. 427–433, 2008.

[242] C. Y. Ho, R. W. Powell, and P. E. Liley, "Thermal conductivity of the elements," *Journal of Physical and Chemical Reference Data*, vol. 1, no. 2, pp. 279–421, 1972.

[243] H. Peng, N. Kioussis, and D. A. Stewart, "Anisotropic lattice thermal conductivity in chiral tellurium from first principles," *Applied Physics Letters*, vol. 107, no. 25, p. 251904, 2015.

[244] S. Lin, W. Li, Z. Chen, J. Shen, B. Ge, and Y. Pei, "Tellurium as a high-performance elemental thermoelectric," *Nature communications*, vol. 7, no. 1, pp. 1–6, 2016.

[245] L. A. Kulakova, V. K. Kudoyarova, B. T. Melekh, and V. I. Bakharev, "Electrical, acoustic, and acoustooptical properties of si(ge)-se-te glasses," *Chalcogenide Letters*, vol. 2, p. 83, 2005.

[246] V. Kozhevnikov, W. Payne, J. Olson, A. Allen, and P. Taylor, "Sound velocity in liquid and glassy selenium," *Journal of non-crystalline solids*, vol. 353, no. 32-40, pp. 3254–3259, 2007.

[247] I. Cox-Smith, H. Liang, and R. Dillon, "Sound velocity in amorphous films of germanium and silicon," *Journal of Vacuum Science & Technology A: Vacuum, Surfaces, and Films*, vol. 3, no. 3, pp. 674–677, 1985.

[248] D. P. Sellan, E. S. Landry, J. Turney, A. J. McGaughey, and C. H. Amon, “Size effects in molecular dynamics thermal conductivity predictions,” *Physical Review B*, vol. 81, no. 21, p. 214305, 2010.

[249] T. Hori, T. Shiga, and J. Shiomi, “Phonon transport analysis of silicon germanium alloys using molecular dynamics simulations,” *Journal of Applied Physics*, vol. 113, no. 20, p. 203514, 2013.

[250] A. Giri, B. F. Donovan, and P. E. Hopkins, “Localization of vibrational modes leads to reduced thermal conductivity of amorphous heterostructures,” *Physical Review Materials*, vol. 2, no. 5, p. 056002, 2018.

[251] H. R. Seyf and A. Henry, “A method for distinguishing between propagons, diffusions, and locons,” *Journal of Applied Physics*, vol. 120, no. 2, p. 025101, 2016.

[252] J. Moon and A. J. Minnich, “Sub-amorphous thermal conductivity in amorphous heterogeneous nanocomposites,” *RSC Advances*, vol. 6, p. 105154, 2016.

[253] J. Chen, G. Zhang, and B. Li, “Remarkable reduction of thermal conductivity in silicon nanotubes,” *Nano Letters*, vol. 10, p. 3978, 2010.

[254] L. Yang, N. Yang, and B. Li, “Extreme low thermal conductivity in nanoscale 3d phononic crystals with spherical pores,” *Nano Letters*, vol. 14, p. 1734, 2014.

[255] M. Popescu, *Non-crystalline chalcogenides*. Dordrecht,: Kluwer Academic Publishers, 2001.

[256] J. Philip and K. Madhusoodanan, “Percolation threshold of thermal conduction in a x iv b 1- x vi chalcogenide semiconducting glasses,” *Physical Review B*, vol. 38, no. 6, p. 4127, 1988.

[257] J. Lonergan, C. Smith, D. McClane, and K. Richardson, “Thermophysical properties and conduction mechanisms in asxse1- x chalcogenide glasses ranging from x= 0.2 to 0.5,” *Journal of Applied Physics*, vol. 120, no. 14, p. 145101, 2016.

[258] L. Wei, M. Vaudin, C. S. Hwang, G. White, J. Xu, and A. J. Steckl, “Heat conduction in silicon thin films: Effect of microstructure,” *Journal of materials research*, vol. 10, no. 8, pp. 1889–1896, 1995.

[259] S.-N. Zhang, J. He, T.-J. Zhu, X.-B. Zhao, and T. M. Tritt, “Thermal conductivity and specific heat of bulk amorphous chalcogenides ge20te80- xsex (x= 0, 1, 2, 8),” *Journal of Non-Crystalline Solids*, vol. 355, no. 2, pp. 79–83, 2009.

[260] A. P. Gonçalves, E. B. Lopes, O. Rouleau, and C. Godart, “Conducting glasses as new potential thermoelectric materials: the cu–ge–te case,” *Journal of Materials Chemistry*, vol. 20, no. 8, pp. 1516–1521, 2010.

[261] R. J. Warzoha, B. F. Donovan, N. T. Vu, J. G. Champlain, S. Mack, and L. B. Ruppalt, “Nanoscale thermal transport in amorphous and crystalline gete thin-films,” *Applied Physics Letters*, vol. 115, no. 2, p. 023104, 2019.

[262] I. Kaban, T. Halm, W. Hoyer, P. Jovari, and J. Neuefeind, "Short-range order in amorphous germanium–tellurium alloys," *Journal of non-crystalline solids*, vol. 326, pp. 120–124, 2003.

[263] G. Wehmeyer, T. Yabuki, C. Monachon, J. Wu, and C. Dames, "Thermal diodes, regulators, and switches: Physical mechanisms and potential applications," *Applied Physics Reviews*, vol. 4, no. 4, p. 041304, 2017.

[264] Z. He, Y. Yan, and Z. Zhang, "Thermal management and temperature uniformity enhancement of electronic devices by micro heat sinks: A review," *Energy*, p. 119223, 2020.

[265] X. Gou, H. Ping, Q. Ou, H. Xiao, and S. Qing, "A novel thermoelectric generation system with thermal switch," *Applied Energy*, vol. 160, pp. 843–852, 2015.

[266] Y. Pei, H. Wang, and G. J. Snyder, "Band engineering of thermoelectric materials," *Advanced Materials*, vol. 24, no. 46, pp. 6125–6135, 2012.

[267] J. F. Ihlefeld, B. M. Foley, D. A. Scrymgeour, J. R. Michael, B. B. McKenzie, D. L. Medlin, M. Wallace, S. Trolier-McKinstry, and P. E. Hopkins, "Room-temperature voltage tunable phonon thermal conductivity via reconfigurable interfaces in ferroelectric thin films," *Nano Letters*, vol. 15, no. 3, pp. 1791–1795, 2015.

[268] Q. Lu, S. Huberman, H. Zhang, Q. Song, J. Wang, G. Vardar, A. Hunt, I. Waluyo, G. Chen, and B. Yildiz, "Bi-directional tuning of thermal transport in $SrCoO_x$ with electrochemically induced phase transitions," *Nature Materials*, pp. 1–8, 2020.

[269] J. Cho, M. D. Losego, H. G. Zhang, H. Kim, J. Zuo, I. Petrov, D. G. Cahill, and P. V. Braun, "Electrochemically tunable thermal conductivity of lithium cobalt oxide," *Nature Communications*, vol. 5, no. 1, pp. 1–6, 2014.

[270] J. Shin, J. Sung, M. Kang, X. Xie, B. Lee, K. M. Lee, T. J. White, C. Leal, N. R. Sottos, P. V. Braun, *et al.*, "Light-triggered thermal conductivity switching in azobenzene polymers," *Proceedings of the National Academy of Sciences*, vol. 116, no. 13, pp. 5973–5978, 2019.

[271] J. Shin, M. Kang, T. Tsai, C. Leal, P. V. Braun, and D. G. Cahill, "Thermally functional liquid crystal networks by magnetic field driven molecular orientation," *ACS Macro Letters*, vol. 5, no. 8, pp. 955–960, 2016.

[272] E. Langenberg, D. Saha, M. E. Holtz, J.-J. Wang, D. Bugallo, E. Ferreiro-Vila, H. Paik, I. Hanke, S. Ganschow, D. A. Muller, *et al.*, "Ferroelectric domain walls in $PbTiO_3$ are effective regulators of heat flow at room temperature," *Nano Letters*, vol. 19, no. 11, pp. 7901–7907, 2019.

[273] J. A. Tomko, A. Pena-Francesch, H. Jung, M. Tyagi, B. D. Allen, M. C. Demirel, and P. E. Hopkins, "Tunable thermal transport and reversible thermal conductivity switching in topologically networked bio-inspired materials," *Nature Nanotechnology*, vol. 13, no. 10, pp. 959–964, 2018.

[274] C. Liu, Y. Chen, and C. Dames, “Electric-field-controlled thermal switch in ferroelectric materials using first-principles calculations and domain-wall engineering,” *Physical Review Applied*, vol. 11, no. 4, p. 044002, 2019.

[275] J.-J. Wang, Y. Wang, J. F. Ihlefeld, P. E. Hopkins, and L.-Q. Chen, “Tunable thermal conductivity via domain structure engineering in ferroelectric thin films: a phase-field simulation,” *Acta Materialia*, vol. 111, pp. 220–231, 2016.

[276] P. E. Hopkins, C. Adamo, L. Ye, B. D. Huey, S. R. Lee, D. G. Schlom, and J. F. Ihlefeld, “Effects of coherent ferroelastic domain walls on the thermal conductivity and Kapitza conductance in bismuth ferrite,” *Applied Physics Letters*, vol. 102, no. 12, p. 121903, 2013.

[277] B. M. Foley, M. Wallace, J. T. Gaskins, E. A. Paisley, R. L. Johnson-Wilke, J.-W. Kim, P. J. Ryan, S. Trolier-McKinstry, P. E. Hopkins, and J. F. Ihlefeld, “Voltage-controlled bistable thermal conductivity in suspended ferroelectric thin-film membranes,” *ACS Applied Materials & Interfaces*, vol. 10, no. 30, pp. 25493–25501, 2018.

[278] C. Liu, P. Lu, Z. Gu, J. Yang, and Y. Chen, “Bidirectional tuning of thermal conductivity in ferroelectric materials using E-controlled hysteresis characteristic property,” *The Journal of Physical Chemistry C*, vol. 124, no. 48, pp. 26144–26152, 2020.

[279] O. Fesenko, R. Kolesova, and Y. G. Sindeyev, “The structural phase transitions in lead zirconate in super-high electric fields,” *Ferroelectrics*, vol. 20, no. 1, pp. 177–178, 1978.

[280] Z. Ujma and J. Handerek, “The pyroelectric effect in single crystal and ceramic $PbZrO_3$,” *Ferroelectrics*, vol. 33, no. 1, pp. 37–42, 1981.

[281] A. Mischenko, Q. Zhang, J. Scott, R. Whatmore, and N. Mathur, “Giant electrocaloric effect in thin-film $PbZr_{0.95}Ti_{0.05}O_3$,” *Science*, vol. 311, no. 5765, pp. 1270–1271, 2006.

[282] B. Tuttle and D. Payne, “The effects of microstructure on the electrocaloric properties of Pb (Zr, Sn, Ti) $O_3$ ceramics,” *Ferroelectrics*, vol. 37, no. 1, pp. 603–606, 1981.

[283] B. Jaffe, W. R. Cook, and H. L. Jaffe, “Piezoelectric ceramics. Academic Press, London,” 1971.

[284] R. Gao, S. E. Reyes-Lillo, R. Xu, A. Dasgupta, Y. Dong, L. R. Dedon, J. Kim, S. Saremi, Z. Chen, C. R. Serrao, *et al.*, “Ferroelectricity in $Pb_1+\ \delta ZrO_3$ thin films,” *Chemistry of Materials*, vol. 29, no. 15, pp. 6544–6551, 2017.

[285] D. H. Olson, V. A. Avincola, C. G. Parker, J. L. Braun, J. T. Gaskins, J. A. Tomko, E. J. Opila, and P. E. Hopkins, “Anisotropic thermal conductivity tensor of $\beta$-$Y_2Si_2O_7$ for orientational control of heat flow on micrometer scales,” *Acta Materialia*, vol. 189, pp. 299–305, 2020.

[286] D. H. Olson, J. L. Braun, and P. E. Hopkins, "Spatially resolved thermoreflectance techniques for thermal conductivity measurements from the nanoscale to the mesoscale," *Journal of Applied Physics*, vol. 126, no. 15, p. 150901, 2019.

[287] S. Teslic and T. Egami, "Atomic structure of $PbZrO_3$ determined by pulsed neutron diffraction," *Acta Crystallographica Section B: Structural Science*, vol. 54, no. 6, pp. 750–765, 1998.

[288] G. A. Slack, "Nonmetallic crystals with high thermal conductivity," *Journal of Physics and Chemistry of Solids*, vol. 34, no. 2, pp. 321–335, 1973.

[289] A. Tagantsev, K. Vaideeswaran, S. Vakhrushev, A. Filimonov, R. Burkovsky, A. Shaganov, D. Andronikova, A. Rudskoy, A. Baron, H. Uchiyama, *et al.*, "The origin of antiferroelectricity in $PbZrO_3$," *Nature Communications*, vol. 4, no. 1, pp. 1–8, 2013.

[290] Z. Fu, X. Chen, Z. Li, T. Hu, L. Zhang, P. Lu, S. Zhang, G. Wang, X. Dong, and F. Xu, "Unveiling the ferrielectric nature of $PbZrO_3$-based antiferroelectric materials," *Nature Communications*, vol. 11, no. 1, pp. 1–8, 2020.

[291] X.-K. Wei, C.-L. Jia, H.-C. Du, K. Roleder, J. Mayer, and R. E. Dunin-Borkowski, "An unconventional transient phase with cycloidal order of polarization in energy-storage antiferroelectric $PbZrO_3$," *Advanced Materials*, vol. 32, no. 9, p. 1907208, 2020.

[292] S. Yamanaka, T. Maekawa, H. Muta, T. Matsuda, S.-i. Kobayashi, and K. Kurosaki, "Thermophysical properties of $SrHfO_3$ and $SrRuO_3$," *Journal of Solid State Chemistry*, vol. 177, no. 10, pp. 3484–3489, 2004.

[293] J. Hidde, C. Guguschev, S. Ganschow, and D. Klimm, "Thermal conductivity of rare-earth scandates in comparison to other oxidic substrate crystals," *Journal of Alloys and Compounds*, vol. 738, pp. 415–421, 2018.

[294] Y. Ehara, S. Yasui, J. Nagata, D. Kan, V. Anbusathaiah, T. Yamada, O. Sakata, H. Funakubo, and V. Nagarajan, "Ultrafast switching of ferroelastic nanodomains in bilayered ferroelectric thin films," *Applied Physics Letters*, vol. 99, no. 18, p. 182906, 2011.

[295] J. Callaway, "Model for lattice thermal conductivity at low temperatures," *Physical Review*, vol. 113, no. 4, p. 1046, 1959.

[296] P. D. Thacher, "Effect of boundaries and isotopes on the thermal conductivity of lif," *Physical Review*, vol. 156, no. 3, p. 975, 1967.

[297] N. Mingo, L. Yang, D. Li, and A. Majumdar, "Predicting the thermal conductivity of si and ge nanowires," *Nano Letters*, vol. 3, no. 12, pp. 1713–1716, 2003.

[298] B. M. Foley, E. A. Paisley, C. DiAntonio, T. Chavez, M. Blea-Kirby, G. Brennecka, J. T. Gaskins, J. F. Ihlefeld, and P. E. Hopkins, "Phonon scattering mechanisms dictating the thermal conductivity of lead zirconate titanate (pbzr1- x ti x o3) thin films across the compositional phase diagram," *Journal of Applied Physics*, vol. 121, no. 20, p. 205104, 2017.

[299] E. A. Scott, K. Hattar, E. J. Lang, K. Aryana, J. T. Gaskins, and P. E. Hopkins, "Reductions in the thermal conductivity of irradiated silicon governed by displacement damage," *Physical Review B*, vol. 104, no. 13, p. 134306, 2021.

[300] T. Yoshida, Y. Moriya, T. Tojo, H. Kawaji, T. Atake, and Y. Kuroiwa, "Heat capacity at constant pressure and thermodynamic properties of phase transitions in $PbMO_3$ (M= Ti, Zr and Hf)," *Journal of Thermal Analysis and Calorimetry*, vol. 95, no. 2, pp. 675–683, 2009.

[301] J. L. Braun, C. J. Szwejkowski, A. Giri, and P. E. Hopkins, "On the steady-state temperature rise during laser heating of multilayer thin films in optical pump–probe techniques," *Journal of Heat Transfer*, vol. 140, no. 5, 2018.

[302] S. Lee, B. A. Apgar, and L. W. Martin, "Strong visible-light absorption and hot-carrier injection in $tio_2$/$srruo_3$ heterostructures," *Advanced Energy Materials*, vol. 3, no. 8, pp. 1084–1090, 2013.

[303] M. Salinga and M. Wuttig, "Phase-change memories on a diet," *Science*, vol. 332, no. 6029, pp. 543–544, 2011.

[304] W. Xu, S.-Y. Min, H. Hwang, and T.-W. Lee, "Organic core-sheath nanowire artificial synapses with femtojoule energy consumption," *Science Advances*, vol. 2, no. 6, p. e1501326, 2016.

[305] I. Boybat, M. Le Gallo, S. Nandakumar, T. Moraitis, T. Parnell, T. Tuma, B. Rajendran, Y. Leblebici, A. Sebastian, and E. Eleftheriou, "Neuromorphic computing with multi-memristive synapses," *Nature Communications*, vol. 9, no. 1, pp. 1–12, 2018.

[306] T. Tuma, A. Pantazi, M. Le Gallo, A. Sebastian, and E. Eleftheriou, "Stochastic phase-change neurons," *Nature Nanotechnology*, vol. 11, no. 8, p. 693, 2016.

[307] M. Salinga, B. Kersting, I. Ronneberger, V. P. Jonnalagadda, X. T. Vu, M. Le Gallo, I. Giannopoulos, O. Cojocaru-Mirédin, R. Mazzarello, and A. Sebastian, "Monatomic phase change memory," *Nature Materials*, vol. 17, no. 8, pp. 681–685, 2018.

[308] D. R. Clarke and S. R. Phillpot, "Thermal barrier coating materials," *Materials today*, vol. 8, no. 6, pp. 22–29, 2005.

[309] R. Simmons and R. Balluffi, "Measurements of equilibrium vacancy concentrations in aluminum," *Physical Review*, vol. 117, no. 1, p. 52, 1960.

[310] P. Buffat and J. P. Borel, “Size effect on the melting temperature of gold particles,” *Physical Review A*, vol. 13, no. 6, p. 2287, 1976.

[311] C. M. Rost, J. Braun, K. Ferri, L. Backman, A. Giri, E. J. Opila, J.-P. Maria, and P. E. Hopkins, “Hafnium nitride films for thermoreflectance transducers at high temperatures: Potential based on heating from laser absorption,” *Applied Physics Letters*, vol. 111, no. 15, p. 151902, 2017.

[312] D. H. Olson, J. A. Deijkers, K. Quiambao-Tomko, J. T. Gaskins, B. T. Richards, E. J. Opila, P. E. Hopkins, and H. N. Wadley, “Evolution of microstructure and thermal conductivity of multifunctional environmental barrier coating systems,” *Materials Today Physics*, vol. 17, p. 100304, 2021.

[313] B. Wang, K. Aryana, J. T. Gaskins, P. E. Hopkins, S. V. Khare, and D. Gall, “Structural stabilization and piezoelectric enhancement in epitaxial (ti1- xmgx) 0.25 al0. 75n (0001) layers,” *Advanced Functional Materials*, vol. 30, no. 30, p. 2001915, 2020.

[314] M. S. B. Hoque, Y. R. Koh, J. L. Braun, A. Mamun, Z. Liu, K. Huynh, M. E. Liao, K. Hussain, Z. Cheng, E. R. Hoglund, *et al.*, “High in-plane thermal conductivity of aluminum nitride thin films,” *ACS Nano*, 2021.

[315] M. S. B. Hoque, Y. R. Koh, K. Aryana, E. R. Hoglund, J. L. Braun, D. H. Olson, J. T. Gaskins, H. Ahmad, M. M. M. Elahi, J. K. Hite, *et al.*, “Thermal conductivity measurements of sub-surface buried substrates by steady-state thermoreflectance,” *Review of Scientific Instruments*, vol. 92, no. 6, p. 064906, 2021.

[316] Y. R. Koh, M. S. B. Hoque, H. Ahmad, D. H. Olson, Z. Liu, J. Shi, Y. Wang, K. Huynh, E. R. Hoglund, K. Aryana, *et al.*, “High thermal conductivity and thermal boundary conductance of homoepitaxially grown gallium nitride (gan) thin films,” *Physical Review Materials*, vol. 5, no. 10, p. 104604, 2021.

# Appendix A

# Laser Heating

Thermal conductivity measurements for thin films at temperatures above 500°C could be challenging as it requires various equipment to prevent the sample from oxidation as well as a cooling system to maintain the components other than the sample at room temperature. In this appendix, using a continuous laser beam as an external heating source, I demonstrate how optically delivering heat to the surface of the sample can raise the surface temperature up to 500°C and successfully measure the thermal conductivity with time-domain thermoreflectance technique. In addition, I provide some insight on the choice of transducer for high temperature measurements. Optical heating not only provides a more simplistic approach for locally heating the surface of a material, but also allows for rapid changes in the temperature of up to hundreds of degrees in a few nanoseconds. In addition, using an electro-optic modulator, various heating profiles from nanosecond pulses to sinusoidal and square waves can be delivered to the surface of the sample.

Thermal conductivity measurement at high temperatures has a variety of applications, from thermal barrier coatings to thermoelectrics and electronics [16, 308]. Traditionally, for measuring thermal conductivity of materials at temperatures higher than the environment, a resistive heating stage has been used. In this technique, the sample is attached to a metallic chuck that heats up with a resistive element through Joule heating and raises the temperature of the sample accordingly. Although, the use of a resistive heating stage is simple and accurate, there are certain drawbacks that limit their applications. For instance, in resistive heating the entire sample is heated to the temperature of interest and it is impossible to locally heat a small area on the sample while keeping the other regions intact. This is particularly important for testing electronic devices on the order of micrometer where there are many other components that would damage upon exposure to high temperatures. Second, there is a delay time associated with raising the temperature of the entire sample to hundreds of degrees above room temperature in resistive heating which could be up to several minutes. Third, the use of complicated equipment such as water pump to circulate the water around the stage and vacuum pump to remove oxygen around the sample would add instabilities during the measurements. All these limitations, however, can be resolved by using a laser beam to rapidly and locally heat the sample to the temperature of interest. Using a high-power laser source integrated with a electro-optic modulator allows for delivering heat with various waveforms, i.e. sinusoidal, square, pulsed, and etc. In this appendix, I demonstrate how integrating a continuous wave laser with TDTR system enables fast and reliable measurement of thermal properties at elevated temperatures.

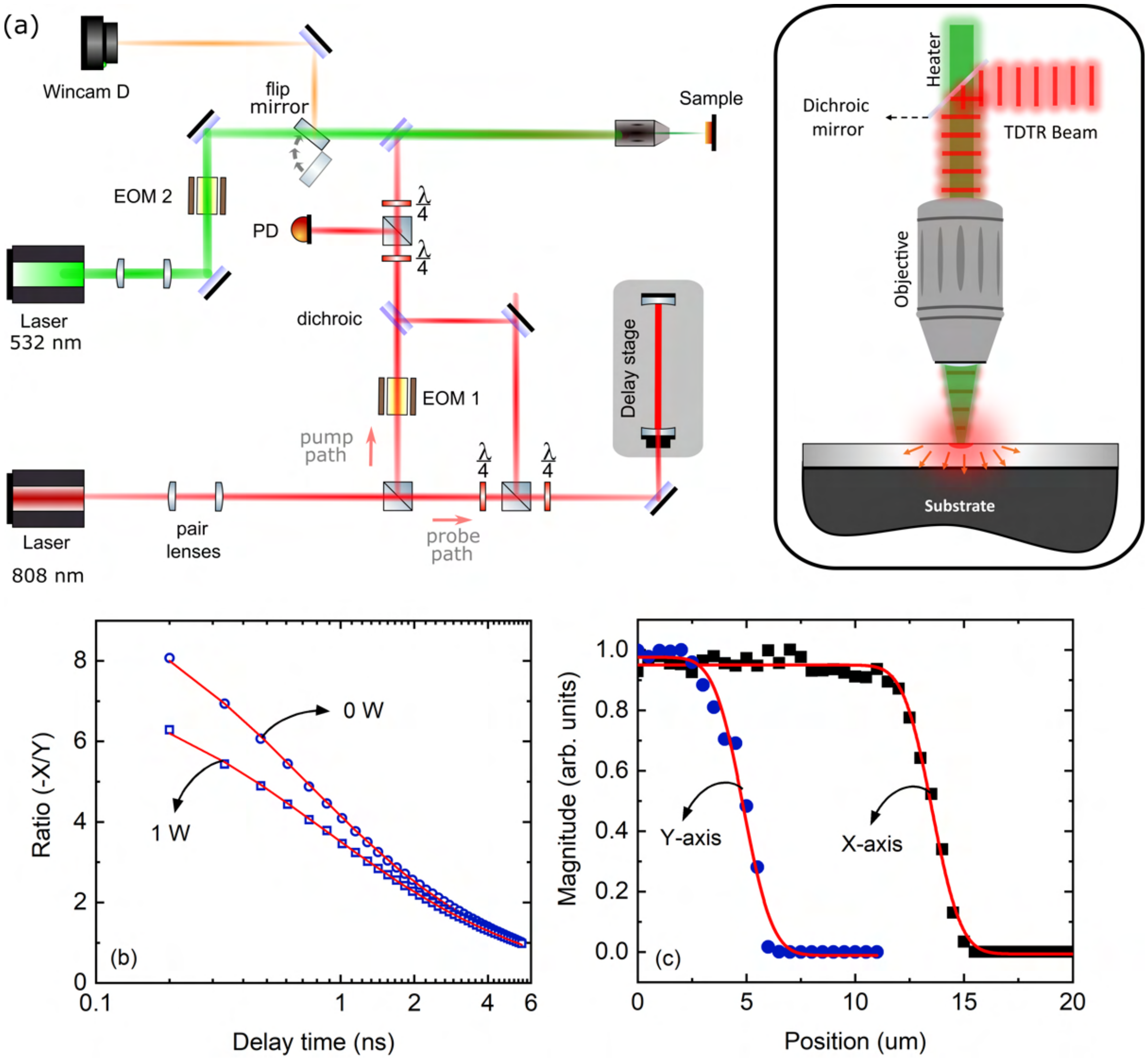

Figure A.1: (a) Laser heating configuration schematics showing the TDTR setup and the added heater laser. (b) TDTR experimental data for Al/Sapphire with its corresponding theoretical fit at two different laser powers. (c) Knife-edge measurements showing the spot sizes for the pump and probe beams.

Here, I demonstrate how locally heating the measurement area using a separate laser beam from that of the TDTR can create a large temperature gradient and change the thermal conductivity of materials by more than a factor of two. For this purpose, we use a continuous wave (CW) laser operating at wavelength of 532 nm. The schematic of the TDTR and the added heater laser configuration is depicted in Fig. A.1. In order to ensure the heater beam is precisely overlapped with the TDTR beams, prior to taking the measurements, the heater beam is modulated passes through an additional electro-optic modulator (EOM) at the similar frequency as the TDTR pump beam (8.4 MHz). By blocking the pump and locking into the modulation frequency of the heater beam and maximizing the signal magnitude, we can ensure the heater beam is overlapped with the TDTR probe beam. Once it is ensured that the heater beam is overlapped with the TDTR, the modulation is turned off and only CW laser is delivered at the surface of the sample for steady state heating.

In order to obtain the spot size for the pump and probe beams, the thermal conductivity of our calibration sample $Al_2O_3$ is measured and by using the known thermal conductivity as an input to our thermal model, the spot sizes are adjusted to obtain the expected thermal conductivity. According to this method and using a 20× objective, a spot size of $\sim$4.3 $\mu$m in diameter is obtained for the pump and probe beams. Although pump and probe beam in our TDTR setup have different sizes, since the thermal model takes their weighted average, I assume that they have the same size. In order to ensure the accuracy of our measurements, the spot sizes are measured using knife-edge technique that yields a spot size of $\sim$4.2 $\mu$m for both pump and probe in close agreement with the fitting for the spot size.

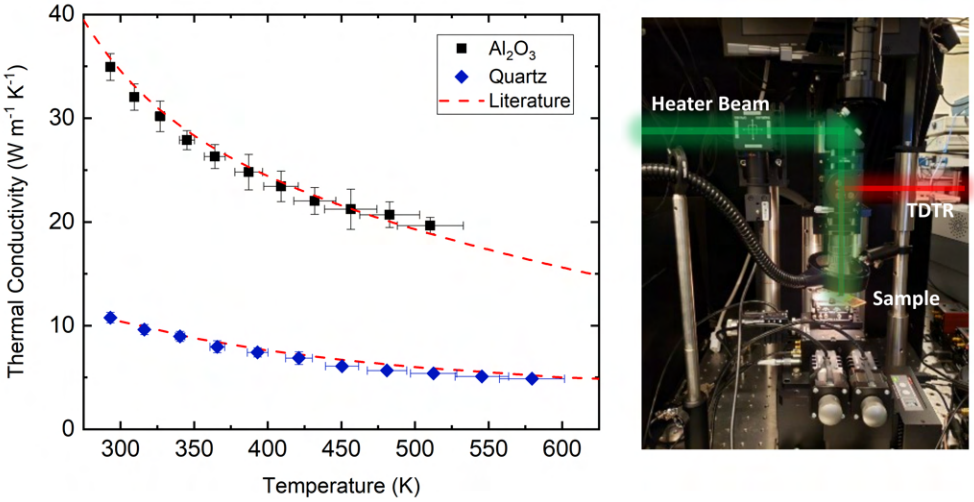

Figure A.2: Thermal conductivity of $SiO_2$ and $Al_2O_3$ as a function of calculated temperature rise from the heater beam.

In order to validate the laser heating experiment, I perform thermal conductivity measurements as a function of laser power for different standard calibration substrates, i.e., quartz ($SiO_2$) and sapphire ($Al_2O_3$). One of the challenges with laser heating experiment is estimation of temperature rise within the probed region. Since laser locally heats the surface of the sample, not only a radial temperature gradient exist from the center of the beam towards the edges, but also there is a temperature gradient in the through-plane direction. For estimating the temperature rise as a result of laser heating, I turn to finite element simulations and assuming a Gaussian beam shape with a thermal penetration depth of $d_{p,z} = \sqrt{\kappa_z/\pi f_{mod} C}$ an average temperature rise within the probed volume is predicted based on the heater beam spot size and power (see Fig. 7.2(d)). The result of these measurements with their corresponding literature values is plotted in Fig. A.2, showing great agreement between the measure value and the estimated temperature rise within the probed volume. In addition, a snapshot of the experimental setup showing the configuration of the heater beam with the TDTR beams is given in Fig. A.2.

In the previous section, the laser heating experiment was performed on samples that were coated with an Al transducer, which prevented measurements at high laser powers

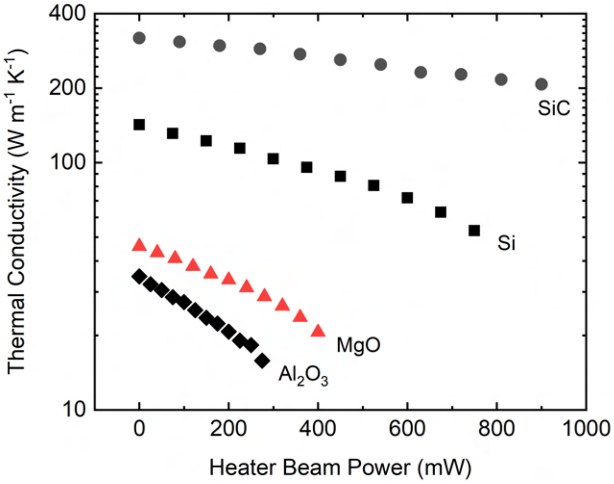

Figure A.3: Thermal conductivity of various substrates as a function of laser power.

due to its low melting temperature (660 °C) [309]. This led me to explore alternative transducer materials to induce larger temperature gradients with the laser beam. For this, gold seems a suitable material candidate for high temperature measurements due to it relatively high melting temperature (1064°C) and resistance against oxidation [310]. Nonetheless, gold is infamous for its poor adhesion to other materials, leading to low thermal boundary conductances that prevent it from optimally delivering heat to the substrate [103]. Hafnium nitride (HfN) is an electrically conductive ceramic with an extremely high melting point of 3385°C that has been employed as transducer for laser heating [311]. For this, different substrates like $Al_2O_3$, MgO, Si, and SiC are prepared and coated with HfN. After performing laser heating experiment and thermal conductivity measurement as presented in Fig. A.3, it is observed that the samples damage at power densities not significantly higher than Al transducer. I repeat this measurement under Argon flow and with low increase rate in power, but a similar result is observed. According to the measured thermal conductivity, the HfN is damaged at temperatures below 600°C which is not expected. This could be partially due to the low thermal conductivity of HfN. More detailed characterizations and experiments are required to pinpoint the underlying reason behind this low melting point of HfN which is beyond the scope of this dissertation. The thermal conductivity measurements thus far, have demonstrated that laser heating could be a suitable approach to locally heating materials and measuring their thermal properties.

A recently developed technique in our lab thermal conductivity mapping if a two-dimensional area on the surface of the sample [312]. Combining a phase-change material, laser heating, and thermal conductivity mapping, an arbitrary pattern with distinct thermal conductivity can be encrypted underneath the transducer and subsequently mapped. To demonstrate this, I take a 160 nm thick as-deposited amorphous GST sample that is coated with 80 nm of Ru transducer and heat it with the heater laser introduced in this appendix. The heater laser induces phase transition at the location of the beam with a spatial resolution of beam diameter, and by moving the sample in certain directions, a specific pattern can be created. Since the thermal conductivity of GST can change by an order of magnitude upon heating, optically heating GST can create a pattern where the thermal conductivity in the heated regions is almost an order of magnitude higher than the background. In this approach, the blanket coated a-GST sample serves as a thermal canvas and the heater laser serves as a thermal pen. To demonstrate this, the heater laser is used to write "UVA" on the GST sample, and using thermal conductivity mapping, we can see the changes in thermal conductivity on the surface of the sample as presented in Fig. A.4(a). As can be seen in Fig. A.4(b), the reflectivity of the sample remains intact during the laser heating which is an indicative of changes in the thermal conductivity of GST film rather than damages to the transducer. This technique can be used to create any arbitrary pattern or encrypted texts with a few microns resolution depending on the heater beam spot size, in this case, ∼4 um.

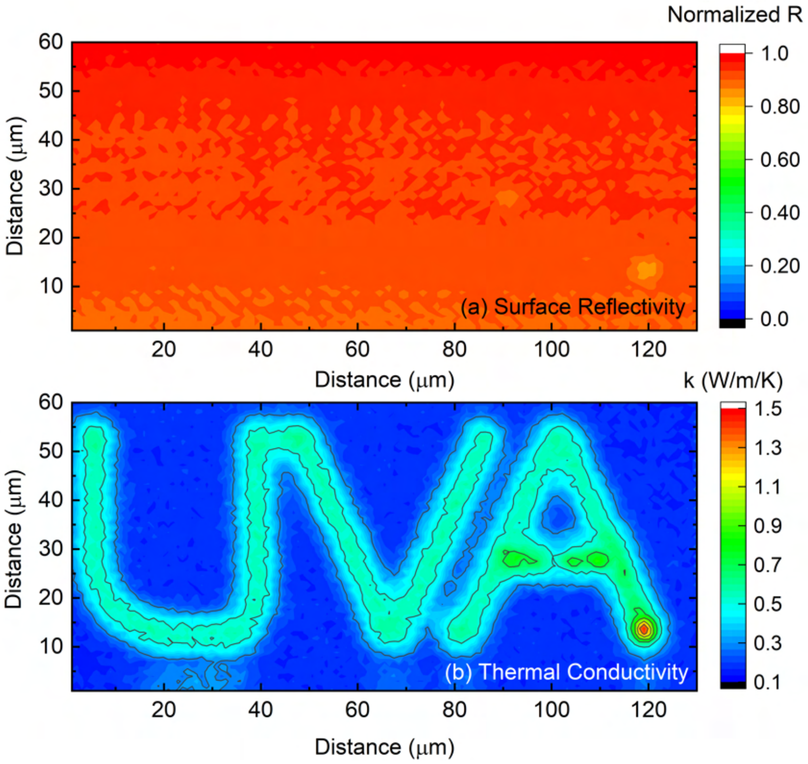

Figure A.4: (a) Surface reflectivity signal (b) thermal conductivity map for a 160-nm-thick blanket coated GST film, showing regions with distinct thermal conductivity as a result of phase transition induced by heater beam with a spot size of ∼4 um.

# Appendix B

# Published Work

Thus far, I have made several contributions in the form of peer-reviewed journal publications to the scientific community and have published five first-author papers, four of which are published in the journal of *Nature Communications* [16, 41, 62, 195]. In addition to my projects, I collaborated with several researchers within academia and industry, which resulted in six co-authored publications [226, 299, 313–316]. The following publications are the result of my studies during my Ph.D. in reverse chronological order:

11. **Aryana, K., Tomko, J.A., Gao, R., Hoque, M.S.B., Pfeifer, T.W., Salanova, A., Olson, D.H., Braun, J.L., Hoglund, E.R., Nag, J., Read, J.C., Grobis, M.K., Howe, J.M., Opila, E.J., Martin, L.W., Ihlefeld, J.F., Hopkins, P.E., Observation of solid-state bidirectional thermal conductivity switching in antiferroelectric lead zirconate (PbZrO$_3$),** ***Nature Communications*****, 13 (1):1-9, 2022.**

10. **Aryana, K., Zhang, Y., Hoque, M.S.B, Tomko, J.A., Hoglund, E.R., Olson, D.H., Nag, J., Read, J.C., Ríos, C. Hu, J., and Hopkins, P.E., Suppressed electronic contribution in thermal conductivity of Ge$_2$Sb$_2$Se$_4$Te,** ***Nature Communications*****, 12 (1):1-9, 2021.**

9. Koh, Y.R., Hoque, M.S.B., Ahmad, H., Olson, D.H, Liu, Z., Shi, J., Steven, W., Huynh, K., Hoglund, E.R., **Aryana, K.**, Howe, J.M., Goorsky, M.S., Graham, S., Luo, T., Hite, J.K., Doolittle, W.A., and Hopkins, P.E., High thermal conductivity and thermal boundary conductance of homoepitaxially grown gallium nitride (GaN) thin films, *Physical Review Materials*, 5, 104604, 2021.

8. Scott, E.A., Hattar K., Lang, E.J., **Aryana, K.**, Gaskins, J.T., and Hopkins, P.E., Reductions in the thermal conductivity of irradiated silicon governed by displacement damage, *Physical Review B*,104, 134306, 2021.

7. **Aryana, K., Stewart, D.A., Gaskins, J.T., Nag, J., Read, J.C., Olson, D.H., Grobis, M.K. and Hopkins, P.E., Tuning network topology and vibrational mode localization to achieve ultralow thermal conductivity in amorphous chalcogenides..** ***Nature Communications*****, 12(1):1–9, 2021.**

6. Hoque, M.S.B., Koh, Y.R., **Aryana, K.**, Hoglund, E., Braun, J.L., Olson, D.H., Gaskins, J.T., Ahmad, H., Elahi, M.M.M., Hite, J.K. and Leseman, Z.C., Hopkins, P.E.,Thermal conductivity measurements of sub-surface buried substrates by steady-state thermoreflectance. *Review of Scientific Instruments* **92**, 064906, 2021.

5. Hoque, M.S.B., Koh, Y.R., Braun, J. Mamun, A.,Liu, Z., Huynh, K., Liao, M., Hussain, K., Cheng, Z, Olson, D., Tomko, J., **Aryana, K.**, Galib, R., Gaskins, J., Elahi, M.M.M., Leseman, Z., Luo, T., Graham, S., Goorsky, M., Khan, M.A., Hopkins, P.E. High in-plane thermal conductivity of aluminum nitride thin films. *ACS Nano* **15**, 9588–9599, 2021.

4. **Aryana, K., Gaskins, J.T., Nag, J., Stewart, D.A., Bai, Z., Mukhopadhyay, S., Read, J.C., Olson, D.H., Hoglund, E.R., Howe, J.M. and Giri, A., Hopkins, P.E., Interface controlled thermal resistances of ultra-thin chalcogenide-based phase change memory devices. *Nature Communications*, 12(1):1–11, 2021.**

3. Wang, B., **Aryana, K.**, Gaskins, J.T., Hopkins, P.E., Khare, S.V. and Gall, D., Structural stabilization and piezoelectric enhancement in epitaxial $(Ti_{1-x}Mg_x)_{0.25}Al_{0.75}N(0001)$ layers. *Advanced Functional Materials* **30**, 2001915, 2020.

2. Giri, A., Chen, A.Z., Mattoni, A., **Aryana, K.**, Zhang, D., Hu, X., Lee, S.H., Choi, J.J. and Hopkins, P.E., Ultralow thermal conductivity of two-dimensional metal halide perovskites. *Nano Letters* **20**, 3331-3337, 2020.

1. **Aryana, K., Gaskins, J.T., Nag, J., Read, J.C., Olson, D.H., Grobis, M.K. and Hopkins, P.E., Thermal properties of carbon nitride toward use as an electrode in phase change memory devices. *Applied Physics Letters*, 116(4):043502, 2020.**